Jako Greuters

BSc (hons.)
Technical University of Rijswijk
The Netherlands

Thesis submitted for the Doctor of Philosophy degree of the University of Hull

UV LASER MICROMACHINING OF PHOTONICS MATERIALS

November 2005

Abstract

UV laser micromachining processes have been developed for materials typically used in photonics devices, i.e. indium phosphide, silicon, lithium niobate and fused silica, with the aim to provide alternative solutions for the currently established micromachining technologies of chemical etching and diamond enhanced blade dicing.

The novel micromachining processes were developed with direct writing and mask projection systems. The direct writing system consisted of a 3rd harmonic Nd-YAG solid-state laser while KrF and ArF excimer lasers and a F_2 laser, were integrated into mask projection laser micromachining systems.

The material removal behaviour of all four materials was investigated by determining the average etch rate per laser pulse versus incident fluences. Comparison between the calculated and the experimentally determined threshold fluence for ablation was made and an Arrhenius type thermal model was tested against the material removal behaviour.

Both x and z-cut lithium niobate was used for UV laser micromachining processing and no difference between average etch rate or the final machined microstructures could be seen. With newly developed processes for cutting and passive fibre alignment v-groove machining, a passive fibre alignment platform was produced in x-cut orientated lithium niobate.

Complex 2-D structured microbenches were isolated from silicon wafers with the use of a newly developed laser cutting process based on the direct writing system. By combining this process with that developed for machining v-grooves, self-aligning microbenches with passive fibre alignment v-grooves were fabricated.

Planar and fibre based fused silica materials were machined with a fluorine laser micromachining system. In the planar substrates, ridge optical waveguides and micro-mirrors were machined and the shaping and side polishing of optical fibres tips was attempted. Within photosensitive optical fibre, long period gratings were inscribed by use of mask projection technology. After process development, a combined gain flattening filter was produced.

These studies show that laser micromachining can fulfil a useful role in photonics device manufacture.

Contents

Chapter 5 **Lithium niobate**

Chapter 6 **Silicon**

Chapter 7 **Fused silica**

Chapter 8 **Long period gratings**

1 General introduction

In optical telecommunications, light as an information carrier is transported from a beginning point through a highly transparent optical network to its destination point. Light is generated with a laser diode and coupled into an optical fibre. The information to be transmitted is added by modulating the generated light and is transported through the optical network to its chosen end point where the information is retrieved by converting the light into an electronic signal via an optical detector and decoded. The light signal can be transported through different types of optical networks: ultra-long-haul, long-haul, metro core, access, enterprise and residential. Within ultra-long-haul networks, the signal is sent across thousands of kilometers without electrical signal generation while in long-haul networks the signal is transported across typically one thousand kilometers before signal amplification is required. Through metro core type networks, the type of network mainly installed in large cities or built up areas, the signal travels over several hundreds of kilometers. The access network provides the connection from metro core network to the end-user and the residential network brings the optical fibre into homes.

The devices used within each type of network follow specific selection criteria [1]. In ultra-long-haul networks, the device performance is critical and cost is a secondary requirement while in the relatively short length networks: access, enterprise and residential, cost is a critical factor and the device performance is secondary. In general, there are two groups of telecommunications devices, passive and active, and the difference between them is their requirement for electrical power. The task of a passive device can be carried out without the supply of any electrical power. Examples of passive devices are splitter/combiners based on fused optical fibres, Fibre Bragg Gratings (FBG) [2, 3] inscribed in optical fibres, Mach-Zender interferometers (MZI) and arrayed waveguide gratings (AWG) [4] on planar-based technology. For active devices, a sub-division can be made based on actuation, semiconductor materials and hybridization technology. The actuation devices consist of switches, modulators and tuning devices and their functionality can be based on thermo-, electro-, acousto- and magneto-optical effects. Moving fibre switching technology or microelectromechanical systems (MEMS) and micro optical electromechanical systems (MOEMS) belong to the actuation division. Semiconductor materials are used for making devices for light generation, light detection, amplification, switching and modulation in the form of laser diodes (LD), detectors and semiconductor amplifiers (SOA). The development of devices based on hybridization technology is driven by the desire to reduce device costs while the complexity of the device increases. The manufacture of these devices begins with a planar base material where passive alignment technology components are assembled to form a functional device which consists of different material based components. There is small scale integration of different components into one device. Indium Phosphide based SOA is an example of this integration technology; this device is principally a silicon base material, a microbench, on which an InP chip is assembled and fused silica planar lightwave circuitry is used to couple the light from the fibre in and out of the device [5].

By far the most frequently used material within optical telecommunication is fused silica (SiO_2); it is used for the manufacture of optical fibres and for the planar lightwave circuit (PLC) technology of silica-on-silicon. Both passive and active devices are made with fused silica including couplers [6], switches [7], attenuators [8], lasers [9] and amplifiers [10]. Silicon (Si) is a versatile material for photonics devices as infrared light above 1.2μm can be detected, waveguided, modulated, emitted and switched within silicon [11] and it can be used to make 'microbenches' for devices assembled based on hybridisation technology [12]. The crystal lithium niobate ($LiNbO_3$) has been used, due to its large electro-optic and acousto-optic coefficients, to manufacture active devices of which modulators and switches are the most common [13]. Lasers [14], amplifiers [15], filters [16] or detectors [17] can also be made with this crystal. Indium Phosphide (InP) is a semiconductor material which finds applications for both active and passive components of which lasers [18], detectors [19] and semiconductor optical amplifier [20] are most common. It is also used to make electro-absorption modulators [21], couplers [22], switches [23] and attenuators [24]. Other materials used for manufacturing passive and active devices are Gallium Arsenide, sol-gels and polymers but for the experiments presented here, the materials InP, $LiNbO_3$, Si, and SiO_2 will be used.

The manufacture of planar telecommunication devices consists of two major steps. Firstly multiple components are manufactured onto a wafer-based material, followed by a packaging step where each component is isolated from the wafer, followed by attachment of optical fibres (pigtailing), assembly within durable package and finally testing. The process used to, for example, manufacture $LiNbO_3$ based modulators [25] starts with a blank $LiNbO_3$ wafer on which with chemical etching and diffusion, optical waveguides are added, followed by deposition of electrodes. Multiple modulator chips are prepared on one wafer and are then separated into single chips by dicing with diamond enhanced saw blades. A similar process is carried out for fused silica planar devices where firstly the waveguide structures are chemically etched and separated into single chips via diamond enhanced saw blade cutting. In both cases, optical fibres are attached to the single components and are further packaged as required for the end product [26].

Devices using hybridisation technology are manufactured following an assembly process where predominantly a silicon microbench forms the material on which active components, like InP for SOA, and passive components, like optical fibre arrays, are assembled. The microbench shape and alignment structures on the top surface are used for the alignment of the sub components. Diamond enhanced saw blade cutting and chemical etching are used to produce silicon microbenches with alignment structures as discussed and optical fibre array assemblies.

Chemical etching and diamond enhanced saw blade cutting are used within manufacturing of optical telecommunication devices. Both micromachining technologies have been extensively used within the semiconductor manufacturing industry and due to this, both technologies are well quantified, developed and engineered and with minor process parameter changes the same technology can be applied to other materials, like $LiNbO_3$ and fused silica. Chemical etching and mechanical dicing technology, however, also have drawbacks that could limit future development of optical telecommunication devices.

Chemical etching is a multiple step process where firstly a contact mask is applied to the top surface and patterned with the desired pattern via photolithography, followed by chemical etching of the pattern into the material. After etching the pattern into the material substrate, the contact mask is removed and the material substrate is prepared for further processing. The contact mask has to be applied to the whole surface of the wafer as the etching process exposes the whole wafer area.

Diamond enhanced saw blade cutting technology as used for the dicing of wafer substrates is a technology based on a fast rotating circular disc which by making mechanical contact with the substrate, leads to material being crushed, removed and a cut made. The circular motion of the blade only allows straight cuts; it is not able to make circular or complex 2-D shape cuts. This limits the applications in which diamond blade dicing is used but has in for example square or rectangular integrated circuits, MEMS or planar based photonics devices so far not proven to be a factor. The limits of the dicing technology mean that only rectangular shaped silicon optical microbenches are possible. Currently the passive alignment structures available on the microbenches only allow alignment on the top surface of the bench.

The use of laser micromachining for the manufacturing of photonics telecommunication devices could be beneficial as it is a flexible process and only has local interaction with the material. If the laser is integrated into a micromachining system with motion of the substrate being handled by computer controlled translation stages, complex micromachining structures can be made. Two different types of laser micromachining systems can be applied. One involves a direct writing system where a Gaussian intensity laser beam profile is focused to a small focal spot. Focusing creates high intensities within the focal spot which provides significant material removal when being exposed to the substrate. This technology is known as direct writing and is used for hole drilling, cutting or marking. The alternative is to use a micromachining system mask projection technology and can work satisfactorily even with a low coherence of the laser beam. Micromachining with this technology images mask patterns onto the material substrate with a high-resolution projection lens while the laser beam illuminates the mask. Using a demagnification factor, the projection lens can reduce the mask pattern at the image plane to increase the intensity sufficiently to remove material and pattern the substrate. A major benefit of this technology is its flexibility as by simply replacing the mask with a different pattern, the structures machined into the material substrate can be changed.

These two laser micromachining processes are potentially capable of producing results similar to the those currently used in the manufacturing of photonics device, i.e. chemical etching and mechanical dicing. However, unlike chemical etching, laser technology does not use contact masks, the machining is local and the process is carried out in an atmosphere. Alternatively, if structures are cut with a laser direct writing system they are not limited by the mechanical interaction of a circular blade with the substrate and therefore the cutting of complex 2-D structures could be possible.

The research presented in this thesis deals with the development of ultraviolet laser micromachining processes for four materials typically used within the telecommunication industry: InP, $LiNbO_3$, Si and SiO_2. The aim was to provide novel and alternative micromachining processes to established manufacturing techniques used within the semiconductor industry. Certain limitations on device design and manufacturing are imposed by the use of these semiconductor based technologies which might be avoided with laser based micromachining.

Chapter 2 describes the micromachining technologies currently used within the manufacturing processes of telecommunication devices: chemical etching and diamond enhanced saw blade cutting. The technical principle behind both wet and dry etching, and the process of mechanical dicing of substrates is discussed.

The UV laser micromachining systems used in the experimental studies in this thesis are described in chapter 3. The reasoning behind the use of UV lasers and the principle of photon generation typically related to each laser is described. The design, installation and characterization of each mask projection and direct writing laser system used is described.

The average etch rate per laser pulse and the process of laser material ablation of the semiconductor material InP is reported and discussed in chapter 4. At all four available UV laser wavelengths the average etch rate per pulse versus the incident fluence was determined. Material and radiation related parameters were calculated to allow comparison with the experimental ablation threshold fluence and an Arrhenius type thermal model was fitted to the determined ablation data in an effort to provide a mechanistic description of removal.

Chapter 5 describes experiments carried out on the semiconductor silicon. Firstly, the average etch rate per pulse was measured and a similar comparison to that carried out in chapter 4 was made. A laser based silicon cutting process was developed with the UV direct writing laser system, to machine complex 2-D optical microbenches for passive components alignment. The same laser system was used to develop a novel micromachining process to produce v-grooves in silicon.

In chapter 6 both UV laser direct writing and mask projection systems were applied to the ferro-electric material Lithium Niobate. Firstly, the average etch rate at all four available wavelengths were measured for x-cut and z-cut orientated crystals, followed by the development of a micromachining process for complex 2-D cutting and to machine passive fibre alignment structures. Both development processes were used to machine a passive fibre alignment platform in $LiNbO_3$.

Within chapter 7, the results obtained using a fluorine laser mask projection system to machine optical structures into fused silica based optical telecommunication materials are described. Here, laser processes for the machining of optical waveguides and micro mirrors in planar based substrates were developed and an attempt was made to polish fibre tips and side-polish the cladding of an optical fibre.

Chapter 8 describes the use of a KrF UV laser based mask projection system to inscribe long-period gratings into photosensitive fibre. By investigating different process parameters, a combined long-period grating was written in photosensitive fibre.

At the beginning of each chapter, an introduction is given on how the materials are manufactured, how the manufacturing process currently used is applied and where relevant, where laser micromachining has been used. An overall conclusion is provided in chapter 9 together with an outline of suggestions for possible future work to the work carried out.

Throughout this thesis, particular attention has been paid to explain the development of the final UV laser based micromachining processes which allow novel structures to be machined and which could improve or simplify current technologies.

1.1 References

1. Eldada, L., Optical communication components, *Rev. Sci. instrun.*, 75, 575-593 (2004)
2. Othonos, A., Kalli, K., *"Fiber Bragg Gratings"* (Artech House, 1999)
3. Kashyap, R., *"Fiber Bragg Gratings"* (Academic Press, 1998)
4. Okamoto, K., Recent progress in integrated optics planar lightwave circuits, *Opt. Quantum Electron.* 31, 107-129 (1999)
5. Kelly, A. E., Lealman, I. F., Rivers, L. J., Perrin, S. D., Silver, M., Low noise figure (7.2Bd) and high gain (29db) semiconductor amplifier with a single layer Ar coating, *Electron. Lett.* 33, 536-538 (1997)
6. Lai, Q., Bachmann, M., Melchior, H., Low-loss 1xN multimode interference couplers with homogeneous output power distributions realised in silica on Si material, *Electron. Lett.* 33, 1699-1700 (1997)
7. Goh, T., Yasu, M., Hattori, K., Himeno, A., Okuno, M., Ohmori, Y., Low-loss and high-extinction-ratio silica-based strictly nonblocking 16×16 thermooptic matrix switch, *IEEE Photon. Technol. Lett.* 10, 810-812 (1998)
8. Lenzi, M., Tebaldini, S., Di Mola, D., Brunazzi, S., Cibinetto, L., Power control in the photonic domain based on integrated arrays of optical variable attenuators in glass-on-silicon technology, *IEEE J. Sel. Top. Quantum Electron.* 5, 1289-1297 (1999)
9. Kitagawa, T., Hattori, K., Hibino, Y., Ohmori, Y., Neodymium-doped silica-based planar waveguide lasers, *J. Lightwave Technol.* 12, 436-442 (1994)
10. Kitagawa, T., Hattori, K., Shuto, K., Yasu, M., Kobayashi, M., Horigushi, M., Amplification in erbium-doped silica-based planar lightwave circuits, *Electron. Lett.* 28, 1818-1819 (1992)
11. Soref, R., Silicon-based optoelectronics, *Proc. IEEE* 81, 1687-1706 (1993)
12. Reed, G. T., The optical age of silicon, *Nature* 427, 595-596 (2004)
13. Heismann, F., Korotky, S. K., Veselka, J. J., Lithium niobate integrated optics: selected contemporary devices and system applications, in *Optical fiber telecommunications III* (Academic Press, 1997)
14. Becker, C., Oesselke, T., Pandavenes, J., Ricken, R., Rochhausen, K., Schreiber, G., Sohler, W., Suche, H., Wessel, R., Balsamo, S., Montrosset, I., Sciancalepore, D.,

Advanced Ti:Er:$LiNbO_3$ waveguide lasers, *IEEE J. Sel. Top. Quantum Electron.* 6, 101-113 (2000)

15. Baumann, I., Bosso, S., Brinkmann, R., Corsini, R., Dinand, M., Greiner, A., Schafer, K., Sochtig, J., Suche, H., Wessel, R., Er-doped integrated optical devices in $LiNbO_3$, *IEEE J. Sel. Top. Quantum Electron.* 2, 355-366 (1996)
16. Wehrmann, F., Harizi, C., Herrmann, H., Rust, U., Sohler, W., Westenhofer, S., Integrated optical, wavelength selective, acoustically tunable 2×2 switches (add-drop multiplexers) in $LiNbO_3$, *IEEE J. Sel. Top. Quantum Electron.* 2, 263-269 (1996)
17. Lehman, J. H., Radojevix, A. M., Osgood, Jr., R. M., Levy, M., Pannell, C. N., Fabrication and evaluation of a freestanding pyroelectric detector made from single-crystal $LiNbO_3$ film, *Opt. Lett.* 25. 1657-1659 (2000)
18. Moller, L., Doerr, C. R., Joyner, C. H., Zirngibl, M., Multifrequency laser based on integrated Vernier-Michelson cavity for mode stabilisation, *Electron. Lett.* 36, 540-542 (2000)
19. Chandrasekhar, S., Zirngibl, M., Dentai, A. G., Joyner, C. H., Storz, F., Burrus, C. A., Lunardi, L. M., Monolithic eight-wavelength demultiplexed receiver for dense WDM applications, *IEEE Photon. Technol. Lett.* 7, 1342-1344 (1995)
20. Agrawal, G. P., Habbab, I. M. I., Effect of a four-wave mixing on multichannel amplification in semiconductor laser amplifiers, *Quantum Electron.* 26, 501-505 (1990)
21. Ougazzaden, A., Devaux, F., Strained InGaAsP/InGaAsP/InAsP multi-quantum well structure for polarization insensitive electroabsorption modulator with high power saturation, *Appl. Phys. Lett.* 69, 4131-4132 (1996)
22. Zirngibl, M., Doerr, C. R., Joyner, C. H., Demonstration of a splitter/router based on a chirped waveguide grating router, *IEEE Photon. Technol. Lett.* 10, 87 -89 (1998)
23. Nakatsuhara, K., Mizumoto, T., Hossain, S., Jeong, S.-H., Tsukishima, Y., Ma, B.-J., Nakano, Y., GaInAsP-InP distributed feedback waveguides for all-optical switching, *IEEE J. Sel. Top. Quantum Electron.* 6, 143-149 (2000)
24. Maat, D. H. P., Zhu, Y. C., Groen, F. H., van Brug, H., Frankema, H. J., Leijtens, X. J. M., Polarization-independent dilated InP-based space switch with low crosstalk, *IEEE Photon. Technol. Lett.* 12, 284-286 (2000)

25. Wooton, E. L., Kissa, K. M., Yi-Yan, A., Murphy, E. J., Lafaw, D. A., Hallemeier, P. F., Maack, D., Attanasio, D. V., Fritz, D. J., McBrein, G. J., Bossi, D. E., A review of lithium niobate modulators for fiber-optic communications systems, *IEEE Jour. Sel. Top. Quan. Elec.,*6, 69-82 (2000)
26. Moyer, R. S., Grencavich, R., Judd, F. F., Kershner, C., Minford, W. J., Smith, R. W., Design and qualification of hermetically packaged lithium niobate modulator, *IEEE trans. Comp. Pack. Manu. Tech.* 21, 130-135 (1998)

2 Review

The materials indium phosphide, silicon, lithium niobate and fused silica have found application within a wide range of areas, including integration into photonics devices for the telecommunication industry. The micromachining used to process each of these materials into a photonics device can be divided into a two main types; (i) chemical based etching for micro-structuring and (ii) mechanical interaction based dicing for component separation.

2.1 Chemical etching

Microstructures from the materials discussed in this thesis can be produced with chemical etching technologies and depending on the material and type of structures desired, either wet or dry based etching can be used.

Chemical etching technology is a process step in the manufacture of integrated circuits (IC) and in general can be described by the following sequence:

1. Deposition of a mask layer onto the material surface
2. Exposure and development of a desired mask pattern into the mask layer with photolithography
3. Transferral of a patterned structure into the material substrate by chemical etching
4. Removal of the resist layer

This sequence is known as the 'planar process' [1, 2]. Due to its use within the IC manufacturing, the planar process and chemical etching are highly developed and have been applied to several materials including Si, InP, $LiNbO_3$ and SiO_2. The purpose of the chemical etching process is to transfer the patterned structure, defined by a developed contact mask on the material's surface, into the substrate by selectively removing a significant amount of material. This is done by a chemical reaction between the material and the chemical environment in which the material substrate is placed. These chemical etching reactions can be carried out within a liquid (wet chemical etching), or within a reactive vapour atmosphere, (dry chemical etching). The type of etching structures that can be achieved with both wet and dry chemical etching depend on the material used and the reactive environment. The type of structure etched differs between one with identical etch rate in lateral and downwards direction, isotropic etch, and one with very little lateral activity and etch mainly in the vertical direction, an anisotropic etch. The structures produced with isotropic etching are mainly round with an undercut under the contact mask while anisotropic etching results in structures with straight edges.

2.1.1 Wet etching

The transfer of photoresist patterns on material substrates with wet etching is achieved by submerging the substrate with patterned photoresist in a liquid acid. The etching process is based on oxidization of exposed areas of the substrate material to form compounds which can physically be removed from the surface. This process was first characterized in the 60's and 70's for pattern relay within the planar process of IC manufacturing [3-7]. The most commonly used wet chemical etching acids are hydrofluoric acid (HF), hydrochloric acid (HCL), nitric acid (HNO_3), acetic acid (CH_3COOH) and alkali hydroxide based etchants like potassium hydroxide (KOH). Isotropic structured etching is carried out with one or a combination of the first four acids while anisotropic etching of crystalline substrates, like silicon, can be carried out with the alkali hydroxide based etchants [8]. The advantage of wet etching technology is its simplicity and low processing costs as wet etching can be carried out in wet bench baths. However, due to the added removed material to the etchant, the acid used has a limited lifetime and a risk of contaminating the material substrate is present.

2.1.2 Dry etching

The process of pattern transfer with dry etching involves placing the material substrate within an active gas environment. To contain the reactive gases and to control contact of the gas with the substrate, the etching process is carried out within a vacuum chamber. Several dry etching based processes are available: vapour/gas, photon driven vapour/gas and plasma based etching, of which the plasma-based etching is the most commonly used.

2.1.2.1 Plasma based etching

Plasma etching processes are conducted in a pressure range of 1mTorr to several Torr using halogen-based gases such as CF_4, SF_6, CL_2, HBr and mixtures of these gases with O_2, H_2, Ar and He. The central part of the system is a vacuum chamber in which an RF voltage is applied to one electrode, on which the planar substrate is placed, and a counter electrode. The electric field applied accelerates the electrons and increases their kinetic energy. These energetic electrons collide with the gas atoms and molecules present. The highly energetic electrons are then capable of ionizing and dissociating the gas atoms or molecules of the reaction gases. The atoms and radicals produced via this inelastic collision react further to produce reactive species which come in contact with the material substrate. The adsorbed species react to form volatile products which can desorb into the gas phase and be transported away into the bulk of the plasma. The removed products can either be pumped away or re-disassociated and take part in a new cycle of reactions [8-11]. Ions, electrons and photons also bombard the substrate surface and it has been shown that the etch rate achieved when the substrate is exposed with positive ions is higher and becomes anisotropic as the directionality of the etching is greater in a vertical direction than in a lateral direction [11, 13]. This ion bombardment plasma etching technique is known as Reactive Ion Etching (RIE) and is currently the most commonly used dry etching technology, not only within IC manufacturing processes but also for other 'planar based' manufacturing processes like microelectromechanical systems (MEMS) [14] or fused silica based planar photonics devices [15]. Plasma etching itself, without the ion bombardment, has isotropic etching characteristics and is carried out at a gas pressure around 1 Torr. This process is mainly used for photo resist stripping.

2.1.2.2 Vapour etching

Vapour etching is a spontaneous process carried out within a vacuum chamber in which the material substrate is etched when exposed to a fluorine-based gas. This type of etching process is isotropic and produces a granular structured etched surface which makes this etching process unsuitable for applications where smooth surfaces are required. Costs related to this vapour/gas etching process are low compared to the plasma etching or RIE technologies and when the rough surfaces can be tolerated it is a preferred economical alternative.

2.1.2.3 Laser beam assisted photo chemical etching

Instead of using a plasma or ion bombardment to activate the etching process, a laser beam can be used. Here, the etching process between the reactive gas and the material substrate is activated by photons to achieve localized material removal. The benefit of this is the removal of several 'planar process' steps as no mask layer has to be applied and consequently the photolithography definition of a mask pattern and the spinning and removal of the photoresist. Deep and anisotropic based patterns are possible and are fully dependent on movements of the laser beam over the material substrate. This process is called photochemical etching.

The material substrate is positioned within a reactive gas (halogen, alkyl halides or inorganic halides) and an incident laser beam exposes the substrate surface. The incident laser beam can be a direct writing beam, focused to a small spot, or a mask imaging system. One or several surface etching mechanisms are promoted by the laser beam [16]: (i) the laser radiation is absorbed by the gas phase molecules, photodissociation occurs and free radicals are created that subsequently react vigorous with the nearby surface, (ii) some reactive gas is absorbed by the material surface and the incident laser beam may stimulate the etching reaction and (iii) the laser beam can be absorbed by the material itself and can form electron-hole pairs and /or surface heating and have an positive effect on the chemical etching process.

The advantage of photochemical etching is the type of structures that can be made: overhanging and deep multi level structures are possible and also etching submerged channels within the substrate for microfluid devices is possible. Numerous photochemical etching process combinations have been studied, ranging from laser emitting wavelengths between $\lambda = 157$nm to $\lambda = 11\mu$m with materials like metals, insulators, semiconductors and polymers, including the four materials discussed in this thesis [16-20]. The disadvantage of this technology is that the materials still have to be sealed within a vacuum chamber and the whole substrate surface is exposed to the reactive gasses or liquids.

2.2 Dicing

The dicing process is the first step in the assembly process of each device and in this step the processed wafer is divided into single components for subsequent packaging, including optical surface polishing, fibre pigtailing, and testing. The dicing process is performed by mechanical interaction between the material substrate and an a diamond enhanced dicing blade.

Planar based devices which are used within the telecommunication industry are predominately manufactured on wafer substrates on which multiple components are processed to increase the manufacturing yield. Separating each individual component to allow it to be incorporated into a fully working device is performed with wafer dicing technology. This process has been used within the IC manufacturing industry in the last 30 years [21] without fundamental changes to its steps or mechanisms.

The dicing process is based on a fast rotating abrasive blade making mechanical contact with the wafer substrate. By crushing the wafer material during contact a cut is made and with continued rinsing of de-ionised water during the dicing, debris is flushed away. The dicing blades operate at rotation speeds between 30,000 to 60,000rpm and consist of abrasive diamonds embedded in an electroplated nickel matrix binder. This dicing technology is applied to many substrates, including the materials discussed here of InP, Si, $LiNbO_3$ and SiO_2 but has several drawbacks. Edge chipping and cracks on the top or bottom side of the substrate wafer can occur during the dicing process and reduce the reliability of the separated devices [22]. Also, the circular shape of the dicing blade and its rotational motion allows only linear cuts and orthogonal structures. In the current dicing applications, especially within IC manufacturing and the telecommunication industry this does not impose restrictions, but for future complex 2-D structures; for instance devices based on hybridisation platforms and passive optical alignment structures, it could limit their design and functionality.

2.3 Micromachining of InP, Si, $LiNbO_3$ and SiO_2

The chemical etching and mechanical based micromachining technologies used for the four materials discussed within this thesis are presented at the beginning of each relevant chapter of paragraph. Also, a review of pulsed laser ablation of materials and its mechanism is discussed in the section discussing average etch rates of Indium Phosphide, in Chapter 4.

2.4 References

1. Clemens, J. T., Silicon microelectronics technology, *Bell Lab. Tech. J.* Autumn, 76-102 (1997)
2. Hoerni, J., Planar silicon transistors and diodes, *IRE trans. On electron devices* ED-8, 178 (1961)
3. Robbins, H. R., Schwartz, B., Chemical etching of silicon I. The system HF, HNO_3, H_20 and $HC_2C_3O_2$, *J. Electrochem. Soc.* 106, 505-508 (1959)
4. Robbins, H. R., Schwartz, B., Chemical etching of silicon II. The system HF, HNO_3, H_20 and $HC_2C_3O_2$, *J. Electrochem. Soc.* 107, 108-111 (1960)
5. Robbins, H. R., Schwartz, B., Chemical etching of silicon III. A temperature study in the acid system, *J. Electrochem. Soc.* 108, 365-372 (1961)
6. Robbins, H. R., Schwartz, B., Chemical etching of silicon IV. Etching technology, *J. Electrochem. Soc.* 123, 1903-1909 (1976)
7. Bogenschutz, A. F., Krusemark, W., Locherer, K. H., Mussinger, W., Activation energies in the chemical ethcing of semiconductors in HNO3-HF-CH3COOH, *J. Electrochem. Soc.* 114, 970-973 (1967)
8. Kovacs, G. T., Maluf, N. I., Petersen, K. E., Bulk micromachining silicon, *Proc. IEEE* 86, 1536-1551 (1998)
9. Oehrlin, G. S., Rembetski, J. F., Plasma-based dry etching techniques in the silicon integrated circuit technology, *IBM J. Res. Develop.* 36, 140-157 (1992)
10. Oehrlein, G. S., Surface processes in low pressure plasmas, *Surf. Sci.* 386, 222-230 (1997)
11. Oehrlein, G. S., Doemling, M. F., Kastenmeier, B. E. E., Matsuo, P. J., Rueger, N. R., Schaepkens, M., Standaert, T. E. F. M., Surface science issues in plasma etching, *IBM J. Res. Develop.* 43, 181-197 (1999)
12. Coburn, J. W., Winters, H. F., Ion- and electron-assisted gas-surface chemistry-an important effect in plasma etching, *J. Appl. Phys.* 50, 3189-3196 (1979)
13. Winters, H. F, Coburn, J. W., Surface science aspects of etching reactions, *Surf. Sci. Rep.* 14, 161-269 (1992)
14. Bustillo, J. M., Howe, R. T., Muller, R. S., Surface micromachining for microelectromechanical systems, *Proc. IEEE* 86, 1552-1573 (1998)

15. Kawashi, M., Silica waveguides on silicon and their application to integrated-optics components, *Opt. Quantum Elec.* 22, 391-416 (1990)
16. Jackman, R. B., Photochemical etching of III-V Semiconductors in "*Photochemical processing of electronic materials*", ed. Boys, I. W., Jackman, R. B., (Academic Press, 1992)
17. Bäuerle, B., "*Chemical processing with lasers*" (Springer Verlag, 1986)
18. Boyd, I. W., "*Laser processing of thin films and microstructures*" (Springer Verlag, 1987)
19. Boyd, I. W., Jackman, R. B., "*Photochemical processing of electronic materials*" (Academic Press, 1992)
20. Ehrlich, D. J., Osgood, R. M., Deutsch, T. F., laser chemical technique for rapid direct writing of surface relief in silicon, *Appl. Phys. Lett.* 38, 1018-1020 (1981)
21. Pennings, M. D., von Arx, H. R., New semiconductor wafer dicing system, *Solid-state technology*, 15 (9), 27-28 (1972)
22. Shi, D., Weisshaus, I., Step 1: The back-end process, *Advanced Packaging* Jan, (2000)

3 UV laser micromachining systems

3.1 Introduction

Laser based micromachining processes of photonics materials can be carried out with a wide range of lasers with emission from vacuum ultraviolet (VUV) to infrared (IR). The wavelength is usually selected according to the proposed micro application and photonics materials to be processed and the desired resolution.

For the development of a cutting process, focusing of the laser beam to a small spot is required to achieve high incident fluences, which in turn, results in a high material etch rate. A direct correlation between laser emission wavelength and the focal spot size exists; the shorter the laser emission wavelength used, the smaller the focal spot size. The machining of high resolution patterns onto various material substrates was carried out with mask projection technologies. With these technologies a similar correlation between the pattern resolution achievable and the laser emission wavelength exists; the shorter the wavelength the higher the resolution possible.

Absorption of laser photons by the material substrate is another important parameter. It is described that the energy applied to material surfaces is absorbed in a short depth to achieve material removal in order to minimise thermal damage to the area surrounding the ablation site. Each of the materials investigated; InP, $LiNbO_3$, Si and SiO_2 are used in telecommunication applications where infrared (IR) wavelengths (surrounding λ = 1500 and 980nm) are used and are chosen because of their high transmission in the IR spectrum. Within the visible part of the photon spectrum, between λ = 400nm and λ = 800nm, both $LiNbO_3$ and SiO_2 are transparent and would therefore not be able to be machined with lasers at these wavelengths, as the radiation would not be absorbed, at least not by a single-photon process.

The low resolution, low absorption, and large focal spot achieved when machining with IR lasers and the low absorption achieved by visible lasers mean that they are not suitable for the micromachining applications required to manufacture optical telecommunication devices. However, UV emitting lasers are suitable due to their high absorption and high-resolution characteristics and so are used in the development of laser micromachining processes now discussed further.

3.2 Laser micromachining systems

Currently, two main technologies are used to process photonics materials. Cutting of wafer based substrates for component isolation or for microbench technology and chemical etching of structures into material substrates. Development of laser micromachining could possibly provide an improved alternative to the current methods. In the investigation of this new technique, two different laser micromachining systems were used. A direct writing system, for cutting photonics materials and a mask projection system for the structuring of material surfaces.

3.2.1 Direct writing system

The experiments which investigated the cutting of photonics materials were carried out with a direct writing system based on the 3rd harmonic neodymium yttrium aluminium garnet (YAG) solid-state laser with an emission wavelength of $\lambda = 355$nm. The characteristics of this laser make it very suitable for cutting applications. The transverse laser mode of the beam is TEM_{00} which allows it to be focused to a small spot. Due to this, high incident fluences are achieved, which, together with its high pulse repetition rate of 10 kilohertz or more, allow a relatively large quantity of material to be removed. This Nd:YAG laser consists of several basic components: (i) a laser gain medium, (ii) resonator, (iii) Q-switching device and (iv) harmonic generation crystal.

3.2.1.1 Laser gain medium

The laser gain medium consists of a solid YAG crystalline rod, grown using the Czochralski technique with an Nd doping concentration of 1 to 2%. To achieve population inverse and stimulated emission, the neodymium ions have to be excited to higher energy levels. The energy needed for the excitation is supplied via photons and absorbed by the Nd^{3+} ions. This optical pumping was traditionally done by flash lamps mounted together with the neodymium host in a high reflectivity mirror arrangement but is nowadays done with laser diodes. The latter generate light at a wavelength of ~ 810nm, which corresponds to a strong absorption band of the Nd:YAG, and achieve higher coupling efficiencies at lower thermal loading (see Figure 3.1). As a result, higher pulse repetition rates are possible.

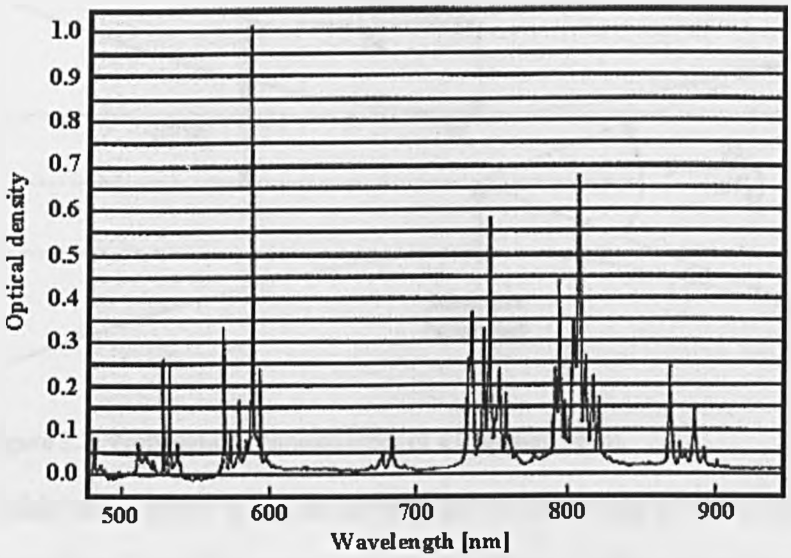

Figure 3.1: Optical density of Nd:YAG versus photon wavelength [1].

Two different diode based pumping schemes can be employed, side pumping or end pumping of the crystal. With side pumping, the diodes are placed along side the rod and are focused to a line in the center of the rod. Single mode operation is difficult to achieve with this scheme and due to the number of diodes, the thermal load on the rod is high. With end pumping, the laser diode beams are delivered on the end face of the rod. The pumping beam(s) are focused into the rod and overlap the oscillating mode of the cavity and depending on the resonators, a Gaussian beam TEM_{00} output beam may be achieved.

3.2.1.2 Resonator

The resonator of the solid-state laser determines various laser beam properties and the propagation of the laser beam within the resonator and beyond, is described by Gaussian beam optics. The variation of irradiance with distance r from the axis for the fundamental Gaussian beam is:

$$I = I_0 e^{\frac{-2r^2}{w^2}} \qquad \text{eq. : 3-1}$$

Here I_o is the maximum on-axis irradiance and w is the distance from the axis where the irradiance has dropped to the $1/e^2$ level. The Gaussian beam has its minimum diameter, $2\omega_0$, at its so-called waist and at this location the wavefront is planar (see Figure 3.2).

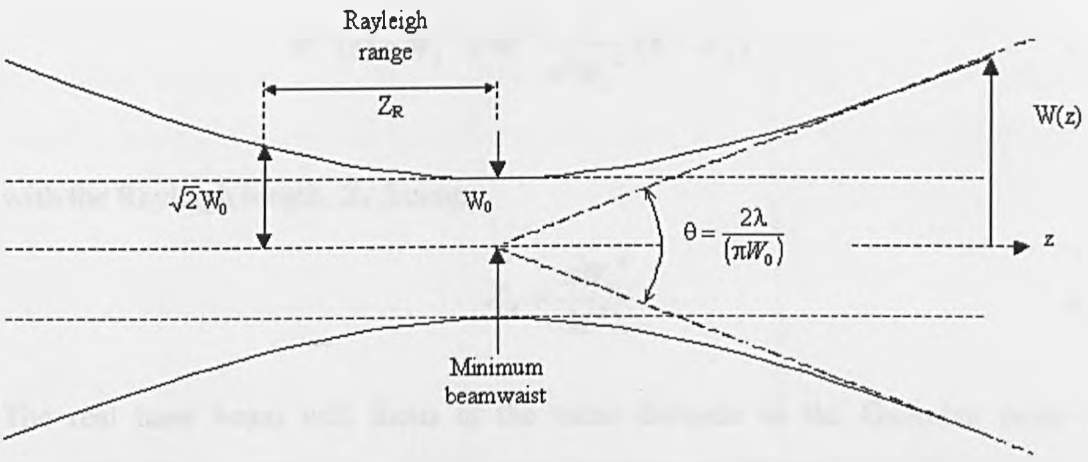

Figure 3.2: Propagation characteristics of a Gaussian beam.

If this waist point is set to correspond to the origin of the z-axis (i.e. at z = 0), the beam propagates from this point such that its beam radius ω_z varies with z as:

$$w_z = w_0\sqrt{1+\left(\frac{\lambda z}{\pi w_0^2}\right)^2} \qquad \text{eq. : 3-2}$$

At distances satisfying $z >> z_R = \frac{\pi\omega_0^2}{\lambda}$, the Rayleigh range, the characteristic beam divergence angle 2β becomes constant:

$$2\beta = \frac{2\omega_z}{z} = \frac{2\lambda}{\pi\omega_0} \qquad \text{eq. : 3-3}$$

The parameters associated with the propagation and dimensions of an ideal Gaussian-shaped beam, often called diffraction limited, has been described but in practice real laser beams are not perfectly Gaussian. Therefore the formulas described above most be modified. A measure of how close a given real laser beam is to the ideal Gaussian laser beam was suggested in 1989 by Siegman and is termed the propagation factor, M^2 [2]. It corresponds to the ratio of the theoretical minimum beam waist attainable for a given divergence to the actual measured minimum beam waist observed. M^2 is defined as:

$$M^2 = \frac{\pi\theta W_0}{2\lambda} \qquad \text{eq. : 3-4}$$

with W_0 as the measured minimum beam radius and θ the measured full angle beam divergence. By using the M^2 factor, the beam radius of a propagating beam along the z-axis can be calculated with its waist as zero point with:

$$W^2(z) = W_0^{\ 2} + M^4 \frac{\lambda^2}{\pi^2 W_0^{\ 2}} (Z - Z_R)^2 \qquad \text{eq.: 3-5}$$

with the Rayleigh length, Z_R, being:

$$Z_R = \frac{\pi W_0^{\ 2}}{M^2 \lambda} \qquad \text{eq.: 3-6}$$

The real laser beam will focus at the same distance as the Gaussian beam when converted by the same lens, but the beam diameter at the focal position is larger. The beam diameter of a focused beam is defined by:

$$\phi_s = \frac{4}{\pi} \frac{f}{2W_z} M^2 \lambda \qquad \text{eq.: 3-7}$$

where f is the focal length of the lens and W_z the beam radius at the aperture of the lens. The $1/e^2$ beam diameter is calculated with the assumption of perfect optics, i.e. no aberrations. Gaussian beam propagation theory was taken from [3].

3.2.1.3 Q-switching

If the neodymium laser is used in continuous wave (CW) mode, the laser output reaches a saturated intensity long before its maximum potential is reached. If it is possible to put a cavity in place after the laser gain medium is pumped to its maximum inversion, the laser will produce a giant pulse with maximum intensity. This technique is called Q-switching; the laser cavity is held at a low Q until the population inversion has reached is maximum value and then suddenly switched to a high Q to produce a giant laser pulse. The laser beam can them be in the form of a train of pulses with the Q-switching device controlling the repetition rate. A Q-switching device is placed within the laser cavity and can be based on rotating mirrors, electro-optic or acousto-optic shutters or on saturable absorbers.

3.2.1.4 Harmonic generation crystal

Harmonic conversion of the Nd-YAG laser fundamental emission wavelength of λ = 1064nm to the 3rd harmonic wavelength of λ = 355nm is carried out with non –linear optical crystals. The conversion is a two-stage process where first the fundamental laser wavelength is converted to the second harmonic at λ =532nm whereafter the remaining fundamental laser emission and the second harmonic radiation are fed through a second non-linear crystal to achieve the third harmonic at λ =355nm. Several suitable non-linear crystals can be used for harmonic generation, e.g. potassium dihydrogen phoshate (KDP), lithium triborate (LBO) and beta barium borate (BBO). An in-depth description of the physical process of harmonic generation is beyond the scope of this chapter but further details can be found in reference [1] and [3].

3.2.1.5 UV solid-state laser micromachining system

The UV solid-state laser micromachining system used for the dicing and cutting of photonics materials in the experiments in this chapter, incorporated a 3rd harmonic Nd-YAG laser manufactured by *Lightwave Electronics*, Model 210s-355-5000 with the laser parameters presented in Table 3.1.

Parameter	**Value**
Emmision wavelength	355 nm
Spatial mode	TEM_{00}
Operating pulse repetition rate	10 kHz
Energy per pulse	500 μJ
Polarization	Horizontal
Waist radius, W_0	0.1mm
Beam divergence (full angle) θ	2.5 mrad

Table 3.1: Laser parameters of *Lightwave Electronics* Model 210s-355-5000.

Using these parameters and equation 3.4, an M^2 value of 1.11 was calculated for the *Lightwave Electronics* laser.

The laser head was integrated into a granite base workstation (see Figure 3.3) where the substrate was held onto a kinetic chuck, positioned on a computer controlled X, Y and Z-axis stage stack. The linear positioning accuracy of the X and Y air bearing stages was 0.1μm with a maximum velocity of V = 3000mm/min. The Z-axis could place the material substrate height to an accuracy of 0.1μm.

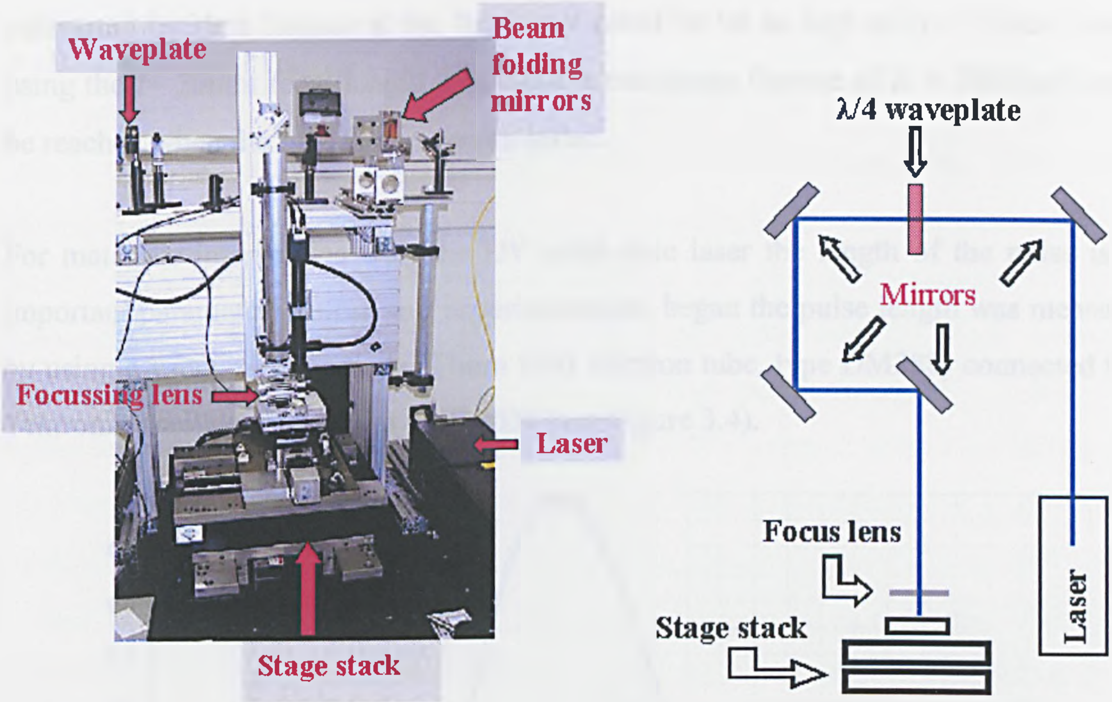

Figure 3.3: (a) UV solid-state laser micromachining system (b) schematic optical layout.

A simple beam delivery system was integrated into the micromachining system, consisting of multi-layer 45° turning mirrors, a λ/4 wave plate and a spherical surface focusing lens (see Figure 3.3). The λ/4 wave plate was included in the beam path to convert the polarization of the laser beam from horizontal to circular to achieve the same etch rates per laser pulse independent of the scan direction. For the laser etch rate experiments and the dicing applications with silicon substrates, a lens of focal length f = 50mm was used while for the experiments with lithium niobate crystal. This was replaced with one of f = 157mm.

With the distance between the beam waist radius W_0 and the position of the lens along the Z-axis being Z = 4080mm, the radius of the laser beam at the lens aperture was calculated by using equation 3.5 and 3.6. The Rayleigh length, following equation 3.6, was calculated to be Z_R = 80mm and a beam radius at the lens aperture of W_z = 5 mm was calculated.

With this value, the spot diameter ϕ of the laser beam after focusing was calculated for each of the two lenses used. For the f = 50 mm lens this gave $\phi_{f=50mm} = 2.5\mu m$ while a larger diameter of $\phi_{f=157mm} = 8\mu m$ was determined for the f = 157 mm lens. The calculated incident fluence at the focal spot could be set as high as $H = 7kJ/cm^2$ when using the f= 50mm focal length lens while a maximum fluence of $H = 700J/cm^2$ could be reached when the f = 157mm was installed.

For materials interactions with the UV solid-state laser the length of the pulse is an important parameter. Before any experimentation began the pulse length was measured by using a vacuum photodiode (Thorn EMI electron tube, type DM288) connected to a Tektronix oscilloscope, model TDS 3034 (see Figure 3.4).

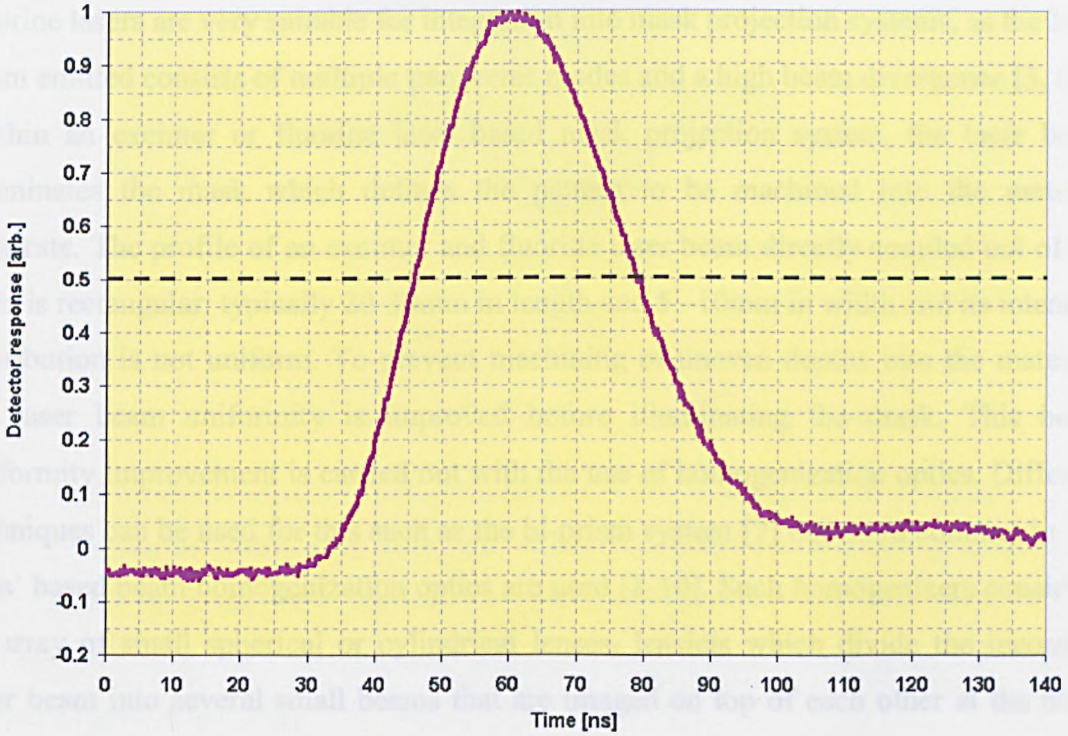

Figure 3.4: Pulse shape of the UV solid state laser micromachining system.

The pulse length of the UV solid-state laser was measured to be T = 30ns at full width half maximum (FWHM). For future referencing, this laser micromachining system will be referred to as the 'UV solid state laser micromachining system'.

University Library Hull

3.2.2 Mask projection systems

Mask projection techniques for micro-structuring are based on imaging a desired pattern onto a substrate using a high-resolution projection lens. The interaction between the photon radiation used and the substrate has to be such that exposed material is removed, leaving a machined structure behind. To minimize the residual interference effects of homogenisation optics at the image plane, the lasers used with the mask projection system must have poor spatial coherence and high beam divergence. Lasers with sufficient transverse modes can be used [4] and in UV systems, Rare Gas Halide and fluorine lasers are very suitable for integration into mask projection systems, as the laser beam emitted consists of multiple transverse modes and a high beam divergence [5, 6]. Within an excimer or fluorine laser based mask projection system, the laser beam illuminates the mask which defines the pattern to be machined into the material substrate. The profile of an excimer and fluorine laser beam directly coupled out of the laser is rectangular: typically 20-30mm in length and 5 –10mm in width and its intensity distribution is not uniform. To prevent machining of uneven depths into the material, the laser beam uniformity is improved before illuminating the mask. This beam uniformity improvement is carried out with the use of homogenization optics. Different techniques can be used for this such as the bi-prism system [7] but more commonly 'fly eyes' based beam homogenization optics are used [8-10]. Such homogenizers consist of an array of small spherical or cylindrical lenses, lenslets which divide the incoming laser beam into several small beams that are imaged on top of each other at the mask plane (see Figure 3.5).

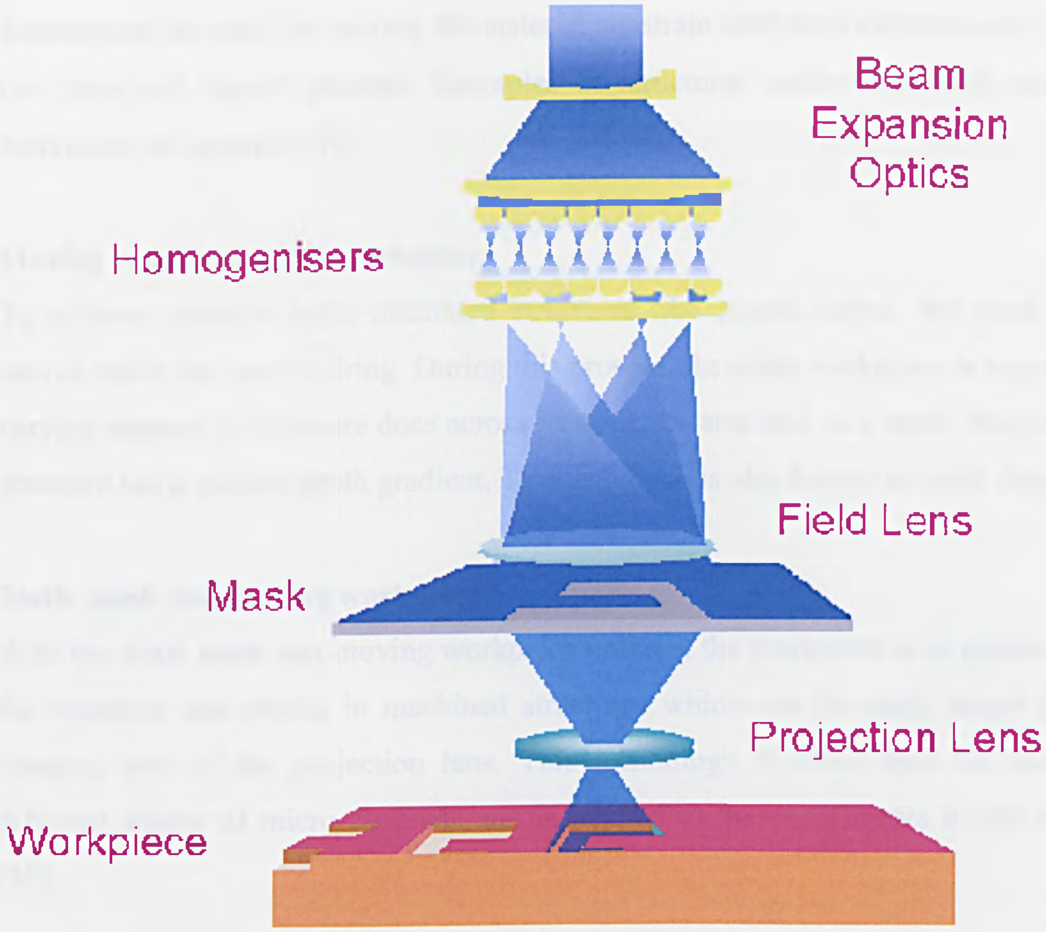

Figure 3.5: 'Fly's eye' homogenizer based mask projection system (courtersey of Dr. N. Rizvi)

By dividing the incoming laser beam into many small parts and overlaying these at the same place at the mask plane, the intensity distribution shows a 'top – hat' profile at this position and is directly imaged onto the material substrate. As a result, the etched structure depth is uniform.

To machine the desired structures into the material substrates, there are five different mask projection technologies which can be used: (i) static mask and workpiece, (ii) moving mask and static workpiece, (iii) static mask and moving workpiece, (iv) moving mask and workpiece and (v) synchronized image scanning.

Static mask and workpiece

In the static mask and static workpiece projection technique, the mask and workpiece are both fixed and the structure to be machined into the substrate has to be small enough to fit within the image area of the projection lens. This technique is most commonly applied in hole drilling or small feature machining. An array of holes or multiple features can be made by moving the material substrate after each exposure and is called the 'step and repeat' process. Examples of structures made with static mask and workpiece are given in [11].

Moving mask and static workpiece

To achieve variable depth machined structures like sloped ramps, the mask can be moved while the laser is firing. During this process, the static workpiece is exposed to a varying amount of exposure dose across its structure area and as a result, the machined structure has a smooth depth gradient. This technique is also known as mask dragging.

Static mask and moving workpiece

With the static mask and moving workpiece process, the workpiece is in motion during the exposure and results in machined structures which can be much larger than the imaging area of the projection lens. This technology is often used for machining different shapes of micro channels and is applied to the experiments in this research [10].

Moving mask and workpiece

This technique is used when structures much larger than the imaging area of the projection lens are to be machined into the substrate. To be able to machine such structures both the mask and its workpiece are in motion and are carefully synchronised with the firing of the laser. Often the projection lens has a de-magnification factor and to compensate for this during machining, the mask moves a the de-magnification factor larger than the workpiece motion. This technique is also referred to as synchronised scanning [12, 13].

Synchronised image scanning

Synchronised image scanning (SIS) is similar to the moving mask and static workpiece technique with the major difference being that the substrate moves continuously during the pulsed laser triggering such that with each laser pulse the image projection onto the substrate has moved by exactly one image repeat pitch. Structures like inkjet printer nozzle holes and microlenses can be machined without complex optical components or substrate rotations. For a full explanation of the SIS techniques see [4, 14].

As mentioned, the static mask – workpiece-dragging technology will mainly be used in the experiments to follow and excimer and fluorine laser based mask projection systems were designed, installed and commissioned with this micromachining process in mind.

3.2.2.1 Excimer lasers based mask projection system

Micromachining experiments were carried out with two different type of excimer laser: a Krypton Fluorine (KrF) laser and an Argon Fluorine (ArF) laser with emission wavelengths of respectively λ = 248nm and λ = 193nm. Before discussing the characteristics of these two micromachining systems, a short description of the laser fundamentals are briefly outlined.

The excimer laser is a pulsed gas laser that makes use of electronic transitions within excited molecules. These excimer molecules have a bound upper state but repulsive ground, and following photoemission they dissociate very rapidly ($\sim10^{-12}$ $\sim10^{-13}$ seconds). Excimer lasers consist typically of three main parts: (i) a laser gas tube, (ii) a high voltage power supply and (iii) control units. The laser tube consists of pumping electrodes, a gas circulation system to ensure purified gas is available between the discharge electrodes, and an optical resonator. The resonator is parallel with the long axis of the discharge electrodes. The gas mixture is contained within the laser tube and consists of rare-gas atoms, a halogen donor and a buffer gas. The laser is excited using a transient discharge, with energy being supplied from a bank of low inductive capacitors charged at a high voltage (~20-40 kV). Normally a thyratron switch is used because of its high pulse rate and low jitter properties. Before the high voltage discharge is applied, the area between the electrodes is seeded with free electrons, usually by transient UV pre-ionization. This pre-ionization process reduces the resistance between the electrodes and is also effective in stabilizing the volume discharge in the gain medium against arc formation.

Various Rare-Gas-Halide excimer lasers are available and their radiation wavelength is determined by the type of rare gas and halogen used (see Table 3.2).

Laser	**Rare Gas**	**Halogen**	**Radiation wavelength λ [nm]**
XeF	Xenon	Fluorine (F_2)	348.8-354.0, 483,486
XeCl	Xenon	Hydrogen chloride (HCl)	307-308.43
KrF	Krypton	Fluorine (F_2)	248.4-249.1
ArF	Argon	Fluorine (F_2)	193.3

Table 3.2: Examples of possible Rare-gas-halide laser.

In the laser micromachining experiments of the photonics materials which follow, a krypton fluoride (KrF) and an argon fluoride (ArF) laser were used. The excitation mechanisms of these transitions are as follows: when an electrical discharge is initiated within a KrF laser gas mixture, the noble gas atoms are excited and ionized, producing Kr^+ and Kr^*. At the same time, fluorine molecules are dissociated, leaving excited fluorine atoms, and after collection of free electrons, negative fluorine ions. Excited excimer molecules KrF^* are then produced by collisions between these two species via the reactions:

$$B + Kr^+ + F^- \rightarrow (KrF)^* + B \quad \text{(B – buffer gas species)}$$

$$Kr^* + F_2 \rightarrow (KrF)^* + F$$

$$(KrF)^* \rightarrow Kr + F + h\nu$$

Following photon emission (or collisional quenching) molecules are returned to the repulsive ground state and dissociate rapidly. A similar process is involved in the ArF excimer laser creating ArF^* molecules. After emission of a photon $(ArF)^* \rightarrow Ar + F + h\nu$, the ArF molecule dissociates in its repulsive ground state.

3.2.2.1.1 KrF excimer laser mask projection system

For the excimer laser based mask projection micromachining processes the Exitech S-7000 micromachining system has been used. This system allowed the ‘static mask and workpiece dragging’ type of mask projection processes (Figure 3.6).

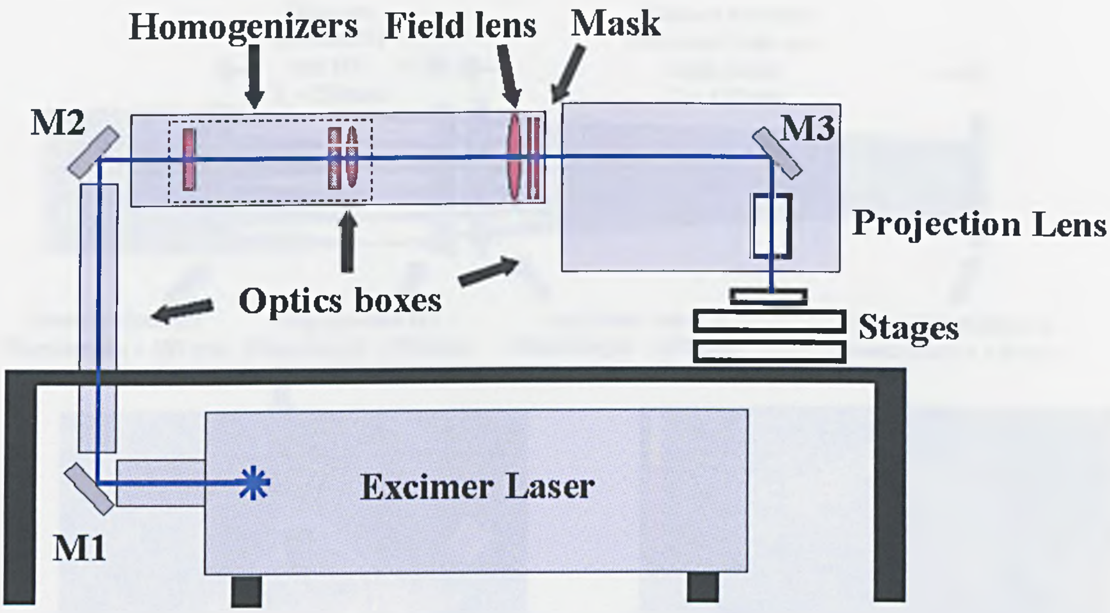

Figure 3.6: Schematic layout S-7000 micromachining system.

For the beam delivery optics and a mask projection system, moderate to high demagnification systems (2x to 30x) can be installed. For the experiments carried out at λ = 248nm, a Lambda Physiks LPX 210i KrF laser was used capable of producing pulses at a repetition rate of 100Hz and typical pulse energy of 200 mJ.

The optical mask projection system installed within the S-7000 system consisted of a double fly's eye beam homogenizer system and an imaging lens with a demagnification of 10x and a numerical aperture of 0.2. The raw laser beam was passed through a double fly's eye homogenizer set; a 6 x 6 matrix of 4mm spherical lenslet elements. In combination with a condenser lens placed directly behind the second homogenizer, the incident laser beam was converted to a 'Top-Hat' beam intensity profile with dimensions of 8 x 8 mm at the mask plane (see Figure 3.7). The incident fluence at the material substrate could, with a 10x demagnification projection lens system, be set to a maximum value of 10 J/cm^2. Variable attenuator plates were integrated directly after the excimer laser output window which allowed the control of the incident fluence at the substrate surface. The substrate was held on a kinetic vacuum chuck mounted onto a computer controlled stage stack. The X, Y linear stages had a positioning accuracy of 2μm and a maximum velocity of 2000 mm/min while the Z-axis stage could position the substrate to 1μm height accuracy.

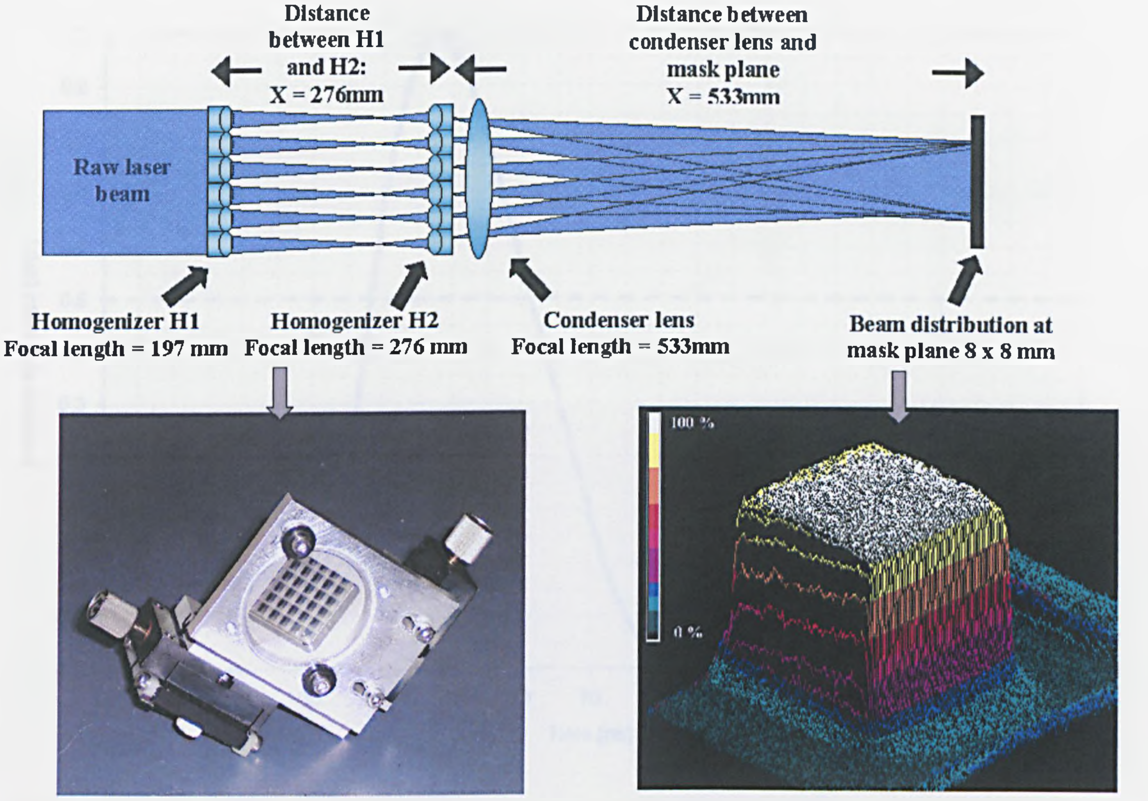

Figure 3.7: KrF laser micromachining system double homogenizer beam shaping system for 'top-hat' laser beam intensity profile at mask plane.

With the 10x, 0.2 N.A. projection lens, the distance between the mask and the image plane, the track length, was designed for 750mm and a working distance between the image plane and the bottom of the lens of 42mm. A field lens, place directly in front of the mask aperture, with a focal length of $f_{field\ lens} = 385mm$, focused the rays through the entrance pupil of the projection lens. With this optical mask projection system, the entrance pupil was fully filled and therefore the partial coherence factor of this imaging system was one.

The length of the pulse generated by the KrF laser was measured with a vacuum photodiode and determined to be $T_{pulse} = 24$ nsec (see Figure 3.8)

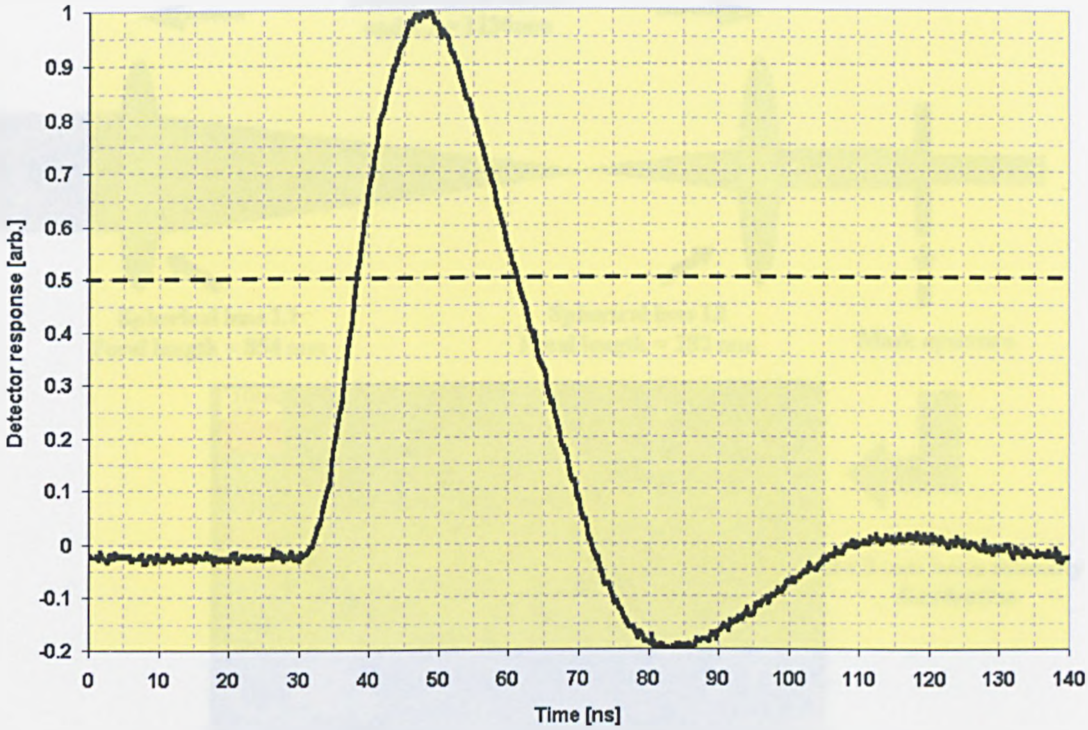

Figure 3.8: Pulse shape of the KrF laser micromachining system.

After normalizing the measured pulse to its starting signal, a negative response can be seen after the pulse duration and could be caused by the intensity of the measured pulse.

This mask projection system, based on an emission wavelength of $\lambda = 248$nm, will be referred to as the 'KrF excimer laser mask projection system'.

3.2.2.1.2 ArF excimer laser mask projection system

The ArF excimer laser mask projection system was based on the same Exitech S-7000 micromachining system as used for KrF laser exposure. However, instead of using a fly's eye double homogenizer system to manipulate the laser beam intensity profile at the mask plane, a spherical lens - based telescope was used with a demagnification factor of 3x. At the mask plane, a rectangular aperture with dimensions of 8 x 3mm was positioned to select the region of the laser beam that was most uniform (Figure 3.9).

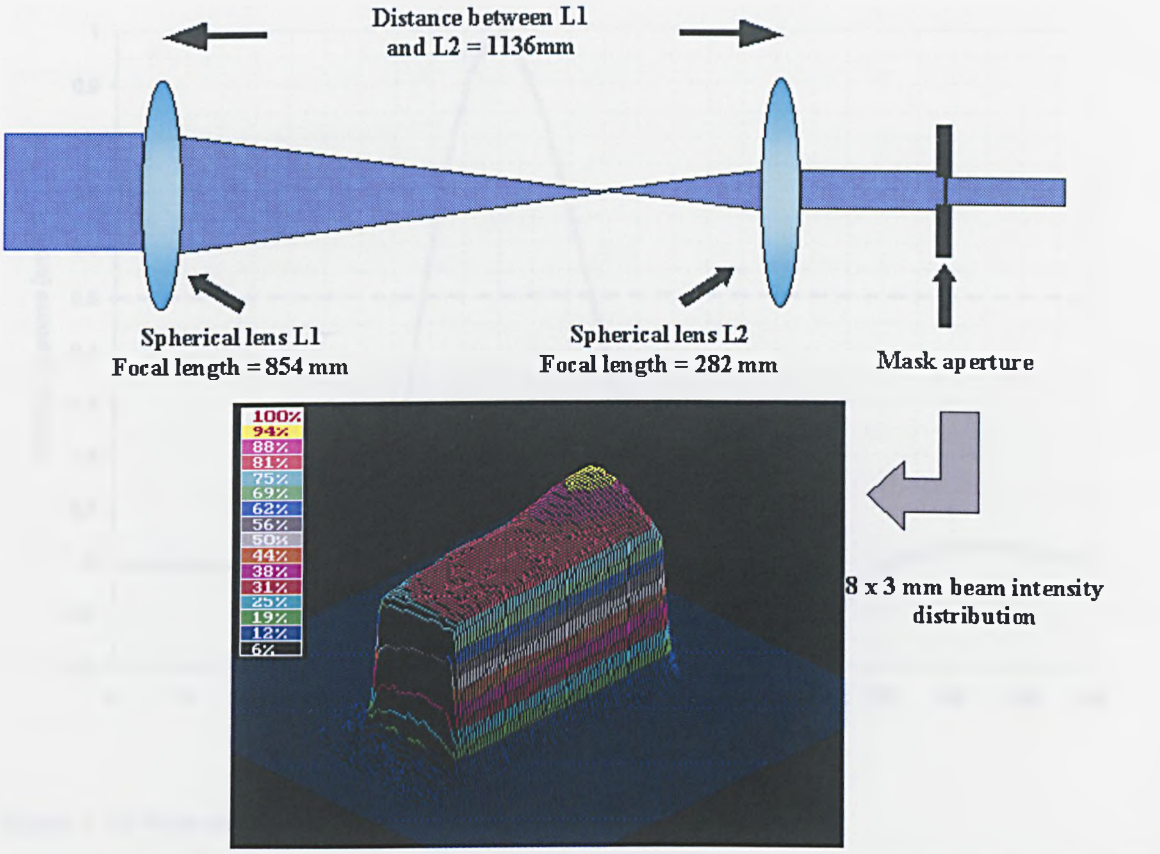

Figure 3.9: ArF laser micromachining system with 3x reduction telescope.

To image the mask plane onto the substrate a 15x demagnification 0.1 NA projection lens was used. No field lens was necessary as the beam size of the mask could directly be transmitted through the projection lens. This mask projection system was able to achieve an incident fluence at the substrate of up to 8 J/cm^2. The pulse length of the ArF excimer laser was measured with the vacuum photodiode and determined to be 25nsec (FWHM) (Figure 3.10).

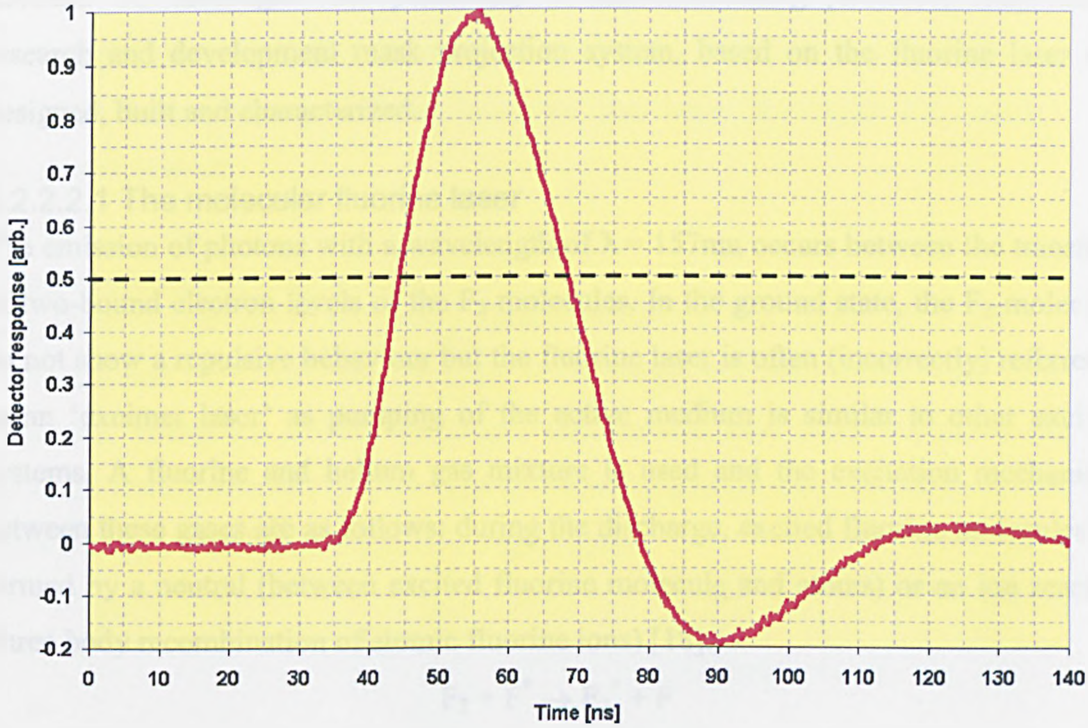

Figure 3.10: Pulse shape of the ArF laser used in the micromachining system.

Again as with the KrF excimer laser, after normalizing the measured pulse to its starting signal, a negative response can be seen after the pulse duration and could be caused by the intensity of the measured pulse as the detector was held directly held into the laser beam while with the solid state and the Fluorine laser, the pulse length was measured via a reflection.

This mask projection system will be referred to as the 'ArF excimer laser mask projection system'.

3.2.2.2 Fluorine laser based mask projection system

The fluorine molecular laser is, due to its vacuum ultraviolet (VUV) wavelength emission, able to ablate materials which are normally difficult to machine. Fused silica is an example of such a material. At the ArF excimer laser emission wavelength of λ = 193nm, the transmission of SiO_2 is still as high as ~ 90% while this is reduced to only 1% at the fluorine laser emission wavelength of λ = 157nm. Even though it is possible to machine fused silica with the ArF or KrF excimer lasers (sample thickness > 1mm) [15-17] a desirable lower incident fluence is possible at the workpiece, leading to clean removal of the material, when using the fluorine laser emission wavelength of λ =

157mm. To investigate the possibility of micromachining photonics materials, a research and development mask projection system, based on the fluorine laser was designed, built and characterized.

3.2.2.2.1 The molecular fluorine laser

The emission of photons with a wavelength of $\lambda = 157$nm occurs between the transition of two-bound electron levels of the F_2 molecules. In the ground state, the F_2-molecules do not show a repulsive behaviour but the fluorine laser is often (incorrectly) referred to as an 'excimer laser' as pumping of the active medium is similar to other excimer systems. A fluorine and helium gas mixture is used and the excitation mechanisms between these gases are as follows: during the discharge, excited fluorine molecules are formed by a neutral (between excited fluorine molecule and atoms) or an ion reaction (three body recombination of atomic fluorine ions) [18].

$$F_2 + F^* \rightarrow F_2^* + F$$

$$F^+ + F^- + He \rightarrow F_2^* + He$$

After returning to the lower energy level and emission of a photon, the fluorine molecule remains in its same bound state. In addition to emission at $\lambda = 157$nm there can also be lasing at longer wavelengths between $\lambda = 600 - 800$nm. This red emission is the result of the fast decay of excited fluorine atoms to their lower energy levels.

3.2.2.2.2 Fluorine laser mask projection system

The VUV laser radiation produced by the fluorine laser requires special consideration when being integrated into a mask projection based micromachining system as oxygen is a strong absorber of $\lambda = 157$nm radiation. To achieve significant transmission, the oxygen concentration has to be below a level of 10 ppm [19]. This required environment can be achieved by creating a vacuum within the laser beam path, but a more practical approach is to purge the beam path with inert gas like argon or nitrogen. Due to the low transmission of fused silica below a wavelength of $\lambda = 190$nm (see Fused Silica Chapter), an alternative material is needed for the VUV optical lens and projection lens. A highly VUV transmitting optical material, like calcium fluoride (CaF_2), must be used. Using an argon purging gas, cylindrical lenslet based homogenizer system and a Schwarzschild or transmission projection lens, the University of Toronto, Microlas and Laser institute Goettingen have been able to create a fully functional fluorine laser mask projection system which is capable of achieving fluences at the substrate of up to 2.5 J/cm^2 [20]. For the fluorine laser based applications presented here, a simplified and more compact mask projection system to increase the incident fluence at the material substrate has been developed for research and development work.

Mask projection optical set-up

The fluorine laser mask projection system developed was based on a 36x, 0.5 NA Schwarzschild projection lens. To improve the beam uniformity at the mask plane, two bi-prisms, positioned on the horizontal and vertical axes were integrated into the micromachining system [7]. This type of system is simple, compact and achieves high incident fluences at the substrate (see Figure 3.11).

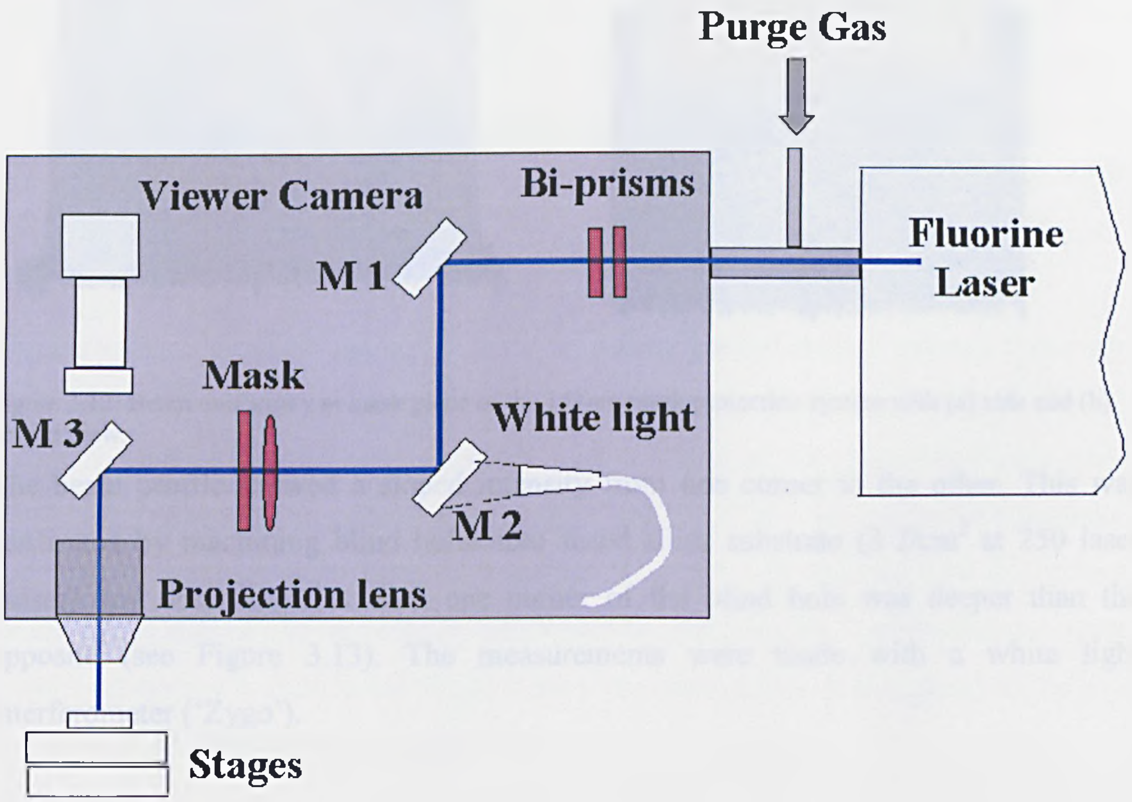

Figure 3.11: Layout of fluorine laser mask projection system.

CaF$_2$ crystal was used for the bi-prisms and field lens, and on flat substrates, multi-layer based mirror were deposited. By using these transparent mirrors, white light could pass through mirror M2 and an image of the mask on the material surface could be made visible via the CCD camera through the projection lens. Due to the use of a reflection based imaging lens, the mask is imaged at same plane when using either white light or the UV laser radiation. Therefore when the mask is imaged correctly on the material surface with white light, it is also imaged correctly when firing the fluorine laser. To increase the beam uniformity, the horizontal and vertically orientated bi-prisms divide the laser beam into four separate beam parts and overlay them on the mask plane. A square open aperture of 4.5 x 4.5 mm was placed at the mask to define the area at which all four beam parts overlaid. The uniformity of the laser beam was determined and is illustrated in Figure 3.12.

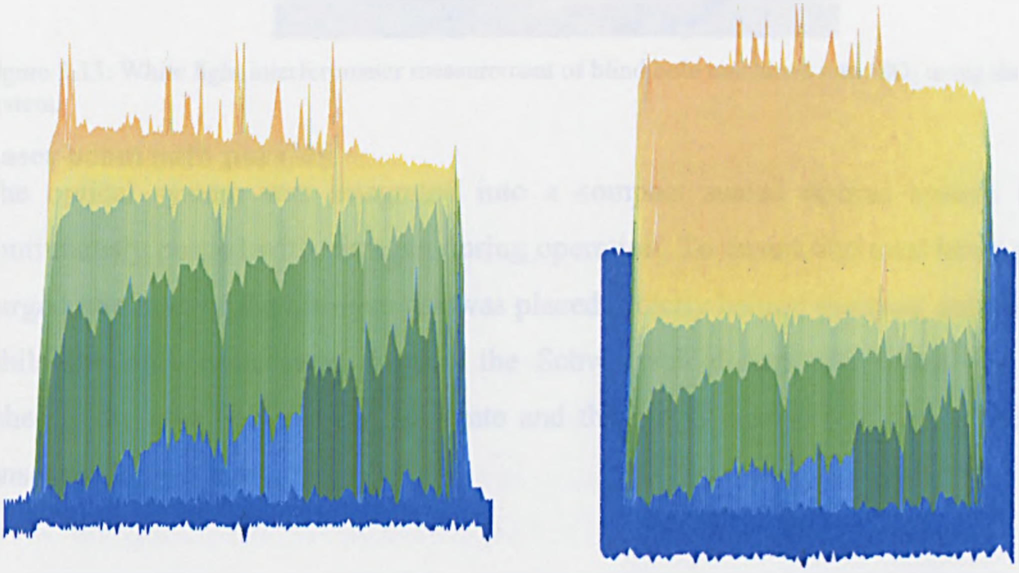

Figure 3.12: Beam uniformity at mask plane of the 157nm mask projection system with (a) side and (b) angled view.

The beam profile showed a sloped intensity from one corner to the other. This was confirmed by machining blind holes into fused silica substrate (3 J/cm^2 at 250 laser pulses) and observing that each one corner of the blind hole was deeper than the opposite (see Figure 3.13). The measurements were made with a white light interferometer ('Zygo').

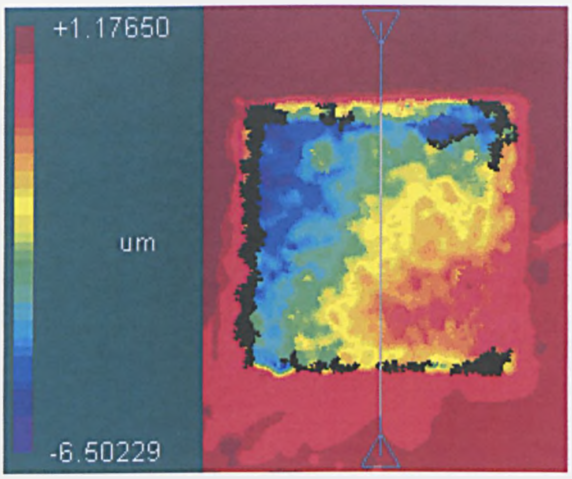

Figure 3.13: White light interferometer measurement of blind hole machined into SiO_2 using the F_2 laser system.

Laser beam path purging

The optical system was integrated into a compact sealed optical system and was continuously purged with nitrogen during operation. To ensure the total beam path was purged, the inlet of the nitrogen gas was placed directly behind the laser output window while the only outlet was through the Schwarzschild lens. By using this purging scheme, the area between the substrate and the output aperture of the Schwarzschild lens was also purged.

To characterize the time needed to achieve a fully purged optical system a two-step experiment was conducted where first the energy output of the fluorine laser directly behind the output window was measured in time. Then providing the laser with a new gas fill, the energy at the image plane was measured. The laser operating parameters remained unchanged, apart from the use of a fresh gas fill, and the laser energy was monitored at intervals of 60 seconds subsequent to commencing the nitrogen gas purge. Results for energy in time at the image plane were compared with the energy at the laser output window and plotted in Figure 3.14.

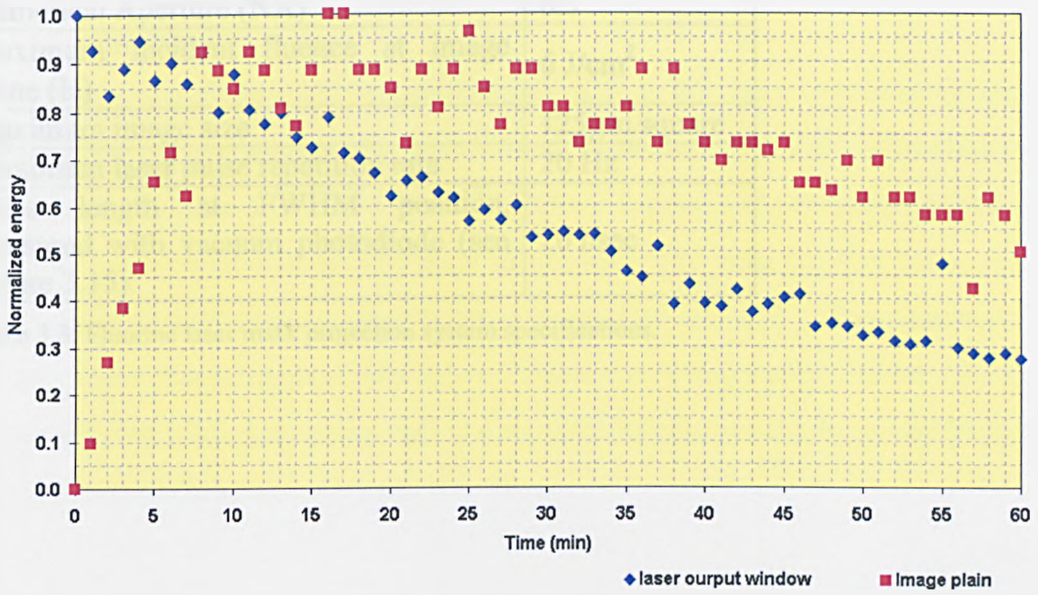

Figure 3.14: Purging characterization of fluorine laser mask projection system.

By comparing the two energy behaviour trends it could be seen that after purging the optical system for 20 minutes, a similarly declining trend can be determined, showing that it takes at least 20 minutes for the system to be purged and achieve sufficient VUV transmission. Before further experiments were carried out with the fluorine laser mask projection system, the system was purged with nitrogen for at least 20 minutes.

System specifications

The fluorine laser used during the period of system installment, optics alignment and characterization was a Lambda Physik LPX 210 device with a gas mixture consisting of 100mbar Fluorine and 3000mbar of Helium. As can be seen in Figure 3.14, the output energy decays over time, i.e. after firing 36.000 laser pulses (one hour operation at 10Hz) the pulse energy was reduced by ~ 66%. Another disadvantage of using this converted excimer laser was the discharge voltage required to achieve high energy VUV photons exceeded its specified operation conditions and resulted in high maintenance requirements. By replacing this laser with a Lambda Physik LPF 205 fluorine laser, the issues of pulse energy decline and high maintenance were removed and all further experiments were carried out with this new system configuration. With the LPF 205 laser integrated, the systems operating specifications were determined and are shown in see Table 3.3.

Parameter	Specification
Mask projection system demagnification	36x

Numerical Aperture (NA)	0.5
Maximum Incident fluence at image plane (H)	6 J/cm^2
Maximum image size	125μm square
Maximum laser pulse repetition rate	20 Hz
Pulse length at FWHM position, measured with vacuum photodiode (see Figure 3.15)	20 nsec

Table 3.3: Fluorine laser mask projection system specifications.

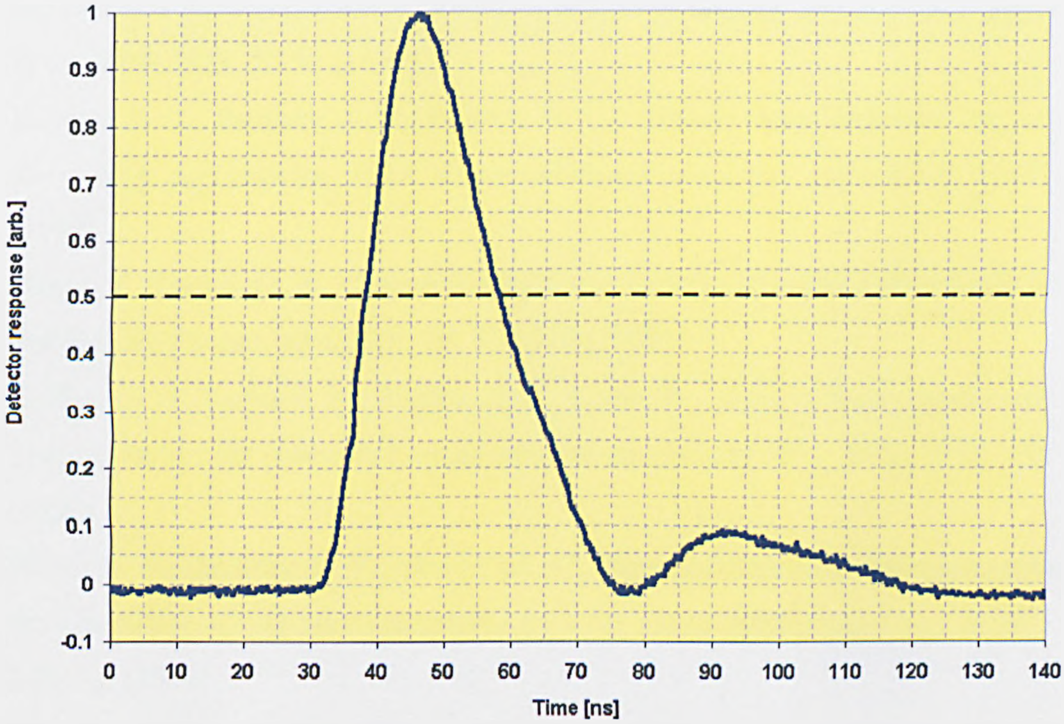

Figure 3.15: Pulse shape of the fluorine laser used in the micromachining system.

The stage stack integrated into the fluorine laser mask projection system consisted of two linear stages for motion in the X- and Y-axes and a stage moving along the Z-axis. The maximum length of travel of the linear stage was 100mm with a positioning accuracy of 1μm and was specifically tuned for velocities below 10mm/min. Samples were placed on top of a kinetic chuck, mounted on top of the stage stack. The samples could be positioning within the Z-axis with an accuracy of 0.1 μm. This system will be referred to as the 'fluorine laser mask projection system'.

3.3 Conclusion

The design, installation and commissioning of four UV laser micromachining system were discussed. One system was based on a 3rd harmonic Nd-YAG solid state laser and will be operated in a direct writing mode by focusing the TEM 00 intensity beam profile down to a small spot with a short focal length lens. The three other systems were based on a mask projection system, two excimer lasers, KrF and ArF gas mixture based, and a fluorine laser was integrated into its own micromachining system. Either 'fly eye's' or bi-prism beam homogenization optics were used to improve the beam uniformity at the image plane of each mask projection system.

3.4 References

1. Koechner, W. H., "*Solid-State Laser Engineering*" (Springer Verslag 1987)
2. Siegman, A. E., New development in laser resonators, *Proc. SPIE* 1224, 2-14 (1990)
3. Silfvast, W. T., "*Laser Fundamentals*" (Cambridge University Press, 2000)
4. Abbott, C., Allott, R. M., Bann, B., Boehlen, K. L., Gower, M. C., Rumsby, P. T., Stassen Boehlen, I., Sykes, N., New techniques for laser micromachining MEMS devices, *Proc. SPIE* 4760, 281-288 (2002)
5. Duley, W. W., *"UV lasers: effect and applications in materials science"* (Cambridge University Press, 1996)
6. Harvey, E., C., Rumsby, P. T., Fabrication techniques and their application to produce novel micromachined structures and devices using excimer laser projection, *Proc. SPIE* 3223, 26-33 (1997)
7. Harvey, E. C., Rumsby, P. T., Gower, M. C., Excimer laser projector for material processing applications, *Prod. Laser advanced materials processing*, 1047-1052 (1992)
8. Ozaki, Y. Takamoto, K, Cylindrical fly's eye lens for intensity redistribution of an excimer laser beam, *Appl. Opt.* 28, 106-110 (1989)
9. Kahlert, H.-J., Sarbach, U., Burghardt, B., Klimt, B., Excimer laser illumination and imaging optics for controlled microstructure generation, *Proc. SPIE* 1835, 110-118 (1992)
10. Rizvi, N. H., Rumsby, P. T., Gower, M., C., New developments and applications in the production of 3D micro-structures by laser micro-machining, *Proc. SPIE* 3898, 240-249 (1999)
11. Rumsby, P. T., Gower, M. C., Excimer laser projector for microelectronics applications, *Proc. SPIE* 1598, 36-45 (1991)
12. Rizvi, N. H., Rumsby, P. T., Gower, M. C., Burt, J. P. H., Talary, M., S., Tame, J. A., Pethig, R., Direct manufacture of miniature bio-particle electro-manipulator devices using excimer laser mask projection techniques, *Int. J. Japan Soc. Pres. Eng.* 33, 100-104 (1999)
13. Rizvi, N. H., Apte, P., Developments in laser micro-machining techniques, *J. Mat. Process. Tech.* 127, 206-210 (2002)

14. Boehlen, K. L., Stassen Boehlen, I. B., Laser micromachining of high-density optical structures on large substrates, *Proc. SPIE* 5339, 118-126 (2004)
15. Ihlemann, J., Excimer laser abltion of fused silica, *Appl. Surf. Sci.* 54, 193-200 (1992)
16. Ihlemann, J. Wolff-rottke, B., Excimer laser micromachining of inorganic dielectrics, *Appl. Surf. Sci.* 106, 282-286 (1996)
17. Dyer, P.E., Farley, R. J., Giedl, R., Karnakis, D. M., Excimer laser ablation of polymers and glasses for grating fabrication, *Appl. Surf. Sci.* 96-98, 537-549 (1996)
18. Hooker, S. M., Webb, C. E., Process in Vacuum Ultraviolet Lasers, *Prog. Quantum Elec.* 18, 227-274 (1994)
19. Gruenewald, P., Cashmore, J., Fieret, J., Gower, M., High-resolution 157nm laser micromachining of polymers, *Proc. SPIE* 4274, 158-167 (2001)
20. Herman, P. R., Chen, K. P., Wei, M., Zhang, J., Ihlemann, J.,Schafer, D., Marowsky, G., Oesterlin, P., Burghardt, B., F_2-lasers: a high-resolution optical processing system for shaping photonics components, *Proc. SPIE* 4274, 149-157 (2001)

4 UV laser pulse removal of indium phosphide

4.1 Introduction

In 1963, the first UV laser radiation was obtained from excited N_2 gas and had an emission spectrum at $\lambda = 300$nm to $\lambda = 400$nm with its strongest emission line at 337.1nm [1]. This discovery led to further theoretical and experimental studies on emissions from H_2 and CO gas, and pulsed and continuous emission, ion lasers.

The formation of bound excited states in diatomic molecules with unstable or weakly bound ground states, was recognized in 1968 as being an efficient way to obtain population inversion and stimulated emission at UV wavelengths [2]. Xe_2 molecules produced an emission at $\lambda = 172.2$nm, but due to high operating gas pressure and the need for electron beam pumping, further development of this type of laser was limited. Emissions from the excited state of XeBr and XeCl molecules suggested that formation by a reaction between metastable Xe atoms and halogens could lead to stimulated emission at UV wavelengths. This was soon confirmed by laser emissions based on rare gas halides like XeBr (λ = 281.2nm) and XeI (λ = 255nm). Today, the discharge based Rare Gas Halide laser is one of the dominant sources for pulsed UV laser micromachining applications with XeF (λ = 351nm), XeCl (λ = 308nm), KrF (λ = 248nm) and the ArF (λ = 193nm) being the most commonly used within research and industry [3].

The early 1980's saw the growing availability of powerful pulsed UV sources based on the Rare Gas Halides (RGH) and widened research abilities in the interaction of UV laser pulsed radiation with materials. In this period, the first reports on the use of ultraviolet excimer lasers to etch polymers in the form of resists [4] or direct etching were published [5]. This photoetching effect was not only tested on the organic polymer of polyethylene terephthalate (PET) but subsequently on polyimide (PI) and polymethyl methacrylate (PMMA). Organic polymers have been extensively studied in the research and development of direct etching of materials with pulsed UV lasers. Srinivasan [6], Yeh [7] and Srinivasan and Braren [8] characterized the events in the 80's while Dyer [9-12]has produced reviews of more recent events.

The amount of material removed per laser pulse is referred to as the etch rate and is commonly expressed as a function of the incident fluence. The etch rate, x, is usually derived by measuring the depth of an etched blind hole, h, ablated by n number of laser pulses, $x = h/x$ and as such is an average value. To achieve significant material removal the incident fluence has to be higher than the threshold fluence, F_t. Below this threshold fluence, finite material removal still occurs but when the incident fluence exceeds the threshold value, the material ablation becomes significant and increases with the incident fluence. Models to describe UV laser ablation have been formulated since the earliest results in the 80's. Due to the lack of thermal damage on the polymer after ablation and because the energy of the incident photons is sufficiently high enough to break the main chain bonds of the polymer, Srinivasan introduced the idea that the ablation was based on a photochemical process and called it ablative photodecomposition (APD) [14]. Within this bond breaking photochemical approach to ablation, fast polymer removal would take place mainly due to electronically excited states and repulsive forces between the species. The energy absorbed during this process would limit thermal damage to the substrate as it restricts the rise in substrate temperature. From a photochemical bond-breaking model of ablation [15] it was possible to describe the required threshold fluence to achieve material removal:

$$F_n = \frac{nh\nu}{\eta\alpha(1-R)} \qquad \text{eq.: 4-1}$$

with n being the number of bonds per unit volume to be broken to achieve material removal, $h\nu$ the photon energy, η the quantum yield for chain scission, α the effective absorption coefficient and R the reflection loss on incident surface. With this model, agreement between the predicted threshold fluence based on the quantum yield for chain scission and the experimental value is difficult to find unless the 'switched cage effect' is postulated [9].

An alternative explanation can be found in a thermal approach to ablation where the material undergoes a rapid thermal degradation [12]. The absorption of the incident radiation is due to the excitation of the electronic transitions and is rapidly converted to heat in the material surface. Depending on the heat conversion within the material and due to thermal degradation, material is being 'removed' from the surface.

4.1.1 Practical consideration of UV laser material ablation

For wavelengths in the ultraviolet, the attenuation of radiation in material is due to the excitation of electronic transitions [3] and simplistic models assume that this absorbed light radiation is rapidly converted to heat which can diffuse according to the conventional heat diffusion equation.

The absorption of light propagation through the material depends on its complex refractive index *m*, defined as $m = n - ik$. Typically the dependence of *n* on wavelength leads to dispersive effects while the absorption is directly related to *k*. For a homogeneous absorbing material the propagation of light through a homogeneous absorbing material characterized by *n* and *k* is described by the Beer-Lambert law:

$$I(z,t) = I_0(t)(1-R)e^{-\alpha z} \qquad \text{eq.: 4-2}$$

Here I(z,t) is the irradiance of the laser light at depth *z* and time *t,* R is the surface reflectance and the attenuation coefficient α is related to k by:

$$\alpha = \frac{4\pi k}{\lambda} \qquad \text{eq.: 4-3}$$

Heating of an irradiated sample is a consequence of the balance between the deposited energy, controlled by the optical parameters of the sample, and the laser pulse shape and heat diffusion into the bulk of the material. The surface temperature rise of the material can be estimated in two limiting cases; in one case the optical absorption depth is much smaller than the thermal diffusion length and in the other, much larger. The second generally applies to polymers [11] while the first to semiconductors and inorganic insulators which are used in the experiments to follow. A useful characterizing parameter is the ratio between the absorption depth of the incident radiation and the thermal diffusion length obtained within the laser pulse duration. The absorption depth is defined as $\frac{1}{\alpha}$ and the thermal diffusion depth, x_D, during the laser pulse by $x_D = \sqrt{D\tau}$ with τ = laser pulse length and the *D* the thermal diffusivity is defined by:

$$D = \frac{\kappa}{\rho C_p} \qquad \text{eq.: 4-4}$$

Here κ is the thermal conductivity, ρ the material density and C_p the specific heat. As a result the characterizing parameter, δ, is defined as:

$$\delta = \frac{1}{\alpha\sqrt{D\tau}} \qquad \text{eq.: 4-5}$$

For values of δ <<1 the heat flow into the material dominates and limits the surface temperature rise. The temperature rise at the sample substrate for a surface heating source, can be estimated using [10, 16]:

$$\Delta T_s = (1-\mathrm{R})\frac{2H}{\kappa}\sqrt{\frac{D}{\pi\tau}} \qquad \text{eq.: 4-6}$$

with H being the incident laser fluence. The temperature rise can only be estimated when edge effects can be neglected and this will be the case in the experiments within this thesis as the cross section of the irradiation laser beam used, between 0.5 and 1mm, is much larger than the removed material thickness per laser pulse, typically less then 1 micron. Assuming a thermal based surface heating process applies, material removal becomes present after an apparent threshold has been exceeded and is reached when the material changes from a solid to liquid state. Following the creation of melt, significant vaporization can occurs from the material's melt pool. Hence, the melting point of the material approximately a lower limit of the ablation process.

Given the likelihood that a surface heating/vaporization mechanism applies to various inorganic materials, an Arrhenius type thermal model can be used [12, 17] which postulates that the vaporisation rate, K, from the material surface will have a temperature dependence of the form:

$$K = A\exp\frac{-E_A}{RT} \qquad \text{eq.: 4-7}$$

where A is the frequency factor, E_A is an activation energy, R is the gas constant and T the absolute temperature. On this basis, if there is a characteristic time over which vaporisation occurs, defined as t_v, material removal is proportional to Kt_v resulting in an etch rate, x, which is then temperature rise dependent:

$$x \propto t_v K = A\exp\frac{-E_A}{RT} \qquad \text{eq.: 4-8}$$

Utilizing equation 4-8 requires knowledge of the frequency factor A, activation energy E_A and temperature T during the ablation process. However these values are not known for the materials studied here. By assuming that the temperature reached during the laser pulse is constant and that this temperature behavior is proportional to the incident fluence, the empirical form of the etch rates is then:

$$x = a\exp\frac{-B}{T_0 + CH} \qquad \text{eq.: 4-9}$$

Where a, B = E_A/R and C are constants, H the incident laser fluence and T_0 the initial temperature. When the melting point of the material is >> T_0, this can be simplified to

$$x = A\exp\frac{-B'}{H} \qquad \text{eq.: 4-10}$$

where B' = E_A/CR is a new constant.

A way of fitting this expression against experimental etch rate data collected is to re-write equation 4-10 into the form of:

$$\ln x = \ln A - \frac{B'}{H} \qquad \text{eq.: 4-11}$$

If a surface heating/vaporization mechanism describable in this way applies to the ablation, a plot of ln (average etch rate) versus 1/(incident fluence) should appear to be linear.

The UV laser ablation process described is assumed to be based on a thermal process where significant amount of material is removed after a threshold point has been reached; the absorbed UV photons are instantly converted to heat and melt the substrate, vaporization occurs and material is removed from the substrate. By increasing the incident fluence beyond this threshold point, the material removal rate should increase following an Arrhenius type thermal model. These two assumptions were investigated in this thesis by carrying out UV laser ablation etch rate experiments on the semiconductor material InP. Each of the UV laser micromachining systems discussed in chapter 3 were used allowing, the average etch rate per pulse to be determined at wavelengths of $\lambda = 355, 248, 193$ and 157nm.

4.1.2 Indium phosphide

InP is a semiconductor used in the telecommunication industry in active components such as laser diodes, but has, due to the increased interest in wavelength dense multiplexing (WDM), also been used for semiconductor optical amplifiers (SOA). These active devices are essentially a semiconductor laser, but care is taken to prevent internal feedback so that an optical signal travels through the device only once, and emerges intensified at the other end.

Manufacture of single crystal InP is based on the Czochralski growth process using Indium and Phosphorus powder or crystal fragments, melted in a crucible. A seed crystal is lowered into a furnace until the tip of the seed crystal touches the molten mixture. Growth of the crystal can be initiated by lowering the melt temperature to just above the melting point of the material. The preparation of InP wafers from grown boules starts with grinding of the rod into a perfect cylindrical shape with a diameter slightly larger than the required dimensions by fixed diamond abrasive wheels. Two methods can be used to slice the rod into wafers; annular or wire saws. Using an annular saw, wafers are cut separately while a wire saw can cut up to one hundred wafers at once. After the wafers are separated, a lapping step ensures consistent surface roughness and controllable wafer thickness. After lapping, the wafers are polished and cleaned. For the experiments here , a 2" single crystal wafer was used with a thickness of 1mm. The wafer was sourced from the manufacturer "Wafertech".

4.1.2.1 Thermal properties

The thermal diffusivity (D) of InP can be found in using the thermal data in Table 4.1[18].

Material parameter	**Value**
Thermal conductivity κ [W cm^{-1} K^{-1}]	0.74
Material density ρ [g cm^{-3}]	4.7
Specific heat C_p [J g^{-1} K^{-1}]	0.35
Melting Temperature [K]	1333

Table 4.1:Thermal parameters and material density of InP.

With semiconductor materials, the thermal conductivity and the specific heat vary with temperature [16] and the values given are between their melting point and room temperature. A thermal diffusivity of D = 0.45 cm^2/s is found and as it does not depend on wavelength this can be used in calculations carried out for the other UV laser micromachining systems.

4.2 UV laser ablation of indium phosphide

The UV laser ablation behaviour of InP was investigated by experimentally determining the average etch rate per pulse at each available laser wavelength.

4.2.1 UV solid-state laser micromachining system

The UV solid-state laser micromachining system was used to determine the ablation behaviour of InP at a wavelength of λ = 355nm. The average etch rate per pulse was determined at various fluences and compared with the calculated laser ablation threshold and the predictions of the Arrhenius type thermal model.

4.2.1.1 Average etch rate per pulse

The surface of the InP substrate was exposed with 20 laser pulses at different incident fluences. The depth of each blind machined hole was measured with an optical microscope with a 1 μm depth resolution, Z-axis positioning read. The wafer surface was imaged onto the optical microscope and the z-axis encoder then set to zero. The bottom of the ablated blind hole was then imaged and the difference in the z-axis reading gave the depth of the hole. Dividing the measured depth by the number of laser pulses (in this case 20) gave the average etch rate per pulse.

This process was carried out at each fluence setting and the average etch rate per pulse was plotted against the fluence and shown by the results in presented in Figure 4.1.

The results presented show a value for the average etch rate per pulse exceeding 1μm at the higher incident fluences (≥ 5000 J/cm^2), while at the lowest fluence of 100 ± 50 J/cm^2, the value is 0.25 ± 0.1μm. It was not possible to determine a threshold value for InP at λ =355nm from this curve.

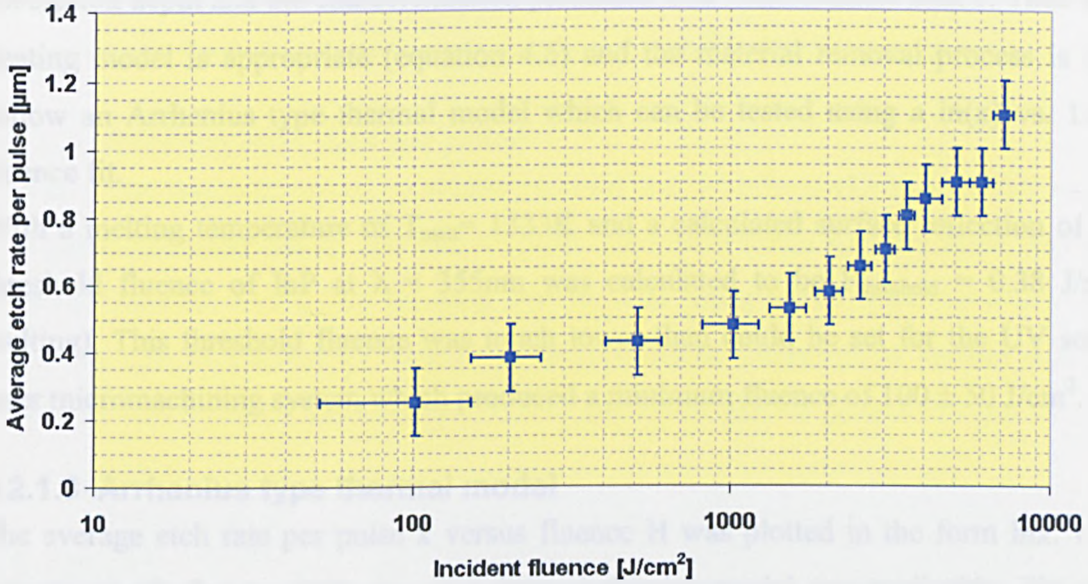

Figure 4.1:Average etch rate per pulse vs. incident fluence of the material InP at a wavelength of λ = 355nm.

4.2.1.2 Laser ablation threshold

Material removal was assumed to start when the material phase transition between a solid to liquid state occurred. This point is defined by the material's melting point and is reported to be T = 1333K [18]. Based on the surface heating theory discussed in paragraph 4.1.1, it is possible to calculate the fluence needed to heat the surface to its melting point by using this given temperature. The applicability of this approach depends on the characterization parameter δ, describing the ratio between the thermal diffusion length and the absorption depth of the incident radiation. To determine δ, the thermal diffusivity, the effective absorption coefficient and the laser pulse length are required.

Effective absorption coefficient

For indium phosphide the value of *k* at a wavelength 355nm is 1.948 [19]. The effective absorption coefficient, calculated with equation 4.3, resulted in $\alpha = 6.9 \times 10^5 \text{ cm}^{-1}$, and a corresponding absorption depth of $\frac{1}{\alpha} = 14.5\,\text{nm}$.

Laser pulse duration

The duration of the laser pulse for the UV solid state laser described in chapter 3, was T_p= 30ns FWHM. The heat diffusion depth $\sqrt{D\tau}$ for this laser pulse duration is 1.15 x10^{-4} cm (1.15µm). Here the thermal diffusion length during the laser pulse is much larger than the absorption depth and the characterization parameter δ is much smaller than 1. Thus a surface heating model is appropriate (equation 4.6) and the material removal process is likely to follow an Arrhenius type thermal model which can be tested using a ln(x) vs. 1/incident fluence fit.

With a melting temperature of T_{melt}= 1333K and a calculated surface reflection of 0.4, the threshold fluence of InP at λ = 355nm was calculated to be $F_{threshold}$ = 0.38 J/cm^2 (for melting). This threshold fluence was much lower than could be set for the UV solid state laser micromachining system which produced a minimum fluence of 100 ± 50 J/cm^2.

4.2.1.3 Arrhenius type thermal model

The average etch rate per pulse x versus fluence H was plotted in the form lnx. v. 1/H to investigate whether an Arrhenius type thermal ablation model was applicable. The results is seen in Figure 4.2.

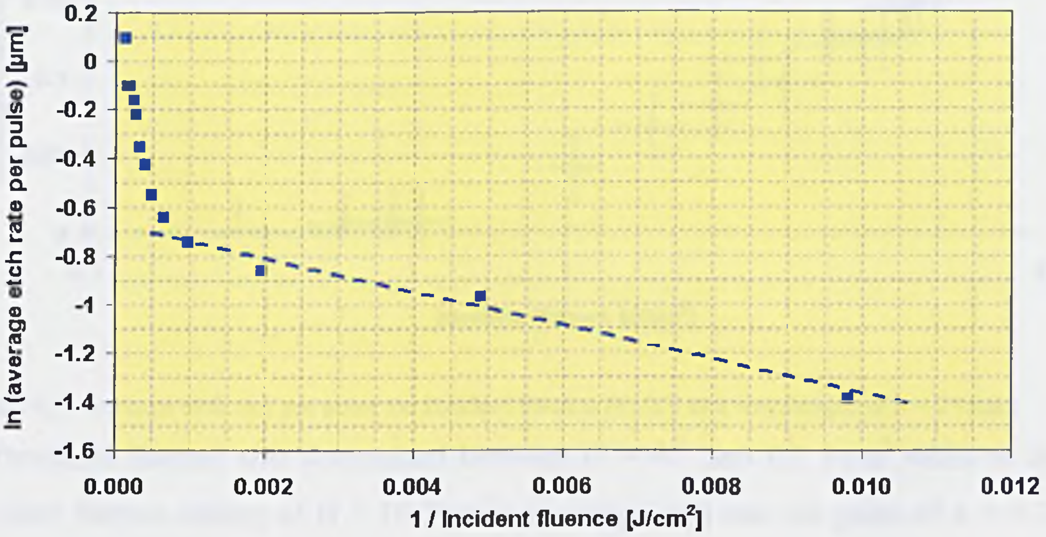

Figure 4.2: ln(average etch rate per pulse) vs. 1/incident fluence for InP at a wavelength of λ = 355nm.

It is evident that a linear dependence is obtained for lower fluence, H, (corresponding to high values of 1/H) in the range 1/H ~ 0.01 cm^2/J to ~ 0.1 cm^2/J. At high fluences, however, there is a sharp upturn of the etch rate suggesting a change occurs in the removal mechanism under these high surface energy density loading levels.

4.2.2 KrF excimer laser mask projection system

The KrF laser mask projection system was used to determine the ablation behaviour of InP at a wavelength of λ = 248nm. The average etch rate per pulse was determined at different incident fluences and the experimental and calculated laser ablation threshold points compared and the removal rate tested against an Arrhenius thermal model.

4.2.2.1 Average etch rate per pulse

The etch rate was determined by ablating a blind hole into the material with 100 laser pulses at a pulse repetition rate of 100 Hz. A square 10x10mm metal aperture mask was used and with the installed 10x 0.2Na imaging system. The depth of the blind hole was measured under an optical microscope following the procedure discussed in section 4.2.1.1. This procedure was repeated for different fluences and the results are plotted in Figure 4.3.

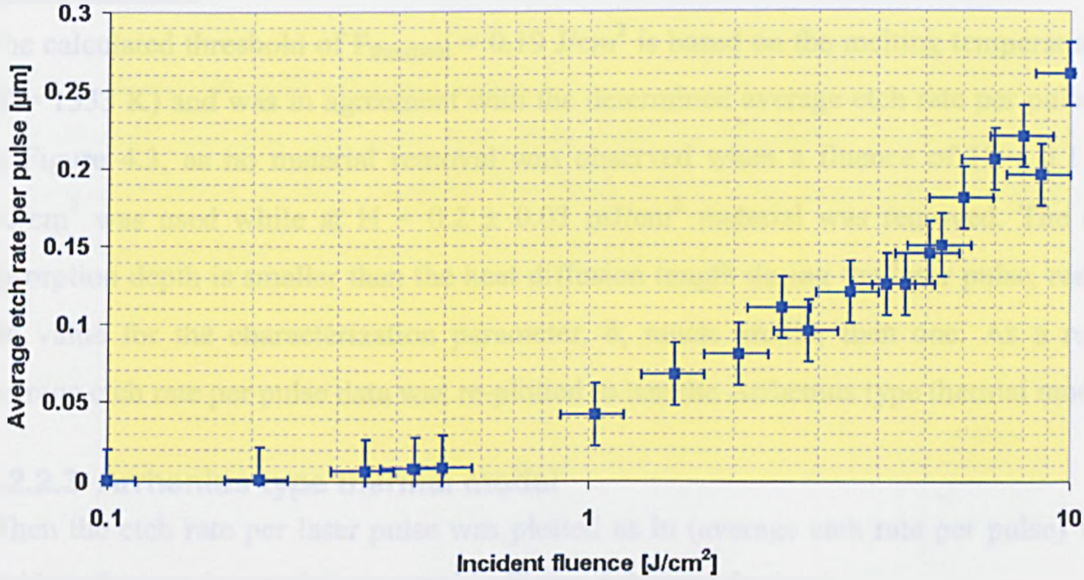

Figure 4.3: Average etch rate per pulse vs. incident fluence for InP at a wavelength of $\lambda = 248$nm.

A threshold fluence was determined between H = 0.1 and 0.2 J/cm^2 while at the highest incident fluence setting of H = 10 J/cm^2 an average etch rate per pulse of x = 0.26µm was measured.

4.2.2.2 Laser ablation threshold

Similar thermal calculations were carried out as for the collected data in the UV solid-state laser micromachining system etch rate experiment. The determined threshold fluence was compared with its calculated value and after determining if a surface heating source applied, the etch rate data was re-plotted to test if an Arrhenius thermal model could be fitted to the determined etch rate data. For these comparisons, the required optical and thermal parameters were calculated and are presented in Table 4.2.

Material parameter	Value
Effective absorption coefficient [cm^{-1}]	$1.77 * 10^6$
Effective absorption depth [nm]	5.65
Heat diffusion length during laser pulse duration $\sqrt{D\tau}$ [μm]	1.04
Calculated threshold fluence [mJ/cm^2]	0.19

Table 4.2: KrF excimer laser micromachining system laser ablation calculations for optical and thermal material parameters.

The calculated threshold of $F_{threshold} = 0.19\ J/cm^2$ is based on the melting temperature of InP (T = 1333 K) and was in agreement with the determined average etch rate per pulse, shown in Figure 4.3, as no material removal was observed when a fluence of $H = 0.1 \pm 0.015\ mJ/cm^2$ was used while at $H = 0.2 \pm 0.03\ mJ/cm^2$ material was removed. The effective absorption depth is smaller than the heat diffusion length during the laser pulse, resulting in the value for the characterization parameter, δ, much smaller then one. As a result, the average etch rate per pulse data was re-plotted to test the Arrhenius type thermal model.

4.2.2.3 Arrhenius type thermal model

When the etch rate per laser pulse was plotted as ln (average etch rate per pulse) versus 1/ incident fluence the results presented in Figure 4.4 were obtained.

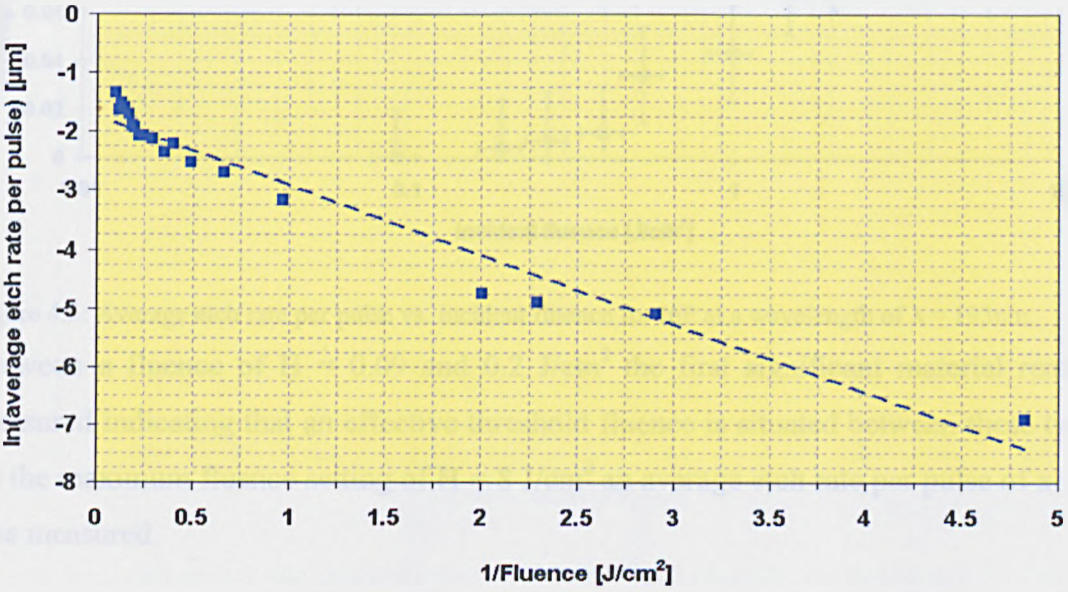

Figure 4.4: ln (Average etch rate per pulse) vs. 1/incident fluence for InP at a wavelength of $\lambda = 248nm$.

An linear trend can be seen in the data points down to a value of $1/H = 0.25$ cm^2/J (4 J/cm^2) but as $1/H$ is further decreased the results deviate from this linear behaviour. The etch rate data below this point had a higher removal rate than predicted by an Arrhenius type process.

4.2.3 ArF excimer laser mask projection system

The material ablation behavior of InP was characterized at a emission wavelength of λ = 193nm with an ArF excimer laser mask projection system. A similar procedure to the previous experiments was used to determine the average etch rate per pulse. A comparison between the calculated and experimental threshold fluence was made and the Arrhenius type thermal model was tested against the determined material ablation behaviour.

4.2.3.1 Average etch rate per pulse

The average etch rate per pulse was determined by machining blind holes into the InP surface at different incident fluences. The depth of the holes was measured using an optical microscope. The results obtained are shown in Figure 4.5.

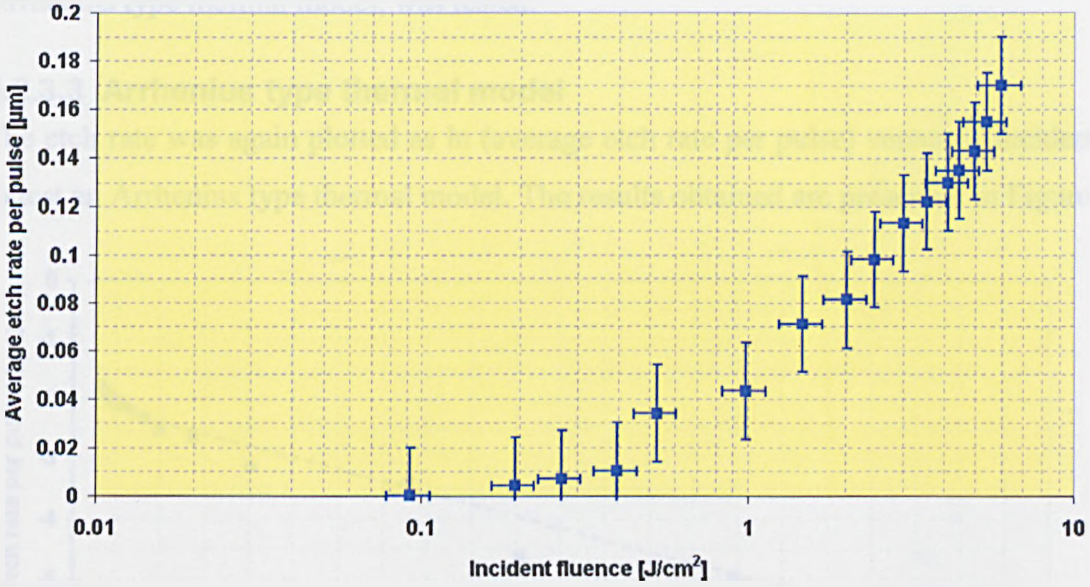

Figure 4.5: Average etch rate per pulse vs. incident fluence for InP at a wavelength of λ = 193nm.

Between a fluence of H = 0.09 and 0.2 J/cm^2 the first significant material removal was measured indicating that an effective threshold fluence is situated between these two points. At the maximum fluence setting of H = 8 J/cm^2 an average etch rate per pulse of x = 0.16µm was measured.

4.2.3.2 Laser ablation threshold

The calculations related to the characterization parameter and threshold fluence were again carried out and the results are presented in Table 4.3.

Material parameter	Value
Effective absorption coefficient [cm^{-1}]	1.31×10^6
Effective absorption depth [nm]	7.65
Heat diffusion length during laser pulse duration $\sqrt{D\tau}$ [μm]	0.95
Calculated threshold fluence [J/cm^2]	0.15

Table 4.3: ArF excimer laser micromachining system laser ablation calculations for optical and thermal material parameters.

A calculated threshold fluence of H = 0.15 J/cm^2 is in agreement with the experimental estimate of between H = 0.09 and 0.19 J/cm^2. The heat diffusion length calculated is much larger than the effective absorption depth and a material removal process, based on an Arrhenius type thermal model, was tested.

4.2.3.3 Arrhenius type thermal model

The etch rate was again plotted as ln (average etch rate per pulse) versus 1/ incident fluence to test an Arrhenius type thermal model. The results obtained are presented in Figure 4.6.

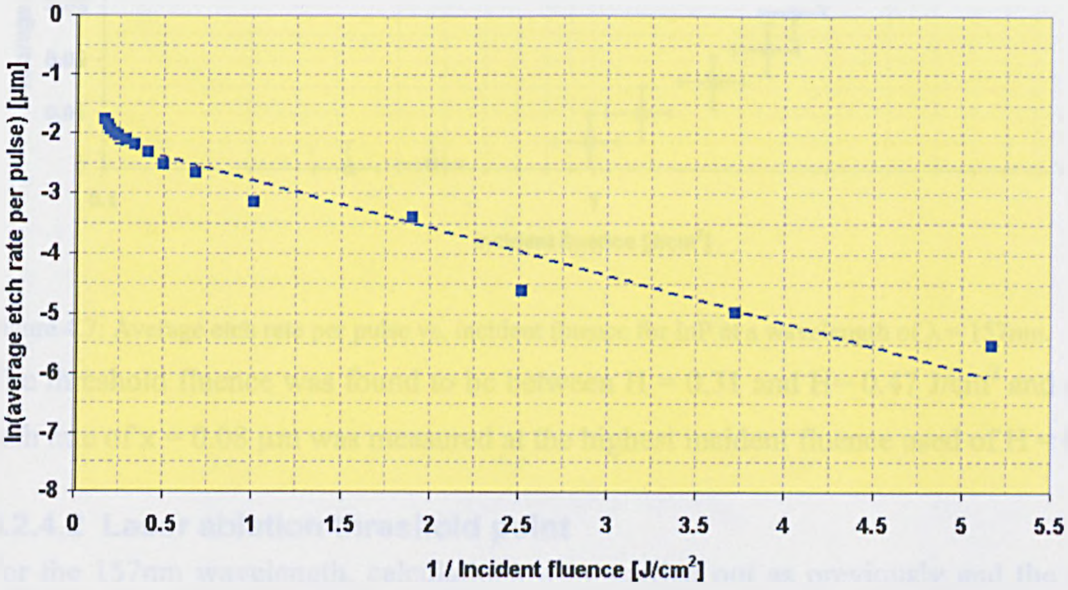

Figure 4.6:ln (average etch rate per pulse) vs. 1/incident fluence for InP at a wavelength of λ = 193nm.

These show a similar trend to those for λ = 248nm with a linear relation down to 1/H = 0.25 cm^2/J (H = 4 J/cm^2). Below this, somewhat higher material removal rates were obtained than predicted by this Arrhenius mode.

4.2.4 Fluorine laser mask projection system

The fluorine laser mask projection system was also used to determine the InP ablation behaviour at a wavelength of λ =157nm. Again, the average etch rate per pulse was determined and also tested against the Arrhenius type thermal model for removal.

4.2.4.1 Average etch rate per pulse

The average etch rate per pulse at different fluence settings was determined by machining blind holes into the InP surface with a 100 shot exposure at a repetition rate of 20Hz. The depth of the machined 100μm square blind hole was measured using a Veeco Dek-Tak[3] surface profiler. The results were plotted and are presented in Figure 4.7.

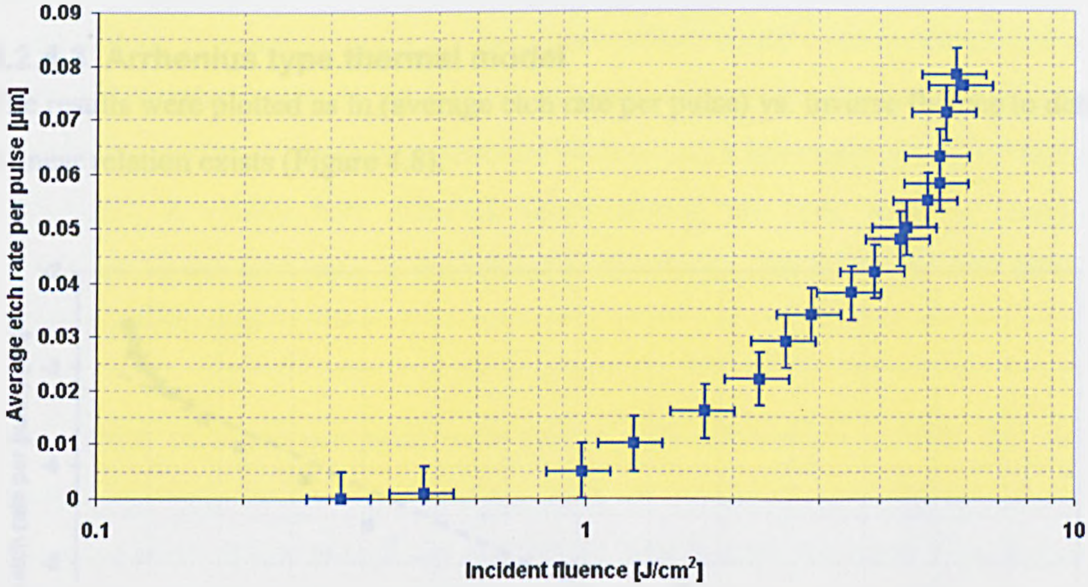

Figure 4.7: Average etch rate per pulse vs. incident fluence for InP at a wavelength of λ = 157nm.

The threshold fluence was found to be between H = 0.31 and H= 0.47 J/cm^2 and an average etch rate of x = 0.08 μm was measured at the highest incident fluence used of H = 6 J/cm^2.

4.2.4.2 Laser ablation threshold point

For the 157nm wavelength, calculations were carried out as previously and the results are presented in Table 4.4.

Material parameter	**Value**
Effective absorption coefficient [cm^{-1}]	1.28 x 10^{6}
Effective absorption depth [nm]	7.84
Heat diffusion length during laser pulse duration $\sqrt{D\tau}$ [μm]	0.95
Calculated threshold fluence [J/cm^{2}]	0.15

Table 4.4: Fluorine laser micromachining system ablation calculations for optical and thermal material parameters.

At this wavelength the absorption depth is much smaller than the heat diffusion length during the laser pulse and hence the characterization factor δ is much smaller than one. The calculated threshold fluence of 0.15 J/cm^2 is approximately a factor of two lower than the experimental value, H = 0.31 – 0.47 J/cm^2.

4.2.4.3 Arrhenius type thermal model

The results were plotted as ln (average etch rate per pulse) vs. inverse fluence to determine if a linear relation exists (Figure 4.8).

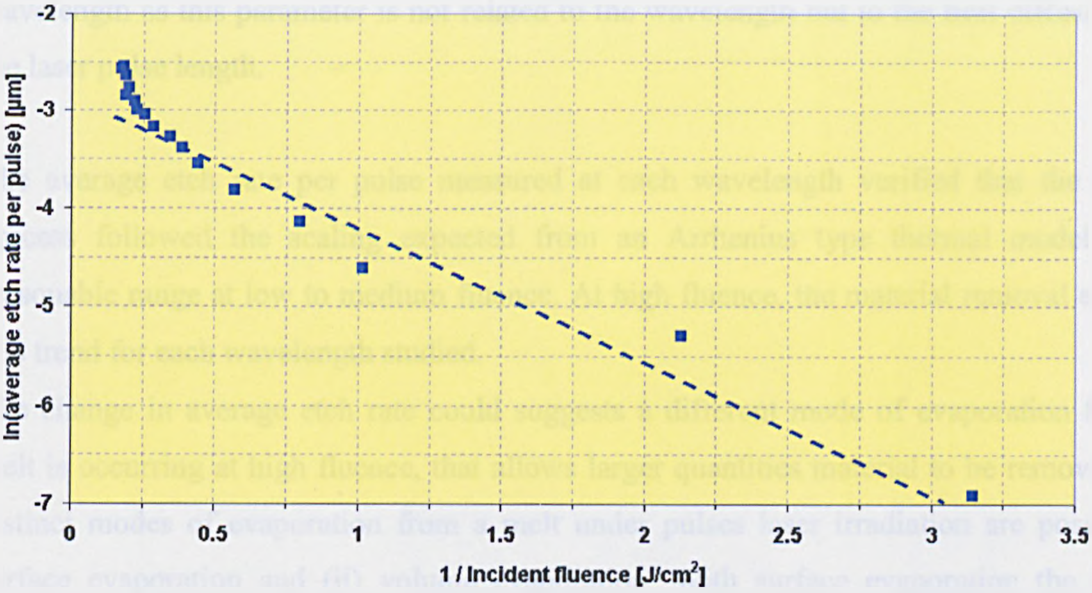

Figure 4.8: ln (Average etch rate per pulse) vs. 1/incident fluence for InP at a wavelength of λ = 157nm.

A linear relation is seen to apply for the lower incident fluence settings but the etch rate behaviour at higher fluences, H > 4 J/cm^2, shows a similar behaviour to the previous experiments, as the etch rate was larger than the Arrhenius type model predicts.

4.3 Discussion

The calculated absorption depth, heat diffusion length during laser pulse and threshold fluence are summarized in Table 4.5.

Material parameter	**Laser radiation wavelength [nm]**			
	355nm	**248nm**	**193nm**	**157nm**
Effective absorption depth [nm]	14.5	5.65	7.65	7.84
Heat diffusion length during laser pulse duration $\sqrt{D\tau}$ [μm]	1.15	1.04	0.95	0.95
Calculated threshold fluence [J/cm^2]	0.38	0.19	0.15	0.15
Estimated threshold fluence [J/cm^2]	N/A	0.1-0.21	0.09-0.19	0.31-0.47

Table 4.5: Summary of calculated and experimental etch rate data for InP ablated at four wavelengths.

A comparison (Table 4.5) shows no significant difference between the calculated absorption depth and threshold fluence for λ =248, 193 and 157nm. For 355nm radiation these were twice as large with an absorption depth of 14.5nm and a calculated threshold fluence of H= 0.38 J/cm^2. A similar heat diffusion length during the laser pulse is found for each wavelength as this parameter is not related to the wavelength but to the heat diffusivity and the laser pulse length.

The average etch rate per pulse measured at each wavelength verified that the ablation process followed the scaling expected from an Arrhenius type thermal model over a reasonable range at low to medium fluence. At high fluence, the material removal exceeded this trend for each wavelength studied.

The change in average etch rate could suggests a different mode of evaporation from the melt is occurring at high fluence, that allows larger quantities material to be removed. Two distinct modes of evaporation from a melt under pulses laser irradiation are possible: (i) surface evaporation and (ii) volume evaporation. With surface evaporation the material surface is 'superheated' but the heat loss within the molten material can occur through the growth of vapour bubbles, producing conventional boiling, and removal of material as vapour. However when the incident fluence of the laser is further increased, a very high temperature within the melt can be achieved and the 'super heated' material approaches its critical temperature, T_c. At this maximum, super heated temperature, the material can no longer sustain tensile forces and the boiling process becomes explosive and causes large levels of material removal. This is called a 'phase-explosion' and indicates the transition from the surface evaporation to volume evaporation [10, 20 – 22]. It is tentatively suggested that this may be the mechanism responsible for the increased etch rate seen in Figure 4.2, Figure 4.4, Figure 4.6 and Figure 4.8.

4.4 Conclusion

The average etch rate per pulse of the semiconductor InP was characterized at UV laser emission wavelengths of $\lambda = 355, 248, 193$ and 157nm. The average etch rate per pulse versus fluence was experimentally determined and plotted, and then tested against the predictions of an Arrhenius type thermal model by plotting ln(average etch rate) versus 1/ Incident fluence. The linear relation expected here was seen at low to moderate fluences but at high fluences, the material ablation rate was above the predicted trend. It is suggested a reason for this maybe a change of vaporization process, i.e. from surface to volume vaporization, in the form of a 'phase explosion'.

4.5 References

1. Heard, H. G., *Nature* 200, 667 (1963)
2. Jortner, J., Meyer, L., Rice, S. A., Wilson E. G., Localized excitations in condensed Ne, Ar, Kr and Xe, *J. Chem. Phys.* 42, 4250-4253 (1965)
3. Duley, W. W., *"UV lasers: effect and applications in materials science"* (Cambridge University Press, 1996)
4. Kawamura, Y., Toyada, K., Namba, S., Effective deep ultraviolet photoetching of polymethyl methacrylate by an excimer laser, *Appl. Phys. Lett.* 40, 374-376 (1982)
5. Srinivasan, R., Mayne-Banton, V., Self-developing photetching of poly(ethylene terephthalate) films by far- ultraviolet excimer laser radiation, *Appl. Phys. Lett.* 41, 576-578 (1982)
6. Srinivasan, R., Ablation of polymers and biological tissue by ultraviolet lasers, *Science* 234, 559-565 (1986)
7. Yeh. J. T. C., Laser ablation of polymers, *J. Vac. Sci.* A 4, 653-658 (1986)
8. Srinivasan, R., Baden, B., Ultraviolet laser ablation of organic polymers, *Chem. Rev.* 89, 1303-1316 (1989)
9. Dyer, P. E., Laser ablation of polymers, in *"Photochemical processing of electric materials"* ed. Boyd, I. W., Jackman, R. B. (Academic Press, 1992)
10. Dyer, P. E., Laser ablation: process and application, *Proc. SPIE* 3092, 412-418 (1996)
11. Dyer, P. E., Excimer laser polymer ablation: The first twenty years, *Proc. SPIE* 4760, 34-42 (2002)
12. Dyer, P. E., Excimer laser polymer ablation, twenty years on, *Appl. Phys. A* 77, 167-173 (2003)
13. Andrew, J. E., Dyer, P. E., Forster, D., Key, H., Directetching of polymetric materials using a XeCl Laser, *Appl. Phys. Lett.* 43, 717-719 (1983)
14. Srinivasan, R., Leigh, W. J., Ablative Photodecomposition: Action of far-ultraviolet (193nm) laser radiation on Poly(ethylene terephthalate) films, *J. Am. Chem. Soc* 104, 6784-6785 (1982)
15. Jellinek, H. H. G., Srinivasan, R., Theory of etching polymers by far ultraviolet, high intensity pulses laser and long term irradiation, *J. Phys. Chem.* 88, 3048-3051 (1984)
16. Baeri, P., Campisano, S. U., Heat flow calculation, in *"Laser annealing of semiconductors"* ed. Poate, J. M., Mayer, J. W. (Academic Press, 1982)

17. Kuper, S., Brannon, J., Brannon, K., Threshold behavior in polyimide photoablation: single-shot rate measurements and surface temperature modeling, *Appl. Phys. A* 56, 43-50 (1993)
18. Pearsall, T. P., "*Properties, processing and applications of indium phosphide*" (INSPEC, 2000)
19. Palik, D. E., "*Handbook of optical constants of solids*" (Academic press, 1985)
20. Dyer. P. E., Farrar, S. R., Key, P. H., Fast time-response photoacoustic studies and modelling of KrF laser ablated $Yba_2Cu_3O_7$, *Appl. Surf. Sci.* 54, 255-263 (1995)
21. Miotello, A., Kelly, R., Critical assessment of thermal models for laser sputtering at high fluences, *Appl. Phys, Lett.* 67, 3535-3537 (1995)
22. Von Allem, M., Baltter, A., "*Laser-beam interactions with materials – physical principles and applications*" (Springer, 1995)

5 Lithium niobate

5.1 Introduction

Lithium niobate is a ferroelectric crystal with a high Curie temperature of 1210°C [1]. Its ferrroelectricity was first discovered in 1949 [2] and the material was successfully grown in the form of large single crystals by the Czochralski technique in 1965 [3].

Due to its unique properties, it has found applications in many different areas [4]; as a piezoelectric material it is often used to make high frequency ultrasonic transducers. Also, its pyroelectric properties in combination with its stable physical and chemical properties make it a suitable material to use in infrared detectors. The crystal exhibits a transmission spectrum between the wavelengths of 0.4μm and 5μm and can therefore be used in optical, laser and telecommunications applications. Its non-linear properties allow it to be used as an optical frequency doubler and with its large linear electrooptical coefficient, $LiNbO_3$ crystals have been widely used for optical modulators, switches and Q-switches.

The Czochralski technique can be used for the growth of $LiNbO_3$ boules with sizes up to 6 inches and with x, y and z crystal orientation. [5]. The preparation of $LiNbO_3$ wafers from grown boules is, with minor modifications, similar to silicon [6] and InP wafer manufacturing as described in chapter 4.

Optical switches can be based on Y-junction shaped waveguides where an input signal can be set to route to one or two output ports, depending on the set refraction index of the output ports. A lower refraction index of the waveguide is preferred by the input signal and will be 'switched' into this waveguide while the other waveguide, with a higher refraction index, will not guide the signal. Applying an electric field to the $LiNbO_3$ based waveguides creates a change in refraction index and allows the switching of the input signal. When no electrical field is applied, the y-junctions functions as a splitter. [7]. An optical directional coupler structure can be used as an optical switching unit or as an optical modulator [8, 9]. With the directional coupler approach, light is split into two channel guides with a separation to allow coupling between them. The applied electric field changes the relative propagation velocities of the odd and even modes, so when the guides are separated at the output end of the coupler, the sum of the optical powers is constant, but the optical power in any one is a function of the applied electrical field. External optical modulators are mostly based on the Mach-Zender interferometer (MZI) structure. With MZI modulators, the input light is split in a Y branch and travels separated in its own waveguide before being recombined. By changing the refraction index of these waveguides with an electric field, the optical path of the light travelling in one waveguide will be different to the other and when recombined, interference can occur and so light can be modulated. The electrooptic constant is significantly larger when the electric field is z-directed and the modulators are designed to exploit this large electrooptic constant by ensuring that the waveguide sees an electric field along the z-axis of the crystal. Due to these requirements, the orientation of the $LiNbO_3$ crystal used in modulator manufacture are x-cut and z-cut.

The process of $LiNbO_3$ modulator manufacturing [10] starts with a high optical quality $LiNbO_3$ wafer with an x-cut or z-cut orientation and consists of: (i) optical waveguide fabrication, (ii) electrode fabrication, (iii) dicing and polishing and (iv) pigtailing, packaging and testing. Optical waveguides are processed onto the wafer by diffusion of titanium [11] or by proton exchange [12, 13]. To apply an electric field to the waveguides, gold electrodes are defined with lithographic processes. One $LiNbO_3$ wafer hosts an array of finished modulators and to end up with individual modulator components, conventional water-cooled diamond saws are used to dice the wafers into separate modulators where the end faces are cut at an angle to the waveguide. The end faces are polished to a good optical finish to ensure a low loss fibre to waveguide coupling. Care has to be taken during the dicing step; with the process, mechanical contact is made between the abrasive diamond saw and the wafer, which can cause the fracture of the partially processed wafer. Contaminants, either from debris or coolant, also can have a negative impact on the modulator performance and long-term reliability. Another disadvantage of the conventional diamond saw cutting process is the one directional cutting motion and limited ability to cut complex 2-D structures, which can lead to a large amount of crystal wastages.

The last process steps are pigtailing, packaging and testing. The fibre to waveguide attachment is a process where five degrees of freedom between the two are actively controlled to maximize the power throughput [14]. Translation and rotational adjustments, together with the bonding of the fibre to the waveguide, are time consuming and add cost and complexity to the manufacturing process. $LiNbO_3$ devices can be packaged in hermetic or non-hermetic housing, depending on their designated application and working environment.

In summary, the manufacturing process of modulators and other similar $LiNbO_3$ based devices includes dicing and a pigtailing process step. Both of these steps add complexity to the process through debris contamination, one directional cutting and complex fibre to waveguide alignment. In this chapter, developments of a UV laser based cutting process for $LiNbO_3$ is discussed and the development of a time-saving passive fibre alignment platform for fibre to waveguide coupling in the pigtailing process.

The work begins with an assessment of the ablation characteristics of x-cut and z-cut $LiNbO_3$ orientated crystals using the four laser wavelengths, 355, 248, 193 and 157nm

5.2 UV laser ablation of lithium niobate

Using the four available UV laser micromachining systems the ablation behaviour of both the x-cut and z-cut $LiNbO_3$ crystals were determined.

5.2.1 UV solid-state laser micromachining system

The ablation behaviour of x-cut and z-cut $LiNbO_3$ were determined at a laser emission wavelength of 355nm by using the UV solid state laser micromachining system. The ablation etch rates were determined by machining blind holes into the $LiNbO_3$ crystal using 100 laser pulses at a repetition rate of 10 kHz. The depths of the holes were measured with an optical microscope as discussed in chapter 4. For the x-cut and z-cut $LiNbO_3$ crystals, the determined average etch rate per pulse were plotted against the incident fluence and are shown in Figure 5.1and Figure 5.2.

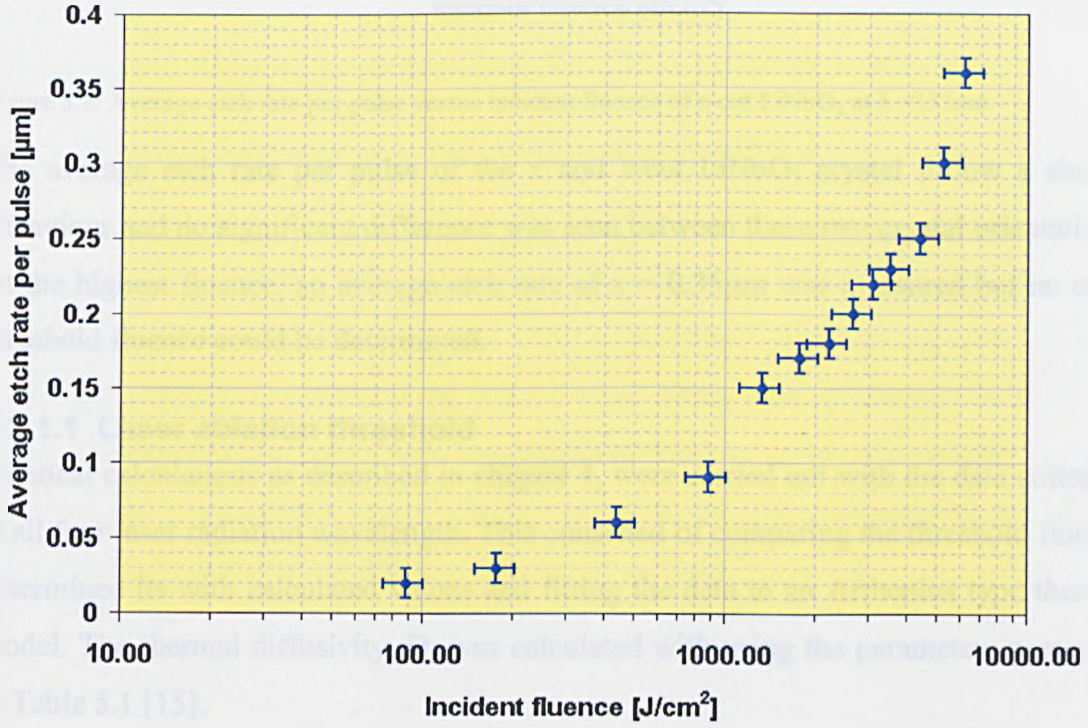

Figure 5.1: Average etch rate per pulse versus incident fluence of x-cut $LiNbO_3$ at $\lambda = 355nm$.

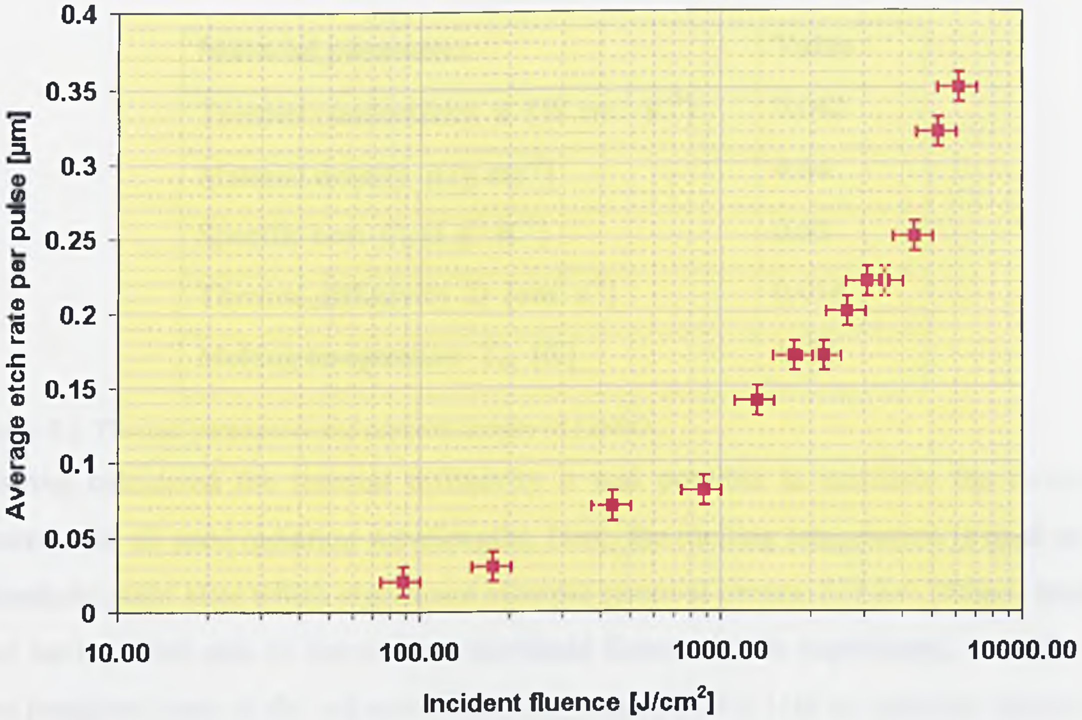

Figure 5.2: Average etch rate per pulse versus incident fluence of z-cut $LiNbO_3$ at λ=355nm.

The average etch rate per pulse of the x and z-cut $LiNbO_3$ crystal follow a similar behaviour and no significant difference was seen between these two crystal orientations. At the highest fluence, an average etch rate of x = 0.35µm was measured but no clear threshold fluence could be determined.

5.2.1.1 Laser ablation threshold

Identical calculations as described in chapter 4, were carried out with the data collected at all four laser radiation wavelength. This consisted of comparing the threshold fluence determined its with calculated values and fitting the data to an Arrhenius type thermal model. The thermal diffusivity, D, was calculated with using the parameters presented in Table 5.1 [15].

Material parameter	**Value**
Thermal conductivity κ [W cm^{-1} K^{-1}]	0.042
Material density ρ [g cm^{-3}]	4.64
Specific heat C_p [J g^{-1} K^{-1}]	0.63
Thermal diffusivity D [cm^{2} s^{-1}]	0.014
Melting temperature T_m [K]	1523

Table 5.1: Thermal parameters and material density of $LiNbO_3$.

Having calculated the thermal diffusivity it was possible to calculate the threshold fluence for all used radiation wavelengths. Here, the melting temperature is used as the threshold point after which significant material removal occurs. For $\lambda = 355$nm, besides not having been able to determine a threshold fluence in the experiment, no value for the imaginary part of the refractive index, k, was available [16] to calculate absorption coefficient and therefore the threshold value at 355nm could not be estimated.

5.2.2 KrF excimer laser mask projection system

The etch rates of the x-cut and z-cut $LiNbO_3$ crystals at 248nm were determined with the KrF excimer laser mask projection system. The etch rates were determined by ablating a blind hole into the crystal at different incident fluence setting with 100 laser pulses at a repetition rate of 100 Hz. A square metal aperture (10x10mm) was used as a mask. The depth of each blind hole was measured with the optical microscope. For both the x-cut and z-cut $LiNbO_3$ crystal, the average etch rate etch rates were plotted against the set incident fluences and are shown in Figure 5.3 and Figure 5.4.

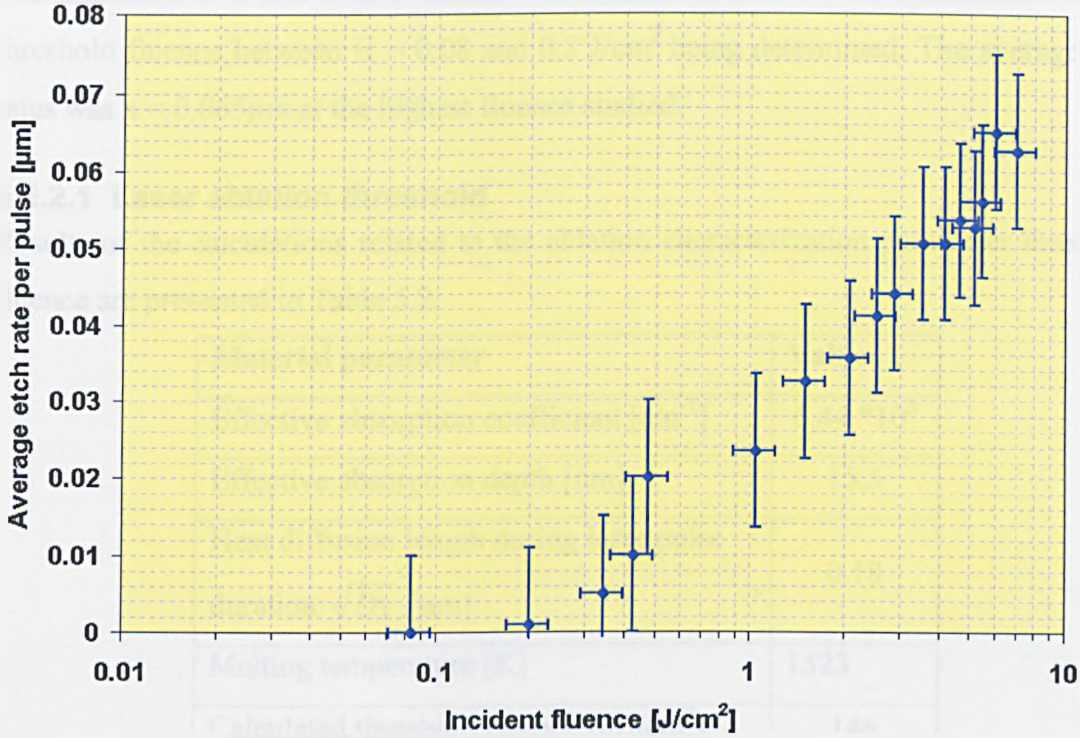

Figure 5.3: Average etch rate per pulse vs. incident fluence for x-cut LiNbO$_3$ at a wavelength of λ = 248nm.

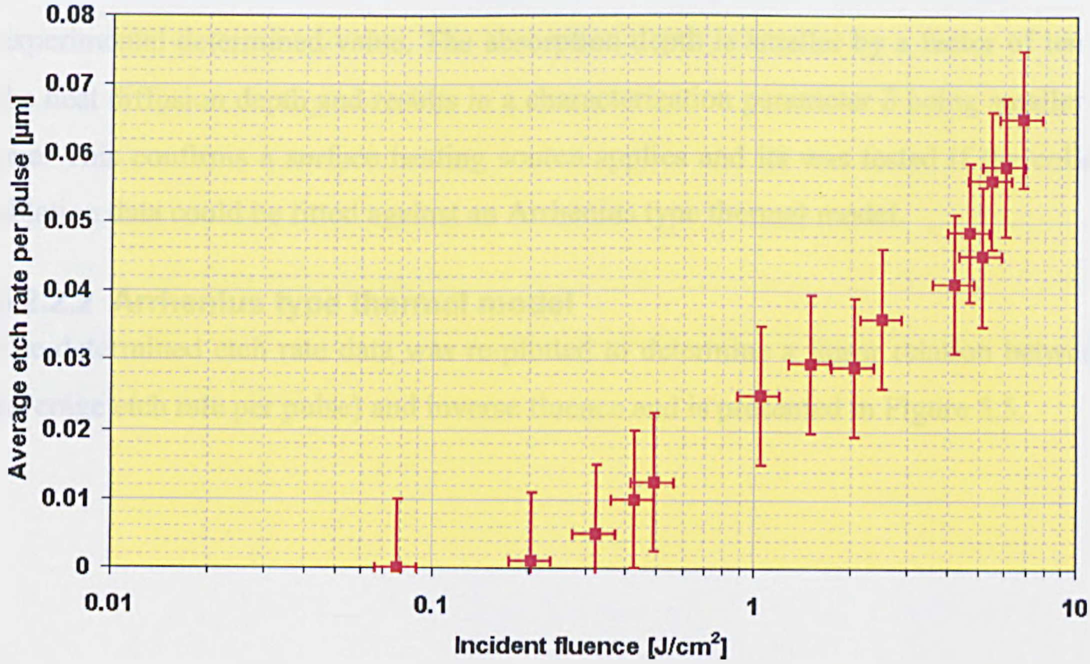

Figure 5.4: Average etch rate per pulse vs. incident fluence for z-cut LiNbO$_3$ at a wavelength of λ = 248nm.

The measured etch rate versus fluence was similar for both crystal orientations with a threshold fluence between H ~ 0.08 and 0.2 J/cm^2 being determined. The average etch rates was x = 0.065µm at the highest fluence studied.

5.2.2.1 Laser ablation threshold

Results of the calculations related to the ablation characterization parameter threshold fluence are presented in Table 5.2.

Material parameter	**Value**
Effective absorption coefficient [cm^{-1}]	6.44 *10^5
Effective absorption depth [nm]	15.5
Heat diffusion length during laser pulse duration $\sqrt{D\tau}$ [µm]	0.18
Melting temperature [K]	1523
Calculated threshold fluence [mJ/cm^2]	146

Table 5.2: KrF excimer laser micromachining system laser ablation calculations for optical and thermal material parameters.

The calculated threshold fluence, based on the melting temperature, did agree with the experimental determined value. The absorption depth is smaller by a factor of ten than the heat diffusion depth and results in a characterization parameter δ being smaller than one. This confirms a surface heating source applies and its was tested if the collected ablation data could be fitted against an Arrhenius type thermal model.

5.2.2.2 Arrhenius type thermal model

The determined etch rate data was re-plotted to determine a linear relation between ln (average etch rate per pulse) and inverse fluence and is presented in Figure 5.5.

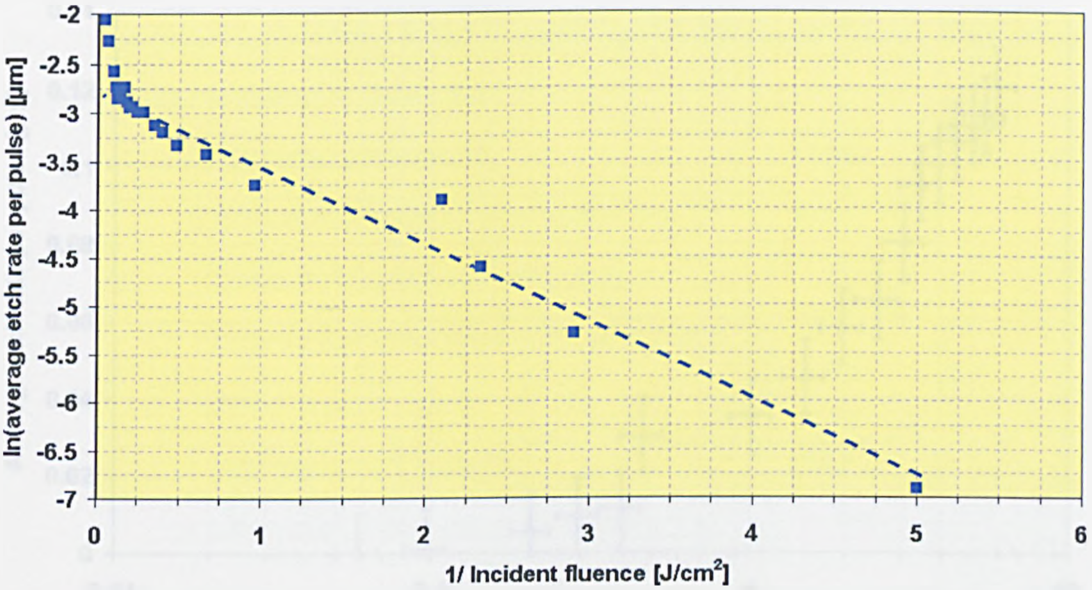

Figure 5.5: ln(average etch rate per pulse) vs. 1/incident fluence of the x-cut $LiNbO_3$ at a wavelength of λ =248nm.

The plot shows a linear relation up to inverse incident in the range 0.2 – 5 cm2/J but the removal rate is higher than the Arrhenius thermal model would predict, when this falls below ~ 0.2 cm^2/J (re fluence > $5J/cm^2$).

5.2.3 ArF excimer laser mask projection system

The laser ablation behaviour of x-cut and z-cut $LiNbO_3$ orientated crystal was determined 193nm with the ArF excimer laser mask projection system. In both crystals, blind holes were machined at different fluences, with 100 laser pulses at a repetition rate of 100Hz, and they were measured by an optical microscope. The etch rate results for both x-cut and z-cut crystals were plotted against the incident fluences and are presented in Figure 5.6 and Figure 5.7.

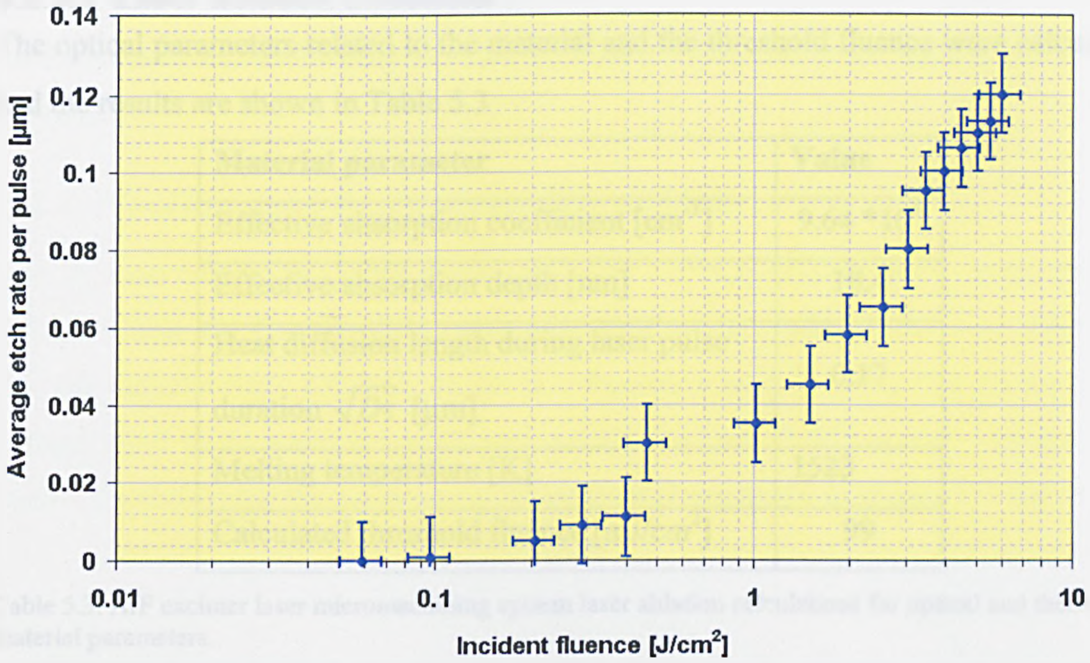

Figure 5.6: Average etch rate per pulse vs. incident fluence for x-cut $LiNbO_3$ at a wavelength of λ = 193nm.

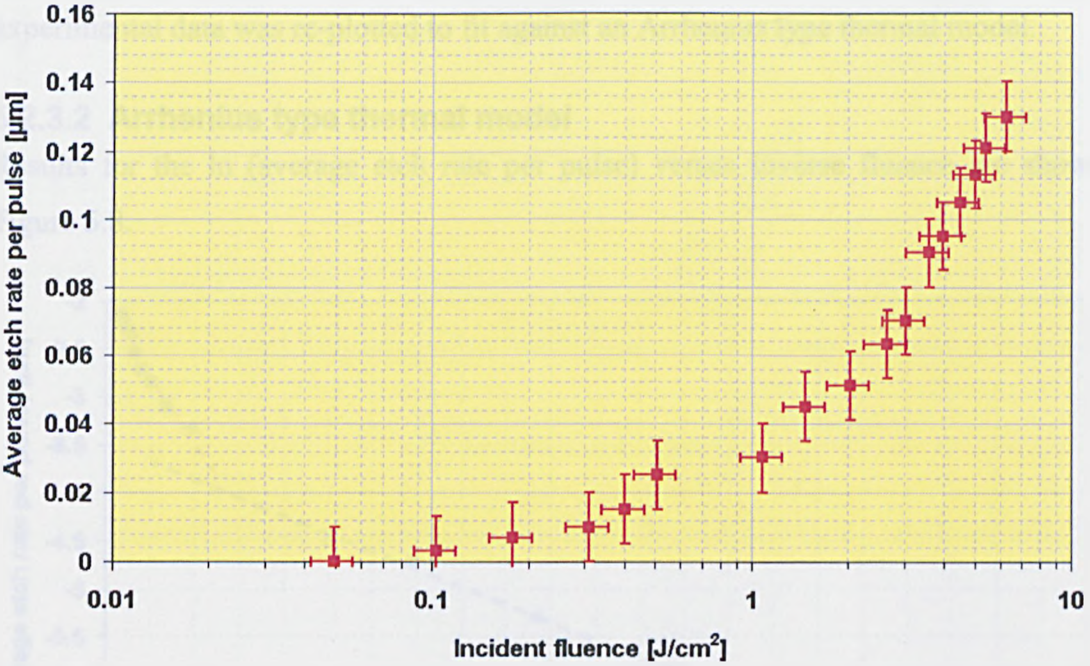

Figure 5.7: Average etch rate per pulse vs. incident fluence for z-cut $LiNbO_3$ at a wavelength of λ = 193nm.

The average etch rates at 193nm were similar for both crystals with a threshold fluence estimated to lie between H = 0.05 and 0.1 J/cm^2.

5.2.3.1 Laser ablation threshold

The optical parameters related to the material and the threshold fluence were calculated and the results are shown in Table 5.3

Material parameter	Value
Effective absorption coefficient [cm^{-1}]	9.64 *10^5
Effective absorption depth [nm]	10.4
Heat diffusion length during laser pulse duration $\sqrt{D\tau}$ [μm]	0.17
Melting temperature [K]	1523
Calculated threshold fluence [mJ/cm^2]	99

Table 5.3: ArF excimer laser micromachining system laser ablation calculations for optical and thermal material parameters.

The measured threshold fluence agreed with the calculated value, based on the melting temperature of the material, and the heat diffusion depth was found to be a factor ten higher than its absorption depth. It suggests that a surface heating model applies and the experimental data was re-plotted to fit against an Arrhenius type thermal model.

5.2.3.2 Arrhenius type thermal model

Results for the ln (average etch rate per pulse) versus inverse fluence are shown in Figure 5.8.

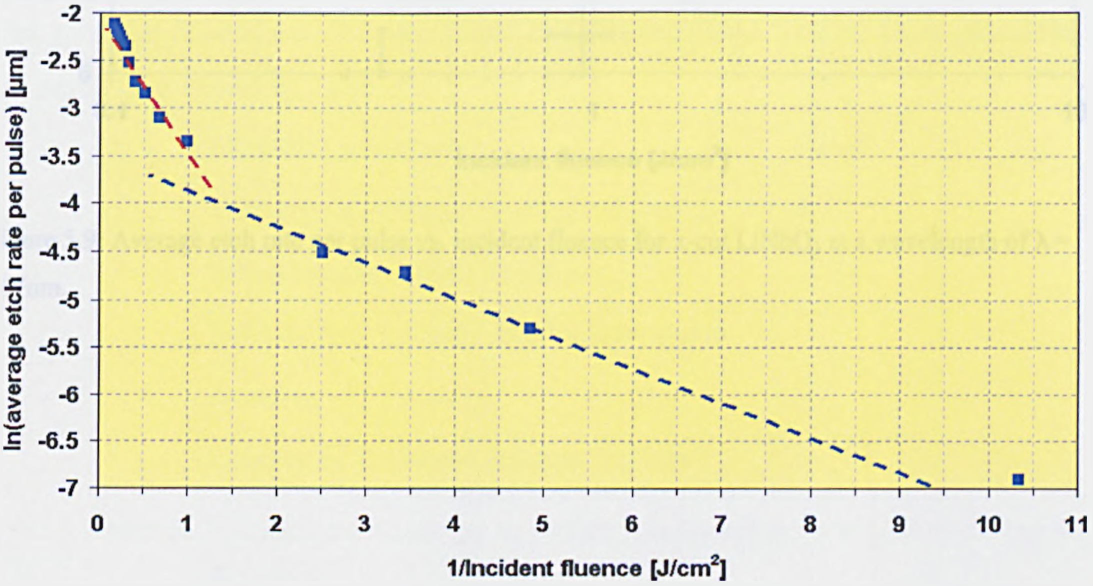

Figure 5.8: ln (average etch rate per pulse)vs. 1.incident fluence of x-cut $LiNbO_3$ at a wavelength of λ =193nm.

A linear relation was found over a limited range of inverse fluence (~1.5-9.5 cm^2/J). At lower values (higher fluence) the etch rate again increased more rapidly the scaling predicted.

5.2.4 Fluorine laser mask projection system

The ablation behaviour of the x-cut and z-cut $LiNbO_3$ crystals were determined at 157nm. Using the fluorine laser mask projection system, blind holes were machined into the material with 100 laser pulses at a repetition rate of 10Hz. The depths of the ablated blind holes were measured with a VEECO DEK TAK^3 surface profiler. The results are shown for the x-cut and z-cut crystals respectively in Figure 5.9 and Figure 5.10.

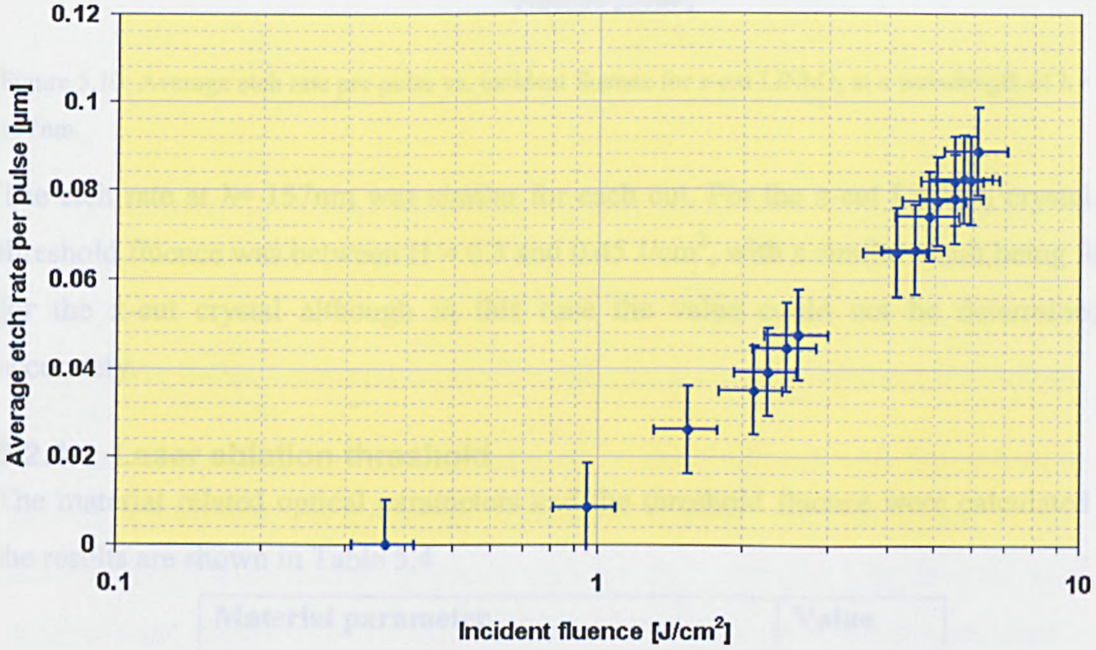

Figure 5.9: Average etch rate per pulse vs. incident fluence for x-cut $LiNbO_3$ at a wavelength of λ = 157nm.

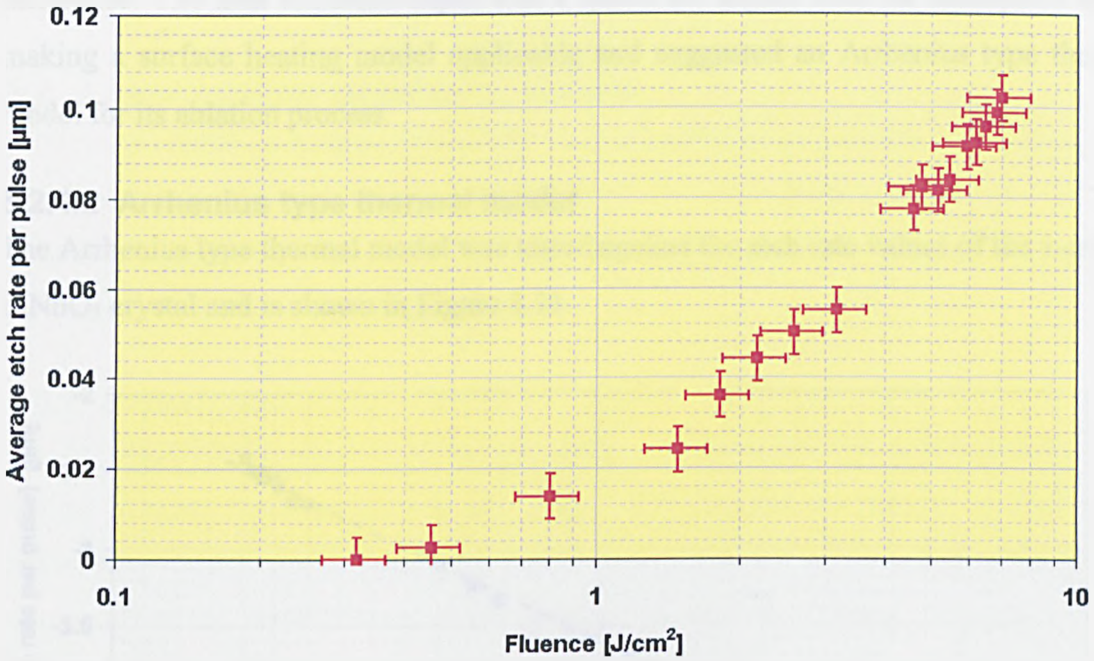

Figure 5.10: Average etch rate per pulse vs. incident fluence for z-cut $LiNbO_3$ at a wavelength of λ = 157nm.

The etch rate at λ= 157nm was similar for each cut. For the z-cut $LiNbO_3$ crystal, the threshold fluence was between H = 0.3 and 0.45 J/cm^2, with a similar result being found for the x-cut crystal although in this case the value could not be determined so accurately.

5.2.4.1 Laser ablation threshold

The material related optical parameters and the threshold fluence were calculated and the results shown in Table 5.4

Material parameter	Value
Effective absorption coefficient [cm^{-1}]	4.72 *10^5
Effective absorption depth [nm]	21.2
Heat diffusion length during laser pulse duration $\sqrt{D\tau}$ [µm]	0.17
Calculated threshold fluence [mJ/cm^2]	93

Table 5.4: Fluorine laser micromachining system ablation calculations for optical and thermal material parameters.

The measured threshold fluence, based on the material reaching the melting temperature, did not agree with the calculated value as a there is a factor of three difference. The heat diffusion depth was a factor ten higher than the absorption depth making a surface heating model applicable and suggested an Arrhenius type thermal model for its ablation process

5.2.4.2 Arrhenius type thermal model

The Arrhenius type thermal model was tested against the etch rate values of the x-cut $LiNbO_3$ crystal and is shown in Figure 5.11.

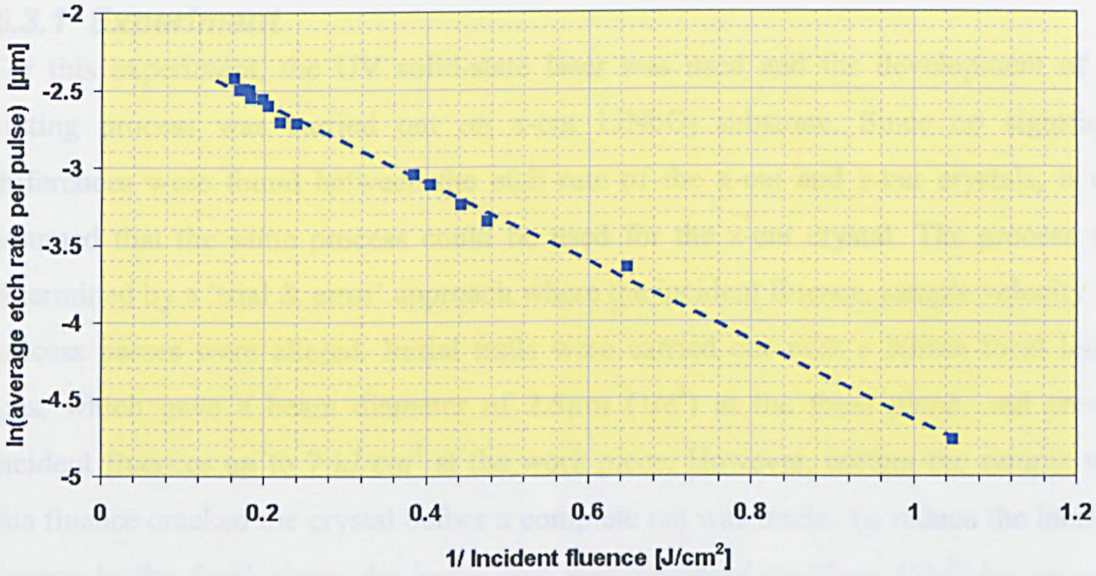

Figure 5.11: ln(average etch rate per pulse)vs. 1/incident fluence of the x-cut $LiNbO_3$ at a radiation wavelength of λ=157nm.

Over the whole range of the data obtained, a linear relation was found between the ln(average etch rate per pulse) vs. 1/incident fluence, confirming that in this case $LiNbO_3$ removal could be described well by an Arrhenius type thermal model. It resembles the classic etch rate versus incident fluence curve where a linear dependence on log fluence indicating that thermal diffusion is controlling the ablation rate, an analysis borne out by the Arrhenius plot.

5.3 Laser cutting of lithium niobate

Within the photonics market, $LiNbO_3$ is used in switching and modulation devices and as part of the production process, both have to be diced from a wafer. As has been discussed already there is interest in using laser machining as an alternative technique for processing $LiNbO_3$ wafers and devices

5.3.1 Experiment

For this experiment, the UV solid-state laser was used and the development of the cutting process was carried out on x-cut $LiNbO_3$ substrate. Since no significant differences were found between the etch rate of the x-cut and z-cut crystals, it was assumed that the same process could be used for the z-cut crystal. The process was determined by a 'trial & error' approach where the incident fluence, sample velocity and process passes were altered. Initial trails were carried out with a 50mm focal length lens, which gave a beam diameter of 2.5μm ($1/e^2$) at the focal plane, and created incident fluences up to 7 kJ/cm^2 at the work piece. However, cutting the sample with this fluence cracked the crystal before a complete cut was made. To reduce the incident fluence in the focal plane, the beam spot was increased to 13μm ($1/e^2$) by use of a 157mm focal length lens and the cutting trails were repeated at a lower average laser power.

5.3.2 Results

The best results for cutting the $LiNbO_3$ x-cut crystal were achieved with an incident fluence of $H = 54\ J/cm^2$, a sample velocity of 750mm/min and 200 single process passes. By using a gas nozzle to apply nitrogen to the focus–crystal interaction point, a clean and debris-free slot was produced. Without gas assist, process debris accumulated in the cutting slots and shielded the laser beam as seen in Figure 5.12.

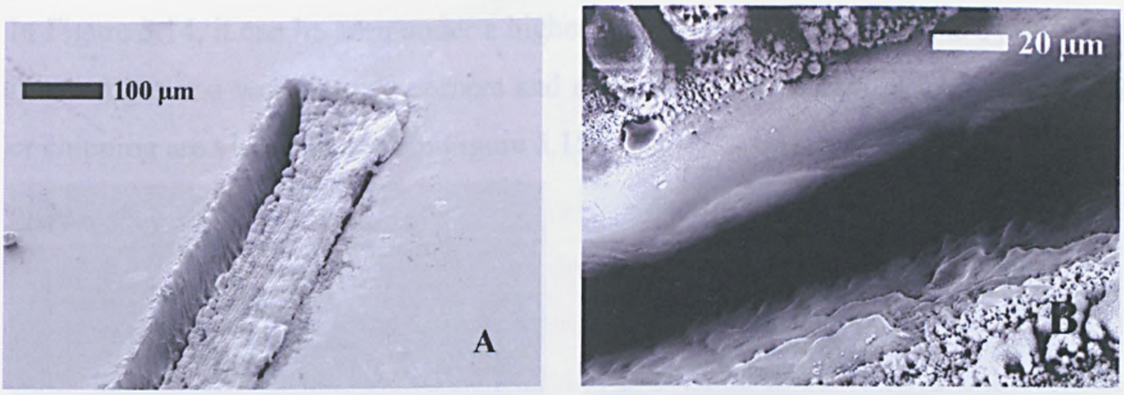

Figure 5.12: $LiNbO_3$ cutting with 355nm without (A) and with nitrogen gas assist (B).

To illustrate this cutting process, a 3 x 3 mm square was cut out of a $LiNbO_3$ x-cut crystal. After processing, the square "plug" and the base material was examined with a scanning electron microscope and results are shown in Figure 5.13, Figure 5.14 and Figure 5.15.

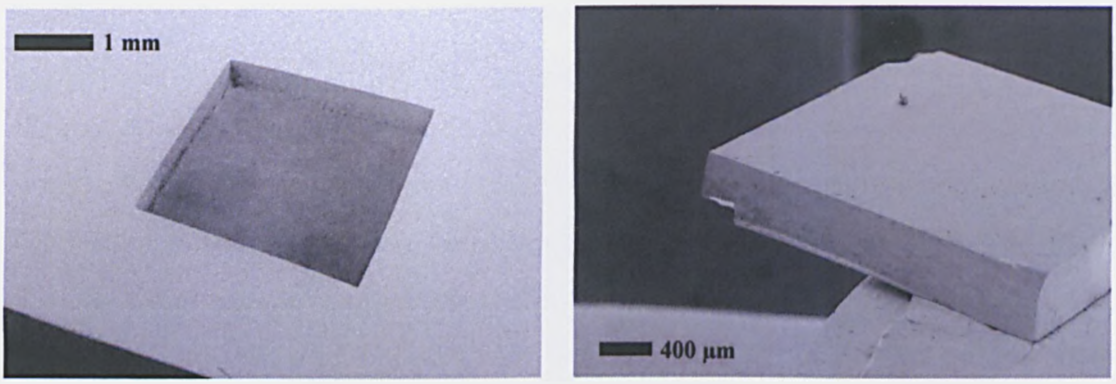

Figure 5.13: SEM pictures of $LiNbO_3$ square at (A) 1mm and (B) 400μm scale.

The $LiNbO_3$ square presented was cut with high accuracy and demonstrated the ability to cut small 2-D shapes without material loss (the chipped corners were a result of handling of the crystal.)

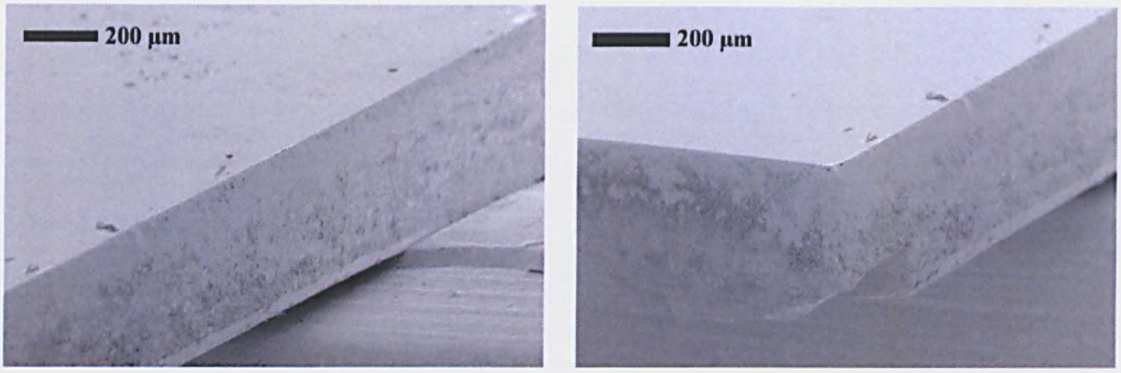

Figure 5.14: SEM pictures of $LiNbO_3$ square, cut with UV solid state laser micromachining system.

In Figure 5.14, it can be seen under a higher magnification, that the $LiNbO_3$ sample has intact edges and well-defined corners and no visible heat damage effects like cracking or chipping are visible as seen in Figure 5.15.

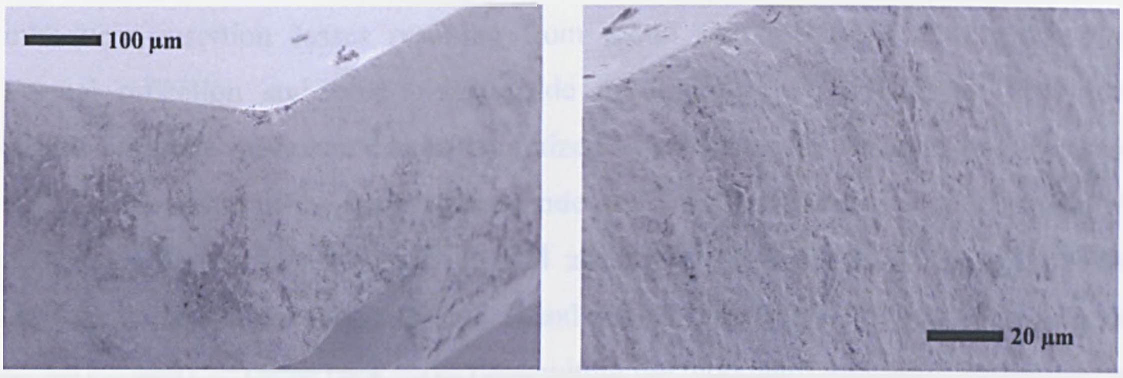

Figure 5.15: SEM pictures of Linbo3 square, cut with UV solid state laser micromachining system. (A) at 100µm and (B) at 20µm scale

5.4 Passive fibre alignment V-grooves

Coupling optical fibres to a $LiNbO_3$ modulator, or other planar lightwave circuits, introduces insertion losses resulting from mode size mismatch, propagation loss, Fresnel reflection and fibre-to-waveguide misalignment [14]. The insertion losses caused by mode mismatch can be minimized by matching the shape of the waveguide mode to the shape of the optical fibre mode and a well-confined waveguide mode will reduce the losses due to scattering and absorption. The refraction index mismatch between the $LiNbO_3$ waveguide ($n \sim 2.2$) and optical fibre ($n \sim 1.5$) will produce a Fresnel reflection and can cause back reflections within the modulator and fibre. Anti-reflection coatings can reduce the insertion loss [17] and likewise suitably angled faces between the fibre and $LiNbO_3$ waveguide can reduce the insertion loss and back reflection [18]. Insertion loss due to misalignment between the fibre and waveguide is minimized as the fibre is positioned relative to the waveguide by active power monitoring. This fibre alignment is part of the pigtailing process where the optical fibre, before being attached to the $LiNbO_3$ chip, is glued into a glass capillary to increase its adhesive surface area. During the five-axis, fibre-to-waveguide alignment, the fibre is manipulated until the position which allows the highest power throughput is found and the fibre-capillary assembly is then glued to the modulator with UV curing glue. For mechanical strength, the optical fibre is attached to the modulator's sealed packaging [19].

This five-degrees of freedom, fibre alignment procedure, is complex and time-consuming. By reducing the number of degrees of freedom, this process would be simplified and the alignment time reduced. The degree of freedom of the fibre can be reduced by using self-aligning structures, where for correct alignment, the optical fibre is placed into an alignment groove. With these kinds of structures, the number of degrees of freedom is reduced to only one; the separation between the fibre facet and the optical waveguide. The first self – alignment approach [20], applicable to $LiNbO_3$, was a "flip-chip" combination between $LiNbO_3$ and silicon with fibre alignment V-grooves. Further development resulted in an "overlap" approach where optical fibres are positioned in silicon V-grooves, placed onto the $LiNbO_3$ substrate [7]. The manufacturing of $LiNbO_3$ based self-alignment platform is limited, due to the low etch rates when using available techniques such as, wet etching [21], reactive ion etching [22] or ion-milling [23]. These typically have shown etch rates in the order of tens of Angstroms per minute. For a fully integrated $LiNbO_3$ based fibre alignment platform, a KrF excimer laser can be used [24] to produce fibre alignment V-grooves using mask projection techniques. Etch rates of 1 µm per laser pulse can be achieved and the shape of the alignment groove defined by the dimensions of the mask used within the projection system. Critical to the fibre alignment platforms and thus the useful application of this technique, is the overall smoothness of the V-groove as this defines how well the fibre is positioned in front of the waveguide. Any irregularities in the V-groove misplace the fibre and reduce the coupling efficiency. The KrF excimer laser mask projection system was used to develop a process for making passive fibre alignment platforms.

5.4.1 Process development of passive fibre alignment V-grooves

The proposed process to machine V-grooves in $LiNbO_3$ was based on the static mask-workpiece dragging technique. With this technique a V-shape mask was imaged onto the surface while the crystal was being translated. This resulted in V-shaped grooves, where the total number of laser pulses fired per area depended on the laser repetition rate, mask dimensions, crystal translation velocity and the number of process passes.

The mask used with the projection systems defines the shape of the machined V-grooves and consequently the position of the optical fibre in the V-groove. In this experiment, the final position of the optical fibre core was chosen to be in line with the crystal surface as the waveguides are positioned just below the surface of the crystal. The correct mask dimensions were determined by the using a schematic drawing; see Figure 5.16, where the circle represented the optical fibre and the black dot the core.

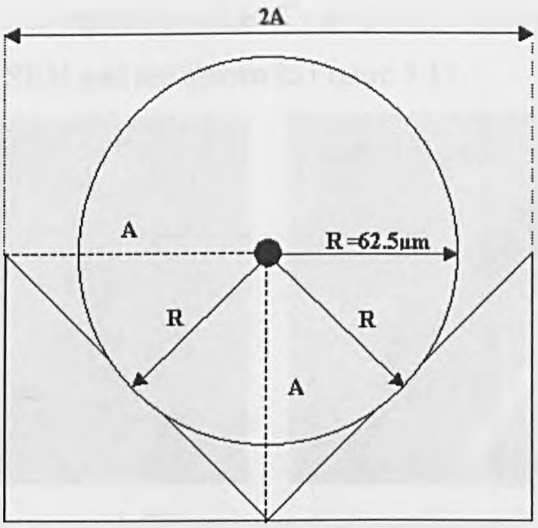

Figure 5.16: Schematic drawing of an optical fibre placed into a 90° angled v-shape.

The value of the length A was defined by the radius of the fibre cladding R i.e. $A = \sqrt{2}R = 88.4\mu m$ which gave a required V-groove width of 176.8μm. As a 10x projection system was being used, the dimensions of the mask were made to be A= 0.9mm and the width of the V-shape; 2A=1.8mm.

The debris produced during the ablation process was deposited onto the crystal surface and into the V-groove. This debris could interfere with correct alignment of the fibre in relation to the waveguide and, therefore, had to be eliminated. A combination of two methods was proposed and examined; (i) using a removable top surface coating and (ii) using gas assist during the ablation process. The gas assist was used to eliminate debris deposition into the V-groove and will be discussed in later parts of this chapter. A suitable top surface coating was investigated before further process development was carried out.

Two different anti-debris surface techniques were explored. The first used an emulsitone coating[1], applied to the surface via spin coating for wafers, or with a brush for smaller pieces. During machining debris would be deposited on the coating but this could then be removed by rinsing the crystal in luke warm water. The second coating was a piece of 'Scotch tape' applied to the surface. This also collected deposited debris and was peeled off the surface after machining. The process conditions used were: Fluence = 3 J/cm^2 , Velocity = 3mm/min, 10 process passes, 400 pulses per area in each

---

[1] Emulsitone laser scribing solution, Emulsitone Co. New Jersey, USA

process pass, 100Hz pulse repetition rate. A comparison between the two V-grooves were examined with an SEM and are shown in Figure 5.17.

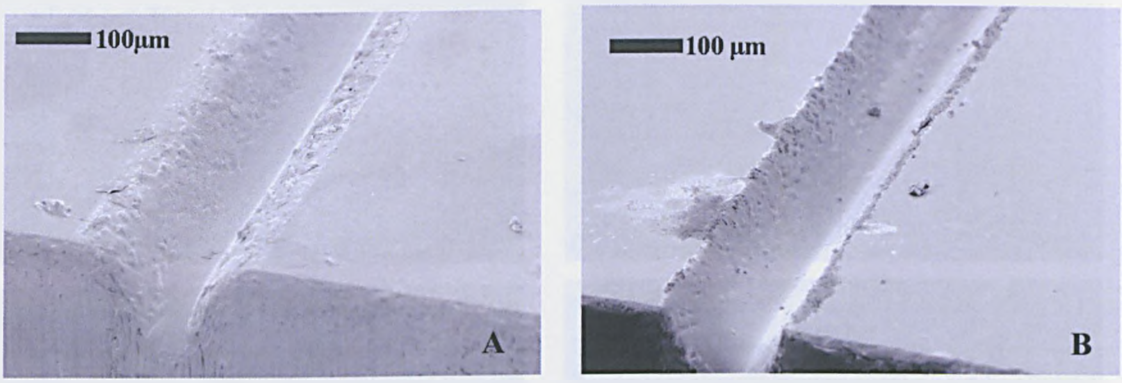

Figure 5.17: V-groove machined with (A) emulsitone and with (B) Scotch tape on top surface.

Machining the V-grooves through the 'Scotch tape' and using it as anti-debris surface material resulted in a better surface quality than the emulsitone. This technique was used during following experiments.

With the design of the mask, the depth needed for the core of the fibre to be level with the crystal surface was 88μm. The previously obtained etch rates at $\lambda = 248$nm were determined without the anti debris tape and could not be used to correlate the number of laser pulses per area required for the correct depth of V-groove. A guide was determined by machining V-grooves into $LiNbO_3$ with different number of laser pulses per area at 3 J/cm^2 incident fluence. The depths of the V-grooves were measured with a Leica optical microscope and it was found that 2000 shots per area resulted in a depth of 58μm, 3000 resulted in a depth of 70 μm and 5000 in 93μm. 5000 shots per area was chosen as a guide in further process development experiments.

During the etch rate experiments, cracking and damage of the $LiNbO_3$ surface occurred with incident fluence of 5 J/cm^2 or higher but not below 4 J/cm^2. Therefore, incident fluences of 1, 2, 3 and 4 J/cm^2 were used for the process development. Machining tests were made on x-cut $LiNbO_3$ crystals. At each fluence, a different number of process passes was used while the sample velocity was altered to maintain the same number of shots per area. The repetition rate of the excimer laser was set to 100Hz. An SEM was used to examine the machined $LiNbO_3$ samples which can be seen in Figure 5.18 to Figure 5.21.

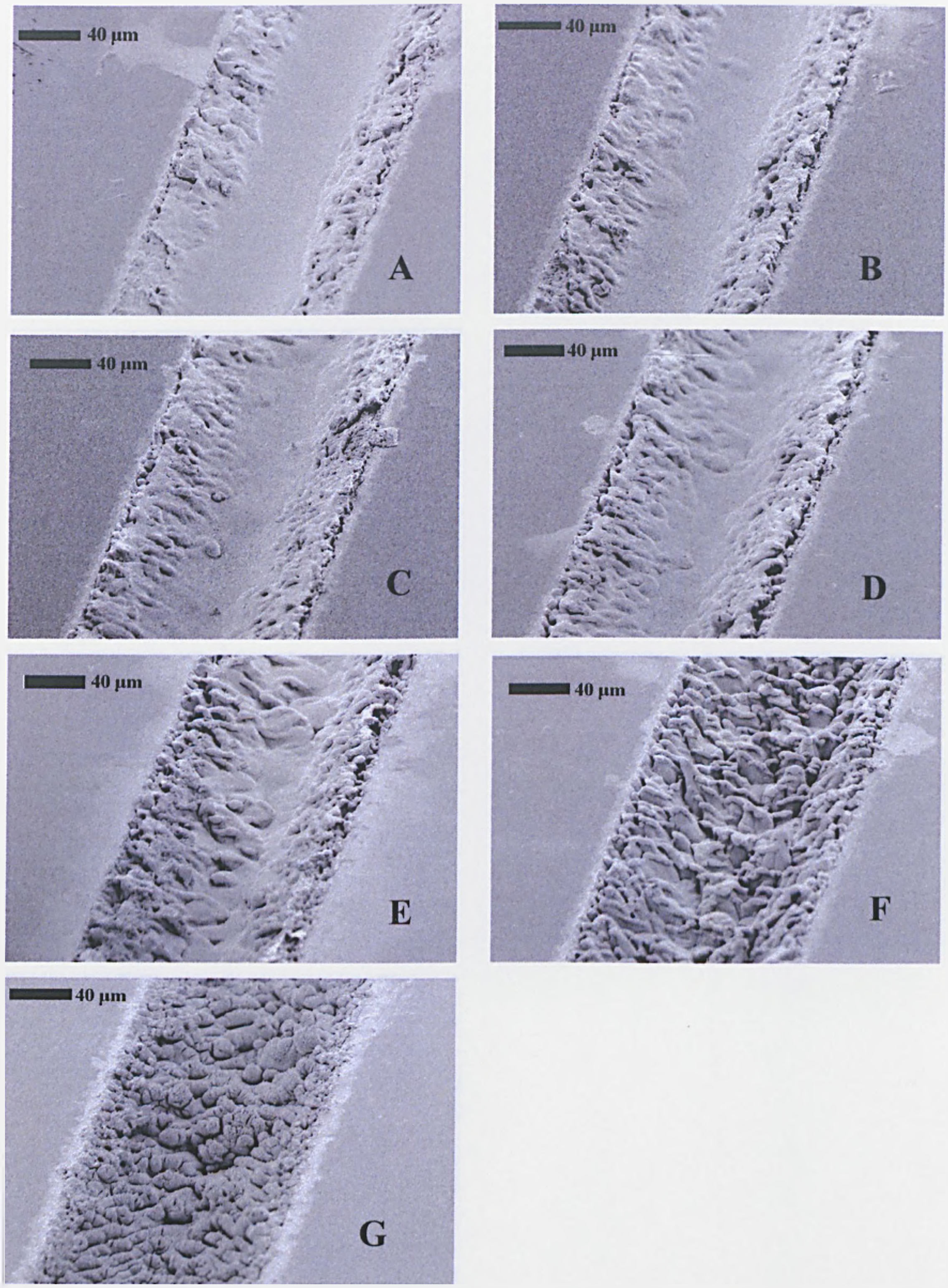

Figure 5.18: Machined v-grooves in $LiNbO_3$ made using KrF laser. Fluence = 1 J/cm^2 and various processing parameters: (A) v = 0.6 mm/min, 1 process pass (B) v = 1.8 mm/min, 3 process passes (C) v = 3 mm/min, 5 process passes (D) v = 4.2mm/min, 7 process passes (E) v = 6mm/min, 10 process passes (F) v = 7.2mm/min, 12 process passes (G) v = 9mm/min, 15 process passes.

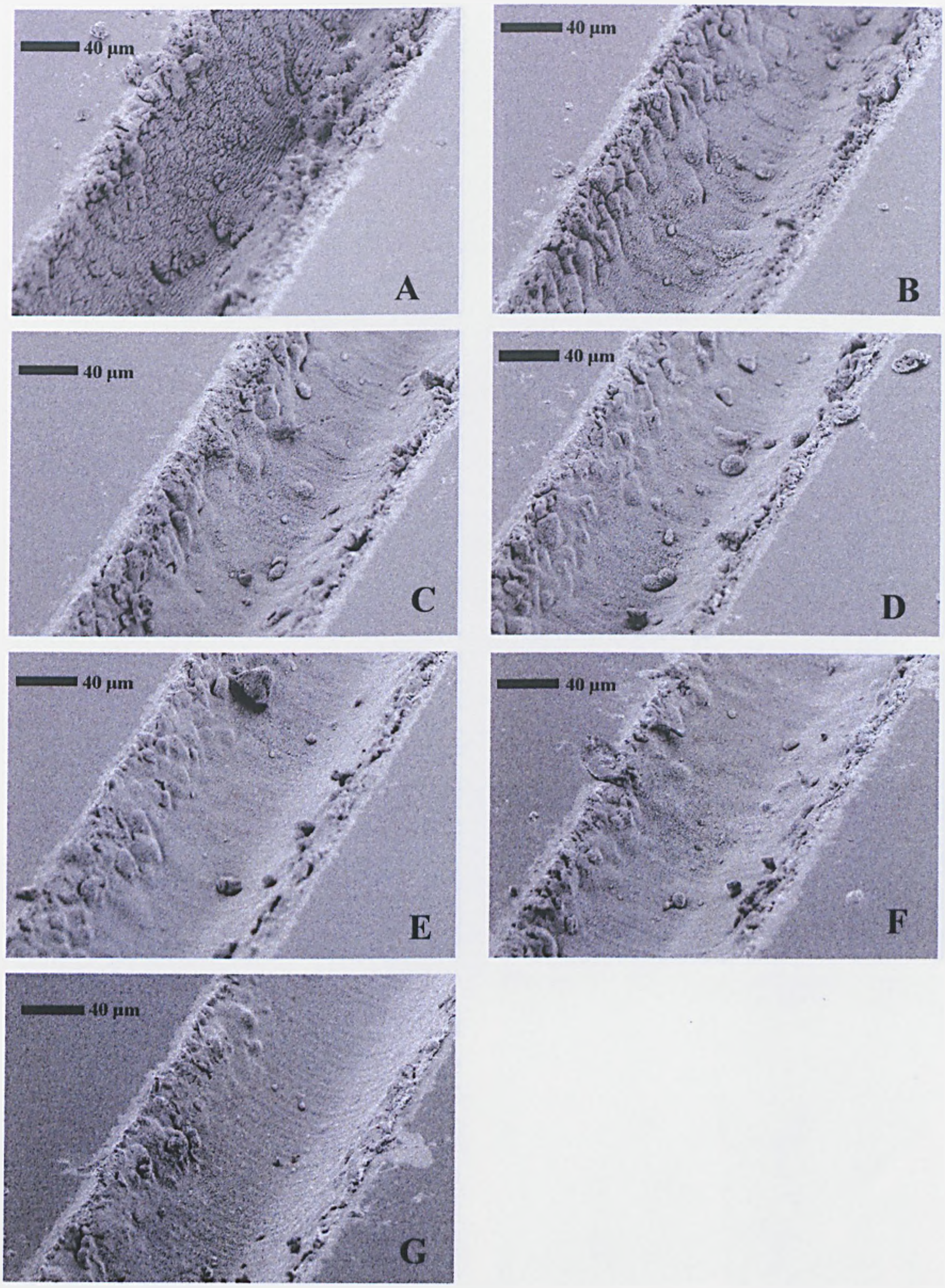

Figure 5.19: Machined v-grooves in $LiNbO_3$ made using KrF laser. Fluence = 2 J/cm^2 and various processing parameters: (A) v = 0.6 mm/min, 1 process pass (B) v = 1.8 mm/min, 3 process passes (C) v = 3 mm/min, 5 process passes (D) v = 4.2mm/min, 7 process passes (E) v = 6mm/min, 10 process passes (F) v = 7.2mm/min, 12 process passes (G) v = 9mm/min, 15 process passes.

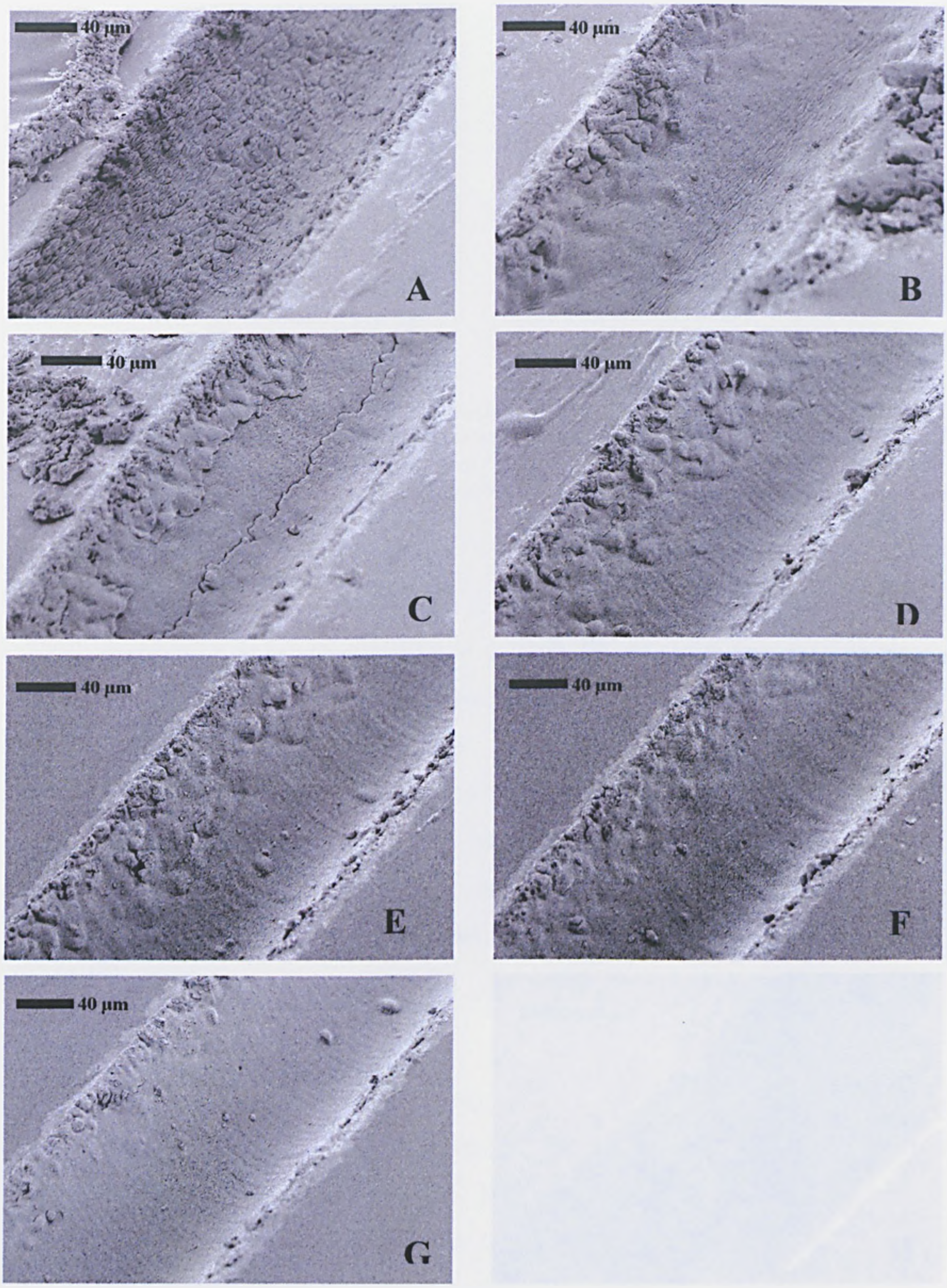

Figure 5.20: Machined v-grooves in $LiNbO_3$ made using KrF laser. Fluence = 3 J/cm^2 and various processing parameters: (A) v = 0.6 mm/min, 1 process pass (B) v = 1.8 mm/min, 3 process passes (C) v = 3 mm/min, 5 process passes (D) v = 4.2mm/min, 7 process passes (E) v = 6mm/min, 10 process passes (F) v = 7.2mm/min, 12 process passes (G) v = 9mm/min, 15 process passes.

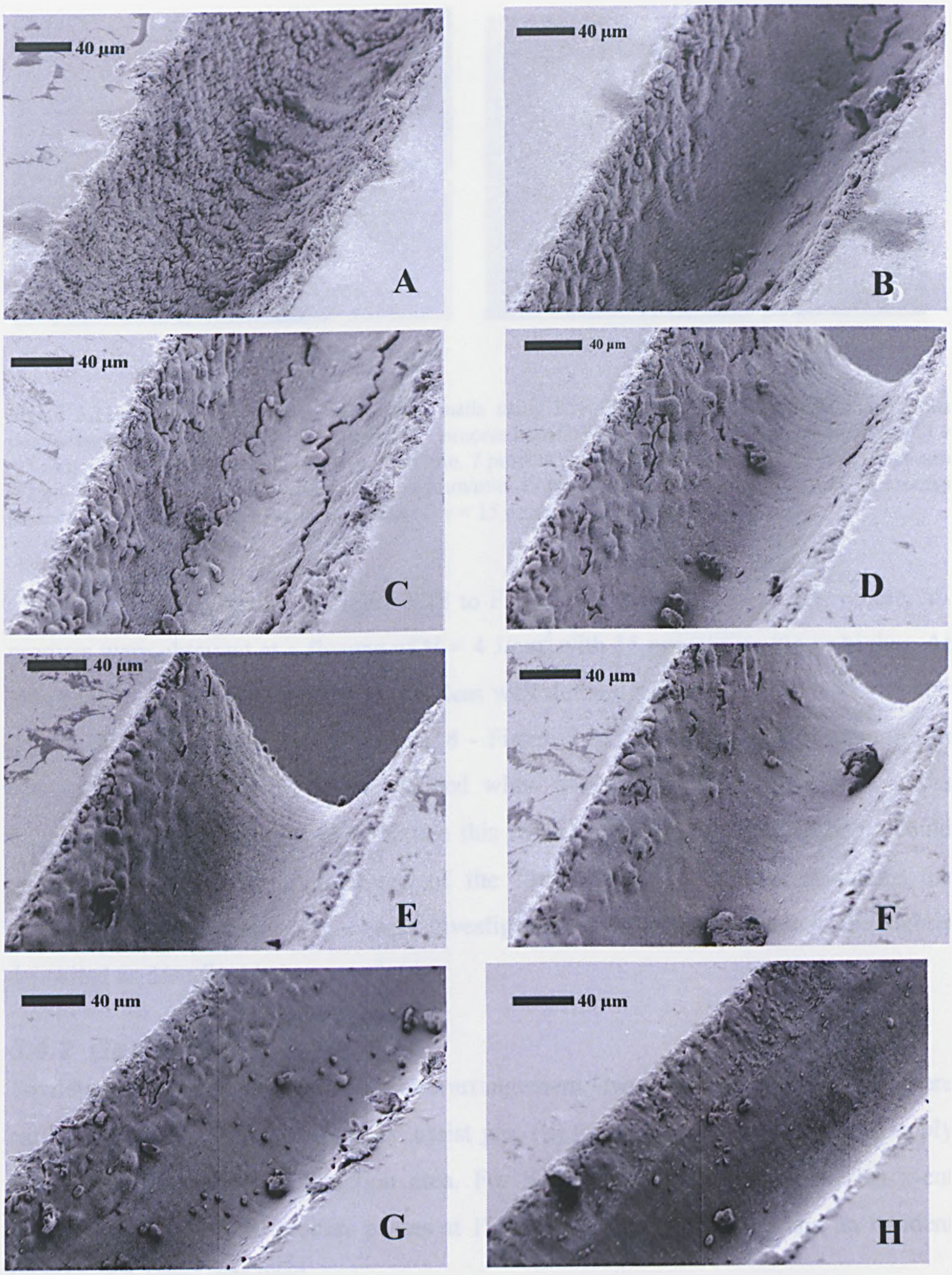
40 µm
A
40 µm
B
40 µm
C
40 µm
D
40 µm
E
40 µm
F
40 µm
G
40 µm
H

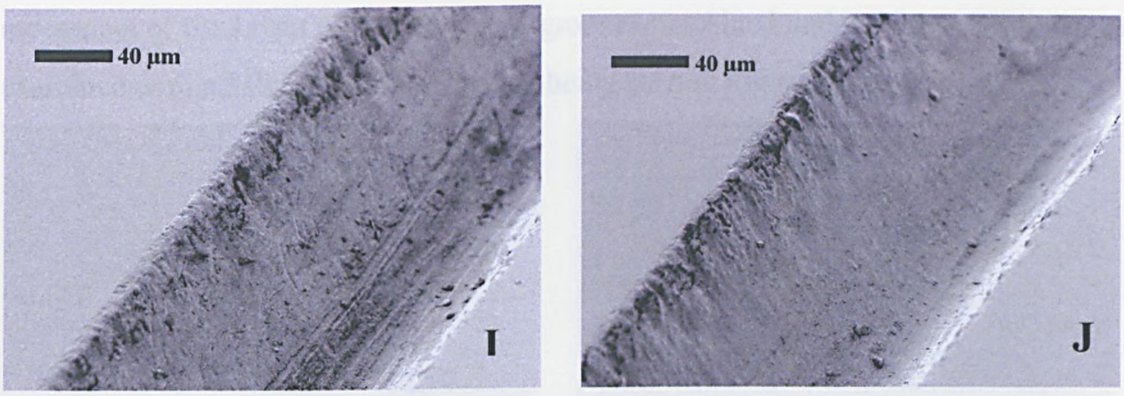

Figure 5.21: Machined v-grooves in $LiNbO_3$ made using KrF laser. Fluence = 4 J/cm^2 and various processing parameters: : (A) v = 0.6 mm/min, 1 process pass (B) v = 1.8 mm/min, 3 process passes (C) v = 3 mm/min, 5 process passes (D) v = 4.2mm/min, 7 process passes (E) v = 6mm/min, 10 process passes (F) v = 7.2mm/min, 12 process passes (G) v = 9mm/min, 15 process passes (H) v = 9mm/min, 15 process passes (I) v = 12 mm/min, 20 process passes (J) v = 15 mm/min, 25 process passes.

Comparison of the results in Figure 5.18 to Figure 5.21 shows that the best quality V-grooves were obtained at a fluence of H = 4 J/cm^2 with 15 process passes or higher. At lower incident fluences, V-grooves had less well defined profiles and showed a higher degree of surface roughness (Figure 5.18 - Figure 5.21). Deposition of process debris was examined and found to be reduced when the number of process passes was increased. It was important to minimize this re-deposition as exessive amounts could possibly prevent passive alignment of the fibre via the V-groove. Assisting the machining with a process gas was investigated as means of reducing the debris deposited as described below.

5.4.2 Gas assist

To determine the optimum gas assist arrangement, two separate experiments were carried out: (i) to determine the best assist gas, (ii) to determine the best way to apply this to the laser-crystal interaction area. For both parts of the experiment an x-cut $LiNbO_3$ crystal with 20 process passes at 12 mm/min sample velocity and an incident fluence of 4 J/cm^2 was used.

For the first part of the experiment, five gases were tested: Argon (Ar), Compressed dried air (CDA), Helium (He), Nitrogen (N_2) and Neon (Ne). These gases were applied to the process area under a pressure of 4 bars by a 4mm bore pipe. The outlet of the gas pipe was held 5 mm away from the ablation area at an angle of 75° from normal incident. The nozzle was positioned to blow the gas into the same direction as the movement of the $LiNbO_3$ crystal. The V-grooves machined under these conditions were examined with a SEM, illustrative results being seen in Figure 5.22.

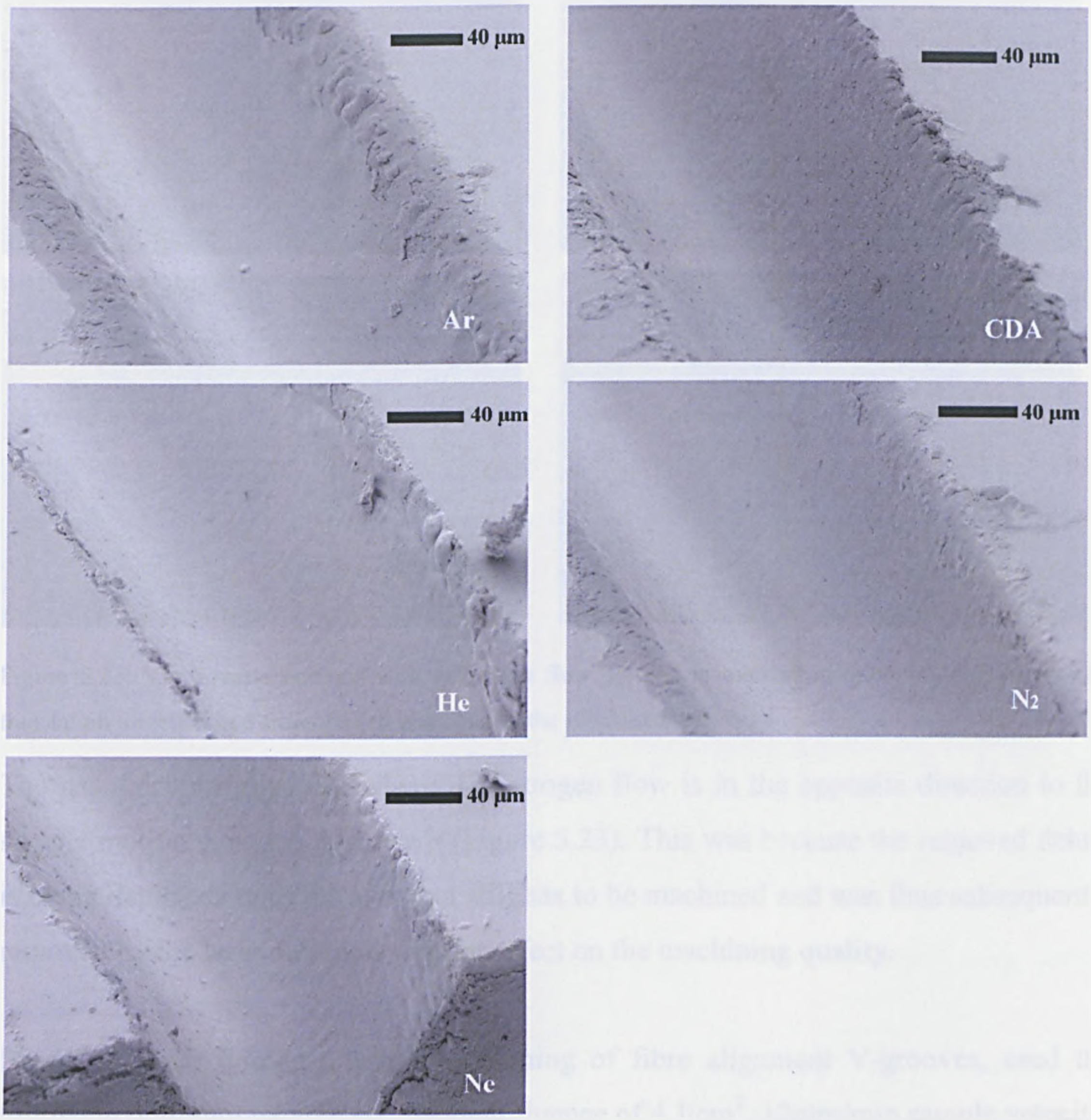

Figure 5.22: V-grooves machined in $LiNbO_3$ with Ar, CDA, He, N_2 and Ne as assist gases.

The inert assist gases all showed results with very little debris and all gasses could be used. As nitrogen is the least expensive, it was used for further experiments.

The influence of the nozzle orientation for nitrogen assist was investigated in a second series of experiments. V-grooves were machined with the same process conditions as used in the first experiment but the position of the gas nozzle was altered in such a way that during machining the direction of the gas flow was (a) in the same, (b) opposite, (c) leftwards and (d) rightwards to the direction of sample motion. SEM results are presented in Figure 5.23.

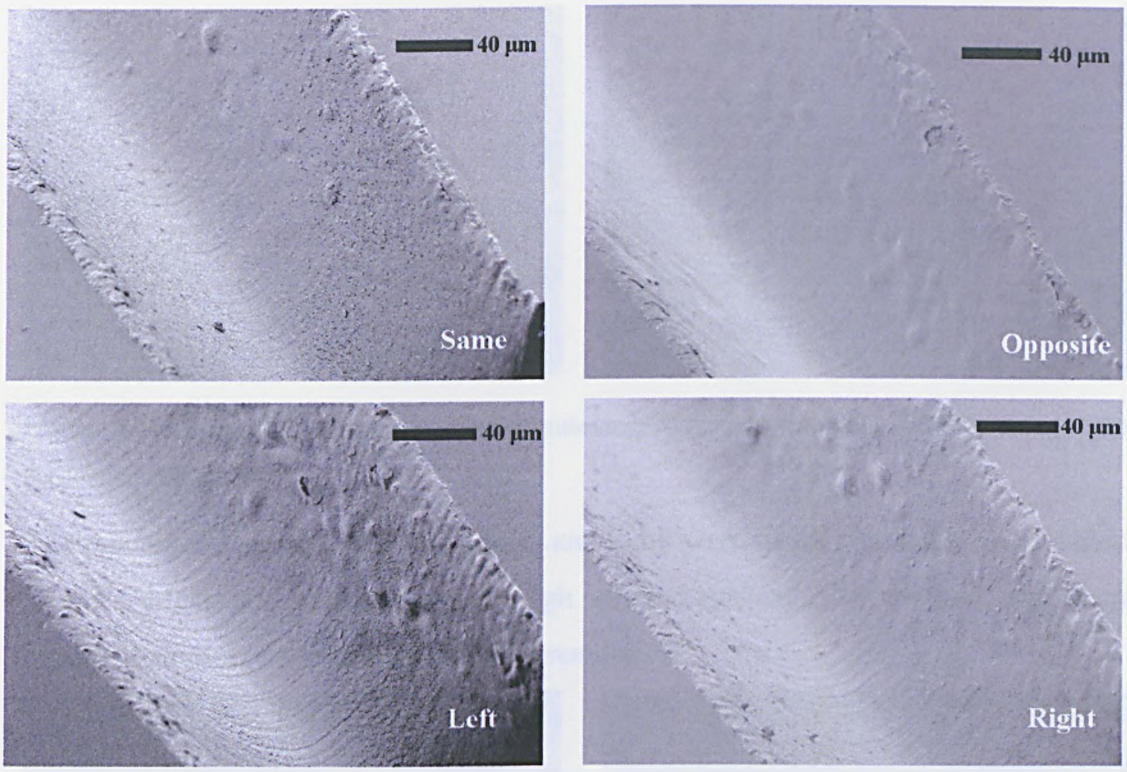

Figure 5.23: V-grooves machined with gas assist flow applied in translation direction, opposite to the translation direction and from the left and right of the machined groove.

The gas assist arrangement where the nitrogen flow is in the opposite direction to the sample motion gave the best result (Figure 5.23). This was because the removed debris is being deposited onto the area that still has to be machined and was thus subsequently removed by the laser radiation without effect on the machining quality.

Based on these findings, further machining of fibre alignment V-grooves, used the following optimum parameters; incident fluence of 4 J/cm^2, 12mm/min sample velocity, 20 process passes, nitrogen gas assist blowing in the opposite direction to the sample velocity and Sotch tape coating on the $LiNbO_3$ crystal.

With this micromachining process, fibre alignment V-grooves were machined in x-cut and z-cut $LiNbO_3$ crystals and were examined with an SEM. Figure 5.24 shows images of the V-groove machined in x-cut and Figure 5.25 for the z-cut material.

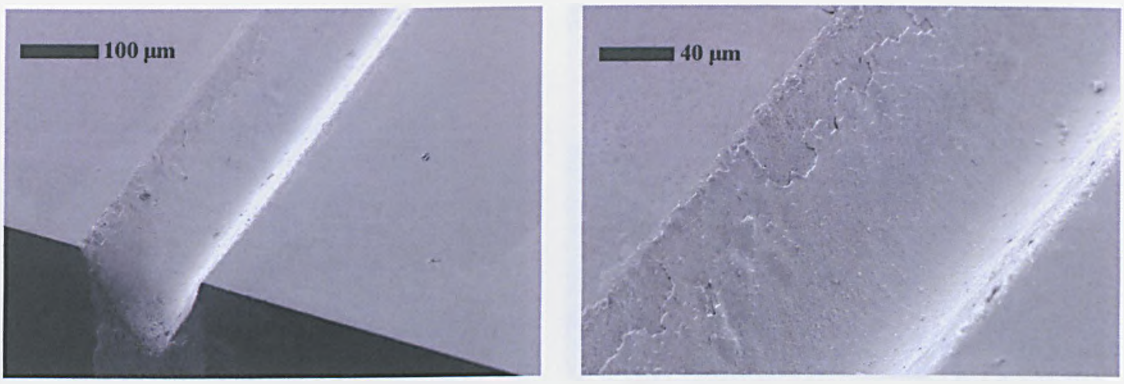

Figure 5.24: Laser micromachined fibre positioning V-grooves in x-cut $LiNbO_3$ using optimum processing conditions.

The machined V-grooves in both the x- and z-cut were similar in shape, free of damage at their edges and had a smooth, high quality surface. The method of gas assist processing ensured virtually debris-free results.

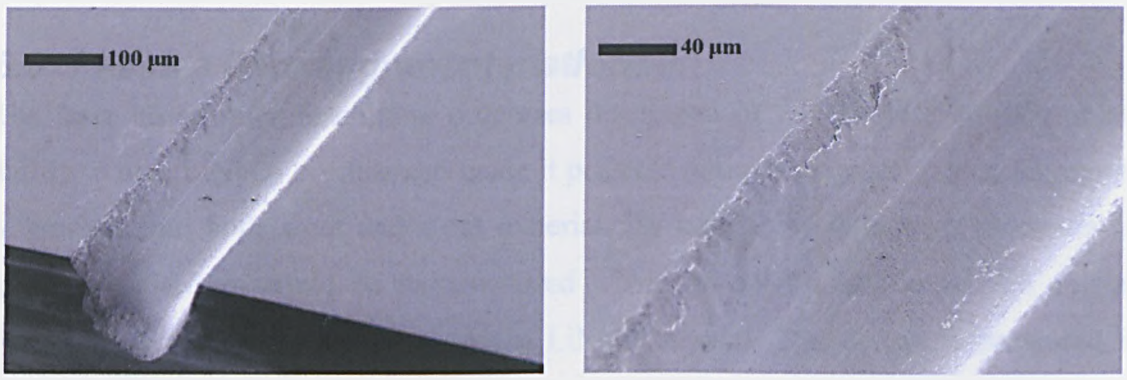

Figure 5.25: Laser micromachined fibre positioning V-grooves in z-cut $LiNbO_3$ using optimum processing conditions.

The etch rate experiments showed no difference between the x and z-cut ablation rate and is evident from the V-groove results, there is no difference in shape and surface quality.

To test how well an optical fibre could be positioned into this structure, a single mode fibre (Corning, SMF-28) was placed into a machined V-grooves and in Figure 5.26 the images obtained with a SEM are presented.

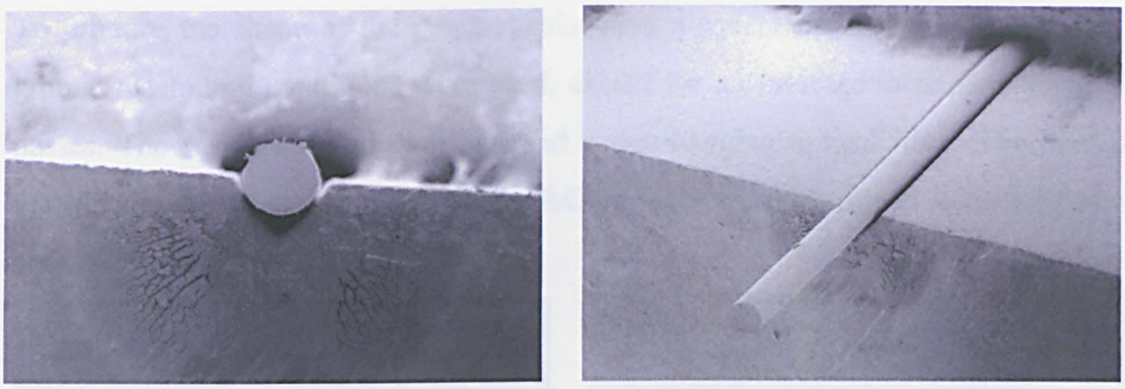

Figure 5.26: SMF-28 single mode fibre (diameter = 125μm) placed into V-grooves machined into x-cut $LiNbO_3$.

The optical fibre positioned well into the groove and sat flush against the edge of the V-groove. The position of the fibre matched expectations based on the mask design, i.e. the core of the optical fibre lay in-line with the crystal substrate surface.

5.5 Passive fibre alignment platforms

The laser based micromachining processes developed in this chapter resulted in the ability to dice $LiNbO_3$ crystals and made it possible to machine passive fibre alignment V-grooves into both x-cut and z-cut material. By combining these two processes an alignment platform could be manufactured where an optical fibre could be aligned passively to a waveguide buried into a $LiNbO_3$ crystal. The design is presented in Figure 5.27.

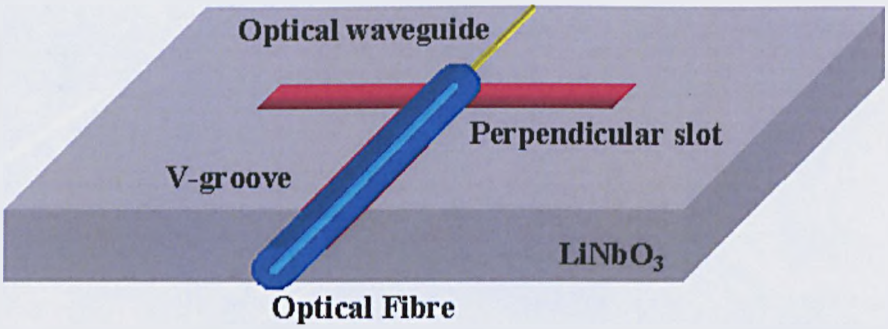

Figure 5.27: Design for optical fibre alignment platform.

For the platform a 3 x 3 mm square base was cut from both the x-cut and z-cut $LiNbO_3$ crystals with the UV solid-state laser micromachining system. The V-groove and the perpendicular slot were machined with KrF excimer laser mask projection system. The perpendicular slot ensured access so that the optical fibre could be positioned against the buried waveguide.

To produce the shape of the perpendicular slot, a square mask was selected. The V-groove machining conditions were used, except for an increase in number of process passes. The result was a deeper slot and a free-hanging optical fibre. The platforms machined into the x-cut and z-cut $LiNbO_3$ crystal were examined with a SEM and results are presented in Figure 5.28.

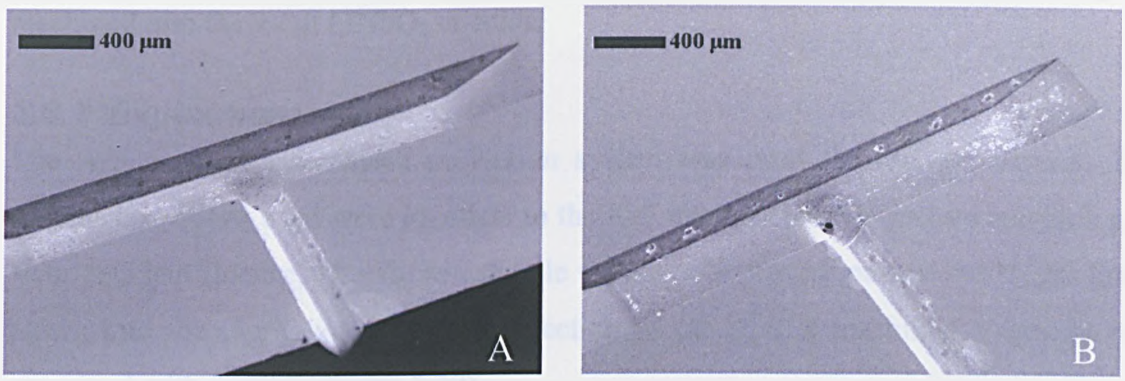

Figure 5.28: Optical fibre alignment platforms machined in x-cut (A) and z-cut (B) $LiNbO_3$.

The passive fibre alignment platforms were equal in quality with sharp edges on the perpendicular slot and a V-groove with a smooth surface.

An optical fibre was placed into an x-cut $LiNbO_3$ alignment platform and examined with the SEM. As can be seen from Figure 5.29 the fibre sits well in the groove indicating overall success in the fabrication of this component.

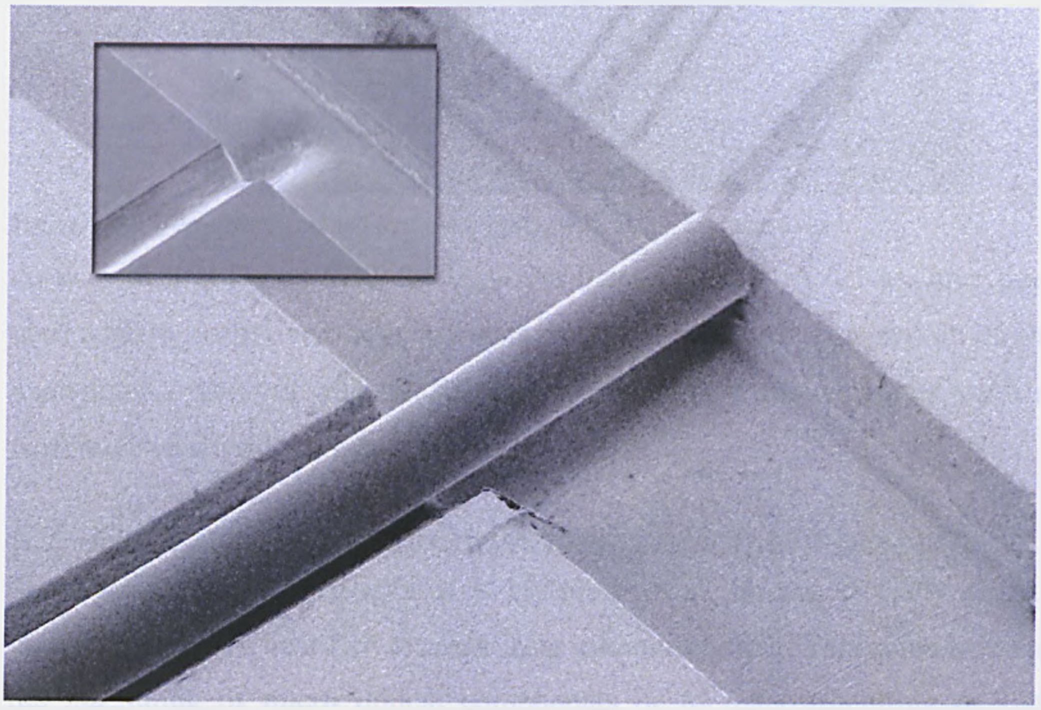

Figure 5.29: Fibre alignment platform machined into x-cut $LiNbO_3$ with and (inset) without fibre.

5.6 V-grooves with ArF excimer laser mask projection system

Ablating $LiNbO_3$ with an ArF excimer laser proved to be more efficient than with a KrF excimer laser. The higher etch rate with the ArF laser could be beneficial for $LiNbO_3$ machining processes if the same quality V-groove and alignment platform could be achieved. To allow a comparison of the two laser wavelengths, V-grooves were machined into the x-cut $LiNbO_3$ crystals.

5.6.1 Experiment

The ArF excimer laser mask projection system was used for this experiment. The process conditions used were identical to the KrF excimer laser V-groove machining; 4 J/cm^2 incident fluence, 12 mm/min sample velocity, 20 process passes and N_2 gas assist blown into the v-groove against the direction of travel. The machined V-groove was examined with a SEM (Figure 5.30).

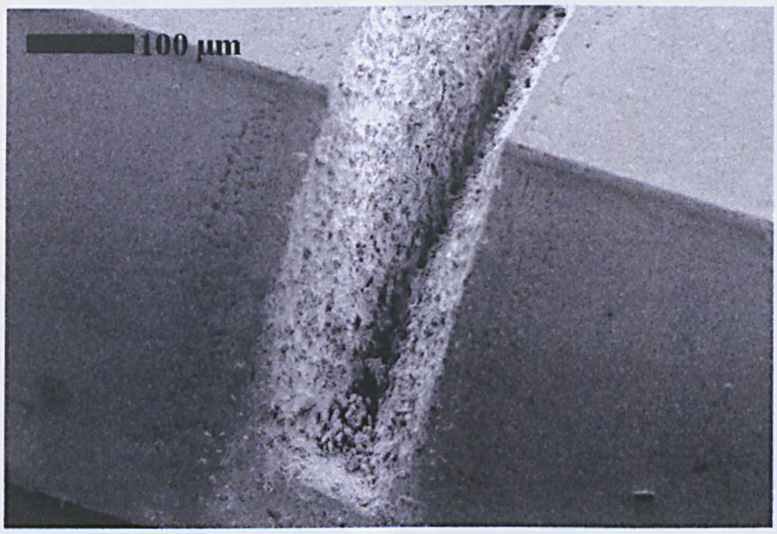

Figure 5.30: V-groove machined in x-cut $LiNbO_3$ with a ArF excimer laser.

As is evident in Figure 5.30, the V-groove machined with an ArF excimer laser showed poor surface quality and large amounts of deposited debris remained on its surface. As machining V-grooves with the KrF excimer laser gave a much better result no further work was continued with the ArF laser.

5.7 Fluorine laser micromachining of lithium niobate

The shorter laser wavelength of a 157nm fluorine laser potentially gives a higher imaging resolution than KrF excimer laser micromachining. This could be beneficial for the machining of micro optical components or for nanostructuring of $LiNbO_3$. To characterize the behavior of $LiNbO_3$ at 157nm wavelength, vertical channels were produced in x-cut $LiNbO_3$.

5.7.1 Experiment

The fluorine laser mask projection system was used with a rectangular mask (3mm x 5mm). By using a static mask – workpiece dragging process, channels were machined with different process passes and sample velocities but with a constant number of shots per area of 325. The incident fluence was set to 3 J/cm^2 and the laser pulse repetition rate to 10 Hz. The machined channels were examined with a SEM and the results are seen in Figure 5.31.

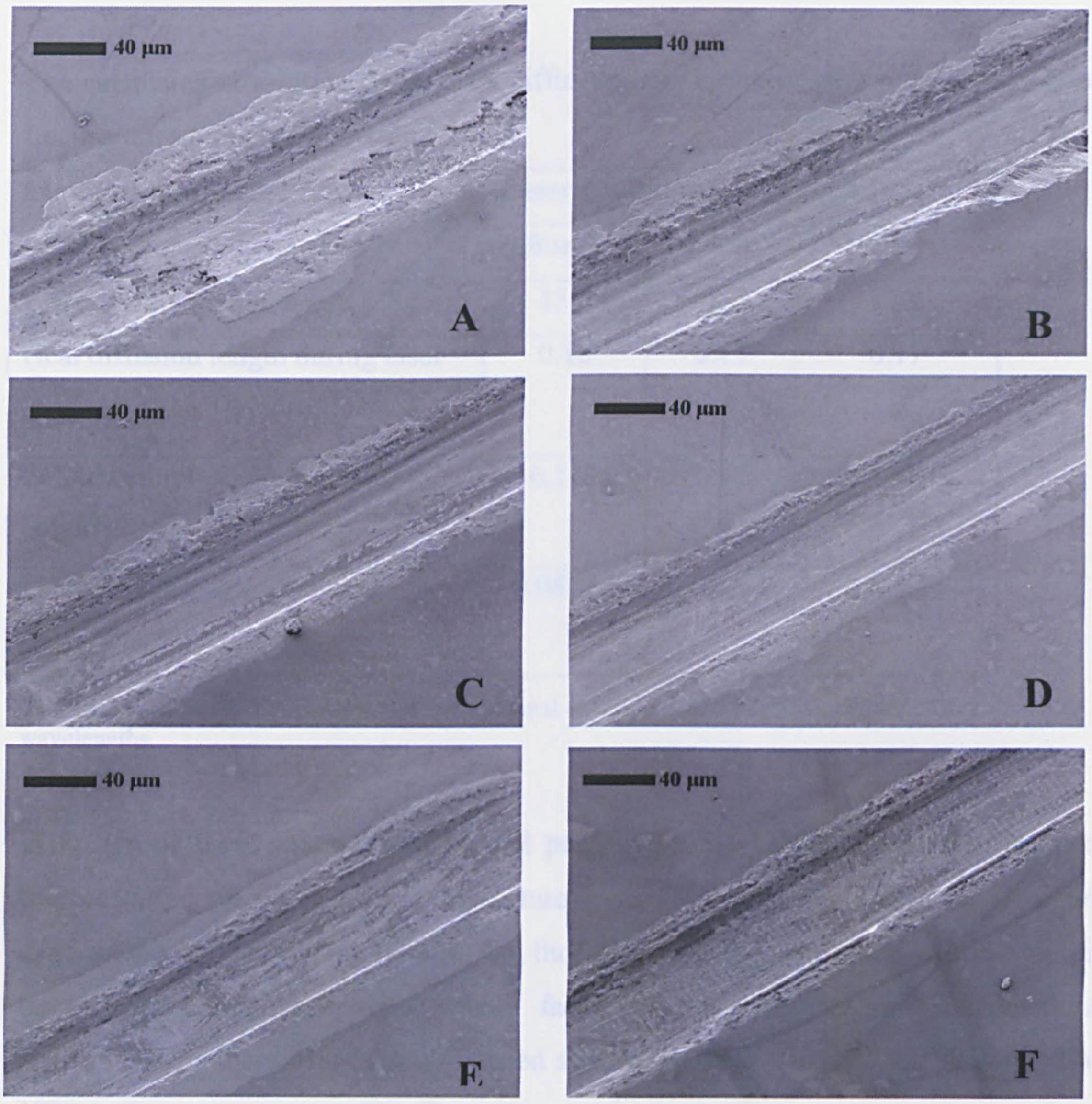

Figure 5.31: Machined channels in $LiNbO_3$ made using Fluorine laser. Fluence = 3 J/cm^2 and various processing parameters: : (A) v = 0.25 mm/min, 1 process pass (B) v = 0.5 mm/min, 2 process passes (C) v = 1 mm/min, 4 process passes (D) v = 1.5mm/min, 6 process passes (E) v = 2mm/min, 8 process passes (F) v = 2.5mm/min, 10 process passes.

The machined channel showed an improved surface quality when the number of process passes was increased but the channel walls were found to be chipped and damaged by the ablation process. This preliminary work showed the possible benefit of processing with the 157nm laser but indicated that further studies would be needed to overcome the damage problem.

5.8 Conclusion

The average etch per pulse versus fluence of the x and z-cut orientation $LiNbO_3$ crystals was determined at all four available laser wavelengths. It was established that at these wavelengths the x and z-cut crystal showed a similar removal rate at each fluence.

The calculated absorption depth, heat diffusion length during laser pulse and threshold fluence are summarized in Table 5.5.

Material parameter	**Laser radiation wavelength [nm]**		
	248nm	**193nm**	**157nm**
Effective absorption depth [nm]	15.5	10.4	21.2
Heat diffusion length during laser pulse duration $\sqrt{D\tau}$ [μm]	0.18	0.17	0.17
Calculated threshold fluence [J/cm^2]	0.146	0.099	0.093
Estimated threshold fluence [J/cm^2]	0.08-0.2	0.05-0.1	0.3-0.45

Table 5.5: Summary of calculated and experimental etch rate data for $LiNbO_3$ ablated at three wavelengths

With use of these thermal and optical parameters for $LiNbO_3$, values of threshold fluence based on the melting temperature were calculated and found to agree with experiments at λ =248 and 193nm. The threshold fluence determined with the fluorine laser micromachining systems was a factor of three higher than calculated. An Arrhenius type thermal model was tested against the etch rate data and at λ =248 and 193nm, this gave a reasonable description in the lower fluence range whereas at high fluence the removal rate exceeded the predicted values. At λ =157nm, the experimental data followed an Arrhenius type model over the full experiment range of fluences studied.

A process was developed to cut $LiNbO_3$ crystal with a 3rd harmonic Nd-YAG laser. This has the ability to cut 2-D shapes with high accuracy, good edge quality and with minimum thermal damage.

KrF and ArF excimer laser, and fluorine laser, mask projection systems were used to investigate micromachining x-cut and z-cut $LiNbO_3$ and the best results achieved with the KrF laser based system. With this system, a micromachining process was developed for the manufacturing of passive fibre alignment V-grooves in x-cut and z-cut $LiNbO_3$. By combining solid-state laser cutting with the V-groove mask projection process, a passive fibre alignment platform was machined in $LiNbO_3$. This allowed the positioning of a standard single mode fibre with its end facet placed flush against the machined fibre-to-waveguide coupling surface, indicating overall success in the fabrication process developed.

5.9 References

1. Nassua, K., Levinstein, H. J., Loiacono, G. M., Ferroelectric lithium niobate. 1. Growth, domain structure, dislocations and etching, *J. Phys. Chem. Solids*, 27, 983-988 (1966)
2. Matthias, B. T., Remeika, J. P., Ferroelectricity in the ilmenite structure, *Phys. Rev.* 76, 1886-1887 (1949)
3. Nassau, K., Levinstein, H. J., Ferroelectric behavior of lithium niobate, *Appl. Phys. Lett.* 7, 69-70 (1965)
4. Xu. T, *"Ferroelectric materials and their applications"* (Elsevier Publictions, 1991)
5. Jundt, D. H., Foulon, G. Boules of $LiNbO_3$ congruently grown by Czochralski technique, in *"Properties of Lithium Niobate"* (INSPEC, 2001)
6. Fang, T., Gordon, L., Jundt, D. H., Preparation of $LiNbO_3$ wafers, in *"Properties of Lithium Niobate"* (INSPEC, 2001)
7. Murphy, E. J., Photonics switching, in *"Optical fiber telecommunications III"* (Academic Press, 1997)
8. Silberberg, Y., Perlmutter, P., Baran, J. E., Digital optical switch, *Appl. Phys. Lett.* 51, 1230-1232 (1987)
9. Schmidt, R. V., Kogelnik, H., Electro-optical switched coupler with stepped $\Delta\beta$ reversal using Ti-diffused $LiNbO_3$ waveguides, *Appl. Phys. Lett.* 28, 503-506 (1976)
10. Wooton, E. L., Kissa, K. M., Yi-Yan, A., Murphy, E. J., Lafaw, D. A., Hallemeier, P. F., Maack, D., Attanasio, D. V., Fritz, D. J., McBrein, G. J., Bossi, D. E., A review of lithium niobate modulators for fiber-optic communications systems, *IEEE J. Sel. Top. Quan. Elec.* 6, 69-82 (2000)
11. Schmidt, R. V., Kaminow, J. P., Metal-diffused optical waveguides in $LiNbO_3$, *Appl. Phys. Lett.* 25, 458-460 (1974)
12. Jackel, J. L., Rice, C. E., Veselka, J. J., Proton exchange for high-index waveguides in $LiNbO_3$, *Appl. Phys. Lett.* 41, 607 (1982)
13. Suchoski, P. G., Findakly, T. K., Leanberger, F. J., Stable low-loss proton-exchanged $LiNbO_3$ waveguide devices with no electro-optic degradation, *Opt. Lett.* 13, 1050-1052 (1988)

14. Murphy, E. J., Fiber attachment for guided wave devices, *J. Lightwave Tech.* 6, 862-871 (1988)

15. Wong, K. K., *"Properties of Lithium Niobate"* (INSPEC, 2001)

16. Palik, D. E., *"Handbook of optical constants of solids"* (Academic press, 1985)

17. Eisenstein, G., Korothy, S. K., Stulz, L. W., Veselka, J. J., Jopson, R. M., Hall, K. L., Antireflection coating on lithium niobate waveguide devices using electron beam evaporated yttrium oxide, *Electron. Lett.* 21, 363-364 (1985)

18. Kincaid, B. E., Coupling of polarization-maintaining optical ibers to Ti:$LiNbO_3$ waveguides with angled interfaces, *Opt. Lett.* 13, 425-427 (1988)

19. Moyer, R. S., Grencavich, R., Judd, F. F., Kershner, C., Minford, W. J., Smith, R. W., Design and qualification of hermetically packaged lithium niobate modulator, *IEEE trans. Comp. Pack. Manu. Tech.* 21, 130-135 (1998)

20. Hsu, H. P., Milton, A. F., Flip-chip approach to endfire coupling between single-mode fibers and channel waveguides, *Electron. Lett.* 2, 404-405 (1976)

21. Laurell, F., Wbjorn, J., Arvidsson, G., Holmberg, J., Wet etching of proton-exchanged lithium niobate- a novel processing technique, *J. Lightwave Tech.* 10, 1606-1609 (1992)

22. Winnall, S., Winderbaum, S., Lithium niobate reactive ion etching, *www.dsto.defence.gov.au/corporate/reports/dsto-tn-0291.pdf,* (2000)

23. Noguchi, K., Mitomi, O., Kawano, K., Yanagibashi, M., Highly efficient 40-GHz bandwidth Ti:$LiNbO_3$ optical modulator employing ridge structure, *IEEE Photon. Tech. Lett.* 5, 52-54 (1993)

24. Ichikave, T, Kagami, M., Ito, H., $LiNbO_3$ platforms for optical fiber alignment, *Opt. Lett.* 23, 1138-1140 (1998)

6 Silicon

6.1 Introduction

Silicon is an abundantly occurring material that composes 26% of the earth crust. Naturally occurring minerals containing silicon have to be refined to obtain polycrystalline or single crystalline silicon. Chemical Vapor Deposition (CVD) is used to produce poly crystalline silicon while single crystalline silicon is made with the Czochralski or Float-Zone technology [1, 2]. The same steps as discussed in chapter 4 are used to process the silicon crystalline rods into wafers.

6.1.1 Silicon age

Even though the first transistors were based on poly germanium, [3] silicon became the preferred semiconducting material due to its better electrical, mechanical and thermal properties. With the use of silicon and the development of metal-oxide semiconductor (MOS) transistors, it became possible to manufacture circuits where more than one transistor was integrated in to one circuit, the so-called integrated circuits (IC). From here onwards, integrated circuits for memory and logic processes have been manufactured with increasing memory capacity and faster operating speeds mainly by decreasing the size of the transistors, with a continuous improvement of the semiconductor manufacturing techniques [4]. One of the unique properties of silicon is the ease with which it produces a silicon oxide layer. This smooth oxide layer acts as a barrier to chemical etching and this characteristic became known as the "planar process" [5]. This planar process is not only used for IC manufacturing but is also used in surface and bulk micromachining of silicon.

The first microprocessor produced contained around 100 transistors while modern ICs have up to 10^8 transistors on one chip and consequently exponentially better memory capacity and operating speed. This increased number of transistors per chips as a result of the reduction in their size and the exponential growth of transistors per chip versus time is known as 'Moore's Law' [6]. To be able to continue this trend, further reduction of transistor size is required as described in the latest future technology roadmap[7]. Possible techniques for the manufacturing of these size transistors have been discussed [8] but the performance of the microelectronic devices will most likely be limited, not by the switching speed of the transistors, but by the delay caused by interconnects between the transistors.

To reduce the delay, the dimensions of interconnects have to be increased; so called 'reduced scaling', to match the performance of the transistors and this makes the interconnect design complex and increases the chip dimensions [9]. A possible solution would be to introduce optical waveguides as signal carries between transistors; optical based interconnect could be made very small and signal delays are not imposed by the dimensions of the waveguide [10]. This would lead to an integration of silicon based photonics and semiconductor components.

6.1.2 Silicon based photonics

Silicon as a base material for photonics components is, compared with semiconductor manufacturing, relatively new [11]. Infrared light above 1.2μm can be detected, waveguided, modulated, emitted and switched within silicon [12]. To date, light emission and fast modulation have been limiting factors for silicon based photonics but by using erbium-doped silicon, light emission is possible [13]. Also, a CMOS capacitor based, Mach-Zehnder interferometer (MZI) modulator, has been used to perform high frequency signal modulation [14]. Silicon has already been used in photonics components such as microbenches, and, with the controlled top layers, is not only a perfect base material for fused silica and silicon on insulator (SOI) waveguides but also for accurate positioning, alignment and attachment of added components [15]. Silicon microbenches are made by chemically etching V-grooves and trenches and the finished microbenches are then cut from the wafer with a mechanical dicing process.

6.1.3 Micromachining of silicon

The micromachining processes for silicon are based on chemical etching, mechanical dicing and grinding.

6.1.3.1 Chemical etching

Chemical etching of silicon is a process step within the modern CMOS technique and has been used for other silicon-based applications. Chemical etching is used for the manufacturing of microelectromechanical systems (MEMS), micro optical electrical mechanical structures (MOEMS) and microbenches that find their applications in areas of sensing, micro mechanical devices and photonics based components. A distinction in micromachining can be made between structures made from added layers where surface micromachining is needed and etching into the silicon base layer itself, where bulk micromachining is needed.

6.1.3.1.1 Surface micromachining

The surface micromachining process is based on the "planar process", where photolithography is used to define the required structure patterns on an added layer. This is subsequently exposed to chemical process steps to define and free the structures [16]. Polysilicon is mostly used for the added layers and is applied with CVD techniques.

Surface micromachining derives from the CMOS semiconductor manufacturing process and therefore integrating electronics to the mechanical structures is possible. By combining these techniques it is possible to manufacture MEMS devices like accelerometers, micro-motors and hinging structures. The development of hinging structures within MEMS devices have made it possible to move mirrors to preferred positions. This allows selective reflection of light and as a result active optical MEMS components can be produced. These so called, micro optical electromechanical systems (MOEMS), can be used for alignment, switching and scanning purposes [17].

6.1.3.1.2 Bulk micromachining of silicon

Bulk micromachining involves selective removal of silicon from a wafer by chemical etching [18]. The etching reactions rely on the oxidation of silicon and formation of silicon based compounds that can be removed from the substrate. Currently three different chemical etching methods are available, wet etching, dry vapor etching and dry plasma etching, and they are discussed in chapter 2.

6.1.3.2 Silicon dicing

The point at which wafer dicing is carried out within a wafer based process is at the beginning of the assembly process by which time the wafer has accumulated a high value. Combined with the fact that dicing is one of the most aggressive operations within silicon wafer manufacturing, damage to the wafer or separated dies are costly.

Laser micromachining could benefit current silicon based manufacturing as due to its non-contact nature, the limitations set by mechanical abrasive processes and processing within a chemical environment are removed, and the risk of damage to the high value wafer, lowered.

This chapter explores the practical aspects of laser micromachining to produce features such as V-grooves, trenches and complex optical microbenches in silicon wafers. Experiments using the UV solid-state laser micromachining system and the fluorine laser mask projection system are described.

6.2 UV laser ablation of silicon

The laser ablation etch rate of silicon was determined at three different laser wavelengths: λ=355nm, λ=193nm and λ=157nm. For these experiments, the UV solid state direct writing system and the ArF excimer and fluorine laser mask projection systems were used.

6.2.1 UV solid-state laser micromachining system

The etch rate of silicon was determined at different incident fluences by machining blind holes into the silicon surface. In total 20 laser pulses were fired at a repetition rate of 10 kHz. The depth of the ablated blind holes was measured with the optical microscope procedure and the etch rate per pulse was found and plotted against fluence (Figure 6.1).

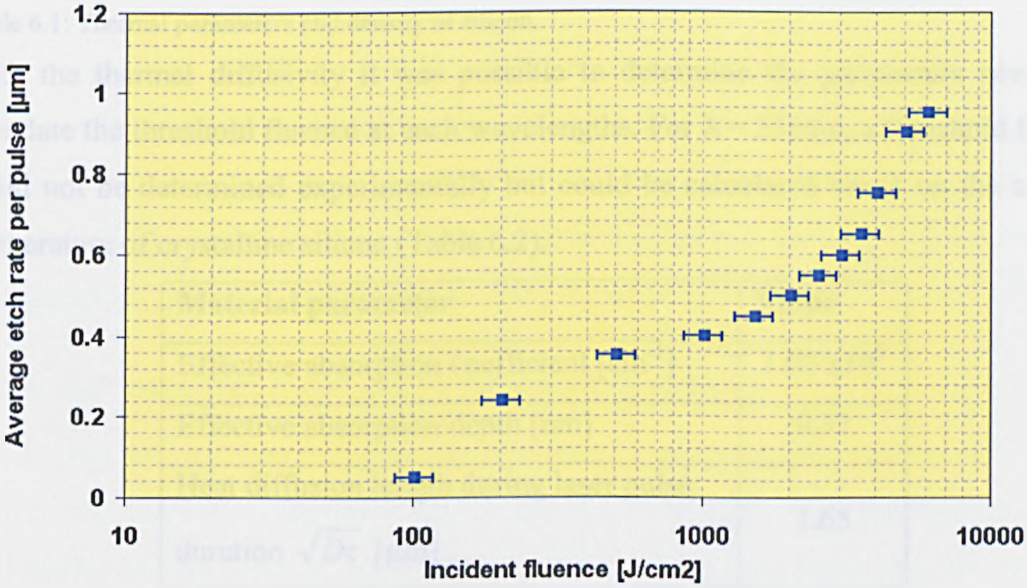

Figure 6.1: Average etch rate per pulse vs. incident fluence for silicon at a wavelength of λ = 355nm.

As evident, the average etch rate reached a high value of x = 0.96μm per pulse at a fluences of $H = 6000$ J/cm^2. However, for the range of fluence investigated it was not possible to determine a clear value for the threshold fluence.

6.2.1.1 Laser ablation threshold

Identical calculations to those in chapter 4 were carried out on the data collected at all three wavelengths. This involved comparing the threshold fluence determined from experiments with calculated values and fitting the data to an Arrhenius type thermal model. For this, the material's thermal diffusivity, the effective absorption coefficient at the appropriate wavelength and the laser pulse length are required. The thermal diffusivity, D, was calculated with parameters [19] presented in Table 6.1.

Material parameter	**Value**
Thermal conductivity κ [W cm^{-1} K^{-1}]	1.5
Material density ρ [g cm^{-3}]	2.33
Specific heat C_p [J g^{-1} K^{-1}]	0.71
Thermal diffusivity D [cm^{2} s^{-1}]	0.91
Melting temperature T_m [K]	1687

Table 6.1: Thermal parameters and density of silicon.

With the thermal diffusivity it was possible to determine the parameters needed to calculate the threshold fluence at each wavelengths. For $\lambda = 355$nm, a threshold fluence could not be determined experimentally but could be calculated based on the melting temperature of crystalline silicon (Table 6.2).

Material parameter	**Value**
Effective absorption coefficient [cm^{-1}]	1.07 x10^{6}
Effective absorption depth [nm]	9.37
Heat diffusion length during laser pulse duration $\sqrt{D\tau}$ [μm]	1.65
Calculated threshold fluence [mJ/cm^{2}]	959

Table 6.2: UV solid state laser ablation calculations for optical and thermal material parameters.

Significant removal of silicon is predicted to start at a threshold incident fluence H = 0.96 J/cm$^{2.}$ The heat diffusion depth during the laser pulse was calculated to be much larger as the effective absorption depth and suggest that a surface heating model is applicable and Arrhenius type thermal model was also used in an attempt to describe the rate of material removal.

6.2.1.2 Arrhenius type thermal model

To test whether an Arrhenius type thermal model could be used to describe the results,etch rate versus inverse fluence was plotted as previously (Figure 6.2).

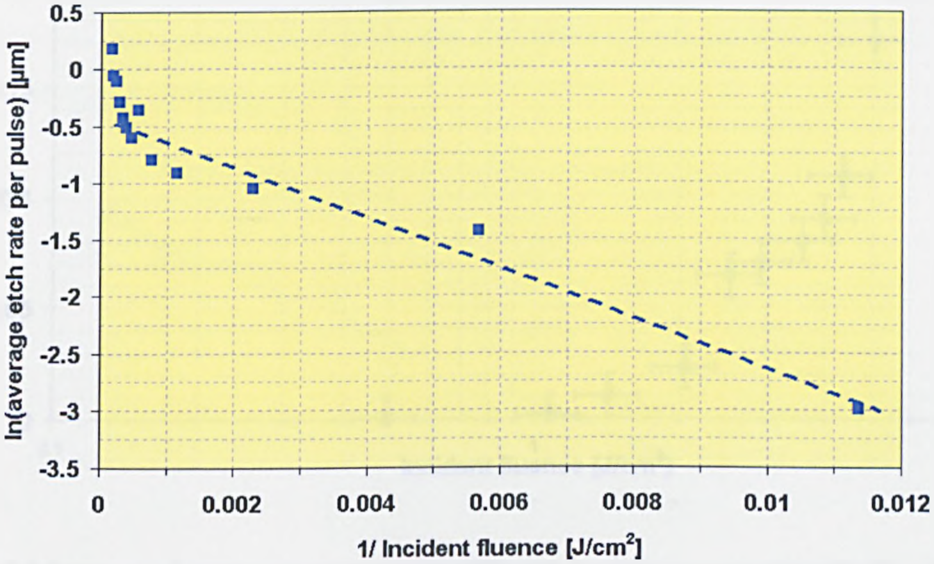

Figure 6.2: ln (average etch rate per pulse) vs. 1/incident fluence of Si at a wavelength of λ=355nm.

A linear relation was found between the ln(average etch rate per pulse) and inverse over the range $5x10^{-4}$ to ~0.15 cm^2/J but below $5x10^{-4}$ cm^2/J the removal rate exceeded that expected using an Arrhenius type thermal model. This behaviour resembles the high fluence data obtained for InP and for $LiNbO_3$ at certain wavelengths.

6.2.2 ArF excimer laser mask projection system

The 193nm ArF excimer mask projection system was also used to determine the etch rates of silicon. With a repetition rate of 100 Hz, blind holes were machined with 100 laser pulses and the depth of the blind holes measured with the optical microscope. The values obtained at various fluences are presented in Figure 6.3.

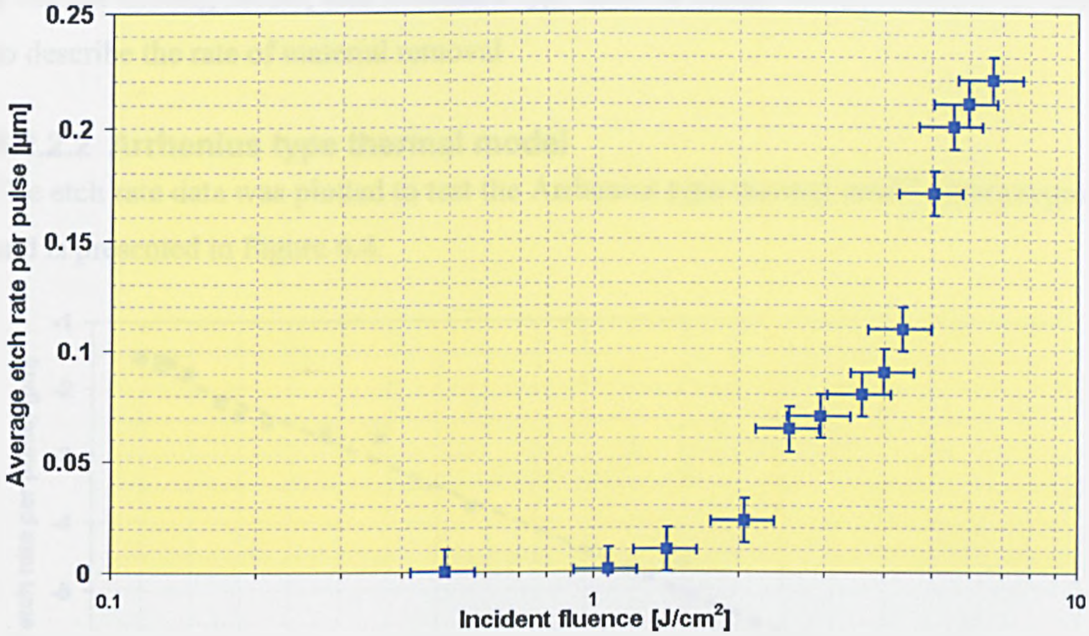

Figure 6.3 Average etch rate per pulse vs. incident fluence for silicon at a wavelength of $\lambda = 193$nm.

A threshold fluence was determined of between H = 0.5 and 1 J/cm^2 and at highest fluence of H = 7 J/cm^2 the etch rate reached x = 0.2 μm was measured.

6.2.2.1 Laser ablation threshold

Results of the calculations related to the ablation characterization parameter and the calculated threshold fluence are presented in Table 6.3

Material parameter	**Value**
Effective absorption coefficient [cm^{-1}]	1.78 x10^6
Effective absorption depth [nm]	5.63
Heat diffusion length during laser pulse duration $\sqrt{D\tau}$ [μm]	1.35
Calculated threshold fluence [mJ/cm^2]	355

Table 6.3: ArF excimer laser micromachining system ablation calculations for optical and thermal material parameters.

The calculated threshold fluence was not in agreement with the measured value but when taking the fluence uncertainty into consideration, the difference between calculated and measured results is less than 75 mJ/cm^2. The heat diffusion length during the laser pulse was much larger than the absorption depth indicating the applicability of a surface heating model, and Arrhenius type thermal model was also used in an attempt to describe the rate of material removal

6.2.2.2 Arrhenius type thermal model

The etch rate data was plotted to test the Arrhenius type thermal model ablation process and is presented in Figure 6.4.

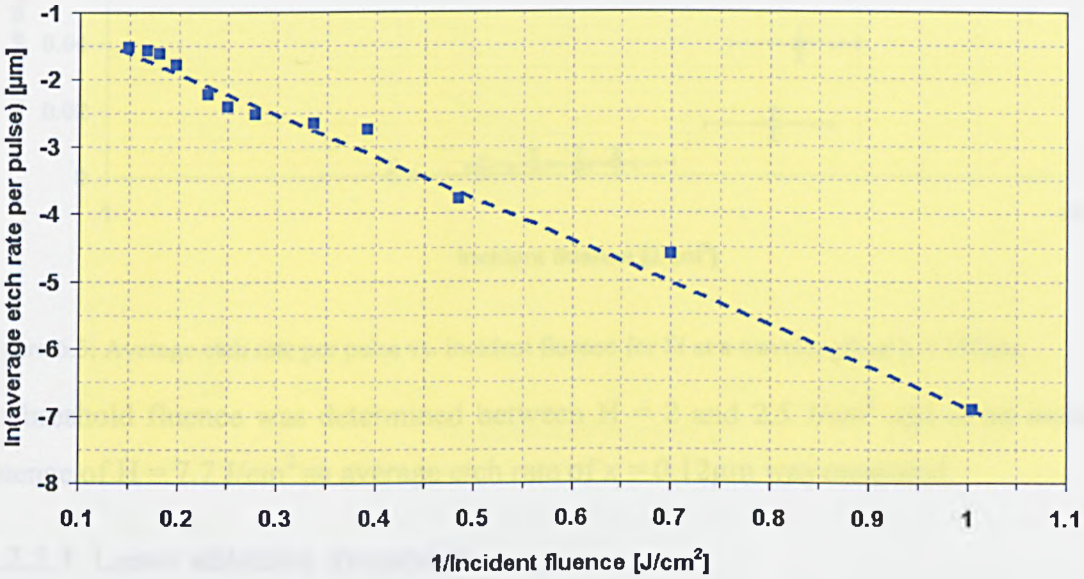

Figure 6.4: ln(average etch rate per pulse) vs. 1/incident fluence of Si at a wavelength of λ =193nm.

A linear relation exists over the whole range of ln(average etch rate per pulse) vs. inverse fluence involved and suggests material removal can be well described by an Arrhenius type mechanism.

6.2.3 Fluorine laser mask projection system

The 157nm fluorine laser mask projection system was used to determine the etch rate of silicon. In total, 100 laser pulses were used at each fluence and the depth of the ablated blind hole was measured with a VEECO Dek Tak^3 surface profiler. The etch rate data is shown versus fluence in Figure 6.5.

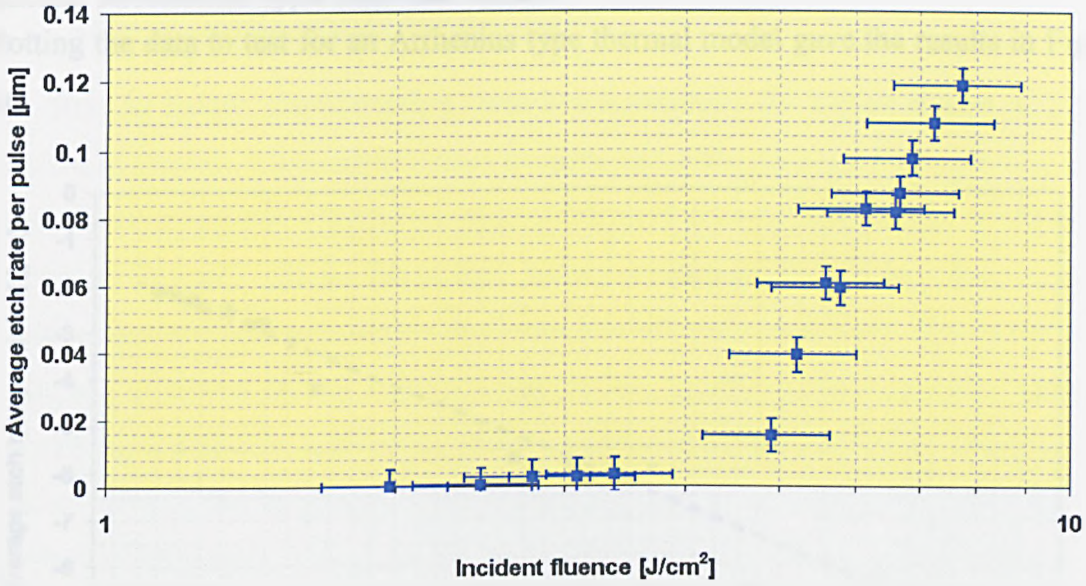

Figure 6.5: Average etch rate per pulse vs. incident fluence for Si at a wavelength of $\lambda = 157$nm.

A threshold fluence was determined between H = 2 and 2.5 J/cm^2 and at an incident fluence of H = 7.7 J/cm^2 an average etch rate of x = 0.12µm was measured.

6.2.3.1 Laser ablation threshold

Results of the calculations related to the ablation characterization parameter and the calculated threshold fluence are presented in Table 6.4.

Material parameter	Value
Effective absorption coefficient [cm^{-1}]	$1.6*10^6$
Effective absorption depth [nm]	6.25
Heat diffusion length during laser pulse duration $\sqrt{D\tau}$ [µm]	1.35
Calculated threshold fluence [mJ/cm^2]	0.381

Table 6.4: Fluorine laser micromachining system ablation calculations for optical and thermal material parameters.

The calculated and measured threshold fluence do not agree, the calculated value being lower than the experimentally determined one. The thermal diffusion length during the laser pulse was found to be much larger than the absorption depth indicating the applicability of a surface heating model and Arrhenius type thermal model was also used in an attempt to describe the rate of material removal.

6.2.3.2 Arrhenius type thermal model

Plotting the data to test for an Arrhenius type thermal model gave the results in Figure 6.6.

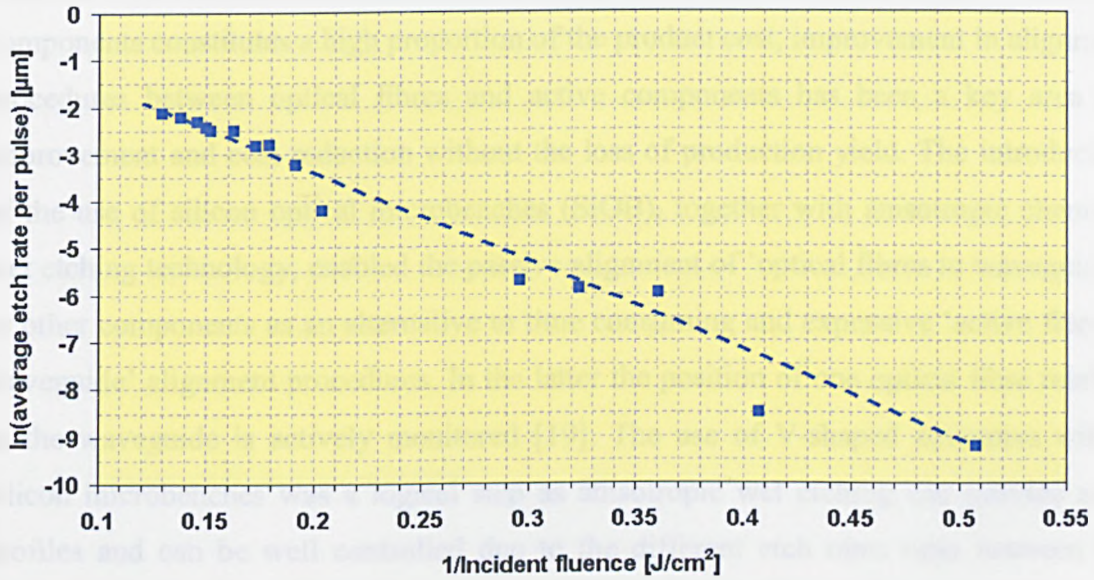

Figure 6.6: ln(average etch rate per pulse) vs. 1/incident fluence of Si at a wavelength of λ=157nm.

As is evident, a linear relationship exists between ln(average etch rate per pulse) versus inverse fluence and suggests that the rate of material removal follows a Arrhenius type model.

6.3 Silicon optical microbenches

The drive to reduce manufacturing costs has accelerated the use of silicon as a base material in (active) telecommunication devices. Since the packaging of opto-electronic components constitutes a high proportion of the product cost, improvement in alignment procedures between optical fibres and active components has been a key area for improvement and cost reduction without the loss of production yield. The introduction of the use of silicon optical microbenches (SiOB), together with anisotropic chemical wet etching technology, enabled the passive alignment of 'optical fibres to waveguides' or other components as an alternative to time consuming and expensive 'active fibre to waveguide' alignment procedures. In the latter the position of one optical fibre relative to the waveguide is actively monitored [19]. The use of V-shaped structures within silicon microbenches was a logical step as anisotropic wet etching can provide such profiles and can be well controlled due to the different etch rates ratio between the crystal planes [21,22]. The angle of the V-shape is defined by the crystal orientation and by careful selection of the chemical etching parameters, the correct size groove can be etched. Anisotropic etching of V-grooves within a SiOB for passive alignment of fibres to another component was established in the mid 70's [23, 24] and has since been used for many different applications. These include chemo-optical sensors [25], aerospace/military components [26], micro solid-state laser assemblies [27], MEMS based devices [28], and most commonly optoelectronics devices. Here, passive alignment packaging is used to integrate active optical components, such as laser diodes, modulators, semiconductor amplifiers (SOA's) and detectors onto a SiOB. This, so called hybridisation, enables the combination of optical components which are difficult to manufacture in a single manufacturing process and are separately optimised for their particular process functionality [29-33].

When examining SiOB, independently from their application, the dimensions are always very similar and each bench is based on a rectangular shape. This is a result of the diamond blade dicing technology which only allows straight cuts and is not able to cut complex 2-D structures. To achieve passive alignment of optical components onto SiOB, wells, plinths or V-shaped structures are used in combination with flip-chip technology and top surface placement [34]. Even with these technologies, misalignment can still occur and great care has to be taken with the placement and packaging of the individual components. A complex 2-D shaped SiOB could simplify the packaging process even further; machining a SiOB which allows an alignment to another matched shaped SiOB by simple pushing the two benches together could remove the current technique of placing components on top of a SiOB. The shape of these SiOB can be compared with a jig-saw puzzle piece, which, when placed together, find alignment.

Machining SiOB with jig-saw piece shapes is not possible with the current diamond saw cutting process but could be possible with direct writing laser micromachining system. Machining of passive aligning "push in" type SiOB was investigated here using with a UV solid-state laser system.

6.3.1 Laser cutting of silicon

To develop SiOB with complex 2-D structures, the process parameters should be determined by optimising laser cutting on a representative SiOB structure. The benches currently used are mainly rectangular but H-shape silicon benches are introduced in hybridisation applications [35]. For an H-shape bench, long and short cutting lengths are needed as well as sharp and obtuse corners. Therefore, for developing the cutting process an H-shape structure of length 40 mm, width 25 mm and a leg width of 5mm was chosen. The silicon wafers used in all the following experiments were 4" in diameter and 525μm thick with surface crystal orientation <100>.

6.3.1.1 Laser cutting process

The UV solid state laser micromachining system used was that described in chapter 3. The first experiment was carried out with the system operating with a sample velocity of 3000mm/min and an incident fluence of 2kJ/cm^2. For these conditions, the shot overlap was calculated to be 0.7 pulses per area and with each pass, 0.56μm of silicon should be removed, based on the data presented in chapter 5.3.1. To cut completely through the wafer, the laser micromachining system should make 960 process passes. After running this experiment, the SiOB was not fully cut out and after close inspection, it was found that although the shorter length of the H-shape were fully cut through the longer sides, were not. An explanation for this result was found in the acceleration of the stages; on the longer length a maximum velocity of 3000 mm/min was reached while on the shorter lengths, the velocity was lower. As a result, the shorter lengths were exposed to a larger number of pulses per area and consequently a full cut through was achieved. To achieve a cut-through on the longer lengths more process passes could be made but this would expose the shorter lengths unnecessarily to the laser beam. To avoid this, the maximum sample velocity was reduced to achieve a much smaller acceleration length so that each length received a similar number laser pulses per area. With the new sample velocity set to 750 mm/min, the number of process passes was reduced to 240 to achieve the same total exposure dose per area. With these parameters, a silicon H-shape was successfully cut from the wafer.

A certain amount of the laser ablated silicon material was found to be deposited on the top surface of the silicon microbench. As this process debris could interfere with the SIOB passive alignment function, different schemes were developed and tested to minimise the formation of process debris.

6.3.2 Debris mitigation

One approach to controlling redeposited debris is to use gas flow over the ablation spot to carry away ejected material from the workpiece. Two different gas assist experiments were carried out; one with a gas tube and one with a gas nozzle assist.

The gas tube blew inert gas at the laser focus – silicon interaction point as shown in Figure 6.7a. The gas tube has an inner diameter of 4mm and was held at an angle of 25° degrees with the tip of the tube positioned 10mm away from the interaction point. The gas nozzle assist used a cone shaped nozzle and is seen schematically in Figure 6.7b. Here the laser beam was aligned through the small exit hole of the nozzle and from which the assist gas was simultaneously pumped. The exit hole had a diameter of 3mm and was placed directly above the silicon surface.

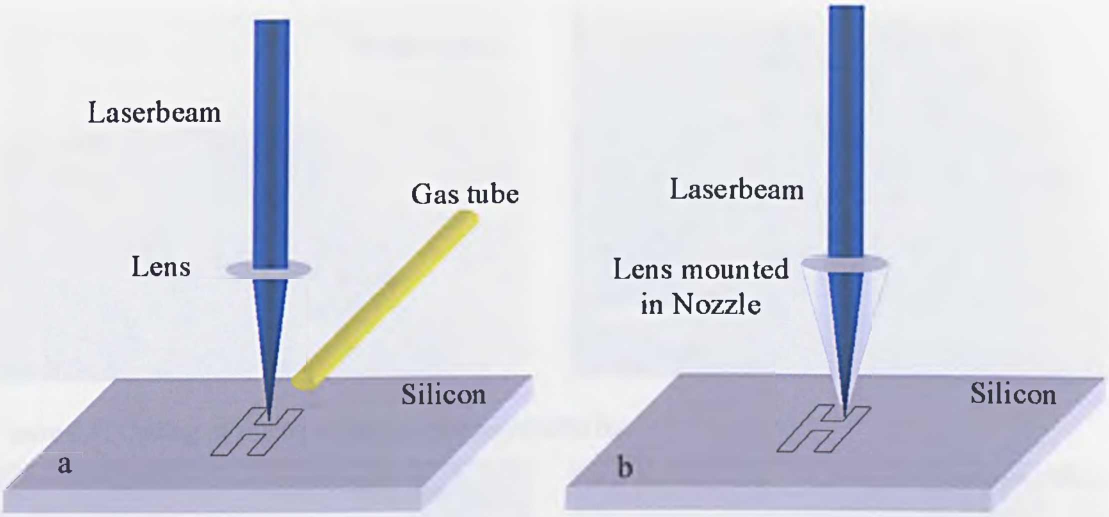

Figure 6.7:Gas assist setup, (a) gas applied to surface by gas tube, (b) gas applied to surface by nozzle.

Three different inert gases were tested with both experimental set-ups: nitrogen, argon and helium. To ensure similar delivery conditions, each gas was applied to the tube and nozzle at a pressure of 2 Bar. The SiOB were cut out at the previously established process conditions of 2kJ/cm^2, with 240 process passes and a sample velocity of 750mm/min. After extraction, all six benches were examined with a SEM without post-process cleaning, the results for the various gases being seen in Figure 6.8 to Figure 6.13.

Gas tube assist

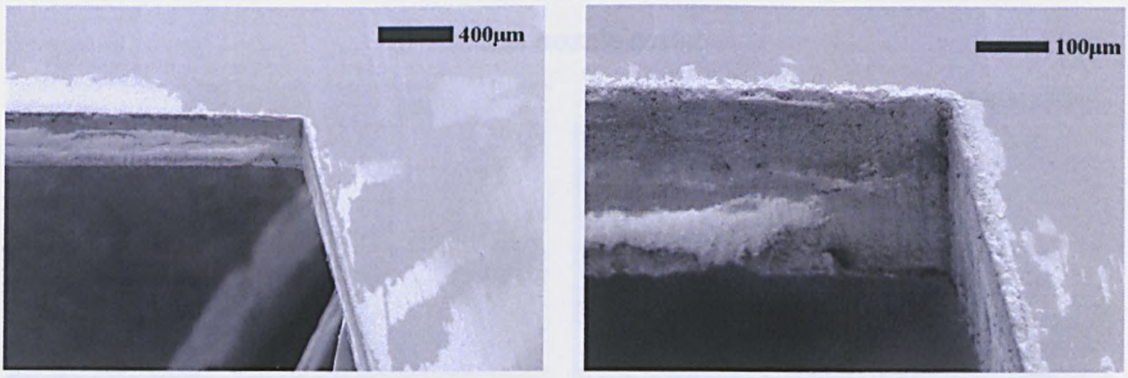

Figure 6.8: Cutting of silicon using gas tube assist with N_2.

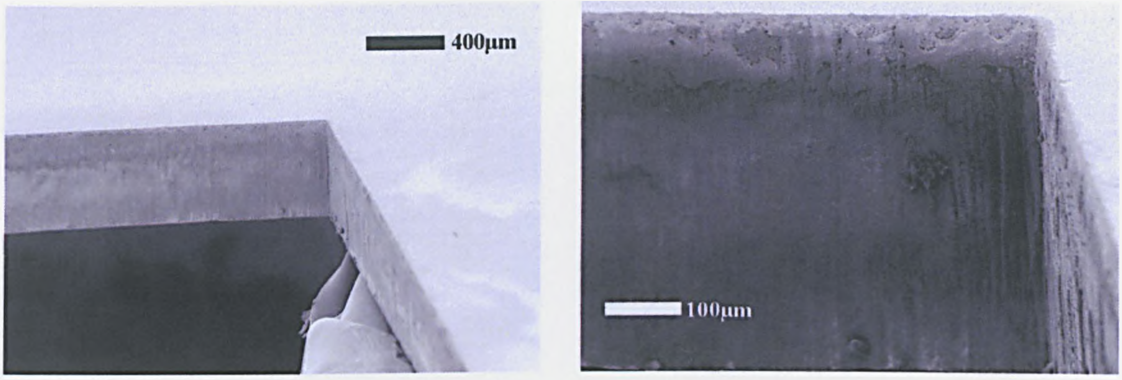

Figure 6.9: Cutting of silicon using gas tube assist with He.

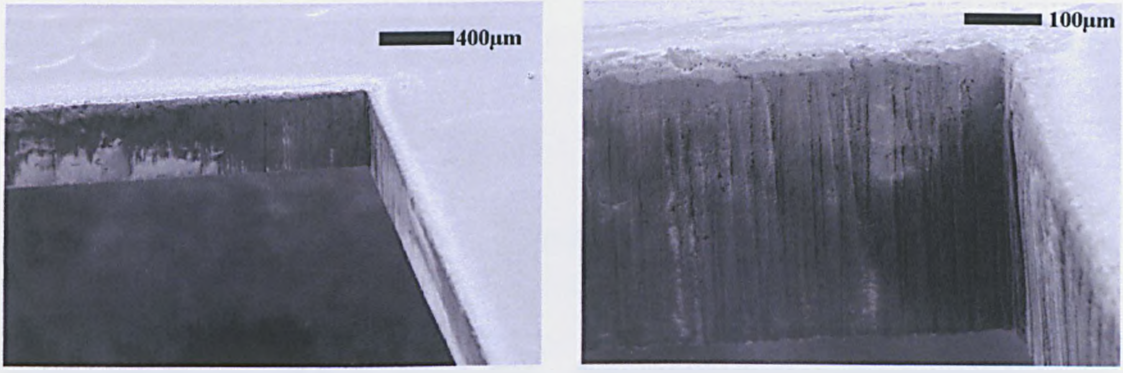

Figure 6.10: Cutting of silicon using gas tube assist with Ar.

A comparison of the results seen in Figures 5, 6 and 7 shows that the bench cut out with helium gas assist delivered using the tube had the least amount of process debris while the benches cut with the argon and nitrogen gas showed edges of a similar quality to each other.

Gas nozzle assist

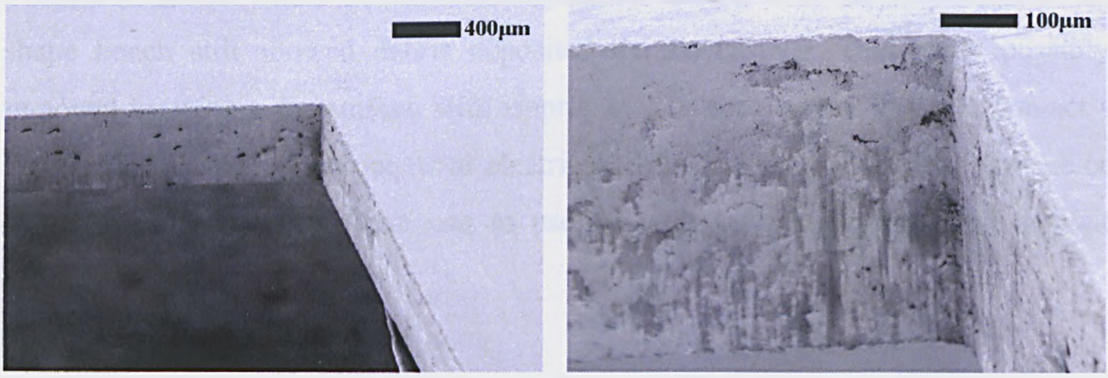

Figure 6.11: Cutting of silicon using gas nozzle assist with N_2.

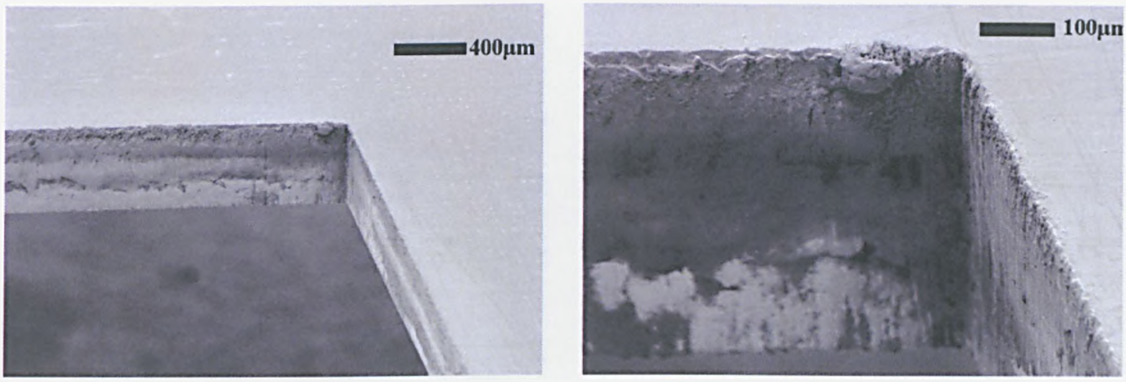

Figure 6.12: Cutting of silicon using gas nozzle assist with He.

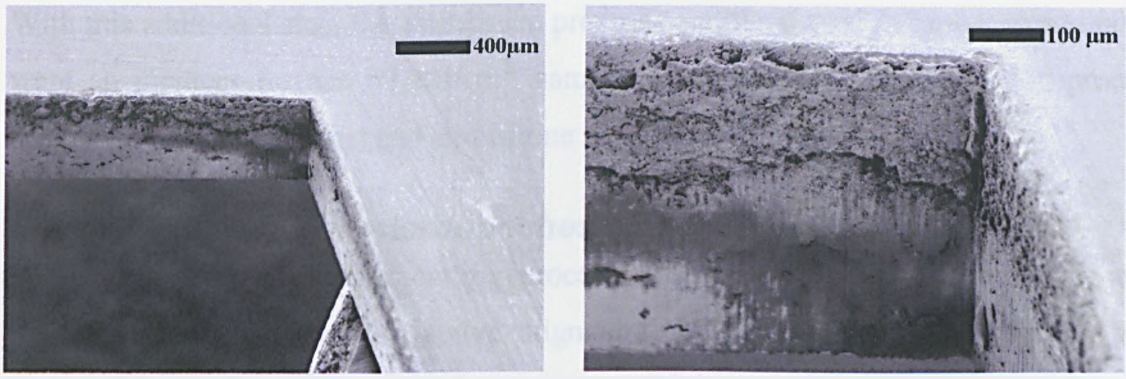

Figure 6.13: Cutting of silicon using gas nozzle assist with Ar.

The results of the gas nozzle assist showed that the bench cut with nitrogen gas had the least amount of process debris. When comparing the best results of both setups, the gas nozzle assist arrangement with nitrogen was found to result in the bench with the least amount of process debris and this setup was therefore used in further experiments.
Despite an almost debris-free surroundings of the cutting area, the middle part of the H-shape bench still showed debris deposited on the surface. This could possibly be removed by wiping the surface with isopropanol or acetone but involves contact with the bench and when components or electrical tracks are already present, damage could occur. An alternative solution was to use, as with $LiNbO_3$, water based emulsitone coating.

A silicon wafer was coated with the emulsitone before a H-shape bench was cut with the established process parameters. After cutting, the bench was washed with warm water to remove the emulsitone coating. Figure 6.14 shows the final result, examined with a SEM and on the surface no process debris could be found.

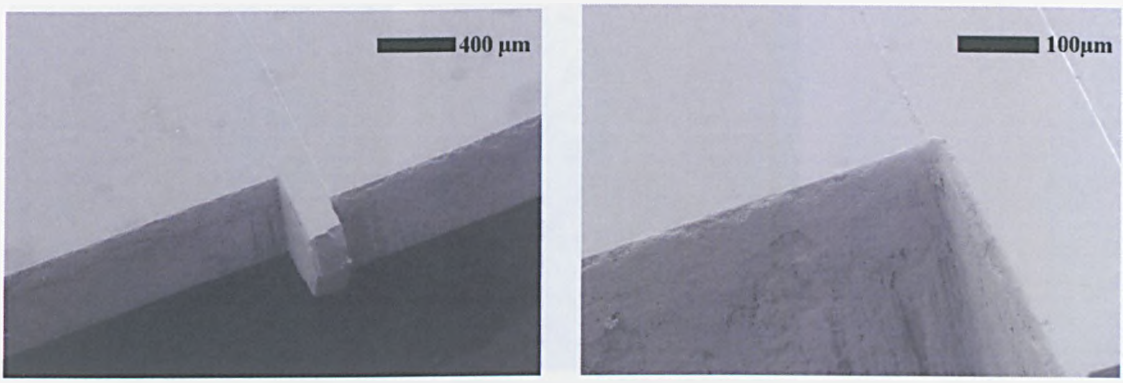

Figure 6.14: SEM pictures of silicon cut with N_2 via gas nozzle assist and emulsitone anti-debris layer.

With this additional step, the established process conditions used in further experiments were an incident fluence of 2kJ/cm^2, sample velocity of 750 mm/min, 250 process passes, N_2 gas nozzle assist and emulsitone anti-debris coating.

6.3.3 Silicon optical microbenches

The developed silicon laser cutting process was used to machine two SiOB with complex 2-D geometry for passive alignment functionality. The first bench was designed to test the ability of the laser micromachining process while the second bench was a prototype hybridization SiOB which was used within the packaging of a fully working prototype Semiconductor Optical Amplifier (SOA).

6.3.3.1 Silicon optical microbench

The first SiOB had a passive alignment structure on one side and on the other side small rectangular structures. The passive alignment teeth were triangular. This shape should ensure correct alignment of the two halves when they were pushed together. Two lines were engraved in the surface to create a reference for correct alignment. This SiOB was cut out with the mentioned process conditions and after washing away the emulsitone coating, the SiOB was examined under the optical microscope (Figure 6.15).

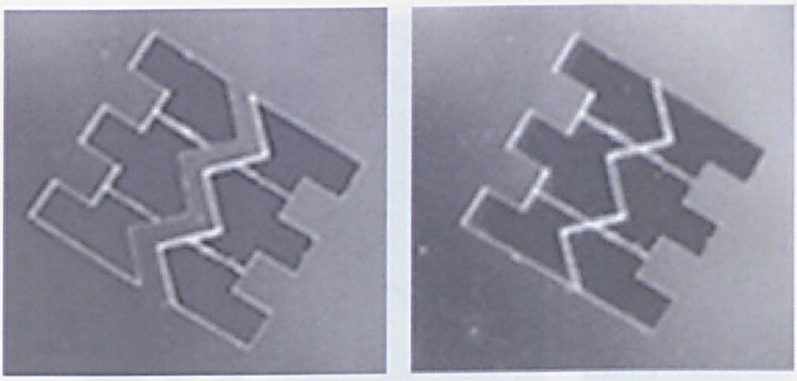

Figure 6.15: Optical micrograph of silicon microbench, open and closed, UV laser processing with 355nm wavelength.

The complex shape of the microbench was cut with high accuracy and edge quality and when pushed together, the two parts fitted flushly and the laser engraved alignment lines on the surface of the bench matched perfectly.

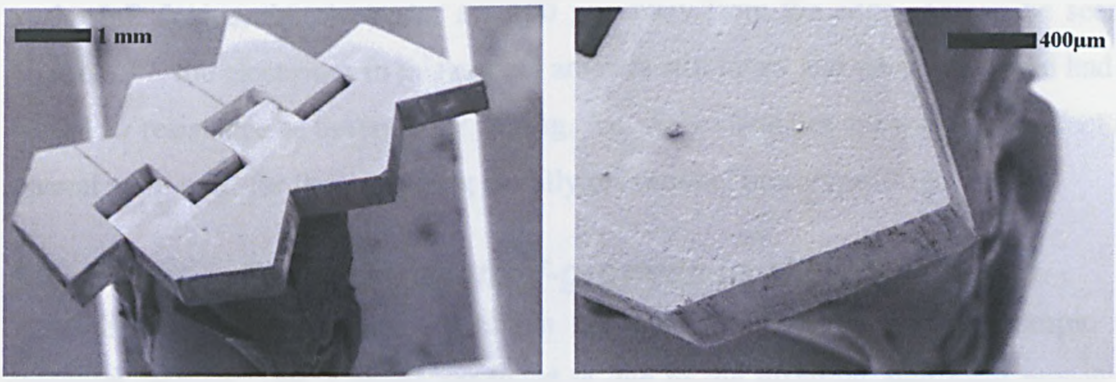

Figure 6.16: SEM pictures of demonstrator SiOB

When examined with a SEM (Figure 6.16), sharp edges were seen on both the top and bottom side of the bench.

6.3.3.2 Hybrid silicon optical microbench

Hybridization benches were cut out for packaging and testing of prototype SOA. A 4" wafer was supplied on which twelve H-shaped benches were manufactured with passive alignment structures and gold plated electrodes [35]. All twelve benches on the wafer were cut out with the established process and after removing the emulsitone, they were examined with an optical microscope and the micrographs being seen in Figure 6.17.

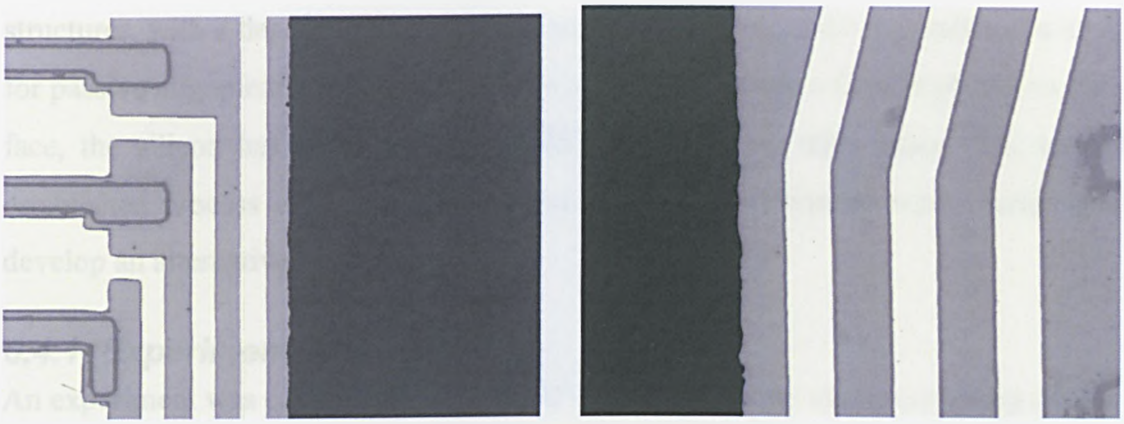

Figure 6.17: Middle bar of the H-shape hybrid microbench with gold plated electrodes, magnification (a) 50x, (b) 100x.

The most critical area on these benches is a horizontal middle bar where an InP device is situated. Due to the limited space and the requirements of the passive fibre alignment to the InP device, the electrodes are 100 μm away from the edge. As can be seen in Figure 6.17, the electrodes in this critical area are still intact and when measured had the same low resistance as before laser cutting. All twelve benches cut were fully intact and several were used for the packaging of fully operational prototype SOA.

6.4 Passive fibre alignment V-grooves in silicon

V-shape alignment structures in silicon are commonly made with anisotropic wet chemical etching. The V-shape produced is due to the different etch rates present on each crystal plane. The high surface quality and extremely repeatable results achieved with anisotropic wet etching allows an accurate and repeatable placement of components but the etch rates achieved, less than 2μm/min, are low compared to those which can be produced with a high repetition rate UV solid-state laser micromachining system. With such a system, etch rates up to 0.8μm/pulse are possible. This, combined with a pulse repetition rate of 10kHz, makes etch rates possible of 480×10^3 μm/min. Such a laser based process for machining V-grooves offers potentially large gains in processing time.

One approach could be to directly focus the beam onto the silicon surface and, by altering the number of laser pulses per area accordingly, a V-groove is machined. This was tried and it was found that the surface directly exposed to the laser beam in this way had a very rough finish and did not allow machining of smooth and accurate structures. In contrast, good surface finish was achieved on the cutting face of extracted silicon structures, with a degree of smoothness that could possibly make it suitable as a surface for passive alignment structures. To create a V-groove where a fibre is placed on the cut face, the silicon has to be oriented at 45° whilst cutting takes place. The currently established process could not do this and therefore experiments were carried out to develop an alternative method.

6.4.1 Experimental setup

An experiment was carried out using the UV solid-state laser micromachining system to ablate silicon samples mounted on an angle to the beam. For this, a special mount was manufactured which allowed 45° positive and negative mounting of the silicon sample, rotation of the silicon sample between laser cuts without removing the silicon and tip-tilt alignment to insure the surface was kept in the focal plane. With this custom-designed mount in place, the process for cutting V-grooves in silicon was as follows:

1. The first 45° cut was made with the sample mounted at a -45° degree angle, horizontally levelled and placed in the focal plane as illustrated in Figure 6.18.

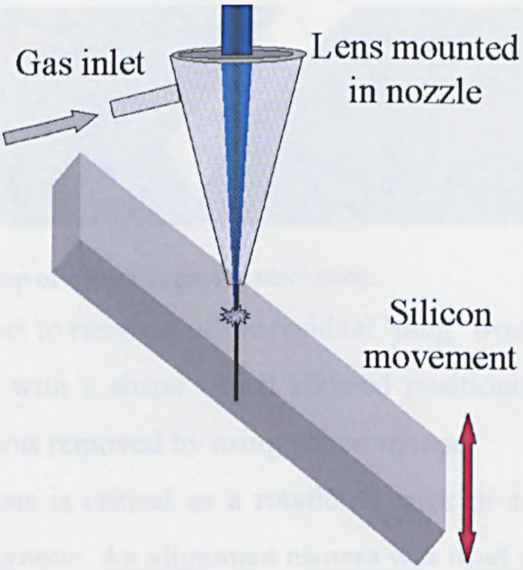

Figure 6.18: First process step of silicon V-groove machining.

2. The silicon sample was then rotated 90° anti-clockwise, refocused and re-aligned to ensure a parallel V-groove. By translating the sample in the same direction as in step 1, the second cut was made.

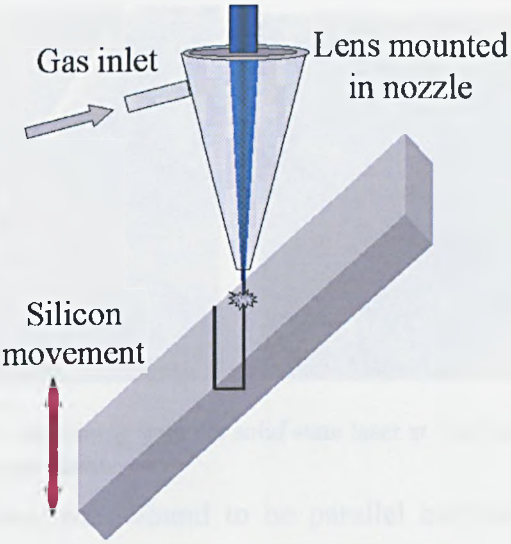

Figure 6.19: Second process step of silicon V-groove machining.

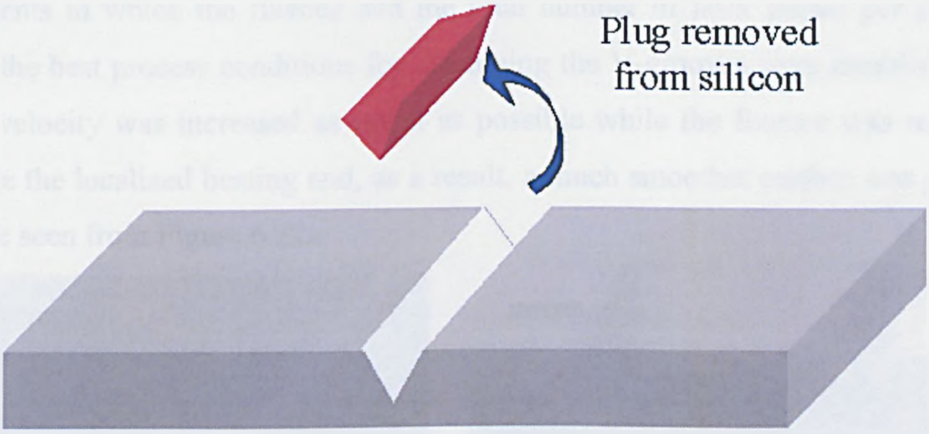

Figure 6.20: Third process step of silicon V-groove machining.

3. The final step was to removal of the residual 'plug' from the silicon, resulting in a 90° V-groove with a shape which allowed positioning of a standard optical fibre. The plug was removed by using adhesive tape.

Alignment in this process is critical as a rotational error or a out-of-focus cut would result in a non-parallel groove. An alignment camera was used to ensure correct rotation and focal position.

6.4.2 Silicon V-groove process development

A first test was carried out with the established cutting process conditions but with only 80 process passes as the required depth for machining V-grooves was much less than a wafer thickness. The result was examined with a SEM and are presented in Figure 6.21.

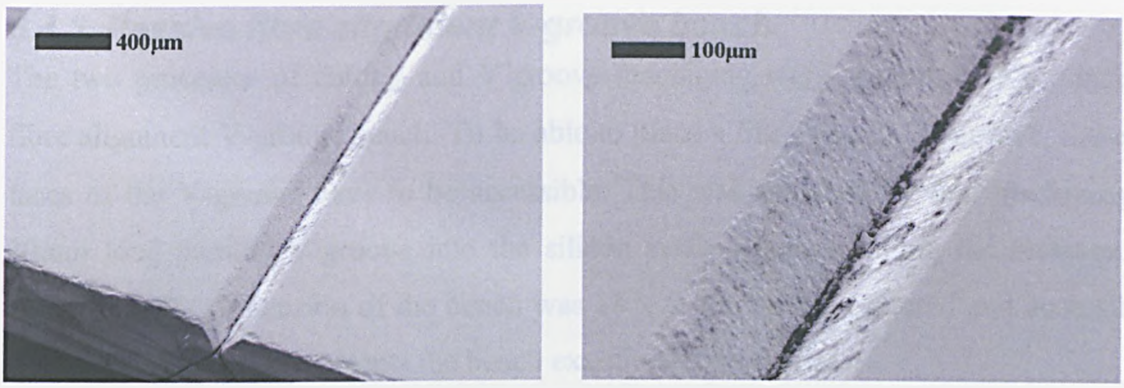

Figure 6.21: Silicon V-groove machining with the solid state laser at 2 kJ/cm^2, velocity = 750mm/min, 80 process passes and N_2 nozzle gas assist.

The sides of the V-groove were found to be parallel but both of the two cuts went deeper into the material than necessary and made the silicon sample fragile. The depth of the cuts only had to allow removal of the plug and by carrying out trial and error experiments in which the fluence and the total number of laser pulses per area were altered, the best process conditions for machining the V-grooves were established. The sample velocity was increased as much as possible while the fluence was reduced to minimize the localized heating and, as a result, a much smoother surface was produced as can be seen from Figure 6.22a.

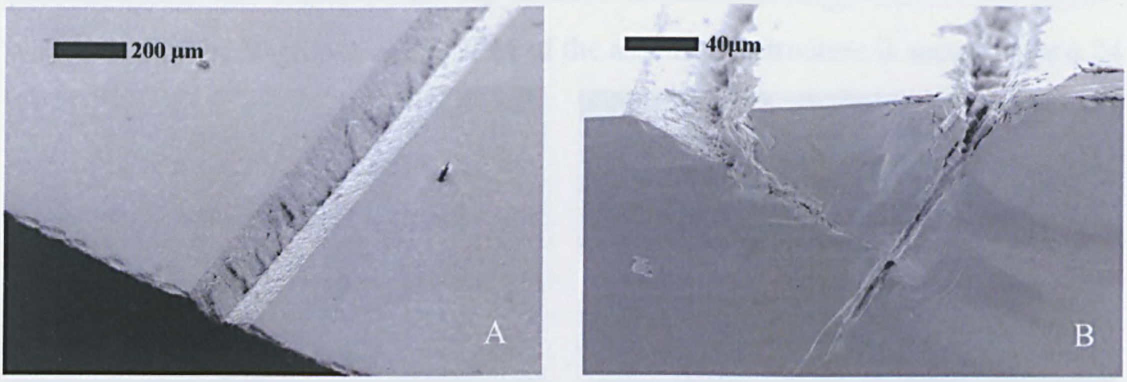

Figure 6.22: Silicon V-groove machined with (A) 2 kJ/cm^2, velocity = 3000mm/min, 20 process passes and N_2 nozzle gas assist and (B) 800 J/cm^2, velocity = 3000mm/min, 10 process passes and N_2 nozzle gas assist.

The result in Figure 6.22 B shows a plug still attached to the silicon and an increased number of laser pulses per area ensured a full release of the plug out of the V-groove. The optimum process conditions were found to be: incident fluence of 800 J/cm^2, sample velocity of 3000mm/min and 20 process passes.

6.4.3 Passive fibre alignment V-groove bench

The two processes of cutting and V-groove machining were combined to produce a fibre alignment V-groove bench. To be able to place a fibre into the V-groove, the end faces of the V-groove have to be accessible. This was achieved by first machining a 20mm long parallel V-groove into the silicon surface before cutting the rectangular shape out. The dimension of the bench was 18 x 5 mm with a centered and accessible V-groove. Figure 6.23 presents the bench examined with a SEM.

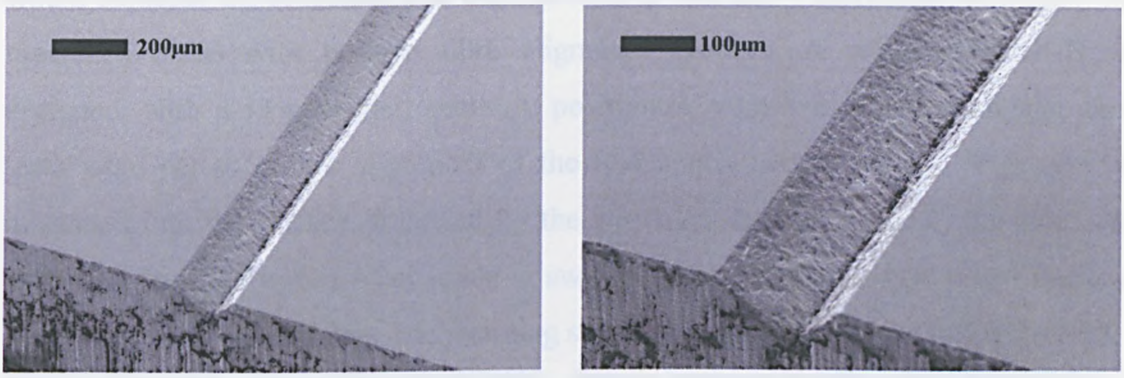

Figure 6.23: silicon V-groove machined with (A) 800 J/cm^2, velocity = 3000mm/min, 20 process passes and N_2 nozzle gas assist.

The edge of the bench and the edges of the V-groove were sharp, smooth and no process debris was found on the top surface. A standard single mode fibre (SMF-28) was placed in the V-groove and a SEM of the assembled structure is seen Figure 6.24.

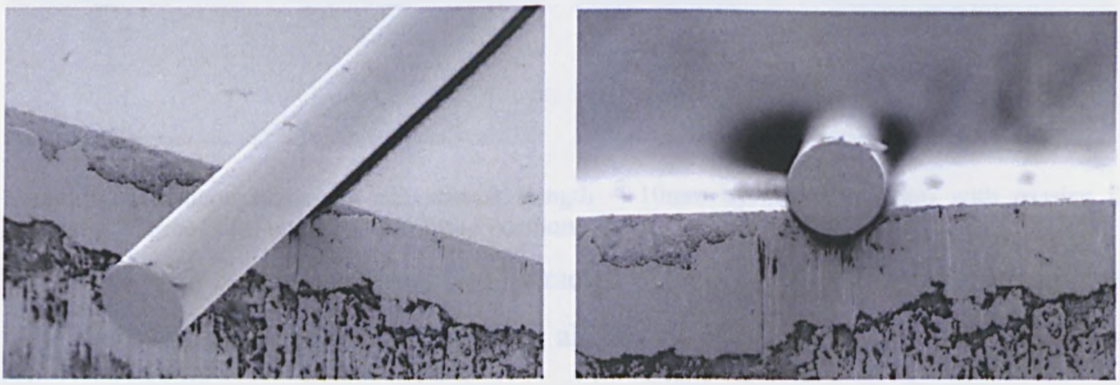

Figure 6.24: Standard single mode fibre (diameter = 125μm) positioned into passive fibre alignment V-groove bench.

The optical fibre could be readily positioned into the V-groove and was found to rest flatly against both edges. The silicon V-groove bench process developed allows the machining to be repeated without the necessity for pre-defined contacts masks. An improvement in this process might be to use a two-beam setup; where each beam addresses the surface at ±45° V-grooves could then be machined without sample rotation which would make the process faster and more repeatable.

6.5 Silicon optical microbench with passive fibre alignment V-grooves

With the processes developed so far, it should be possible to machine a 'push in' alignment SiOB with passive fibre alignment V-grooves. The design of this SiOB would combine the processes that were developed and allow fabrication of a fully laser machined SiOB with passive fibre alignment grooves. A rectangular SiOB was designed, with a longitudinal, centrally positioned, v-groove. Three triangular shape teeth were cut to ensure alignment of the two bench halves. First, a V-groove was machined into the surface, followed by the alignment teeth and finally the bench was extracted from the wafer. After washing away the emulsitone, the bench was inspected under an optical microscope. The resulting structure can be being seen in Figure 6.25.

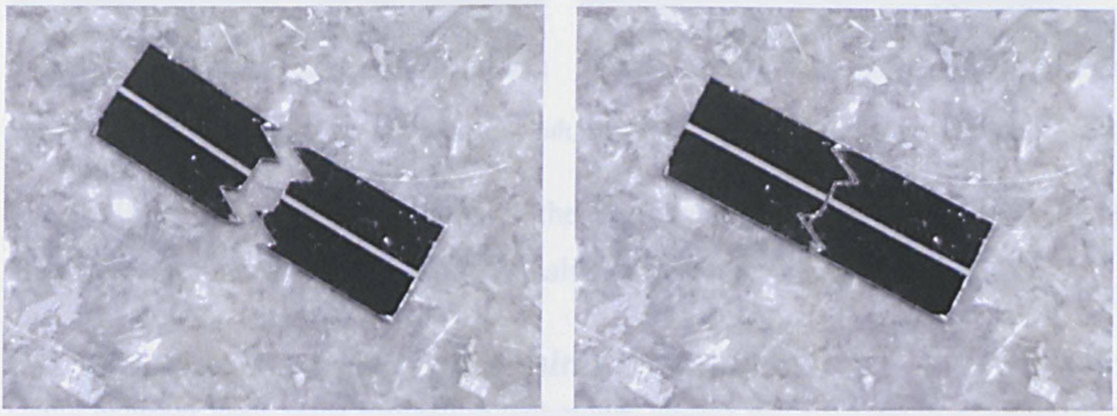

Figure 6.25: Silicon alignment microbench (length = 10mm by width = 3mm) with passive fibre alignment V-groove (a) open and (b) closed position.

The SiOB with central V-groove was extracted without chipped edge and the alignment teeth were sharp. When pushed together, alignment was made between the two halves. When examining the silicon microbench with a SEM, Figure 6.26, the sharp cut edges of the teeth structure and the high degree of smoothness of the V-groove became evident.

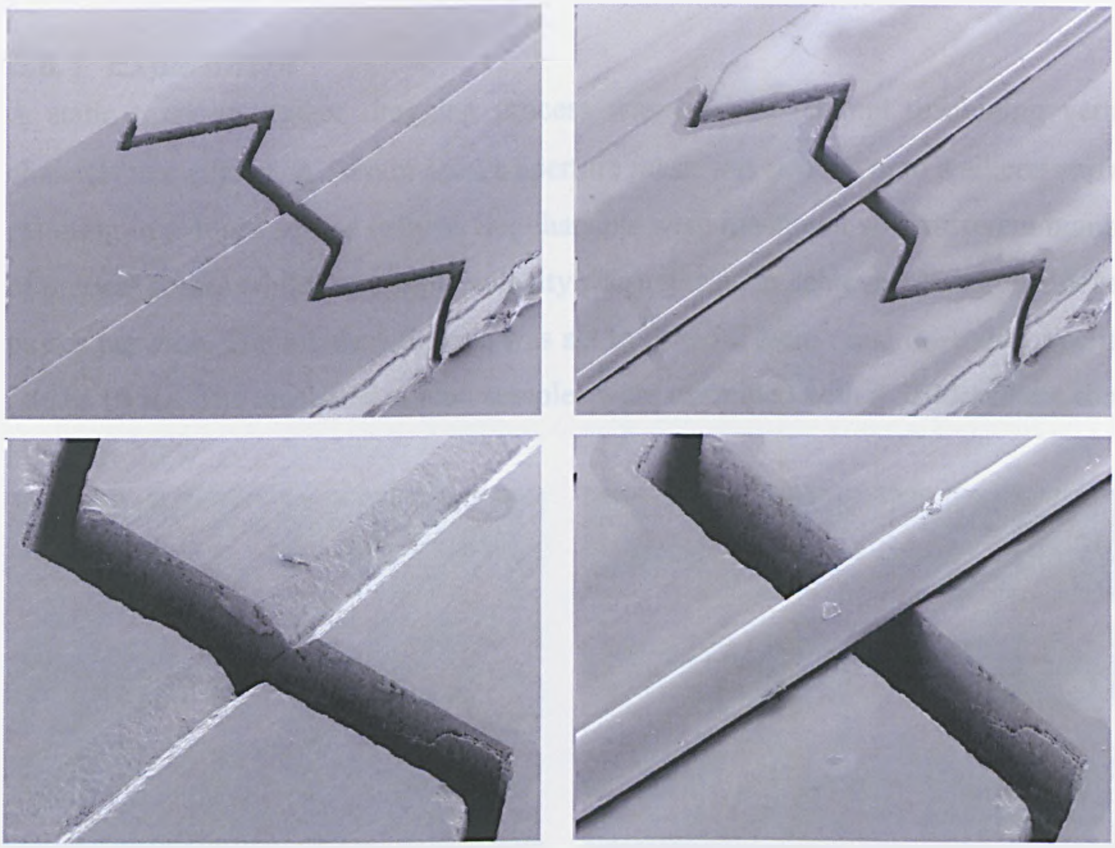

Figure 6.26: Silicon alignment microbench with and without fibre (diameter = 125µm) placed in alignment V-groove.

The ability to place an optical fibre into the V-groove of the closed bench indicated that the alignment made by pushing the two halves together was extremely good.

6.6 Fluorine laser micromachining of silicon

Using excimer laser mask projection techniques allows fast processing of complex 2-D structures. Preliminary experiments show that excimer lasers with emission wavelengths of λ = 248nm and 193nm can be used for silicon mask projection techniques but high incident fluences are required and the final surface quality is poor. The 157nm fluorine laser has not been investigated previously as an alternative means of machining silicon using mask projection techniques. To investigate the suitability of this laser wavelength, an experiment was carried out using fluorine laser mask projection system.

6.6.1 Experiment

A static mask-workpiece dragging process was used to attempt machining vertical channels into silicon. A 1.5mm square aperture mask was imaged onto a silicon surface, resulting in a 40μm square feature. Six channels were machined with different numbers of process passes while the sample velocity was adjusted to achieve 325 number of laser pulses per area. The incident fluence was set to $H = 5.2\ \mathrm{J/cm^2}$ and the pulse repetition rate to 10 Hz. The machined silicon samples were examined with a SEM and are shown in Figure 6.27.

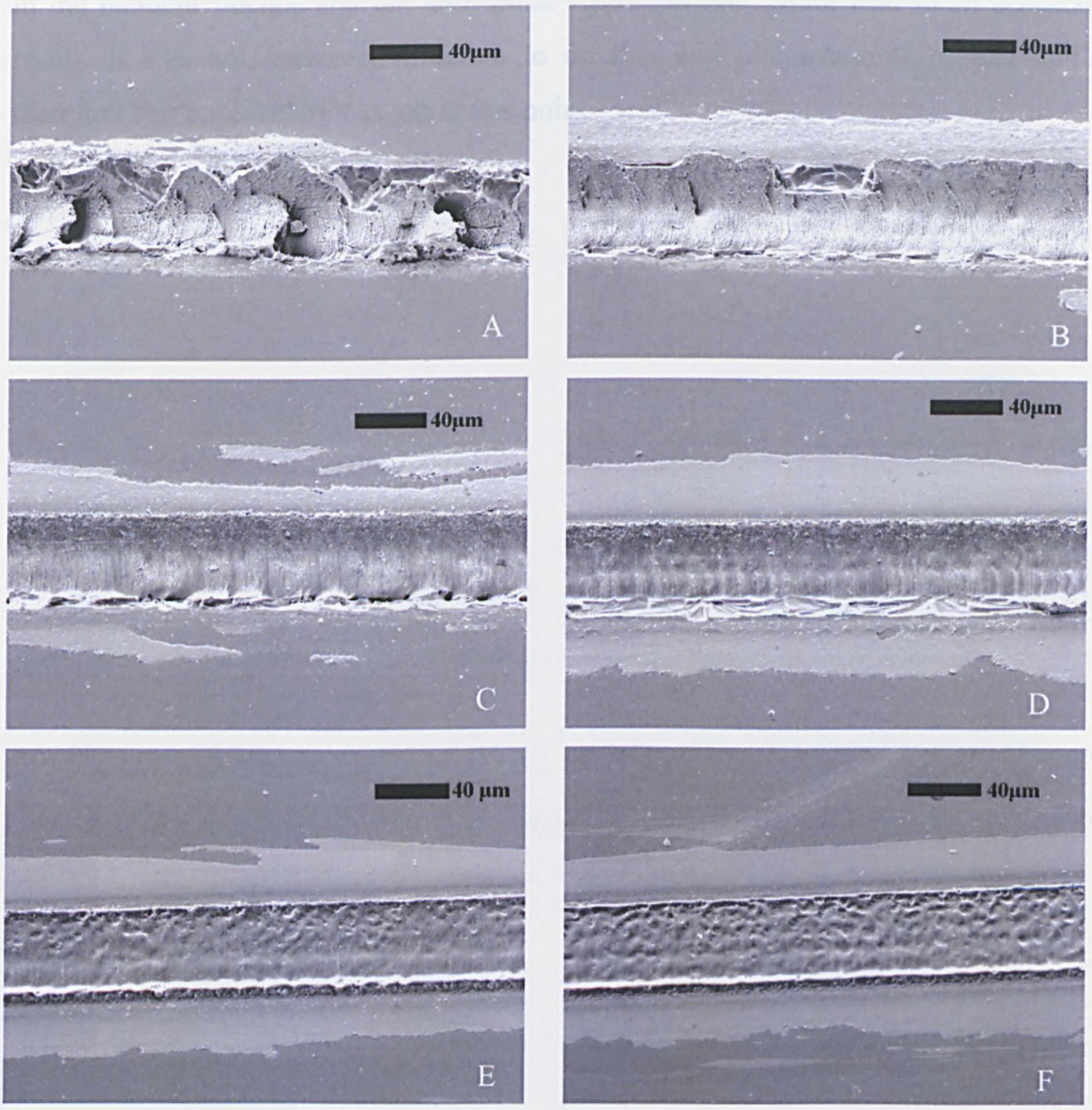

Figure 6.27:Machined channels in silicon using a 157nm laser: (A) 1 pass, V=0.25mm/min (B) 2 passes, V=0.5mm/min (C) 4 passes, V=1mm/min (D) 6 passes, V=1.5mm/min (E) 8 passes, V=2mm/min (F) 10 passes, V=2.5mm/min.

The channels did not have the vertical wall trench shape expected. It was also observed that the quality of each machined channel was significantly different. On the 'lower passes' channels (Figure 6.27 A and B), the machined surface was rough and irregular while machining with 8 and 10 passes barely removed any silicon although it did appear to melt the surface(Figure 6.27 E and F).

This experiment showed that machining structures into silicon using these process conditions does not result in well defined shapes. It is possible that a significant increase in the incident fluence and the laser pulse repetition rate, could lead to an acceptable result. It was not, however, possible to do this with the available system and so therefore this application was left at this point.

6.7 Conclusion

Average etch rate per pulse versus incident fluence experiments were carried out on silicon at λ=355, 193 and 157nm.

The calculated absorption depth, heat diffusion length during laser pulse and threshold fluence are summarized in Table 6.5

Material parameter	**Laser radiation wavelength [nm]**		
	355nm	**193nm**	**157nm**
Effective absorption depth [nm]	9.37	5.36	6.25
Heat diffusion length during laser pulse duration $\sqrt{D\tau}$ [μm]	1.65	1.35	1.35
Calculated threshold fluence [J/cm^2]	0.959	0.355	0.38 E-03
Estimated threshold fluence [J/cm^2]	N/A	0.5-1	2-2.5

Table 6.5: Summary of calculated and experimental etch rate data for Si ablated at three wavelengths

At each wavelength, the threshold fluence was compared with that calculated but in no case was there clear agreement between these values. The experimental data for all three experiments was plotted to test if the removal of material followed an Arrhenius type thermal model. At λ= 355nm, this was only the case at low fluences while at λ=193nm and λ=157nm it was seen to apply over the whole range of fluences studied.

A 355nm UV solid-state laser was found to be the most suitable for micromachining high quality structures in silicon. In combination with the micromachining system's computer controlled stages, this laser allowed the cutting of complex structures in silicon.

With this system, processes were developed to (i) extract complex 2-D microbenches with passive alignment structures, in which accurate alignment was achieved by sliding two bench halves together, (ii) produce passive fibre alignment V-grooves into the silicon material surface and (iii) machine SiOB with passive fibre alignment V-grooves by combining these methods.

6.8 References

1. Plummer, J. D., Deal, M. D., Griffin, P. B., *"Silicon VLSI Technology"* (Prentice-Hall, 2000)
2. Teal, G. K., Single crystals of germanium and silicon – basic to the transistor and integrated circuits, *IEEE Elec. Dev.* ED-23, 621- 639 (1976)
3. J.Bardeen and W.H. Brattain, The transistor, a semiconductor triode, *Phys. Rev.* 75, 1208 –1225 (1949)
4. Clemens, J. T., Silicon microelectronics technology, *Bell Lab. Tech. J.* Autumn, 76-102 (1997)
5. Hoerni, J., Planar silicon transistors and diodes, *IRE Trans. Electron. Devices* ED-8, 178 (1961)
6. Moore, G., VLSI: some fundamental challenges, *IEEE Spectrum* April, 30-37 (1979)
7. International Technology roadmap for Semiconductors (http://public.itrs.net)
8. Risch, L., The end of the CMOS roadmap – new landscape beyond, *Mater. Sci. Eng.* C19, 363-368 (2002)
9. Theis, T. N., The future of interconnection technology, *IBM J. Res. Dev.* 44, 379-389 (2000)
10. Miller, D. B., Rationale and challenges for optical interconnects to electronic chips, *Proc. IEEE.* 88, 728-749 (2000)
11. Soref, R., Silicon-based optoelectronics, *Proc. IEEE* 81, 1687-1706 (1993)
12. Kimerling, L., C., Silicon microphotonics, *Appl. Surf. Sci.* 159/160, 8-13 (2000)
13. Pavesi, J., Will silicon be the photonics material of the third millenium?, *J. Appl. Phys. Cond. Matt.* 15, R1169-1196 (2003)
14. Liu A., Jones, R., Liao, L., Samara-Rubio, D., Rubin, D., Cohen O., Nicolaescu, R., Paniccia, M., A high-speed silicon optical modulator based on metal-oxide-semiconductor capacitor, *Nature* 427, 615-618, (2004)
15. Reed, G. T., The optical age of silicon, *Nature* 427, 595-596 (2004)
16. Bustillo, J. N., Howe, R. T., Muller, R. S., Surface micromachining for microelectromechanical systems, *Proc. IEEE* 86, 1552-1573 (1998)
17. Muller, R. S., Lau, K. Y., Surface micromachined microoptical elements and systems, *Proc. IEEE* 86, 1705-1720 (1998)

18. Kovacs, G. T. A., Maluf, N. I., Petersen, K. E., Bulk micromachining of silicon, *Proc. IEEE* 86, 1536-1551 (1998)
19. Hull, R., *"Properties of crystalline silicon"* (INSPEC, 1999)
20. Hall, S. A., Lane, R., Wang, H., Gareri, A., Assembly of laser-fiber arrays, *J. lightwave Tech.* 12, 1820-1826 (1994)
21. Bassous, E. Fabrication of novel three dimensional microstructures by anisotropic etching of (100) and (110) silicon, *IEEE Trans. Elec. Dev.* ED-25, 1178-1185 (1978)
22. Bean, K. E., Anisotropic etching of silicon, *IEEE Trans. Elec. Dev.* ED-25, 1185-1193 (1978)
23. Hsu, H. P., Milton, A. F., Flip-chip approach to endfire coupling between single-mode optical fibres and channel waveguides, *Electron. Lett.* 12, 404-405 (1976)
24. Boivin, L. P., Thin film laser-to-fiber coupler, *Appl. Opt.* 13, 391-395 (1973)
25. Heideman, R. G., Veldhuis, G. J., Jager, E. W. H., Lambeck, P. V., Fabrication and packaging of integrated chemo-optical sensors, *Sens. and Actuators B* 35-36, 234-240 (1996)
26. Barenek, M. W., Chain, E. Y., Chen, C., Davido, K. W., Hager, H. E., Hong, C., Koshinz, D. G., Rassaian, M., Soares Jr., H. P., St. Pierre, R. L., Anthony, P. L., Cappuzzo, M. A., Gates, C. J., Gomez, L. T., Henein, G. E., Shmulovich, J., Occhionero, M. A., Fennessy, K. P., Passive alignment optical subassemblies for military/aerospace fiber-optics transmitter/receiver modules, *IEEE trans. adv. pack.* 23, 461-469 (2000)
27. Evekull, D., Rydholm, J., Bjurshagen, S., Backlin, L., Kindlundh, M., Kjellberg, L., Koch, R., Olson, M., High-Power Q-switched Nd:YAG laser mounted in a silicon microbench, *Optics Laser Tech.* 36, 383-385 (2003)
28. Ishikawa, K., Zhang, J., Tauntranont, A., Bright, V. M., Lee, Y., An integrated mirco-optical system for VCSEL-to-fiber active alignment, *Sens. and Actuators A* 103, 109-115 (2003)
29. Yamada, Y., Takagi, A., Ogawa, I., Kawachi, M., Kobayashi, M., Silica-based optical waveguide on terraced silicon substrate as hybrid integration platform, *Electron. Lett.* 29, 444- 446 (1993)

30. Son, S., Bu, J., Jeon, Y., Park, C., Jeong, J., Koh, H., Choi, M., Micromachined silicon optical bench for the low cost optical optical module, *Prod. SPIE* 3878, 375-383 (1999)

31. Fan, R. S., Hooker, R. B., Hybrid optical switch using passive polymer waveguides and semiconductor optical amplifiers, *J. Lightwave Tech.* 18, 546-554 (2000)

32. Iwase, M., Nomura, T., Izawa, A., Mori, H., Tamura, S., Shirai, T., Kamiya, T., Single mode fiber MT_RJ SFF transceiver module using optical subassembly with a new shielded silicon optical bench, *IEEE Trans. Adv. Pack* 24, 419-428 (2001)

33. Datta, M., Hu, Z., Dagenais, M., A novel method for fabrication of a hybrid optoelectronic packaging platform utilizing passive-active alignment, *IEEE Photon. Tech. Lett.* 15, 299-301 (2003)

34. Hauffe, R., Siebel, U., Petermann, K., Moosburger, R., Kropp, J.-R., Arndt, F., Methods for passive fiber chip coupling of integrated optical devices, *IEEE Trans. Adv. Pack.* 24, 450-455 (2001)

35. Armstron, I., Andonovic, I., Beddington, J., Michie, C., Tombling, C., Fasham, S., Kelly, A. E., Chai, Y. J., Penty, R. V., White, I. H., Hybridisation platform demonstrating all optical wavelength conversion at 10 and 20Gbit/s, *OFC 2004,* post deadline papers, (2004)

7 Fused silica

7.1 Introduction

Fused silica has properties which allow it to be used in highly specialized industrial applications. It retains its integrity when exposed to high temperatures allowing it to be used as a metal melting crucible. Other properties like its chemical inertness and its low electrical conductivity allow it to be used in medical applications and as an insulator within electronic circuitry.

For optical applications, fused silica is particularly used in deep ultraviolet (DUV) applications as it maintains a low loss transmission down to a radiation wavelength of λ = 160nm, e.g. the KrF and ArF excimer, and the UV solid-state laser system used in the present research were equipped with fused silica optical components. On the other side of the spectrum, the low loss transmission of fused silica is maintained up to a wavelength of λ = 2000 nm (Figure 7.1).

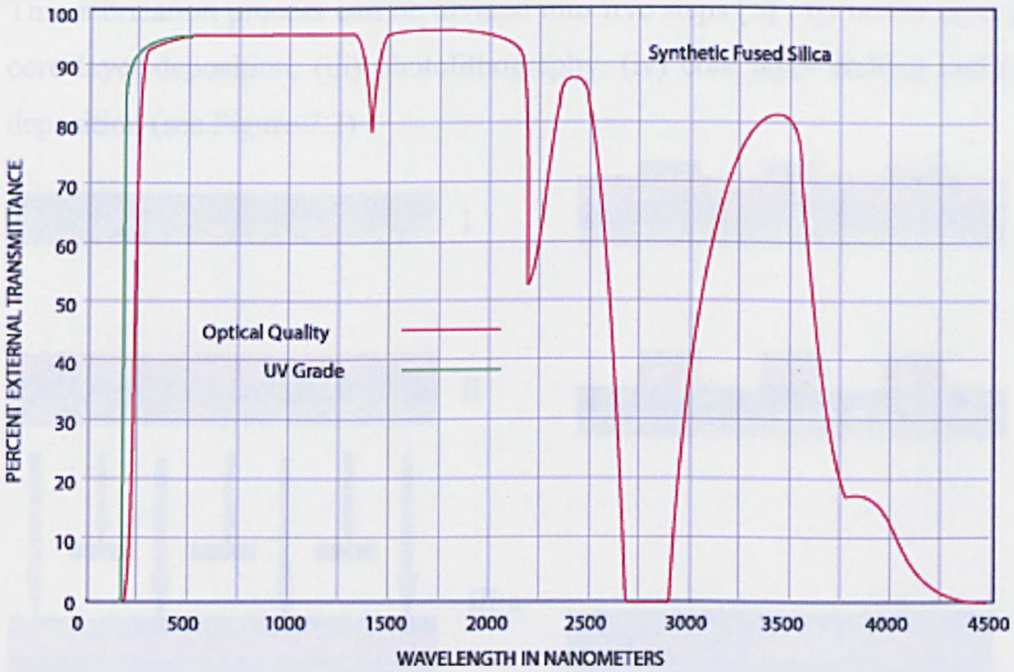

Figure 7.1: Transmission spectrum of silica

The low loss transmission of fused silica is one reason why it is used in telecommunication applications. One other benefit is its low material dispersion around the radiation wavelength of 1.3μm [1]. The combination of these two properties allows data transportation over long distances with low loss transmission and low signal dispersion. As well as being used as optical fibres, fused silica is also used as a base material for planar photonics components, so called Planar Lightwave Circuits.

7.1.1 *Planar lightwave circuits*

Planar lightwave circuits (PLCs) are optical devices based on silica-on-silicon waveguide technology in which the waveguide patterns are defined via photolithography. They can be beneficial for opto-electronics packaging [2] but can also be used as devices like arrayed waveguide gratings (AWG) [3] and as Echelle gratings [4]. The other benefit of using fused silica for PLCs is the lack of a refraction index contrast between the PLC components and the attached optical fibre. As a result, there is no mode coupling mismatch or back reflections on the coupling interfaces of fibre to PLC.

7.1.1.1 Silica-on-Silicon waveguide fabrication

Silica-on-silicon waveguide structures consist of a silicon substrate on which three fused silica layers are grown and deposited to form the buffer, core and cladding layer. This fabrication process can be divided into five steps [5] : (i) buffer layer growth, (ii) core layer deposition, (iii) photolithography, (iv) core layer etching and (v) cladding deposition (see Figure 7.2)

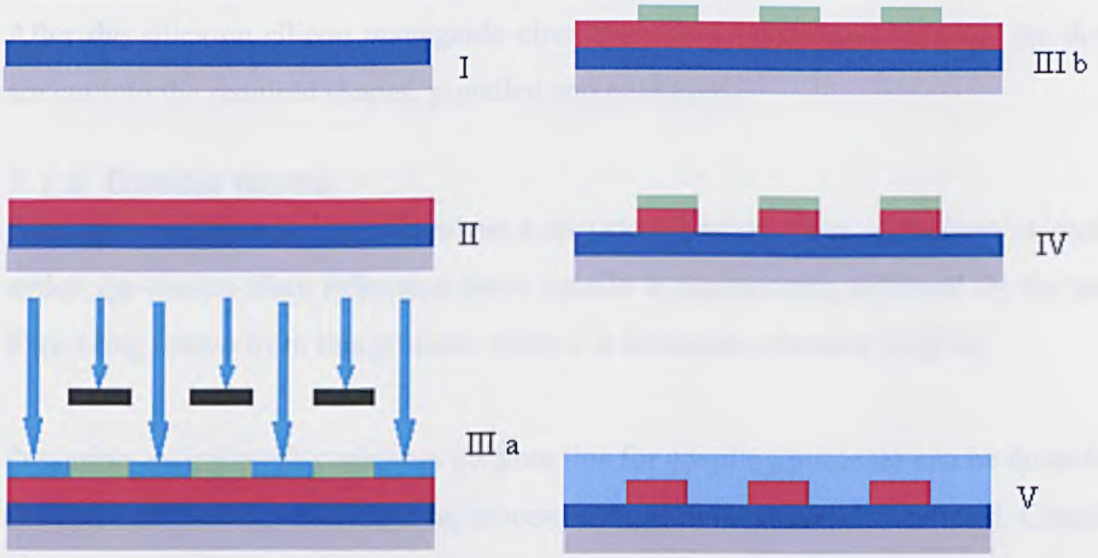

Figure 7.2: Silica-on-silicon waveguide fabrication process (for an explanation of I-V see text)

(i) The buffer layer of pure SiO_2 is grown onto the silicon substrate by thermal oxidization.

(ii) The core layer is deposited onto the buffer layer by using either Flame Hydrolysis Deposition (FHD) [6-8]or Plasma Enhanced Chemical Vapour

Deposition (PECVD) [9, 10]. To increase the refraction index of the core layer, doping agents like Germanium are added.

(iii) (a) The waveguide circuitry patterns are imaged from a mask onto the photoresist on the top surface of the core layer after which (b) the photoresist is developed and creates a contact mask pattern for the waveguide core etching

(iv) The etching of the waveguide pattern into the core layer is carried out with reactive ion etching (RIE) [6, 11-13]. This process allows etching of vertical structures in fused silica as the chemical mixtures used, for instance CHF_3, are highly selective over photoresists. In addition to the RIE process, waveguide definition within the core layer can also be carried out with other techniques such as ion implantation [14] with laser based direct writing technology, either based on continues DUV laser [15][16] or femto second laser inscription [17-20].

(v) After the resist has been stripped, the cladding layer is deposited around the ridge waveguides with FHD or PECVD. Dopant agents of either Boron [21] or phosphorus [22] are used to achieve a refraction index within the cladding layer which matches that of the buffer layer.

After the silica-on-silicon waveguide circuitries have been manufactured, the devices are cut into the required shapes, pigtailed and packaged.

7.1.2 Optical fibres

Fabrication of optical fibres involves a two-step process. First, a preform is made in which the optical fibre refraction index profile is represented, followed by the optical fibre being drawn from this preform while it is heated in a furnace [23][24].

Preparing optical quality surfaces on fibre tips for coupling purposes can be done with a mechanical cleaving and polishing process but a CO_2 laser can also be used. Cleaving a fibre is the simplest way of achieving an optical quality fibre tip and can be done perpendicular to the optical fibre or under a fixed angle. Polishing a fibre end to an optical quality is mainly performed when the optical fibre is to be potted into a connector. The 10.6μm radiation wavelength of a CO_2 laser is absorbed strongly by fused silica and can therefore be used to prepare fibre ends, not only a cleaved flat surface under any particular angle, but this also allows shaping of the fibre tip into micro lenses. [25-29].

7.1.3 Micromachining of fused silica

The micromachining processes commonly used for fused silica components are based on mechanical techniques or on chemical etching. Mechanical processes for cleaving and polishing are used to prepare optical surfaces while for producing sub millimeter structures within fused silica substrates, wet and dry chemical etching technologies are used. The dry RIE process is used for vertical structures, like optical waveguides, while wet chemical etching produces circular etched shapes and can be used for processing microfluid devices [30, 31] and micro optical structures within PLCs devices [32]. The etch rates achieved are limited; for RIE an etch rate is between 0.25- 0.5μm/min [33] while for wet etching this is typically 0.34μm/min [30].

DUV excimer lasers have successfully been used for the ablation of fused silica even though the band gap energy is ~ 9.3eV, equivalent to a photon wavelength of λ=133nm. Both the 308nm XeCl and the 248nm KrF laser have been used to ablate fused silica but high incident fluences, $H > 20$ J/cm^2, are required and lead to rough surfaces [34]. With the ArF laser, high quality structure are possible at moderate incident fluences, $H \sim 5$ J/cm^2 [35, 36]. At 157nm, the energy is strongly coupled into the fused silica via defects or near-band edge states and the clean removal of fused silica at low fluences is possible [37]. With a 157nm fluorine laser integrated into a mask projection system, it is possible to fabricate photonic components or structures like waveguides [38], microlenses [39] and to produce photosensitivity enhancement [40] and to define long period gratings [41].

In this chapter, the ability of the fluorine laser to remove fused silica cleanly is further investigated to develop novel laser-based micromachining processes for planar lightwave circuitry and optical fibre based applications or structures. With planar fused silica samples, the micromachining of ridge optical waveguides and waveguide based micro-mirrors was investigated and fibre tip shaping and fibre side polishing was also attempted. Before these experiments were carried out, the ablation behaviour of fused silica was determined and attempts were made to define a static mask – workpiece dragging micromachining processing window. The planar samples used were Corning HPFS Fused Silica while Corning SMF-28 single mode fibre was used in the optical fibre experiments.

7.2 UV laser ablation of fused silica

The etch rate of fused silica was determined at $\lambda = 157$nm with the fluorine laser-mask projection system. At a laser repetition rate of 10 Hz, 100 laser pulses were fired at different fluences and blind holes were machined into a silica surface. The depth of a blind square hole, 120μm x 120μm, was measured with a surface profiler (VEECO dektak[3]). In Figure 7.3, the average etch rate per pulse is shown plotted against incident fluence.

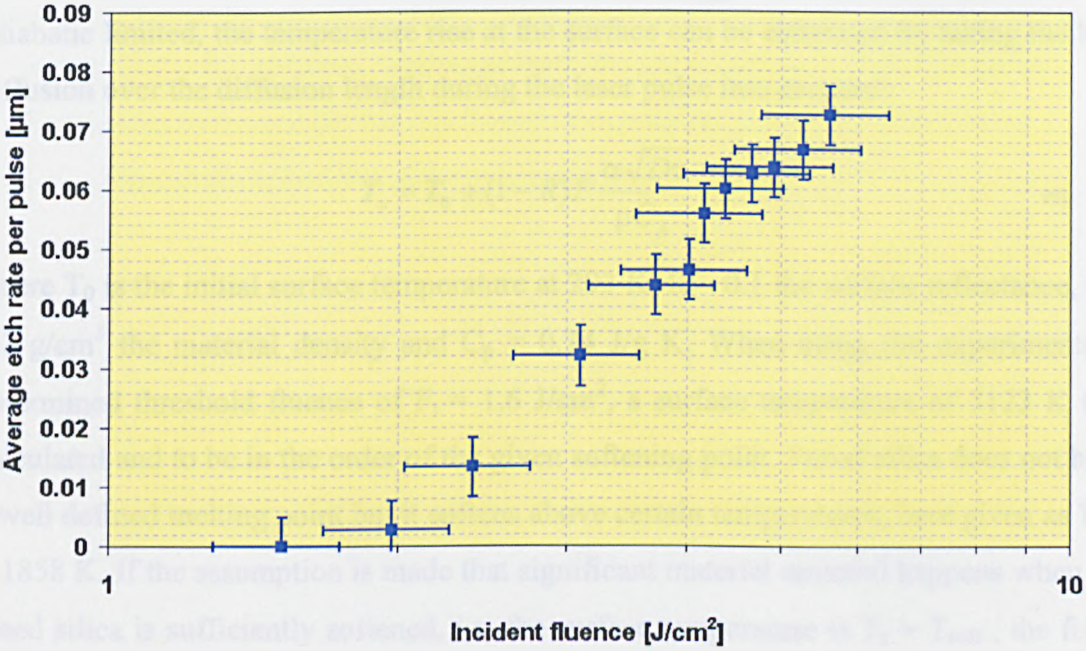

Figure 7.3: Etch rate per pulse of fused silica at a laser wavelength of λ=157nm

The threshold fluence for ablation was determined to be between H = 1.6 and 1.95 J/cm^2 while at a high incident fluence 5.5 J/cm^2, the average etch rate was determined as x = 0.072μm per pulse.

7.2.1.1 Laser ablation threshold

Similar calculations as to those in chapter 4 were carried out on the experimental etch rate data where the value thermal diffusivity, D = 0.0075 cm^2/s, was taken from the fused silica data sheet [42].

The 157nm related optical material parameters and the heat diffusion length during the laser pulse was calculated with use of equation 4-3 and the pulse length of τ = 20nsec (Table 7.1).

Material parameter	**Value**
Effective absorption coefficient α [cm^{-1}]	2.48×10^4
Effective absorption depth [µm]	0.4
Heat diffusion length during laser pulse $\sqrt{D\tau}$ [µm]	0.13

Table 7.1: Fluorine laser micromachining system calculations for optical and thermal material parameters

For SiO_2 at 157nm, the heat diffusion length during the laser pulse, $\sqrt{D\tau}$, is calculated to be only 3 times smaller than the effective absorption depth. In this case the heatflow into the material during the pulse is not negligible and by recognizing this process is adiabatic limited, the temperature rise at the surface can be estimated by taking the heat diffusion over the diffusion length during the laser pulse into account:

$$T_s = T_0 + (1-R)F\frac{\alpha\sqrt{D\tau}}{\rho C_p} \qquad \text{eq.: 7-1}$$

where T_0 is the initial surface temperature at 293 K, R ~ 0.1 the surface reflectance, ρ = 2.2 g/cm^3 the material density and C_p = 0.74 J/g K. When using the experimentally determined threshold fluence of F_t = 1.6 J/cm^2, a surface temperature of 3123 K was calculated and to be in the order of the given softening point. Fused silica does not have a well defined melting point but it softens above certain temperatures, here given as T_{soft} = 1858 K. If the assumption is made that significant material removal happens when the fused silica is sufficiently softened, i.e. the surface temperature is $T_s > T_{soft}$, the fused silica surface has to be exposed with a fluence of 120mJ/cm^2.

7.2.1.2 Arrhenius type thermal model

Even though the determined and calculated threshold fluence was not in agreement, it was tested to see if the process of SiO_2 material removal is based on a thermal vaporization mechanism by fitting an Arrhenius type thermal trend against the determined average etch rate values. For this, the data was re-plotted to a graph of ln(average etch rate per pulse) versus the inverse of incident fluence (Figure 7.4).

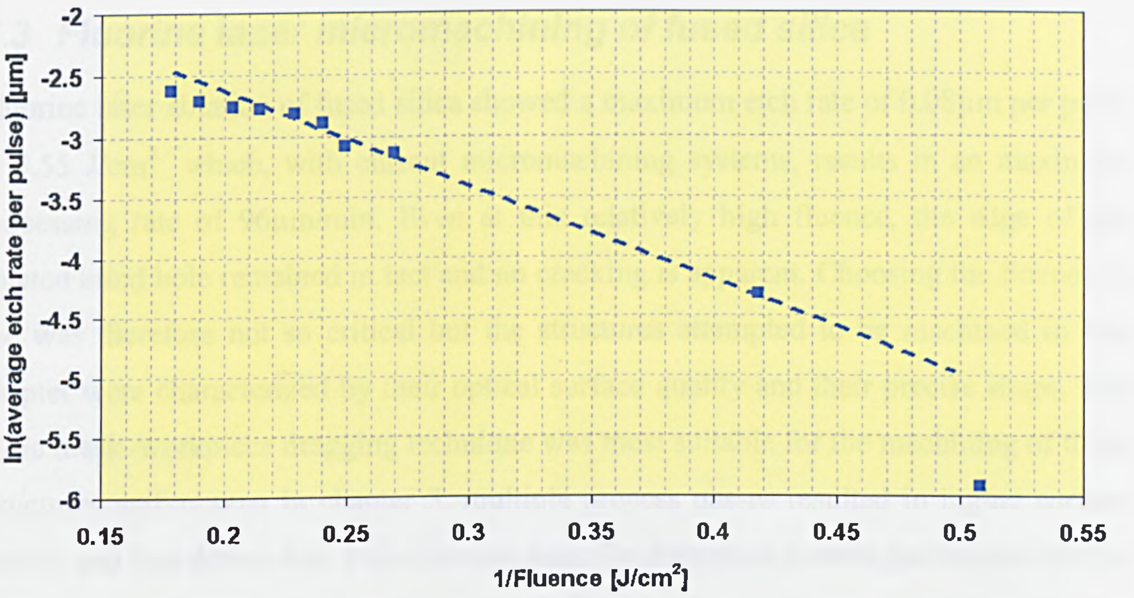

Figure 7.4: ln(average etch rate per pulse) vs. 1/incident fluence of SiO_2 at a wavelength of λ=157nm.

A linear relationship between ln(average etch rate per pulse) versus the inverse of fluence is seen to apply over the full fluence range investigated indicating that an Arrhenius model described the material removal well.

7.3 Fluorine laser micromachining of fused silica

Fluorine laser ablation of fused silica showed a maximum etch rate of 0.08µm per pulse at 5.55 J/cm^2 which, with current micromachining systems, results in an maximum processing rate of 96µm/min. Even at this relatively high fluence, the edge of the ablated blind hole remained in tact and no cracking is apparent. Choosing the fluence to use was therefore not so critical but the structures attempted to be machined in this chapter were characterized by their optical surface quality and their precise shape. The static mask–workpiece dragging technique was most suitable for the machining of these structures and as seen in chapter 5, multiple process passes resulted in higher surface quality and less debris than a one process pass. To determine process parameters for the workpiece dragging techniques, rectangular shape channels were machined under various conditions.

Six slots were machined in the fused silica samples, at a fluence of 3J/cm^2 and pulse repetition rate of 10Hz. A rectangular mask was imaged onto the surface to give a 100x60µm^2 spot whilst being translated in the same direction as the long axis of the rectangular mask. The number of process scans used was set to be between 1 and 10 while the substrate velocity was altered to achieve 325 number of laser pulses per area. The machined samples were wiped with isopropanol before the results were examined with a SEM.

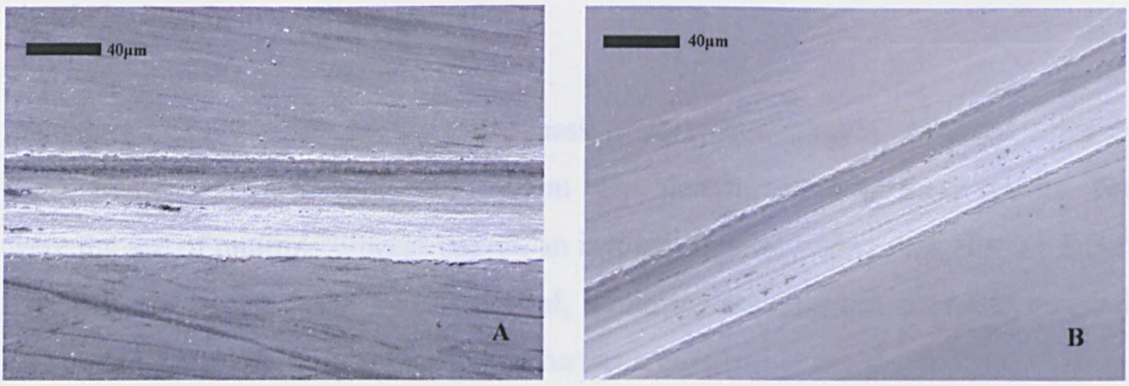

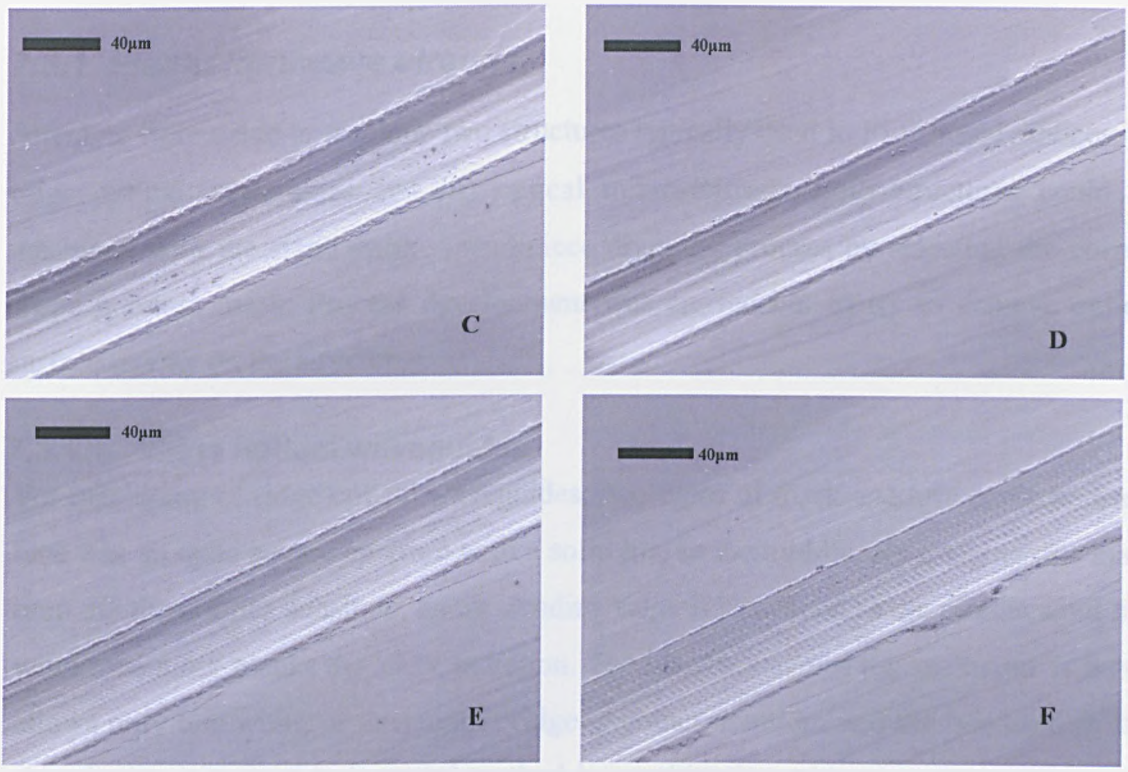

Figure 7.5: Slots machined into fused silica samples with (A) 1 process pass and V= 0.25mm/min, (B) 2 process passes and V= 0.5mm/min, (C) 4 process passes and V=1mm/min, (D) 6 process passes and V=1.5mm/min, (E) 8 process passes and V=2mm/min, (F) 10 process passes and V=2.5mm/min.

Results seen in Figure 7.5 show the channels machined with 2, 4 and 6 process passes had the best surface quality while those with 8 and 10 process passes had a rippled surface profile. This profile is due to the large substrate translation between each laser pulse and to avoid this surface structure it was determined that the substrate velocity should be kept below 0.4 µm per pulse.

Boundaries of a window for the static mask – workpiece dragging of fused silica with the fluorine laser mask projection system were determined from these results. These were the use of multiple process passes, an incident fluence higher than H = 0.8 J/cm^2 to establish significant fused silica removal, while maintaining the substrate translation rate below 0.4µm/pulse to avoid rippled surfaces.

7.3.1 Planar lightwave circuits

Attempts were made to machine two structures typically used in PLC based devices; (i) ridge optical waveguides and (ii) optical micro-mirrors. Both structures could be machined with the static mask – workpiece dragging process by selecting the correct shape aperture mask. Process development was carried out to try to achieve optical surface quality on the structures.

7.3.1.1 Ridge optical waveguides

For machining of ridge optical waveguides, two types of mask aperture could be used. One was an open square aperture with a solid line in the middle. By imaging this mask onto the fused silica substrate, an up standing ridge is machined as the middle solid line within the mask blocks the VUV radiation. The disadvantage of this technique is that it allows only one width of upstanding ridge. Another solution, and the one used in this experiment, is a 'step and repeat' method in combination with an open aperture mask and is schematically described in Figure 7.6.

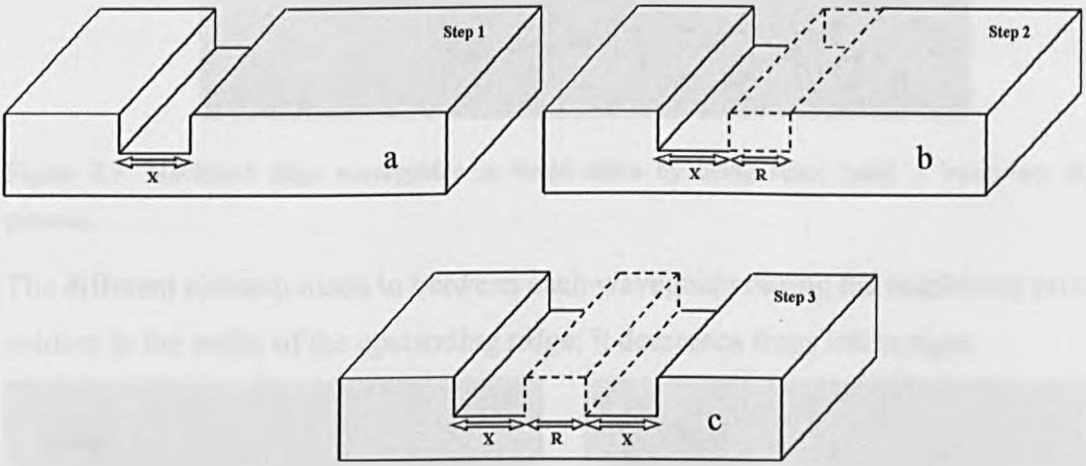

Figure 7.6: Ridge waveguide micromachining steps

a. Step 1 Defining first vertical channel
b. Step 2 Side shift to define ridge width
c. Step 3 Machining second channel to produce the up-standing ridge

In total, four isolated ridges were machined using this process. The fused silica substrate was translated with a velocity of V = 0.5mm/min in the direction of the long axis of the rectangular mask, image size 100 x 60µm. The fluence was set at H = 3 J/cm^2 and a pulse repetition rate of 10 Hz was selected. By using two process passes on each, the total number of laser pulses per area was 220. Four different sidesteps were used; 64μm, 66μm, 68μm and 70μm.

To improve the ability to examine the fused silica ridges, the sample was cleanly broken in half and reassembled seamlessly onto a carrier substrate. This was to avoid rounded edge on the machined structures. By machining perpendicularly onto this cut and afterwards separating the two halves, it was possible to examine the profile of the ridges. The samples were prepared and examined with a SEM without post process cleaning. The results are shown in Figure 7.7, Figure 7.8 and Figure 7.9.

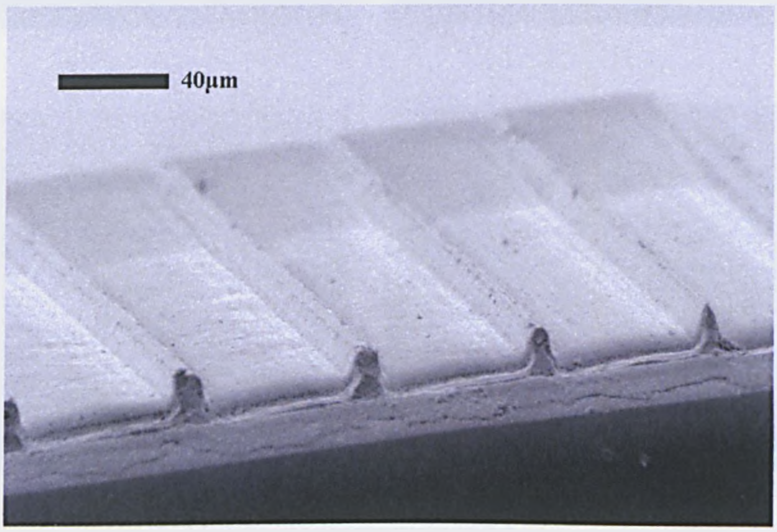

Figure 7.7: Machined ridge waveguides in fused silica by using static mask – workpiece dragging process.

The different sidestep made in between each waveguide during the machining process is evident in the width of the upstanding ridge; it decreases from left to right.

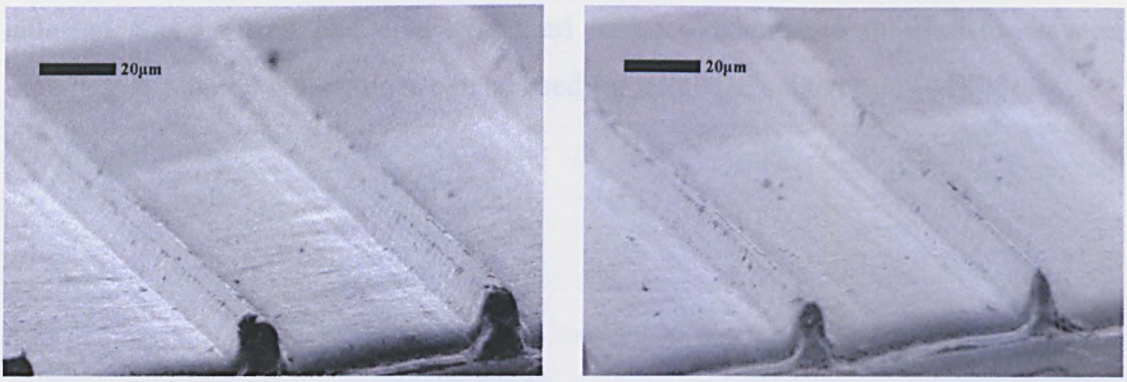

Figure 7.8: Machined ridge waveguides of (a) 10μm, 8μm and (b) 6μm and 4μm wide

On the edges of the upstanding ridges, slight chipping has occurred. Process debris produced during ablation has not been completely removed even with nitrogen flow from a Schwarzschild objective.

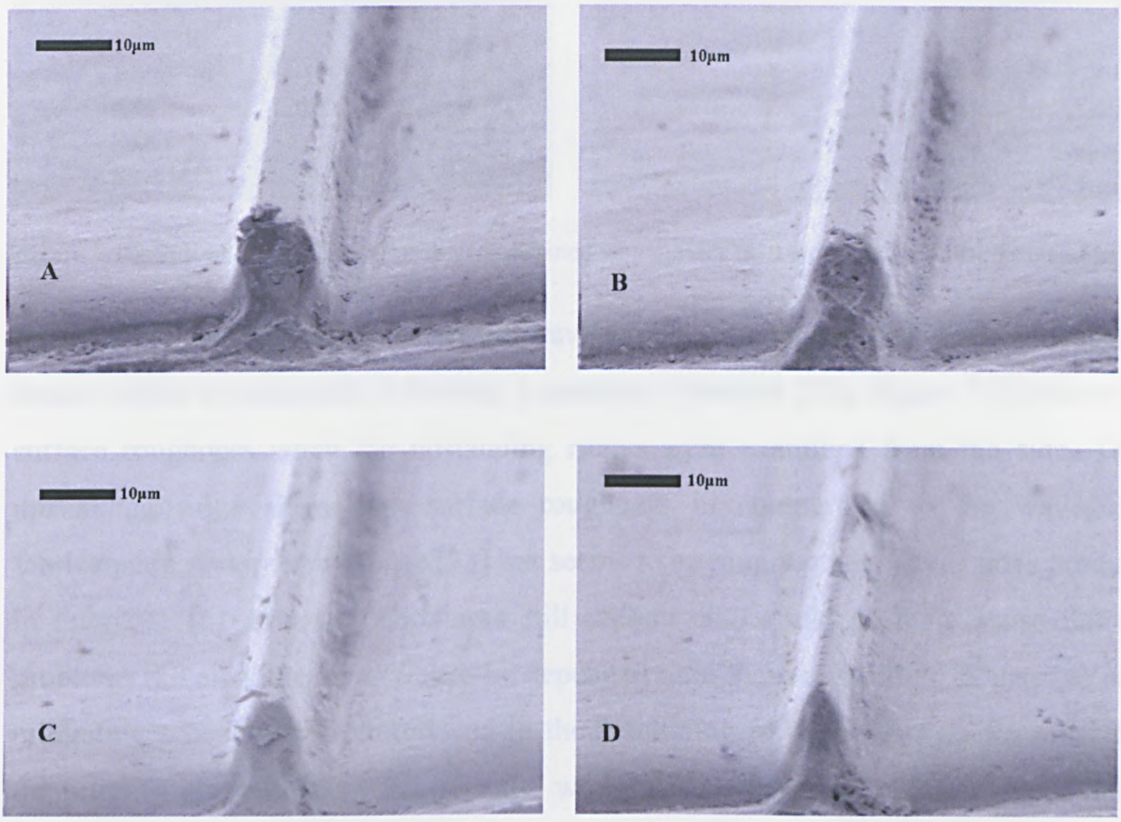

Figure 7.9: Fused silica ridge waveguides machined with a sidestep of (a) 70µm, (b) 68µm, (c) 66µm and (d) 64µm width.

The different sidesteps in ridges with different widths, are estimated to be (a) 10µm, (b) 8 µm, (c) 6 µm and (d) 4µm. Rounding of the ridge became more marked when the sidestep was reduced and could be used to good advantage in fibre to waveguide coupling as tapered waveguides can be used for spot-size conversion [44][45].

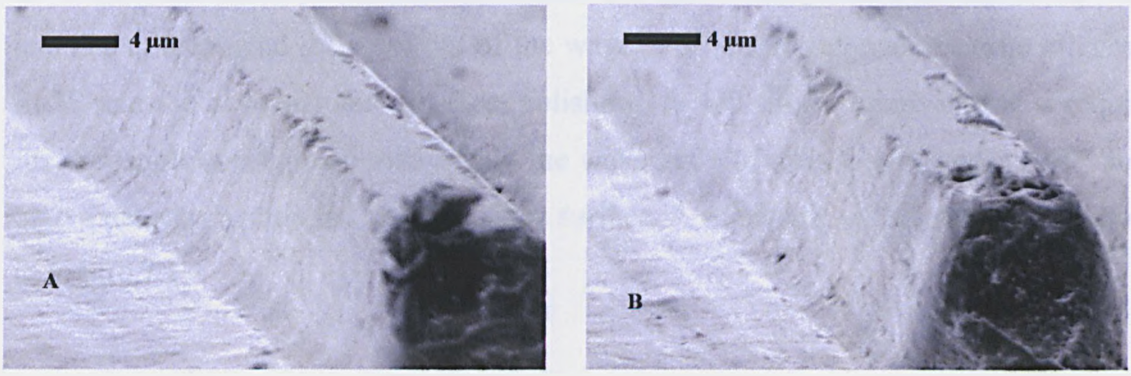

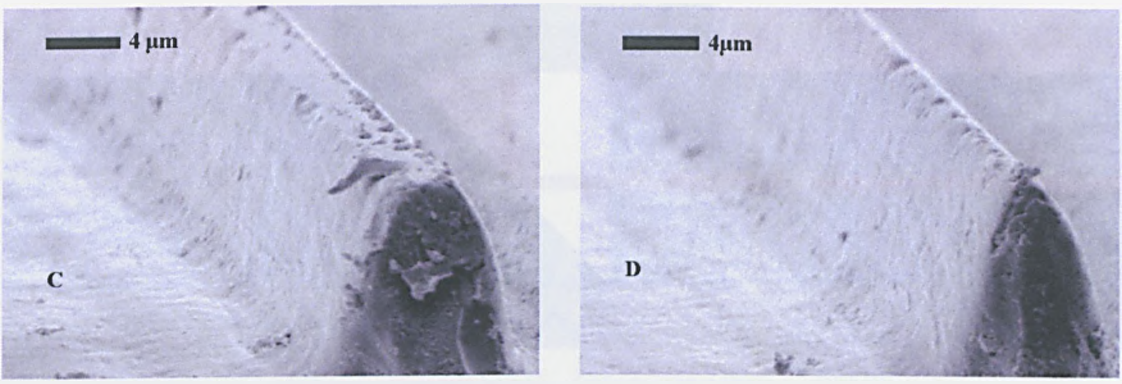

Figure 7.10: Sidewall of 157nm laser micromachined waveguides (a) 10µm, (b) 8µm, (c) 6µm and (d) 4µm.

Surface roughness on the edges of the waveguides is directly related to the propagation losses within a waveguide following a quadratic function [33]. Figure 7.10 shows the surface roughness when the upstanding ridges were examined from the side. These upstanding ridges have less surface roughness in comparison to the waveguides fabricated in previous reference [33] but seems to be rougher than waveguides produced in reference [5]. Process debris was still present and would possibly cause function problems if a cladding layer was to be deposited onto these upstanding ridges. No other mitigating schemes were introduced in the machining of these waveguides other than the purging nitrogen gas flow over the workpiece. It is possible that more advanced debris mitigation or post process cleaning could remove this process debris.

7.3.1.2 Integrated micro mirrors

Silica-on-silicon based planar lightwave circuits are used in device applications such as AWGs and WDMs, and are integrated into hybrid platforms together with active components such as light sources, detectors and amplifiers. In these devices, accurate positioning and low loss coupling between the PLCs and the active components are key to device functionality. The ability to place the active components on top of the PLCs and detect the signal reflected out of the waveguide would remove the extra alignment SiOB and the necessity for end facet polishing. A 45° angled micro mirror is required for this application, positioned within the waveguide to reflect light under a 90° angle onto a detector positioned onto the silica surface. A schematic of this structure is shown in Figure 7.11.

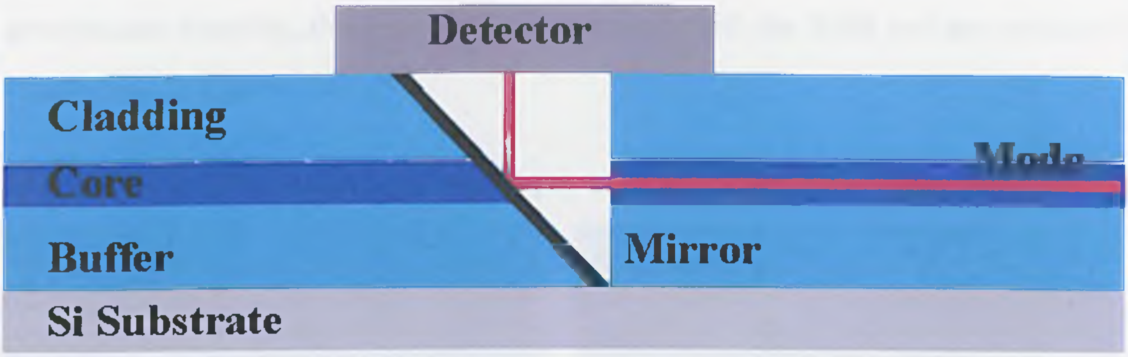

Figure 7.11: Schematic of light detection with integrated micro mirrors

Integration of a mirror within the PLCs waveguide has been achieved with multiple RIE steps, advanced wet etching and metal deposition [32]. By selecting a triangular mask and using the static mask – workpiece dragging process, a sloped surface could be machined into a fully finished PLC device and was investigated with the fluorine laser mask projection system.

The surface roughness of the micro mirror and the surface quality of the waveguide facet are both critical as this is proportional to the level of direct reflection. In an attempt to achieve the lowest surface roughness possible, nine different process parameters were investigated and are presented in Table 7.2.

Laser shots per area	Velocity [mm/min]		
	1 Process pass	5 Process passes	10 process passes
100	0.53	2.65	5.3
500	0.106	0.53	1.06
1500	0.035	0.17	0.35

Table 7.2: Process conditions for laser micromachining of micro mirror in silica

With these conditions, three mirror depths were machined, with three different numbers of process passes. The incident fluence was set to H = 3 J/cm^2 with a laser pulse repetition rate of 10 Hz. The triangular shape mask used had an imaged dimension of length = 90μm and width = 56μm of which the length was in the same direction as the translation direction of the fused silica substrate.

The number of shots per area and the incident fluence of H = 3 J/cm^2 were chosen to simulate the depth of machining required to make micro mirrors within PLC substrates; a 500 shots per area (s/a) exposure will produce a depth of 20μm to 25μm. Without any post process cleaning, the samples were examined with the SEM and are presented in Figure 7.12 to Figure 7.20.

Process conditions: 100 shots per area at 1,5 and 10 process passes

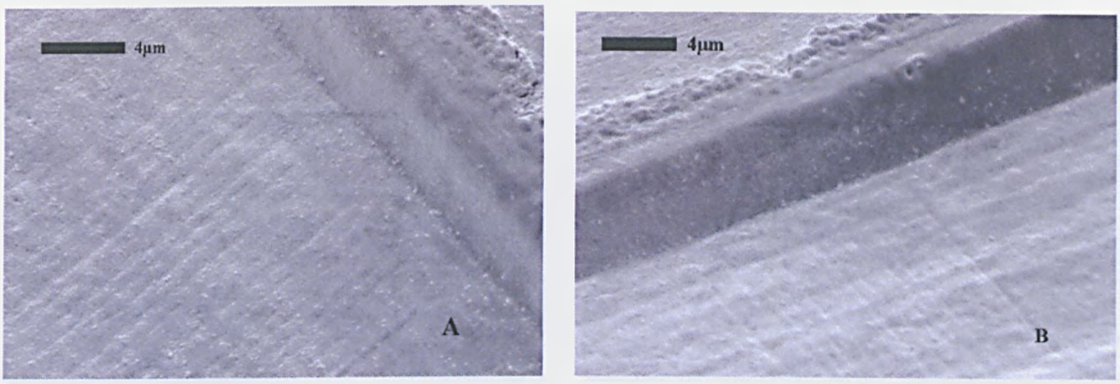

Figure 7.12: 100 shots per area and 1 process pass, (A) micro-mirror area and (B) waveguide end facet

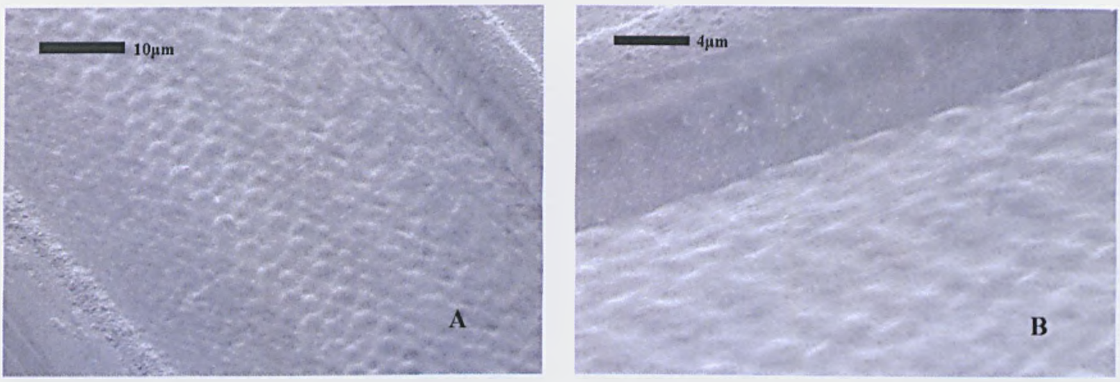

Figure 7.13: 100 shots per area and 5 process pass, (A) micro-mirror area and (B) waveguide end facet

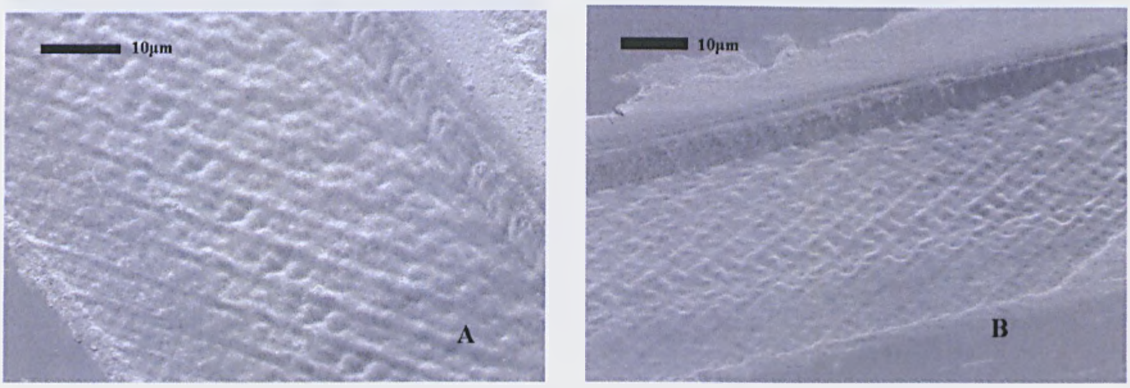

Figure 7.14: 100 shots per area and 10 process pass, (A) micro-mirror area and (B) waveguide end facet

The surface roughness achieved at 100 s/a was directly related to the substrate translation per laser pulse; at 1 process pass the substrate translation was 0.9μm/pulse and was above the indicated 0.4μm/pulse. For the 5 and 10 process passes, the translation per pulse was even higher at 2 and 4 µm/pulse. This established the process window indicated earlier.

Process conditions: 500 shots per area at 1,5 and 10 process passes

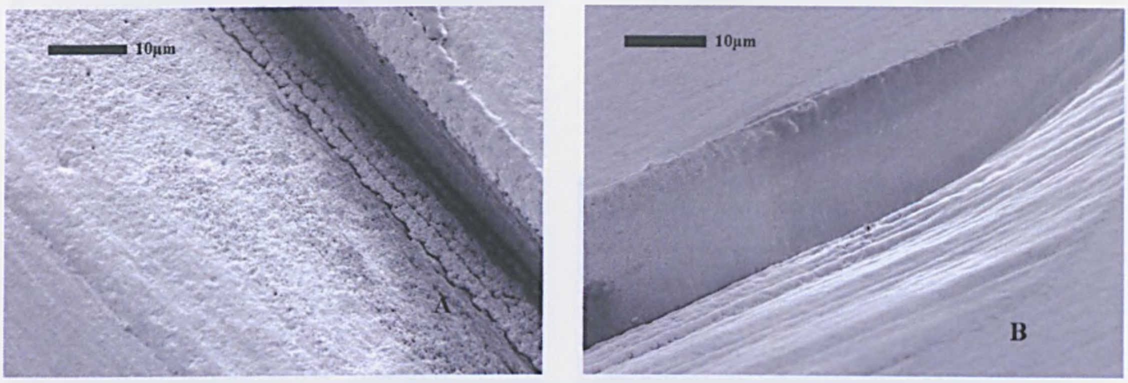

Figure 7.15: 500 shots per area and 1 process pass, (A) micro-mirror area and (B) waveguide end facet

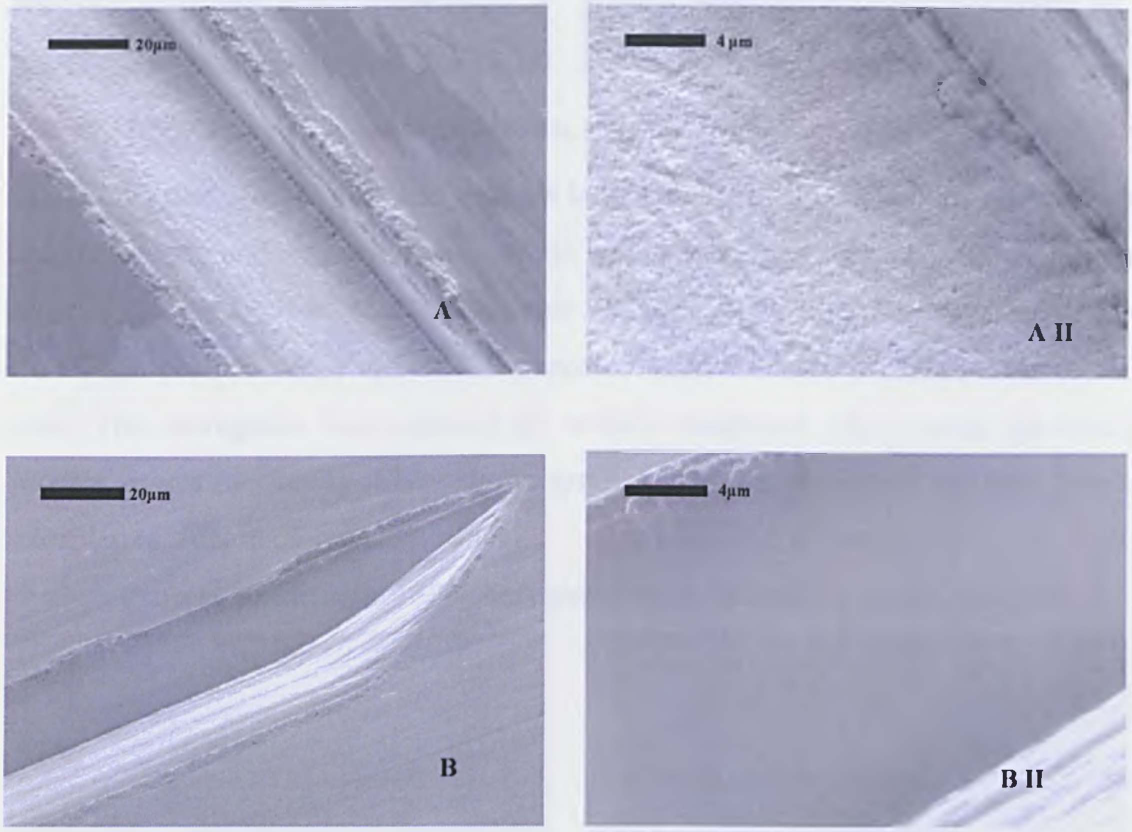

Figure 7.16: 500 shots per area and 5 process pass, (A) micro-mirror area and (B) waveguide end facet

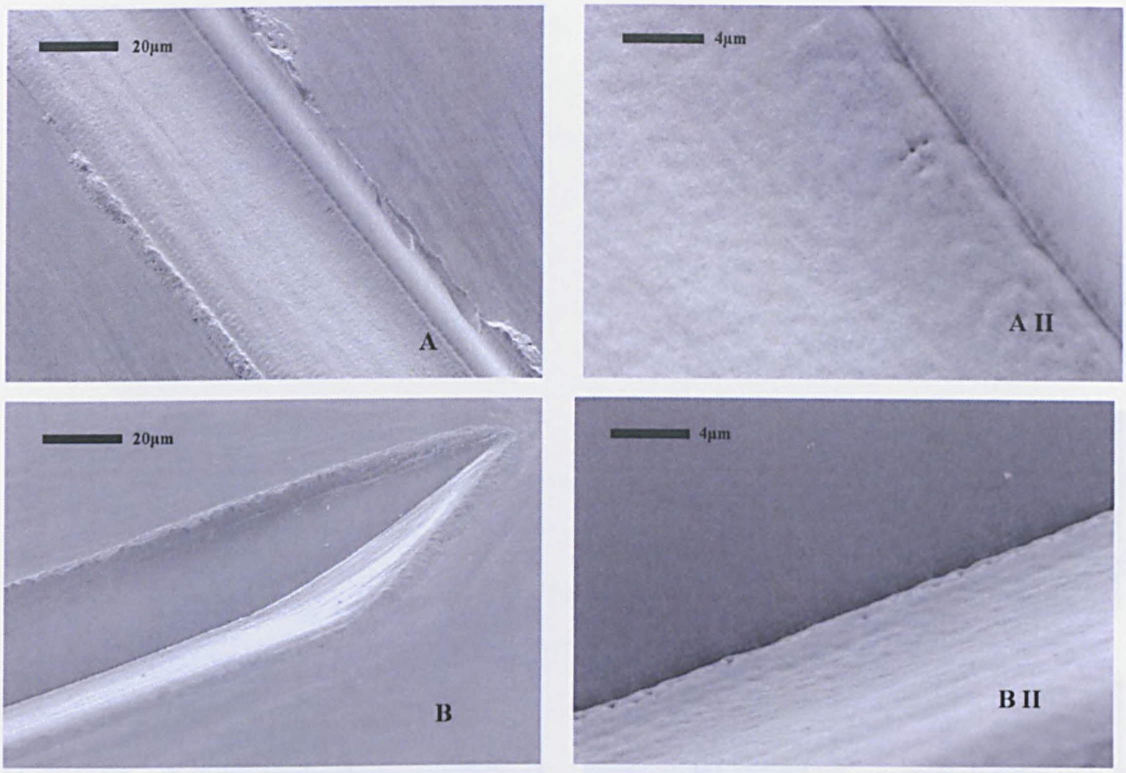

Figure 7.17: 500 shots per area and 10 process pass, (A) micro-mirror area and (B) waveguide end facet

When only one process pass was made, a large amount of process debris was deposited onto the mirror and cleaved surfaces while with 5 and 10 process passes the debris was reduced or could not be seen. The mirror surface roughness was estimated to be less then 1 µm peak-to-valley and no difference between 5 and 10 process passes could be seen. The waveguide facet showed no surface roughness when using the multiple process passes machining. Chipping occurred on the top surface of the facet area and extended to a depth of 4µm.

Process conditions: 1500 shots per area at 1,5 and 10 process passes

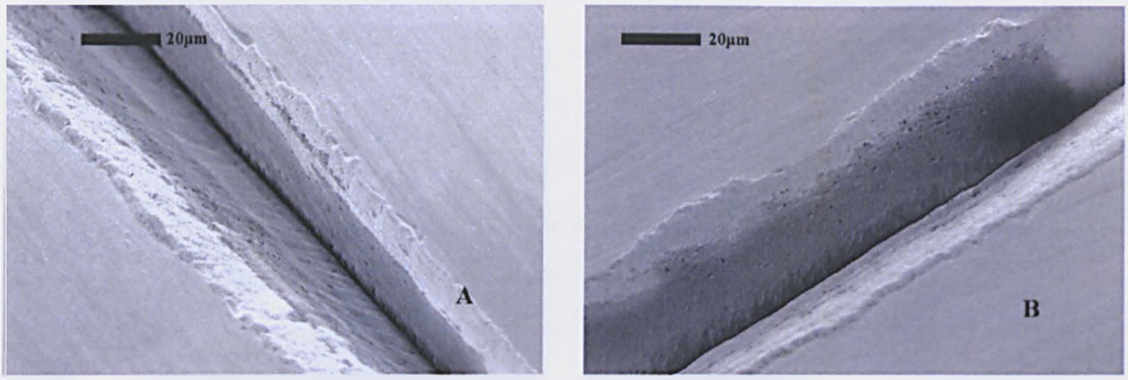

Figure 7.18: 1500 shots per area and 1 process pass, (A) micro-mirror area and (B) waveguide end facet

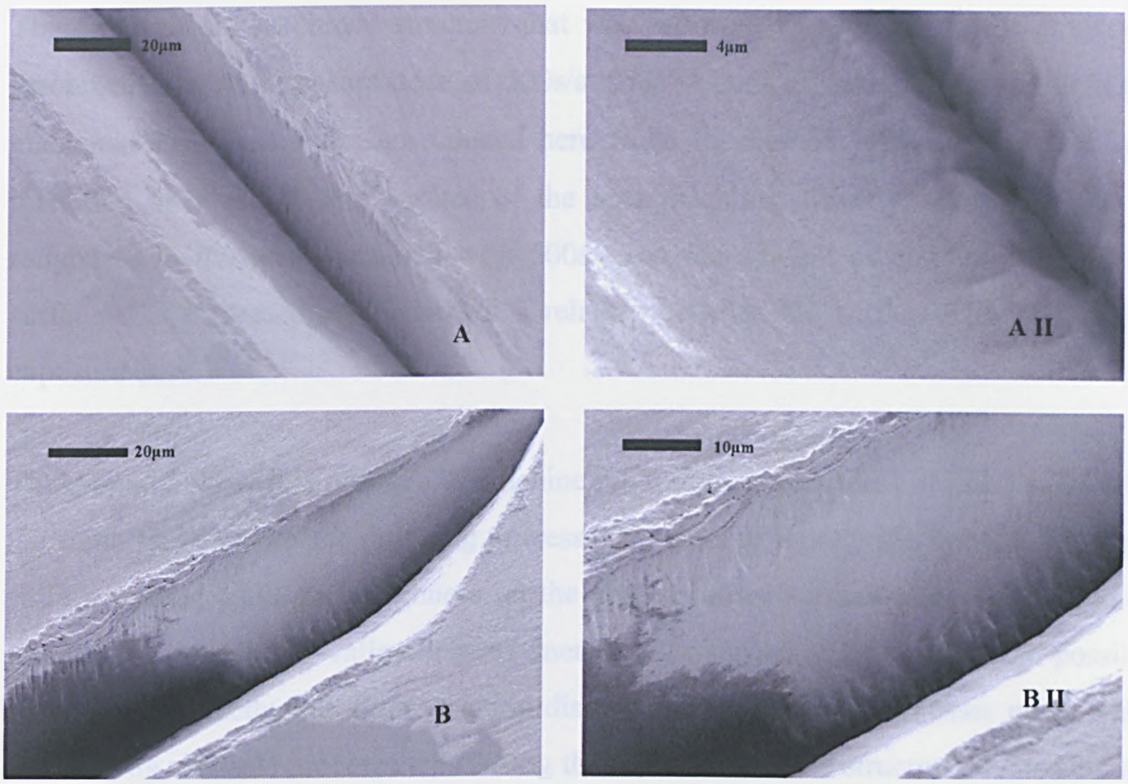

Figure 7.19: Optical surface sample at 1500 shots per area and 5 process passes, (A) direct imaged area and (B) vertical cleaved area

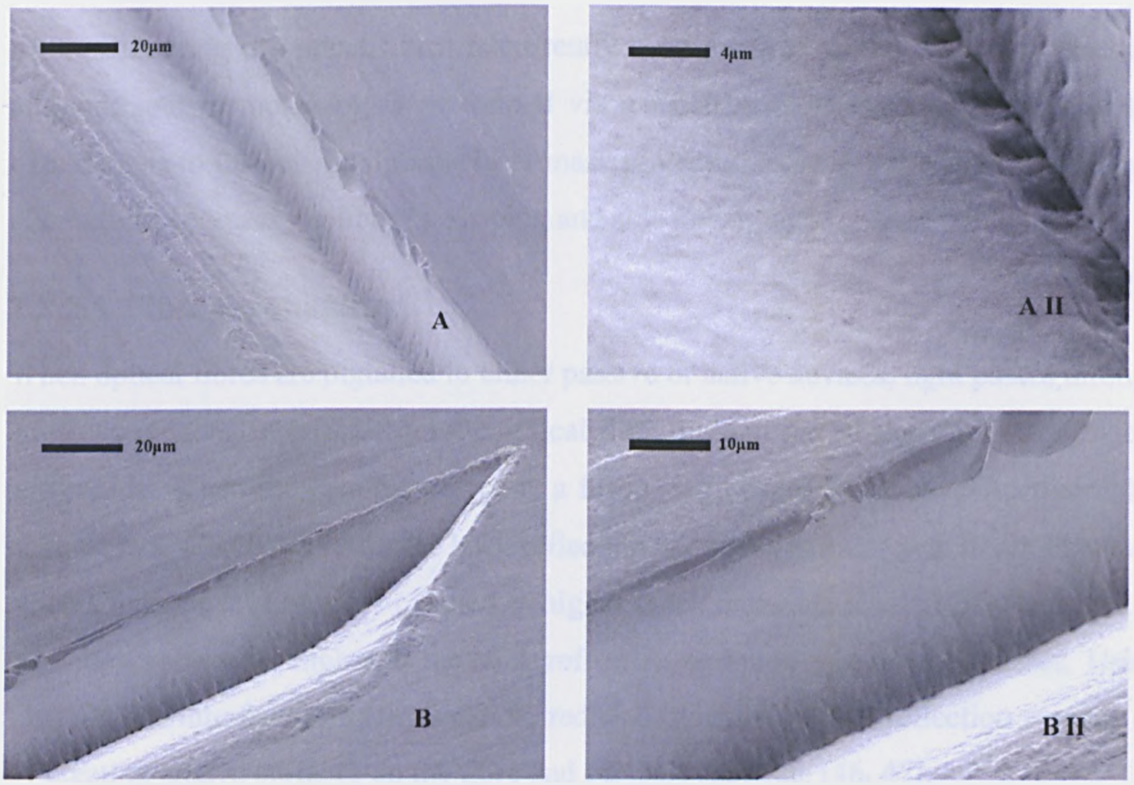

Figure 7.20 Optical surface sample at 1500 shots per area and 10 process passes, (A) direct imaged area and (B) vertical cleaved area

The depth of the machined structure that was achieved was similar to the structures machined with an exposure dose of 500s/a. The amount of debris deposited onto the machined structures was also reduced here when the number of process passes was increased to 5 or 10. The surface of the area machined directly, showed a similar roughness to the area machined with 500s/a but the amount of chipping on the top surface was increased and indicated a relation between the surface damage and the exposure dose.

These results show it is possible to machine micro mirror structures in fused silica with the static mask-workpiece dragging process. The cleaved waveguide facets had a good surface quality while the roughness on the angled mirror surface was estimated to be less then 1μm peak- to- valley. Improvements to the surface smoothness could possible be achieved by reducing the translation distance of the substrate per laser pulse while maintaining multiple process steps during the machining of the structure. Increasing the laser repetition rate or reducing the fused silica substrate velocity could achieve this.

7.3.2 Optical fibres

Micromachining of optical fibres is currently a mechanical process in which cleaving and side and tip polishing is performed via a mechanical interaction process. In the experiments to follow, the fluorine laser mask projection system was used to investigate alternative processes for fibre tip shaping and side polishing of optical fibres.

7.3.2.1 Fibre tip shaping

When optical fibres are pigtailed to either passive or active devices, light passes through a refractive index interface from the optical fibre through the adhesive into the devices waveguide. When the coupled device is a fused silica based PLC, the refractive index contrast is low and as a result the back reflection and mode mismatch is small. However when silica optical fibres are coupled to higher index materials like $LiNbO_3$ with n~2.2, the index contrast is high and the back reflection or mode mismatch increases. Using $LiNbO_3$, the interface reflections can be reduced by using an anti reflection coating, or by creating angled surfaces on the fibre and $LiNbO_3$ substrate [46, 47].

As shown in previous experiments, the fluorine laser mask projection system is able to produce high quality surfaces on different geometries and fibre tip shaping was attempted to utilize the ability to change its aperture mask shape to form the shapes desired.

Static mask – workpiece dragging technology was used with the previously described triangular shape mask to machine angled surfaces onto mechanically cleaved fibre tips. With this setup, the image did not cover the whole area of the tip, but it did ensured that both the core and the cladding were exposed. An angle of 10° was used to reduce back reflection [47] which meant that within the mask dimensions, 10μm had to be removed at the deepest point. At an incident fluence of $H = 3\ J/cm^2$, the etch rate data predicted that 200 shots per area would be required to machine an angled slope 10°. To accommodate these process conditions, five exposures were carried out at a laser pulse repetition rate of 10Hz and are presented in Table 7.3.

Exposure	Process passes	Sample velocity [mm/min]	Shots per area
1	1	0.12	444
2	1	0.24	222
3	1	0.5	111
4	2	0.24	444
5	2	0.5	222

Table 7.3: Process conditions for Corning SMF-28 fibre tip machining

The results were examined with a SEM without post processing cleaning and are presented in Figure 7.21 to Figure 7.25 (fibre diameter = 125μm).

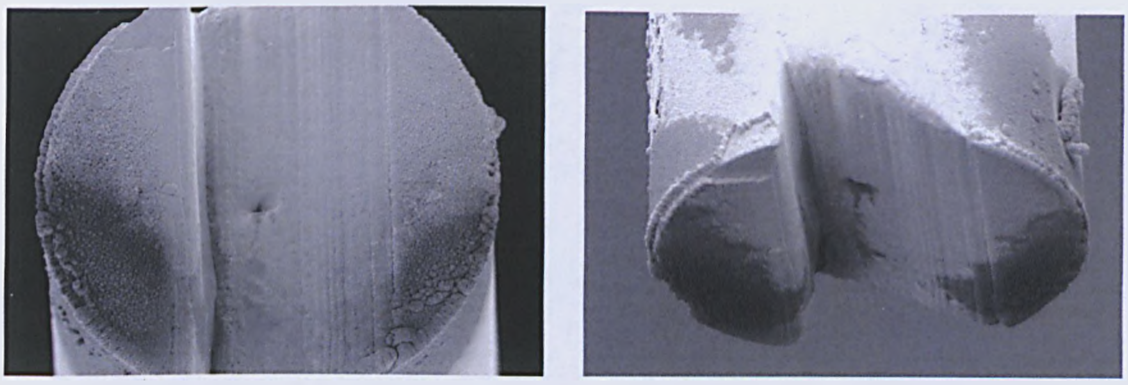

Figure 7.21 Experiment 1: process passes = 1, sample velocity = 0.12mm/min and 444 shots per area

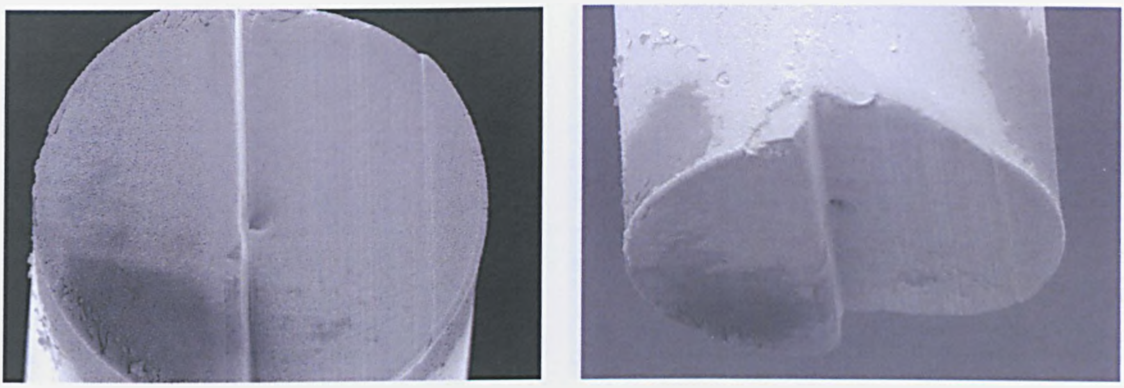

Figure 7.22 Experiment 2: process pass = 1 , incident fluence = 3.5J/cm^2, sample velocity = 0.25mm/min and 222 shots per area

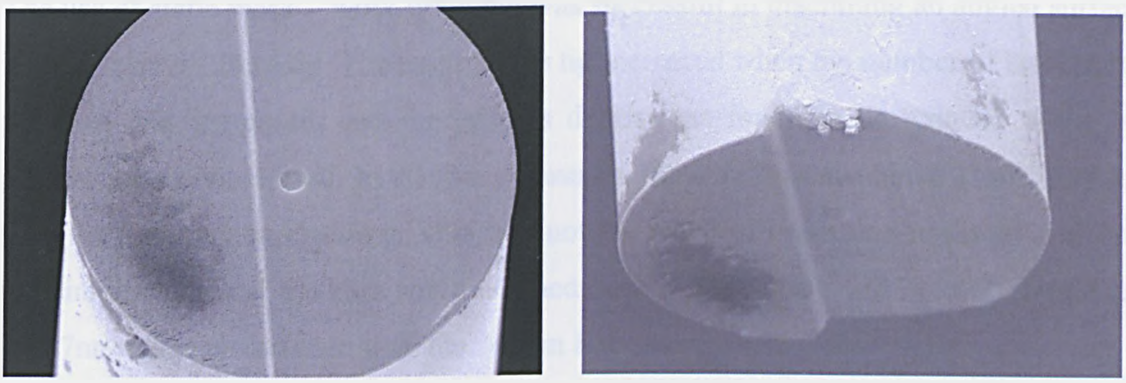

Figure 7.23 Experiment 3: process pass = 1, incident fluence = 3.5J/cm^2, sample velocity = 0.25mm/min and 222 shots per area

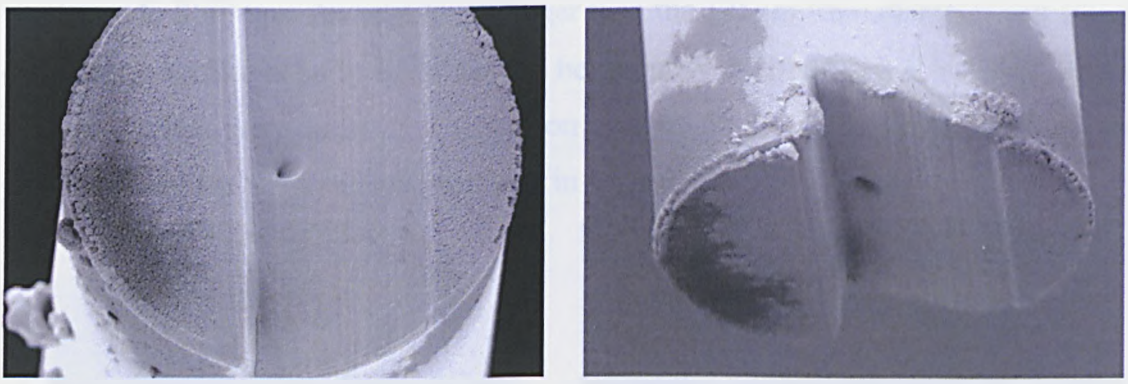

Figure 7.24: Experiment 4: process pass = 2, incident fluence = 3.5J/cm^2, sample velocity = 0.25mm/min and 444 shots per area

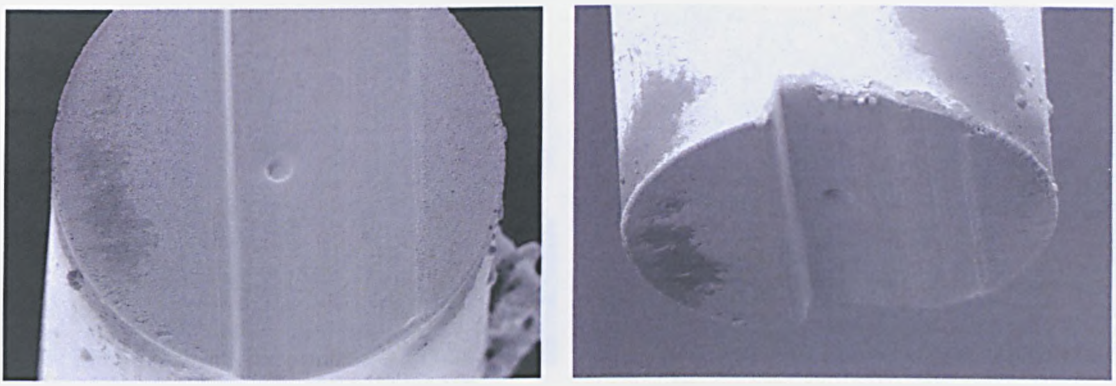

Figure 7.25 Experiment 5: process passes = 2, incident fluence of 3.5J/cm^2, sample velocity = 0.25mm/min and 222 shots per area

The use of static mask – work dragging was successful in machining an angled surfaces into the cleaved fibre tip. The angle of the tip increased when the number of laser pulses per area was increased, and the process debris was found to be reduced when two process passes were used. In all five exposures, the core was machined at a higher rate than the surrounding cladding. This was not the result of beam non-uniformity as only the circular shape of the core was machined deeper. This result was not only found at λ = 157nm but was also seen with the 248nm KrF laser.

A KrF excimer laser mask projection system was used to expose mechanically cleaved single mode fibre tips. An area much larger than the 125μm fibre diameter was imaged onto the tip surface at an incident fluence between H= 1.5J/cm^2 and H = 3J/cm^2. In total 50 laser pulses were used at a repetition rate of 50 Hz. The exposed fibres were examined with an SEM and are presented in Figure 7.26.

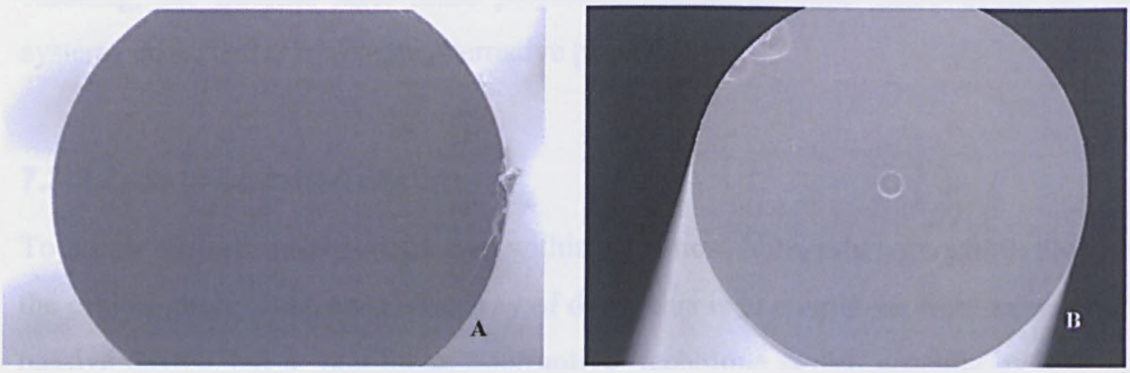

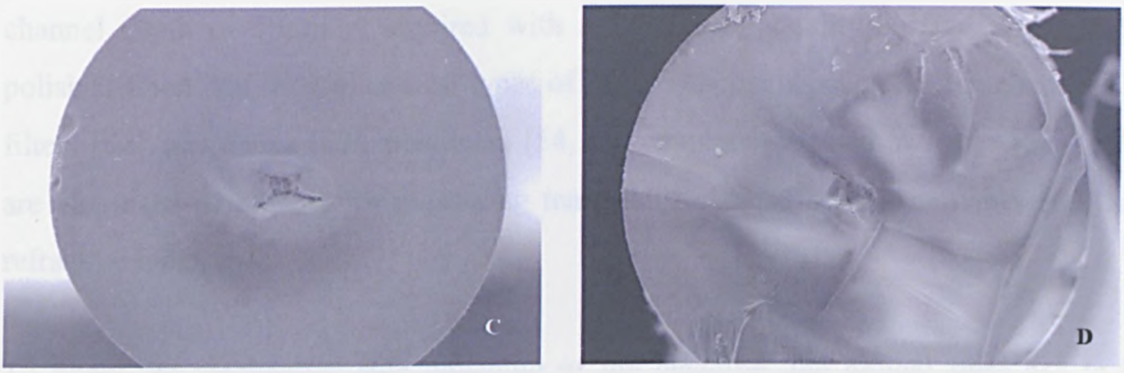

Figure 7.26: Fibre tip subjected to flood exposure with a KrF laser at 248nm and 50 laser pulses at (a) 1.5J/cm^{2}· (b) 2 J/cm^{2}· (c) 2.5J/cm^{2} and (d) 3J/cm^{2}

Below a fluence of H = 1.5 J/cm^{2} , no removal of the core was detected but at an H = 2 J/cm^{2} the core was ablated cleanly. When the incident fluence was increased above H = 2 J/cm^{2} , removal of the core and cracking of the silica occurred.

In both cases, the ablation rate of the fibre core was higher than the surrounding cladding. The mechanism of radiation absorption in fused silica is based on defects within the glass and near bandedge status changes [37, 48]. To raise the refraction index of the core to achieve total internal reflection, germanium is added to the fibre's core during manufacturing. However, by increasing the concentration of Ge in the core, the number of defects increases [49][50] and as a result, the level of UV radiation absorbed increases. Also, the dopant itself increases the level of absorption. This results in a higher material removal rate and is an explanation for why the core was machined deeper than the cladding. Due to the difference in ablation rate between the core and the cladding, the fluorine laser mask projection system or other DUV mask projection systems do not offer a suitable alternative process.

7.3.2.2 Side polished fibres

To access the information contained within an optical fibre, interaction with the field in the optical guide is required. One way of doing this is to couple the fibre to an active or passive device, but a 'non mode interruptive' technique is also possible by interacting with the evanescent field. This field is situated on the interface between the core and the cladding and when monitored or altered, the field within the core can be measured or changed. Gaining access to this evanescent field is currently achieved by partially removing the cladding by mechanical polishing. To access the evanescent field, a channel depth of 58μm is required with a flat optical quality surface. These side-polished fibers are used in several types of fibre components such as modulators [51], filters [52], amplifiers [53], polarizers [54, 55] couplers [56] and switches [57]. They are also used as sensors for measuring temperature [58], Ph [59], humidity [60] and refractive index [61].

To allow the mechanical side polishing of the cladding, the optical fibre has to be supported. Silica or quartz blocks were originally used in this process, but silicon with anisotropic etched v-grooves became the preferred support material [62]. In this technique, the optical fibre is glued into curved v-grooves and then the cladding is polished until the surface of the silicon substrate is reached. With the accurately etched curved V-grooves, the cladding can be polished down to 0.5 – 2.5 μm away from the core and has a typical interaction length of 1-2 cm. This side polishing process contains multiple steps including anisotropic wet etching, securing of the optical fibre and a polishing process to achieve an optical quality interaction surface. Previous experiments that show the ability to laser machine vertical channels in planar fused silica substrates could possibly be applied to machining access channels in the cladding of an optical fibre. This was investigated using the fluorine laser micromachining system.

Two types of exposures were investigated, static and static mask – workpiece dragging. In both exposures, the jacket of a fibre was removed to expose the cladding and this was then cleaned before being held in place onto a substrate with double-sided tape.
To make the static exposure, a rectangular mask was selected with imaged dimensions of 40 x 64μm. The fluence was set to $H = 3$ J/cm^2 and four exposures were made using: 1000, 2000, 3000 and 4000 shots at a laser repetition rate of 10 Hz. Using previously calculated etch rate data (paragraph 7.2), these blind holes were predicted to reach a depth of 30μm (1000 shots) and drilled through the fibre (4000 shots). Without any post process cleaning, the fibres were examined with a SEM (Figure 7.27).

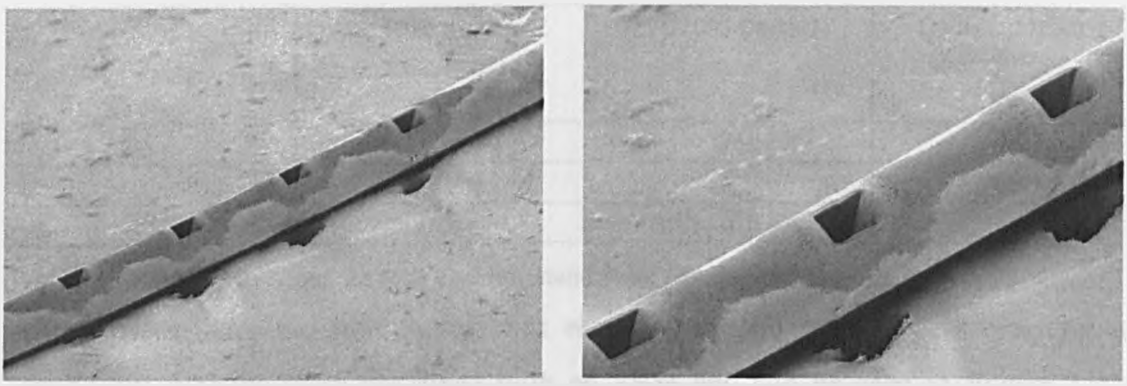

Figure 7.27: Static exposures on Corning SMF-28 single mode fibre. Bottom left = 1000 pulses and top right = 4000 pulses.

The surface edges of the blind holes were sharp and no chipping was visible but the depth of the hole was not in agreement with the predicted value. The depth and the profile of the holes machined with 1000 and 4000 shots did not have a significant difference, as can be seen in Figure 7.28. Both have the same pyramid shape and the higher dose has no effect on the depth or profile

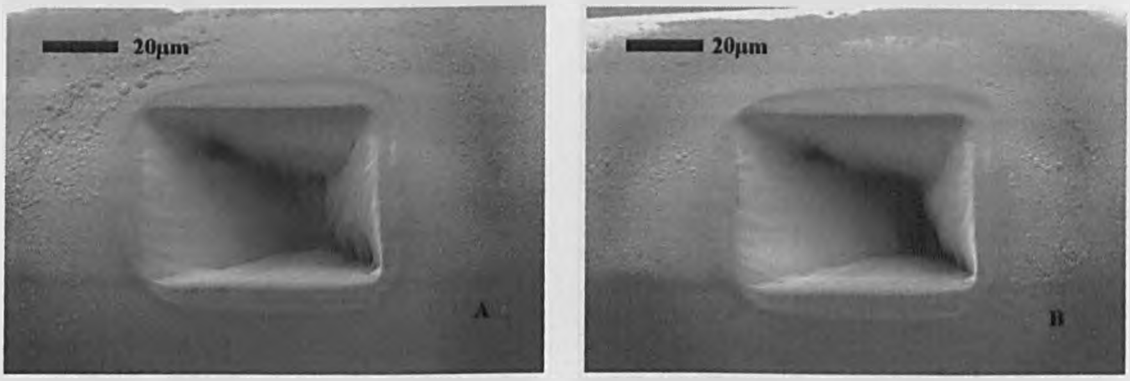

Figure 7.28: Top view of blind hole into fibre at (a) 1000 shots per area and (b) 4000 shots per area

Static mask - workpiece dragging

The effective interaction area of the mechanical side polished fibres is between 1 and 2 mm and this could possibly be machined with the static mask – workpiece dragging process. For this experiment a rectangular mask was selected which, when imaged, had the dimensions of 100 x 25 µm. The translation direction of the fibre was parallel to the long axis of the imaged mask. By using this smaller width mask, the rotational alignment of the fibre became less critical. In total three slots were machined the fluence, the laser repetition rate and the scanning length held constant at $H = 3$ J/cm^2, 10 Hz and $X = 3$mm but with different number of process passes (see Table 7.4).

Slot	Sample velocity [mm/min]	Process passes	Total number of laser pulses per area
1	0.5	2	240
2	0.5	4	480
3	0.5	6	720

Table 7.4 : Process conditions for fibre cladding static mask - workpiece dragging machining

Before processing, the fibre jacket was removed but no post process cleaning was carried out. Results were examined with an SEM and can be seen in Figure 7.29 to Figure 7.31 (fibre diameter = 125µm).

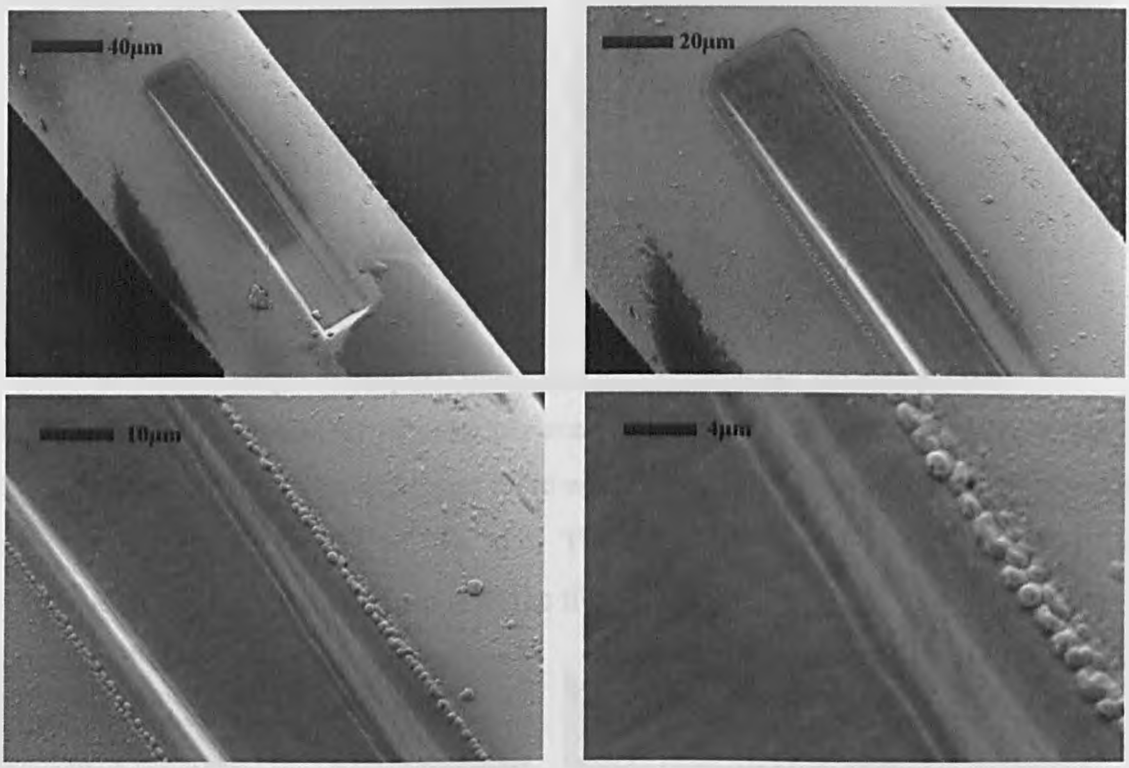

Figure 7.29: Slot 1 produced at sample velocity of 0.5mm/min, 2 process passes and 240 shots per area. Results seen at different magnifications.

A high surface smoothness was achieved on the bottom of the slot and there was no chipping on the edges of the slot. Debris was present on the non machined area of the fibre while the slot itself was debris free. The depth was estimated to be 10µm.

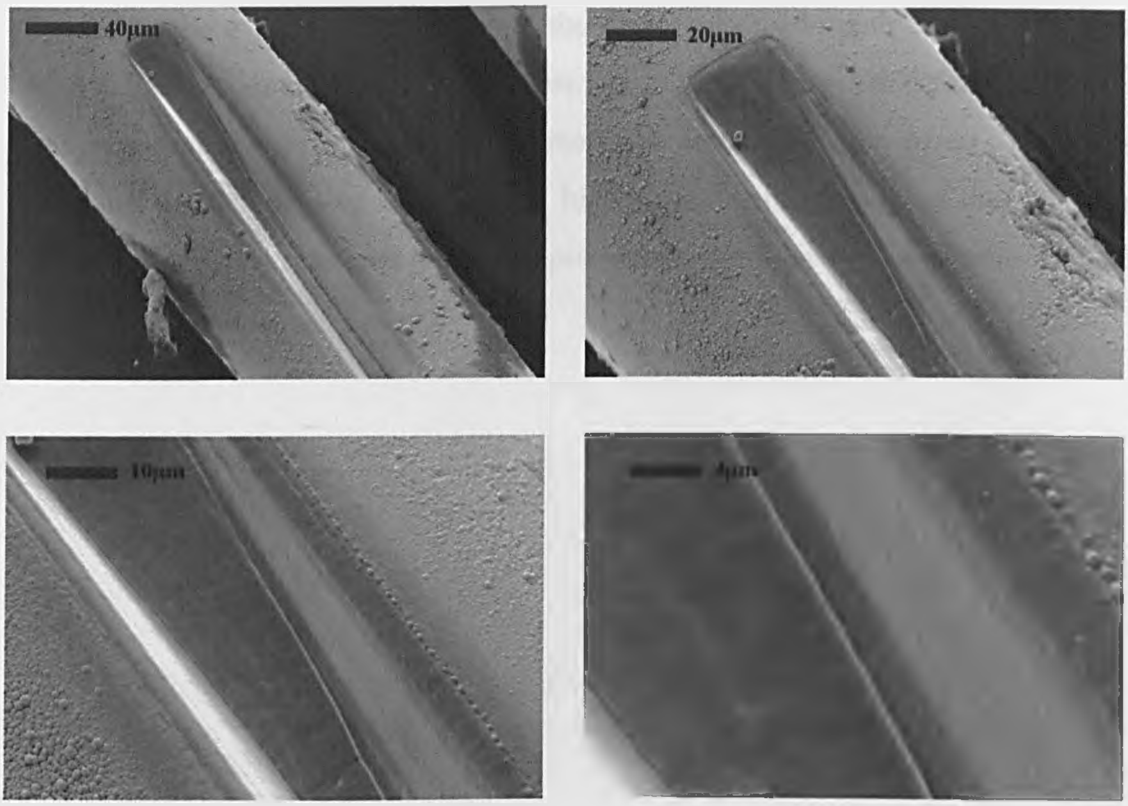

Figure 7.30: Slot 2 at sample velocity of 0.5mm/min, 4 process passes and 480 shots per area.

The doubling of the number of shots per area resulted in a slot with twice the depth of the previous sample, 20μm and again there was a high surface smoothness together with no chipping on the edges of the slot. The slot was however more tapered and consequently not as wide at 20μm as at the fibre surface.

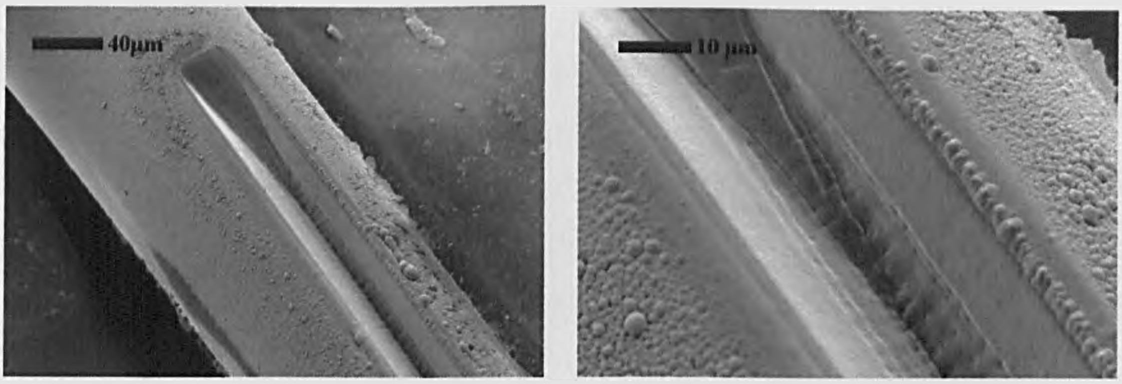

Figure 7.31: Slot 3 at sample velocity of 0.5mm/min, 6 process passes and 720 shots per area

Increasing the number of process passes to 6 and the total shots per area to 720 resulted in a triangular shape slot with a maximum depth of 25μm. No edge chipping occurred but a large amount of process debris was deposited on the non-machined area of the fibre though no debris was found within the slot.

To access the evanescent field within the fibre, a channel depth of 58µm is required with a flat bottom surface and optical surface quality. These could not be achieved in this experiment with the current fluorine laser mask projection system. The lack of chipping on the edges of the slots and high surface quality, suggest that this process warrant further development and could provide an alternative to the current mechanical process.

7.4 Discussion

The results presented show that the machining of deep structures into fused silica substrates with the 157nm laser results in a degree of taper angle of their sidewalls. This was seen in the tapered ridge waveguides, the pyramid shape of the blind holes and the triangular shape slots machined into the planar substrates and the optical fibres.

It has been difficult to predict in detail the shape of the three-dimensional structures formed by mask projection and normally an experimental route has to be followed to optimize these structure shapes. Attempts have been made to relate the taper angles to the incident fluence [63-65] but a model by Paterson *et. al.* [66] is able to make a prediction on the shape of the machined 3-D structures. The model calculates the radiation distribution on the incident surface and the effects it has on the material ablation. This calculation is repeated after each pulse fired with the position and shape of the new incident surface being the results of the previous calculation. A similar approach can be used to explain the profiles of the structures presented here, as the optical arrangement of the mask projection system and the ablation behavior of fused silica at different incident fluences are known.

The fluorine laser micromachining mask projection system consisted of two bi-prisms, placed longitudinally and axially in the incident laser beam, a field lens placed just in front of the mask and a Schwarzschild reflective objective (36x, 0.5NA). Due to the use of the two bi-prisms, the incident laser beam was divided into four separate beams, each with a quarter of the total laser beam energy and overlaid onto the mask plane to increase the beam uniformity. The angle, at which the bi-prisms were polished, was designed to refract the incident laser beam onto the mask under an angle that resulted in using the full numerical aperture of the projection system. A schematic drawing is presented in Figure 7.32.

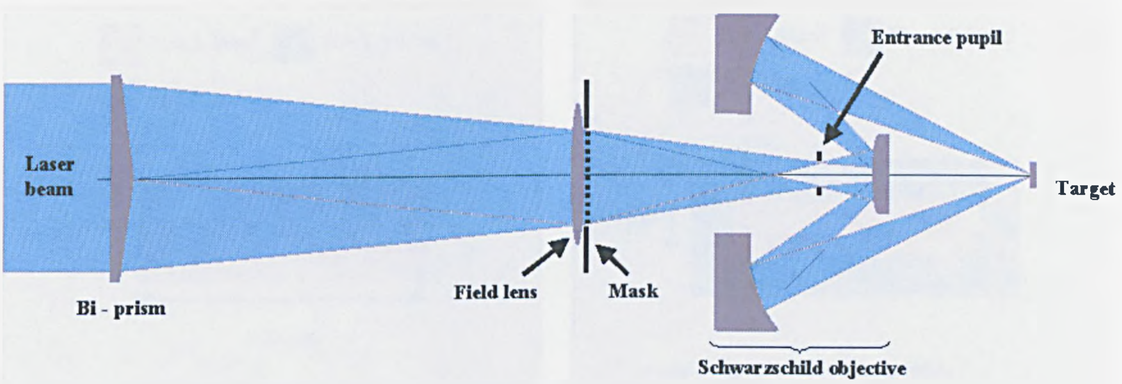

Figure 7.32: optical projection system of fluorine laser micromachining system

The two bi-prisms separated the incident radiation into four beams and as a result, the entrance pupil was filled with four beams and the image is formed by the four incident beams being overlaid at the image plane under the angle of the effective NA. As a result, the angle of the incident radiation the after the projection lens onto the fused silica substrates is 30° (see Figure 7.33).

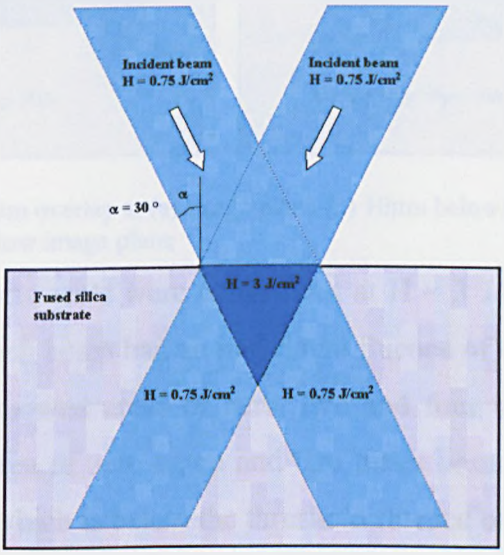

Figure 7.33: Incident laser beam radiation onto the substrate

When following the predicted aerial images at the image plane and further 10μm deeper steps into the fused silica substrate and away from the image plane, the overlap of the four separated incident beams can be identified. Due to the large angles of the incident beams, the full overlap of all four beams at the image plane decreases when getting deeper into the fused silica substrate, as can be seen in Figure 7.34.

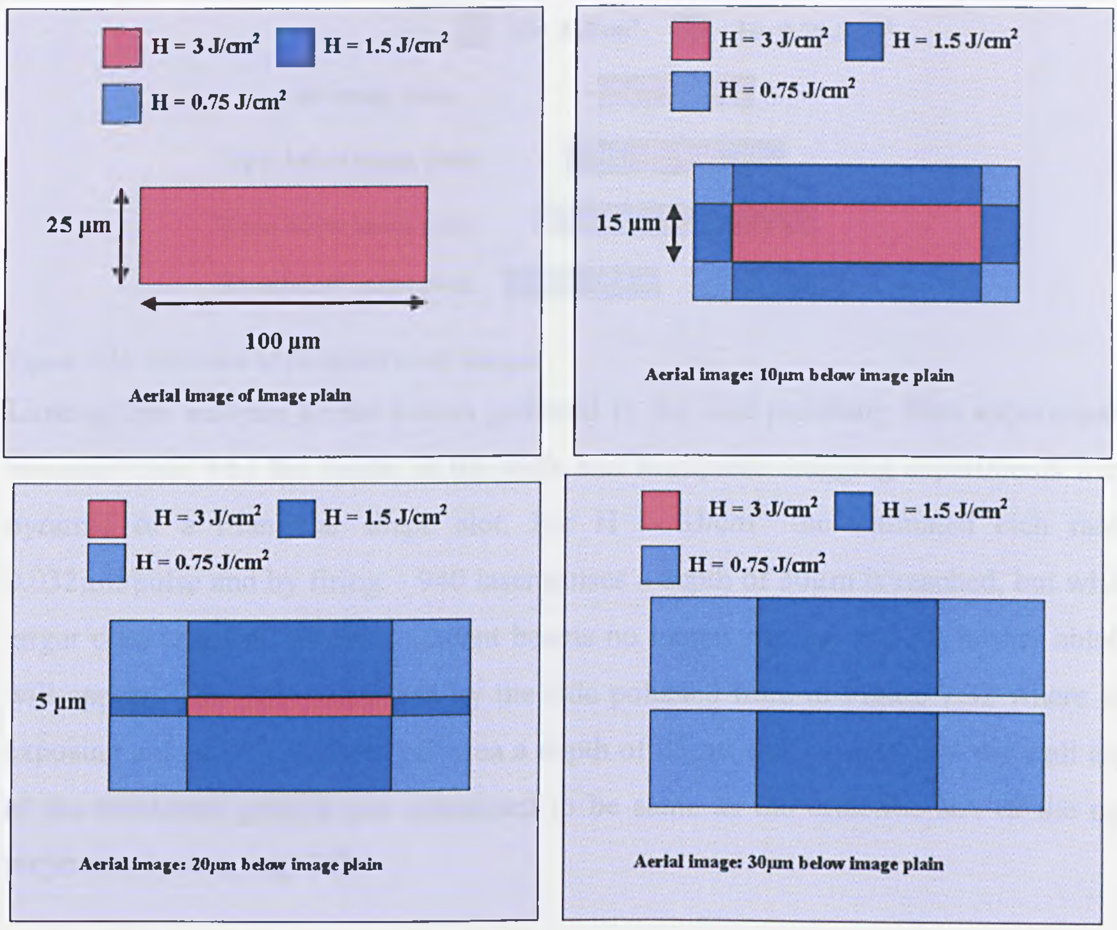

Figure 7.34: Incident laser beam overlap at (a) image plane (b) 10µm below image plane (c) 20µm below image plane and (d) 30µm below image plane

All micromachining experiments were carried out at $H = 3$ J/cm^2, the total of all four beams, and as a result, each beam had an individual fluence of $H = 0.75$J/cm^2. The aerial images of Figure 7.34 showed areas of zero, two and four times beam overlap. The incident fluence in the area of zero beam and two times beam overlap, were $H = 0.75$ J/cm^2 and $H = 1.5$ J/cm^2 which is below the threshold fluence of the fused silica. In these areas, no material will be removed and the only region where the incident fluence exceeds the threshold is where four incident beams overlap. When analyzing the aerial images from a side view, stacked on top of each other, it becomes clear that the area where four beams overlap is in the shape of a triangular, or in 3-D view, a pyramid (Figure 7.35).

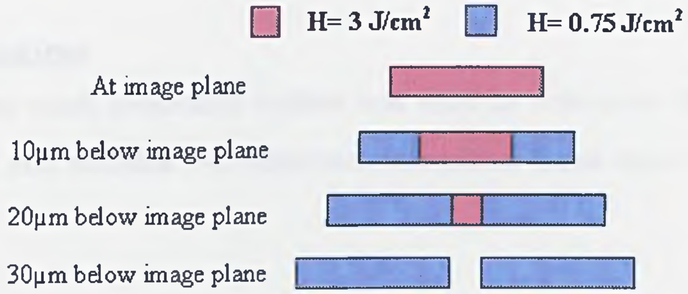

Figure 7.35: side view of predicted aerial images

Linking this analysis to the results gathered in the side polishing fibre experiment, it becomes clear why the results of the static and workpiece dragging experiments were a pyramid or a triangular shape slot. For H = $3J/cm^{2,}$ the estimated etch rate is 0.032µm/pulse and by firing ~ 940 laser pulses a depth of 30µm is reached, but when a larger dose is given, all four incident beams no longer overlap and no further ablation will appear. This was confirmed by the side polished fibre in Figure 7.32 where after exposing a dose of 720 shots per area a depth of 25µm was reached and the wall angle of the machined groove was calculated to be same as the effective NA of the mask projection system, e.g. 30°.

Reducing the effective numerical aperture of the mask projection system will reduce the angle of the incident beam on the substrate after the imaging lens, possibly allowing deeper structures to be machined. Alternatively, increasing the incident fluence by a factor of four provide a solution and as this should result in a negative taper angled wall profile more suitable for this application.

7.5 Conclusion

A fluorine laser mask projection system was used to determine the average etch rate versus fluence, and machine 3-D structures into planar fused silica samples and optical fibres.

A threshold fluence of H = 1.6-2 J/cm^2 was determined and with the determined thermal and optical parameters, see Table 7.5, an calculated threshold value was established, H = 1.23 J/cm^2.

Material parameter	**Laser radiation wavelength 157nm**
Effective absorption depth [μm]	0.4
Heat diffusion length during laser pulse duration $\sqrt{D\tau}$ [μm]	0.13
Calculated threshold fluence [J/cm^2]	0.12
Estimated threshold fluence [J/cm^2]	1.6 - 1.95

Table 7.5: Calculated and experimental etch rate data for Si ablated at three wavelengths

Plotting the ln(average etch rate per pulse) against inverse fluence showed that over most of the fluence range studied the material removal rate follows an Arrhenius type thermal model.

Two types of structures were machined in planar substrates (i) optical ridge waveguides and (ii) micro mirror structures. The ridge waveguides were machined via a step and repeat static mask – workpiece dragging process which allowed different width ridges by altering the substrate sidestep. Widths down to 4μm were possible but all ridges were tapered. Sidewall roughness of $< 1\mu m$ was determined with a SEM. Micromirrors were machined with the static mask – workpiece dragging process and the use of a triangular shaped mask. A surface roughness of $\leq 1\mu m$ was estimated for the directly machined mirror facet, while on the cleaved waveguide facet the surface roughness could not be quantified as the facet had a mirror smooth finish better than the resolution available on the SEM.

Fibre tip shaping and fibre side polishing was attempted on optical fibres. In fibre tip shaping, the core machined at a higher rate than the cladding, a result seen not only at 157nm but also with the 248nm KrF laser. The addition of germanium to the fibre core leads to a higher absorption of the incident radiation, resulting in a higher ablation rate. To side polish the optical fibre, blind rectangular holes and vertical slots were machined into the fibre cladding. The blind holes had pyramidal shape and a depth limit was reached; higher exposure dose did not result in deeper structures. The vertical slots machined to a depth of 10μm showed a smooth bottom surface but when deeper slots were attempted, the slots had a triangular shape.

In all machined structures a wall taper angle was present that prevented the machining of structures deeper than ~30μm. This was due to the mask projection system properties and can not be solved without increasing the incident fluence or changing the optical mask projection system to a lower NA.

7.6 References

1. Lutzke, D., "*Glasvezeltechniek, componenten, systemen en meettechnieken*" (Kluwer Technische boeken, 1989)
2. Henry, C. H., Blonder, G. E., Kazarinov, R. F., Glass waveguides on silicon for hybrid optical packaging, *J. Lightwave Tech.* 7, 1530-1539 (1989)
3. Okamoto, K., Recent progress of integrated optics planar lightwave circuits, *Opt. Quantum Electron.* 31, 107-129 (1999)
4. Janz, S., Balakrishnan, A., Charbonneau, S., Cheben, P., Cloutier, M., Delage, A., Dossou, K., Erickson, L., Gao, M., Krug, P. A., Lamontagne, B., Packirisamy, M., Pearson, M., Xu, D. –X, Planar waveguide Echelle gratings in silica-on-silicon, *IEEE Photon. Tech. Lett.*, 16, 503-505 (2004)
5. Ou, H., Hubner, J., Silica-on-silicon waveguide fabrication, *DOPS-NYT*, 2 39-42 (2001)
6. Kawashi, M., Silica waveguides on silicon and their application to integrated-optics components, *Opt. Quantum Elec.* 22, 391-416 (1990)
7. Takato, N., Yasu, M., Kawachi, M., Low-loss high silica single-mode channel waveguides, *Electron. Lett.* 22, 321-322 (1986)
8. Kilian, A., Kirchhof, J., Kuhlow, B., Przyrembel, G., Wischmann, W., Birefringe free planar optical waveguide made by flame hydrolysis deposition (FHD) through tailoring of the overcladding, *J. Lightwave Tech.* 18, 193-198 (2000)
9. Grand, G., Jadot, J. P., Denis, H., Valette, S., Fournier, A., Grouillet, A. M., Low-loss PECVD silica channel waveguides for optical communication, *Electron. Lett.* 26, 2135-2137 (1990)
10. Vallete, S., State of the art of integration optics technology at LETI for achieving passive optical components, *J. Mod. Opt.* 35, 993-1005 (1988)
11. Suzuki, S., Yanagisawa, M., Hibino, Y., Oda, K., High-density integrated planar lightwave circuits using SiO_2 – GeO_2 waveguides with a high refractive index difference, *J. Lightwave Tech.* 12, 790-796 (1994)
12. Verbeek, B. H., Henry, C. H., Olsson, N. A., Orlowsky, K. J., Kazarinov, R. F., Johnson, B. H., Integrated four-channel Mach-Zehnder multi/demultiplexer fabricated with phosphorous doped SiO_2 waveguides on Si, *J. Lightwave Technol.* 6, 1011-1015 (1988)

13. Bazylenk, M. V., Gross, M., Allen, P. M., Chu, P. L., Fabrication of low-temperature PECVD channel waveguides with significant improved los in the 1.50-1.55μm wavelength range, *IEEE Photon. Technol. Lett.* 7, 774 -776 (1995)
14. Leech, P. W., Faith, M. F., Johnson, C. M., Ridgway, M. C., Bazylenko, M., Channel waveguides formed by ion implantation of PECVD grown silica, *IEEE Proc. Optoelectron.* 144, 97-100 (1997)
15. Zaumer, D., Kulstad, K., Rathje, J., Svalgaard, M., Directly UV-written silica-on-silicon planar waveguides with low insertion loss, *Electron. Lett.* 34, 1582-1584 (1998)
16. Zaumer, D., Kulstad, K., Rathje, J., Svalgaard, M., Directly UV written silica-on-silicon planar waveguides with low loss, *Electron. Lett.* 33, 861-863 (1997)
17. Glezer, E. N., Milosavljevic, M., Huang, L., Finlay, R. J., Her, T.-H., Callan, J. P., Mzur, E., Three-dimensional optical storage inside transparent materials, *Opt. Lett.* 21, 2023-2025 (1996)
18. Miura, K., Jianrong, Q., Inouye, H., Mitsuyu, T., Hirao, K., Photowritten optical waveguides in various glasses with ultrashort pulse laser, *Appl. Phys. Lett.* 71, 3329-3331 (1997)
19. Will, M., Nolte, S., Chichkov, N., Tunnermann, A., Optical properties of waveguides fabricated in fused silica by femtosecond laser pulses, *Appl. Opt.* 41, 4360-4364 (2002)
20. Nasu, Y., Kohtoku, M., Hibino, Y., Low-loss waveguides written with a femtosecond laser for flexible interconnection in a planar light-wave circuit, *Opt. Lett.* 30, 723-723 (2005)
21. Horng, R. H., Chen, F., Wuu, D.S., Lin, T. Y., Refraction index behaviour of boron-doped silica films by plasma-enchanced chemical vapor deposition, *Appl. Surf. Sci.* 92, 387-390 (1996)
22. Heimala, P., Aarnio, J., Refractive index behaviour of phosphorus-doped planar silica waveguides, *J. Phys. D* 25, 733-739 (1992)
23. Jablonowski, D. P., Paek, U. C., Watkins, L. S., Optical fiber manufacturing techniques, *AT&T Tech. J.* 66, 33-44 (1987)
24. Walker, K. L., Directions in optical fibers, *AT&T Tech. J.* Nov/Dec, 92-100 (1990)

25. Markillie, G. A. J., Baker, H. J., Villarreal, F. J., Hall, D. R., The effect of vaporization and melt ejection on laser machining of silica glass micro-optical components, *Appl. Opt.* 41, 5660-5667 (2002)
26. Presby, H. M., Benner, A .F., Edwards, C. A., Laser micromachining of efficient fiber microlenses, *Appl. Opt.* 29, 2692-2695 (1990)
27. Paek, U. C., Weaver, A. L., formation of a spherical lens at optical fiber ends with a CO_2 laser, *Appl. Opt.* 14, 294-298 (1975)
28. Dimmick, T. E., Kakarantzas, G., Birks, T. A., Russell, P. S., Carbon dioxide laser fabrication of fused-fiber couplers and tapers, *Appl. Opt.* 38, 6845-6848 (1999)
29. Nowak, K. M., Baker, H. J., Hall, D. R., Pulses laser machining and polishing of silica micro-optical components using a CO_2 laser and an acousto-optic modulator, *Proc. SPIE* 4941, 15-19 (2002)
30. Grosse, A., Grewe, M., Fouckhardt, H., Deep wet etching of fused silica glass for hollow capillary optical leaky waveguides in microfluidic devices, *J. Micromech. Microeng.* 11, 257-262 (2001)
31. Koutny, L. B., Schmalzing, D., Taylor, T. A., Fuchs, M., Microchip electrophoretic immunoassay for serum cortisol, *Anal. Chem.* 68, 18-22 (1996)
32. Bazylenko, M. V., Gross, M., Gauja, E., Chu, P. L., Fabrication of light-turning mirrors in buries-channel silica waveguides for monolithic and hybrid integration, *J. Lightwave Tech.* 15, 148-153 (1997)
33. Bazylenko, M. V., Gross, M., Effect of reactive ion etching generated sidewall roughness on propagation loss of buried channel silica waveguides, *Appl. Phys. Lett.* 69, 2178-2180 (1996)
34. Ihlemann, J., Excimer laser abltion of fused silica, *Appl. Surf. Sci.* 54, 193-200 (1992)
35. Ihlemann, J. Wolff-rottke, B., Excimer laser micromachining of inorganic dielectrics, *Appl. Surf. Sci.* 106, 282-286 (1996)
36. Dyer, P.E., Farley, R. J., Giedl, R., Karnakis, D. M., Excimer laser ablation of polymers and glasses for grating fabrication, *Appl. Surf. Sci.* 96-98, 537-549 (1996)
37. Herman, P. R., Marjoribanks, R. S., Oettl, A. Chen, K., Konovalow, I., Ness, S., Laser shaping of photonics materials: deep-ultraviolet and ultrafast lasers, *Appl. Surf. Sci.* 154-155, 577-586 (2000)

38. Herman, P. R., Chen, K. P., Wei, M., Zhang, J., Ihlemann, J., Schafer, D., Marowsky, G., Oesterlin, P., Burghardt, B., F_2 – lasers: high resolution optical processing system for shaping photonics components, *Proc. SPIE* 4274, 149-157 (2001)
39. Temme, T., Ostendorf, A., Kulik, C. J., Machining of optical micromachining with 157nm laser radiation, *Proc. SPIE* 5063, 223-237 (2003)
40. Zhang, J., Herman, Lauer, C., P. R., Chen, K. P., Wei, M., 157-nm laser-induced modification of fused-silica glasses, *Proc. SPIE* 4274, 149-157 (2001)
41. Chen, K. P., Herman, P. R., Tam, R., Zhang, J., Rapid long-period grating formation in hydrogen-loaded fibre with 157nm F_2-laser radiation, *Electron. Lett.* 36, 2000-2001 (2000)
42. HPFS Fused Silica data sheet, www.corning.com
43. Dyer, P. E., Maswadi, S. M., Walton, C. D., Interaction if VUV F_2 laser radiation with glasses, *Proc. SPIE* 4760, 1088-1097 (2002)
44. Sugita, A., Kaneko, A., Okamoto, K., Very low insertion loss arrayed-waveguide grating with vertically tapered waveguides, *IEEE Photon. Tech. Lett.* 12, 1180-1182 (2000)
45. Ou, H, Engineering sidewall angles of silica-on-silicon waveguides, *Electron. Lett.* 40, 27-29 (2004)
46. Eisenstein, G., Korothy, S. K., Stulz, L. W., Veselka, J. J., Jopson, R. M., Hall, K. L., Antireflection coatings on lithium niobate waveguide devices using electron beam evaporated yttrium oxide, *Electron. Lett.* 21, 363-364 (1985)
47. Kincaid, B. E., Coupling of polarization-maintaining optical fibers ti Ti:$LiNbO_3$ waveguides with angled surfaces, *Opt. Lett.* 13, 425-427 (1988)
48. Ostendorf, A., The use of vacuum UV wavelenghts and ultrashort laser pulses for micromachining of dielectrics, *Proc. ICALEO 2000* 90, A1-A11 (2000)
49. Zhang, J., Herman, P. R., Lauer, C., Chen, K. P., Wei, M., 157nm laser induced modification of fused silica glasses, *Proc. SPIE* 4274, 125-132 (2001)
50. Kashyap, R., *"Fiber Bragg Gratings"* (Academic Press, 1998)
51. Pan, F., McCallion, K., Chiappetta, M., Waveguide fabrication and high speed in-line intensity modulation in 4-*N*, *N*-4'-dimenthylamino-4'-*N'*-methyl-stilbazolium tosylate, *Appl. Phys. Lett.* 74, 492-494 (1999)

52. Johnstone, W., Thrusby, G., Moodie, D., Varshney, R., Culshaw, B., Fiber optic wavelength channel selector with high resolution, *Electron. Lett.*, 28, 1364-1365 (1992)
53. Gloag, A., Langford, N., Macallion, K., Johnstone, W., Tunable erbium fiber laser using a novel overlay bandpass, *Opt. Lett.* 19, 801-803 (1994)
54. Bergh, R. A., Leferve, H. C., Shaw, H. J., Single-mode fiber-optic polarizer, *Opt. Lett.* 5, 479-481 (1980)
55. Ma, S. Min, S., High-performance side polished fibers and applications as liquid crystal clad fiber polarizers, *J. Lightwave Technol.* 15, 1554-1558 (1997)
56. Digonnet, M. J. F., Shaw, H. J., Analysis of tunable single mode optical fiber coupler, *IEEE J. Quantum electron.* QE-18, 746-754 (1982)
57. McCallion, K., Johnstone, W., Thrusby, G., Investigation of optical fiber switch using electro-optic interlays, *Electron. Lett.* 28, 410-411 (1992)
58. Herrero, A. A., Guerrero, H. Belenguer, T., Levy, D., High-sensitivity temperature sensor based on overlay on side-polished fibers, *IEEE Photon. Tech. Lett.* 12, 1043–1045 (2000)
59. Flannery, D., James, S. W., Tatam, R. P., Ashwell, G. J., pH sensor using Langmuir-Blodgett overlays on polished optical fibers, *Opt. Lett.* 22, 567-569 (1997)
60. Herrero, A. A., Guerrero, H., Levy, D., High-sensitivity of low relative humidity based on overlay on side-polished fibers, *IEEE Sensors J.* 4, 52-55 (2004)
61. Johnstone, W., Thrusby, G., Moodie, D., McCallion, K., Eiber-optic refractometer that utilizes multimode waveguides overlays devices, *Opt. Lett.* 17, 1538-1540 (1992)
62. Tseng, S., Chen, C., Side-polished fibers, *Appl. Opt.* 31, 3438-3447 (1992)
63. Kahlert, H-J., Sarbach, U., Burghardt, B., Klimt, B., Excimer laser illumination and imaging optics for controlled microstructure generation, *Proc. SPIE* 1835, 110-118 (1992)
64. Dyer, P. E., Jenkins, S. D., Sidhu, J., Development and origin of conical structures on XeCl laser ablated polymide, *Appl. Phys. Lett.* 49, 453-455 (1986)
65. Harvey, E. C., Rumsby, P. T., Gower, M. C., Remnant, J. L., Microstructuring by excimer laser, *Proc. SPIE* 2639, 266-277 (1995)
66. Paterson, C., Holmes, A. S., Smith, R. W., Excimer laser ablation of microstructures: A numerical model, *J. Appl. Phys.* 86, 6538-6546 (1999)

8 Long period gratings

8.1 Introduction

A Long Period Grating (LPG) is a transmission filter based on the interaction of a guided core mode with a periodic refraction index modulation. Due to the index modulation, core modes are converted into cladding modes and specific parts of the core mode spectrum are filtered out. Which spectral band is rejected depends on the grating period within the fibre [1]. Due to its selective spectral transmission loss characteristics, LPG are used as band-rejection filters [1] and as gain flattening filters (GFF) for uneven gain amplifiers such as Erbium doped fibre amplifiers (EDFA) [3]. Also, LPGs can be used as sensors [4] for temperature [5, 6], strain, load or radial bending measurements [7-10] and as chemical sensors [11, 12].

Several fabrication processes can be used to produce LPGs within optical fibres. A mechanical approach in which the LPG is produced by applying microbends to the optical fibre [13-15], or these can be induced by using electric discharge [16, 17] or ion implantation [18, 19] but the most common technique is using laser radiation. Several types of lasers have been used for writing LPGs; CO_2 [20-22], third harmonic Q-switched Nd-YAG [23], Femto second [24] and 157nm VUV devices [25], but mostly, UV laser radiation is employed.

The formation of a permanent grating within a fibre was first achieved by Hill *et. al.* [26, 27] and was created by launching Argon-ion laser radiation into a germanium doped fibre length. During the exposure, the intensity of the back reflection grew to almost 100%, caused by the creation of an in-fibre grating; a standing wave was created within the fibre by interference between the back reflection from the end of the fibre and the incoming radiation. At each constructive interference maximum, a permanent index change was produced because of the photosensitivity of the Ge-doped fibre core and resulted in a grating. The change of the refraction index of the fibre core within these so-called "*Hill gratings*" was suggested to be based on a two-photon process. In this arrangement the grating period is restricted to that defined by the laser wavelength

$d = \frac{\lambda}{2n}$ (e.g. for the Argon-ion laser with λ = 488nm). The key improvement came when the fibre was irradiated from the side with a wavelength of λ = 244nm. The refractive index change became more efficient as the photosensitivity was based on a single photon process. Additionally the grating period created within the fibre was not restricted to that of the standing wave but could be varied by a holographic interference of two UV light beams incident on the side of the fibre [28].

8.1.1 Photosensitivity

Photosensitivity in fibres refers to a permanent change in the refractive index produced by optical exposure. At first photosensitivity was thought to only happen in Ge-doped fibres. It was believed that the GeO related defects in the Ge-doped core were responsible for the refractive index change, especially as the number of these defects increased as a function of the Ge-concentration. However, this explanation turned out to be inadequate as photosensitivity was also observed in non Ge-doped fibres. Currently the understanding is that photosensitivity is a function of several mechanisms; (i) photochemical, (ii) photomechanical and (iii) thermochemical [29, 30].

Three different technologies have been developed to enhance the photosensitivity of Ge-doped optical fibres; (i) hydrogen loading, (ii) flame brushing and (iii) co-doping.

Hydrogen loading

In the hydrogen loading photosensitivity enhancement technique, a standard optical fibre is soaked in hydrogen gas in a high pressure. During this process, hydrogen molecules diffuse into the fibre and it is thought due to UV exposure during the writing process, the hydrogen molecule dissociates. This forms Si and Ge based OH bonds and deficient centers which result in a refractive index change. This technology achieves the highest index change by UV radiation [31].

Flame Brushing

Flame brushing is a technique used to enhance the photosensitivity of the fibre locally and is achieved by repeated exposing the optical fibre with a flame, fuelled by hydrogen and a small amount of oxygen. At a flame temperature of ~1700°C, the hydrogen diffuses very quickly into the fibre and reacts with the germanosilicate glass to create a strong absorption band at 240nm [32].

Co-doping

Adding a co-dopant to the germaniosilicate fibre also resultes in an increase in photosensitivity. In particular, Boron has proven to lead to a four-fold increase in saturation index above the standard Ge-doped fibre. Another advantage is that co-doping decreases the refraction index and allows a larger Ge doping without an increase in index contrast between the core and the cladding [33].

8.1.2 Long period grating inscription techniques

Interferometric inscription techniques are mainly used for writing grating based reflection filters, known as Fibre Bragg Gratings (FBG), as the required grating is of the order of the reflected radiation wavelength i.e. around 1500nm. To inscribe FBG into optical fibres, several techniques can be used of which the phase mask interference technique is the most common [29, 30].

For LPGs the grating period is usually larger (Λ= 400μm) than with a FBG. LPGs are mainly inscribed by using amplitude masks in a proximity exposure setup. In this technique, a line spacing mask with the desired grating period is placed against the optical fibre and a UV laser beam exposes the mask, in static or scanning mode. Mask projection systems have also been used to inscribe FBG in optical fibres [34] and should also be able to be used to inscribe LPGs. The pattern for a LPG could be defined onto a mask which is then imaged onto the fibre. This method could possibly remove the need for proximity exposure and the interference of the mask with the fibre. For the inscription of multiple LPGs in a fibre, the different mask patterns needed could be manufactured onto a larger size mask and moving this mask would allow the inscription of a different LPG. In view of these advantages the feasibility of inscribing LPGs into optical fibre with mask projection was investigated. Process parameters were determined and then an attempt was made to produce a combined LPG in one fibre.

8.2 Long period gratings by mask projection

The grating period, the incident fluence and the exposure dose were determined in separate experiments. With a large field 5x, 0.13NA projection system, installed on the KrF excimer laser mask projection system, periodical line spacing patterns were imaged onto a 'Fibercore' PS1250 photosensitive single mode fibre. The exposure wavelength was 248nm. The incident fluence at the fibre could be varied between 50mJ/cm^2 and 500mJ/cm^2, and all exposures were made at a pulse repetition rate of 50Hz.

The effect on the fibre transmission spectrum was monitored *'in situ'* during writing. This involved connecting the 2 meter long photosensitive fibre to a broadband Anritsu Corp. laserdiode (P_{max} = -0.17dBm at λ_c = 1557 ± 70nm) and a spectrum analyser (Agilent 86140B) with bare fibre connectors and pigtails. Index matching gel was used between the fibre and the pigtails to ensure a low loss connection. An area of the fibre jacket was removed by mechanical stripping and then cleaned with isopropanol. To allow the fibre to be handled without breakage and to provide a stable platform for the exposures, the fibre was attached to a microscope slide using easily removable adhesive. An alignment ridge was added to a stage chuck which, together with further alignment marks, ensured the correct positioning of the stripped fibre within the 10 x 1 mm laser beam area. The fibre was positioned to the correct image height by observing and adjusting the fibre under an alignment camera which was set to the same mask image plane as the projection system. The optical fibre was positioned into the image plane by adjusting the z-axis until a sharp image of the cladding was achieved. By moving the fibre back under need the imaging lens, the fibre will be placed at the correct image height position.

During the experiments the transmission spectrum was monitored after each dose of 1000 laser pulses without disrupting the position of the stripped fibre. Before exposing the fibres, an absolute transmission spectrum was measured and used to normalize the subsequent results.

8.2.1 Line spacing mask

The period of the LPG defines which part of the input spectra is filtered. Calculations on which grating period is required to filter a specific spectral feature can be made [1] but for the purpose of this experiment, grating periods whose filtering effect was already known within a single mode fibre were used. [2]

Six different periodical line spacing patterns were imaged onto the photosensitive fibre from a chrome-on quartz mask and are presented in Table 8.1.

Mask	Mask plane		Image Plane	
	Line width [mm]	Period [mm]	Line width [mm]	Period [mm]
1	1.2	2.4	0.24	0.48
2	1.1	2.2	0.22	0.44
3	1.0	2.0	0.2	0.4
4	0.9	1.8	0.18	0.36
5	0.8	1.6	0.16	0.32
6	0.6	1.2	0.12	0.24

Table 8.1: Line spacing of chrome-on-quartz mask and size at image for LPG mask projection

The fluence was set to H = 300mJ/cm^2 and after each 1000 laser pulses, the transmission spectrum was measured. After normalization, the transmission spectrum of each exposed mask pattern was plotted (Figure 8.1).

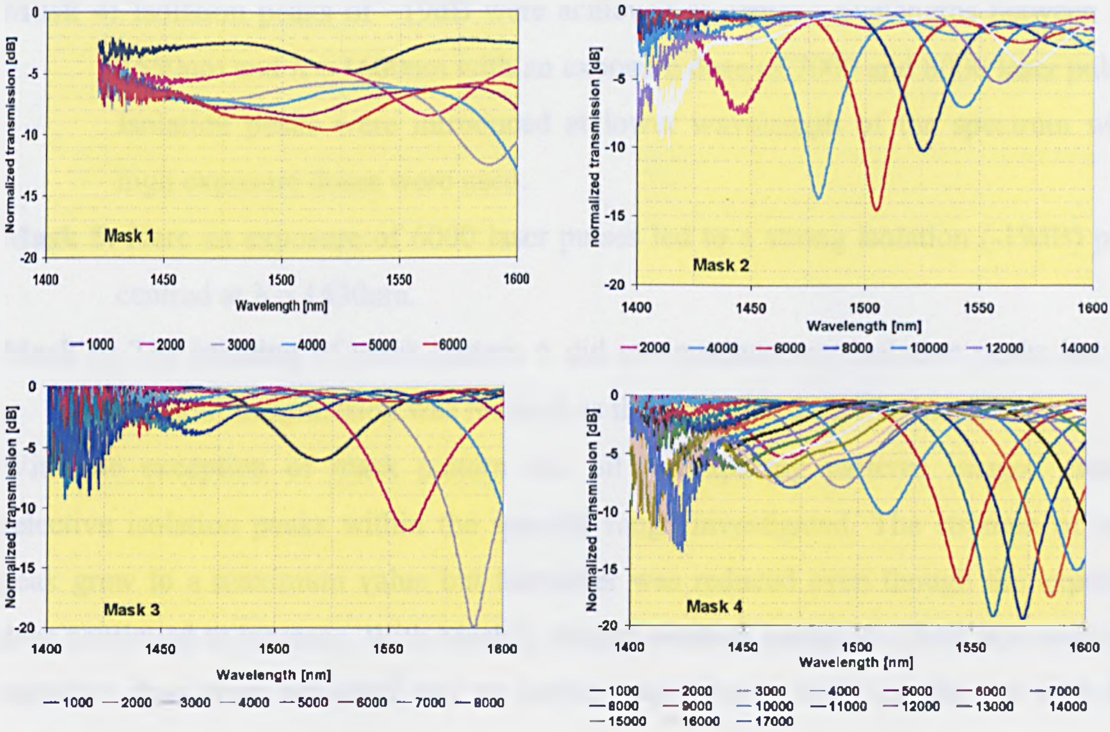

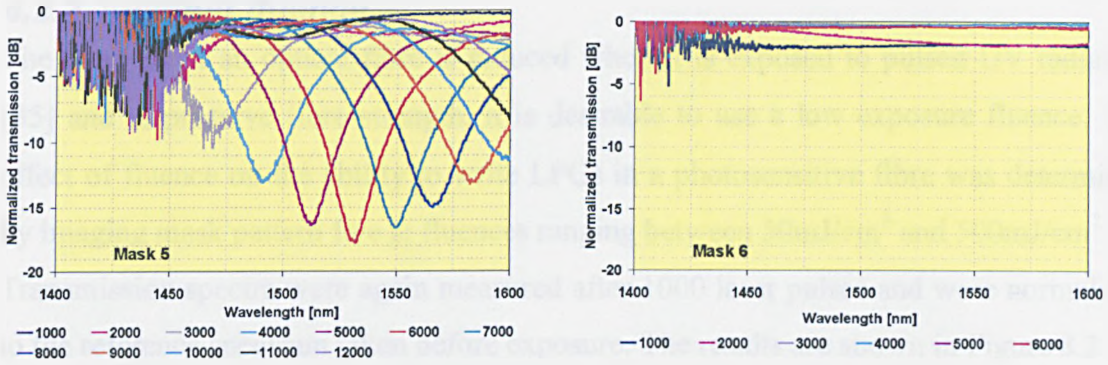

Figure 8.1: Normalized transmission vs photon wavelength for mask patterns 1 to 6 measured after exposure to 1000 pulses.

Mask 1: The selective filtering appeared after 1000 laser pulses at a center wavelength position of 1525nm and shifted towards longer wavelengths as the exposure dose was increased.

Mask 2: A growth and then reduction in the strength of the isolation peak occured while the position of the center wavelength became larger as the exposure dose was increased. At the highest exposure dose, with 14000 laser pulses, two isolation peaks occurred, one at $\lambda_c = 1415$nm and one at 1575nm.

Mask 3: Strong isolation peaks at a low number of laser pulses were produced in this case. At the highest exposure dose, a smaller isolation peak became visible in the lower wavelength region of the scanned spectral range.

Mask 4: Isolation peaks of –19dB were achieved at center wavelengths between $\lambda =$ 1550nm and $\lambda =$ 1600nm with an exposure dose of 7000 and 8000 laser pulses. Isolation peaks were introduced at lower wavelength of the spectrum when high exposure doses were used.

Mask 5: Here an exposure of 6000 laser pulses led to a strong isolation (-19dB) peak centred at $\lambda =$ 1530nm.

Mask 6: The imaging of mask pattern 6 did not produce any isolation peaks but the overall transmission was reduced as the exposure dose was increased.

With the exception of mask pattern six, all line spacing patterns imaged created selective isolation peaks within the spectral range investigated. The strength of each peak grew to a maximum value but thereafter was reduced even though the exposure dose continued to increase. With Mask 5, strong isolation peaks of –18dB at a moderate exposure dose were achieved and so further experiments were carried out with this mask pattern.

8.2.2 Incident fluence

The strength of an optical fibre is reduced when it is exposed to pulsed UV radiation [35] and to preserve fibre strength, it is desirable to use a low exposure fluence. The effect of fluence on the ability to write LPGs in a photosensitive fibre was determined by imaging mask pattern five at fluences ranging between 50mJ/cm^2 and 500mJ/cm^2. Transmission spectra were again measured after 1000 laser pulses and were normalized to the reference spectrum taken before exposure. The results are shown in Figure 8.2.

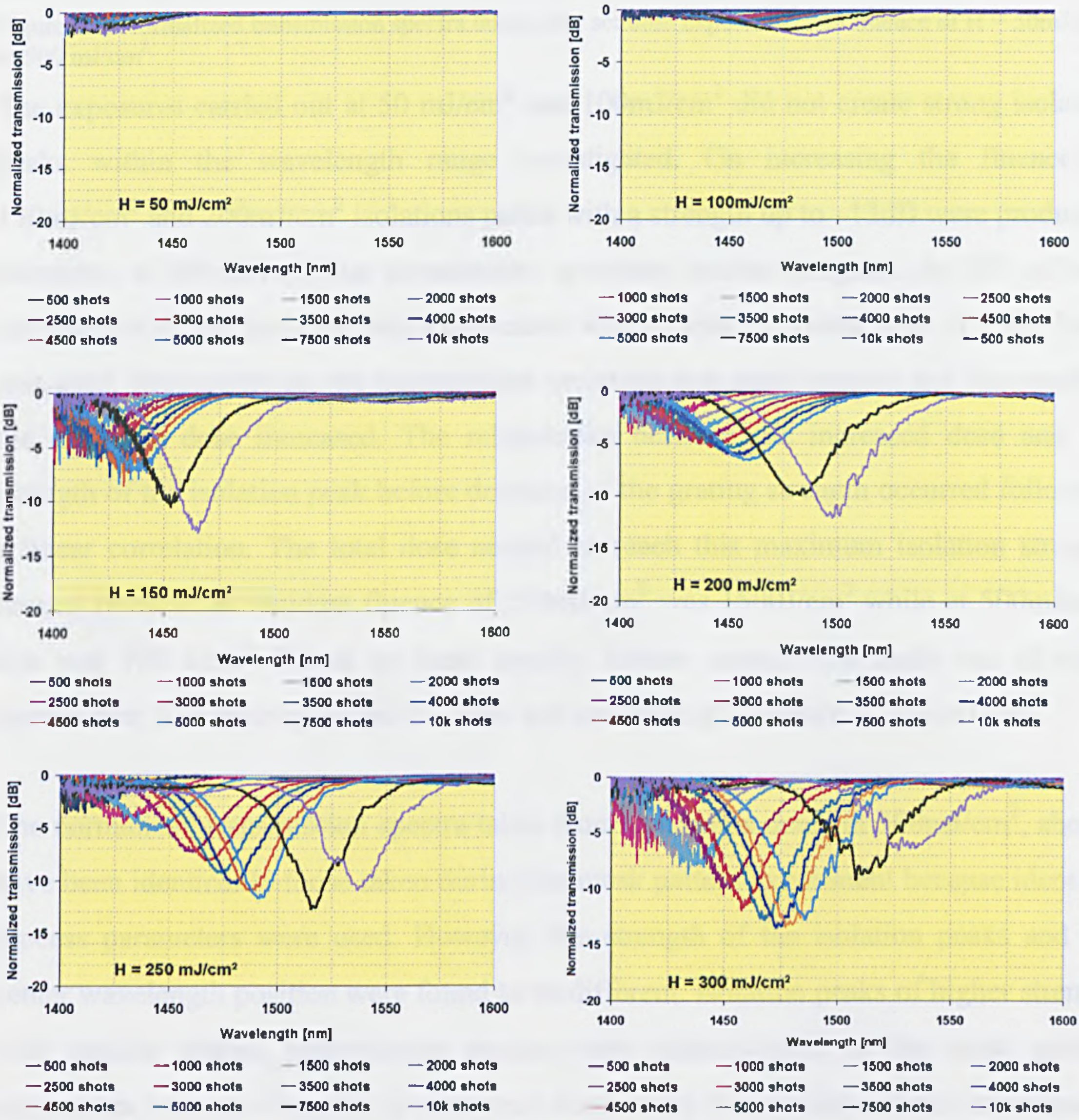

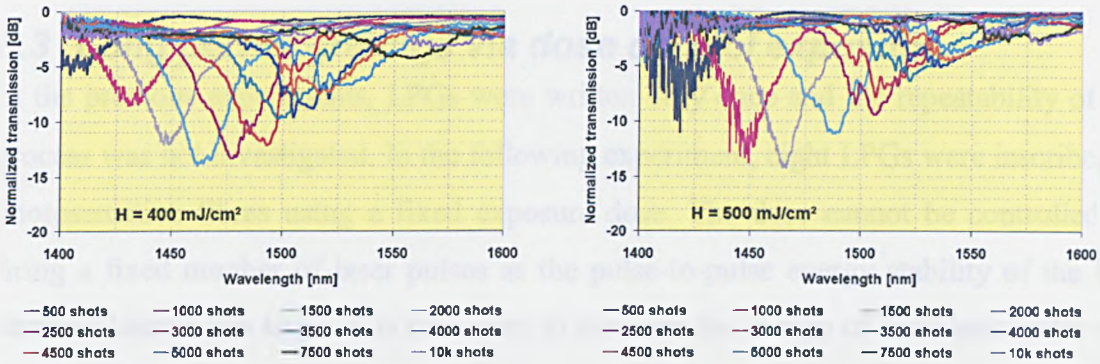

Figure 8.2: Normalized transmission spectra taken after set dose exposures at an fluence of H = 50mJ/cm^2 to 500 mJ/cm^2

The exposures carried out at 50 mJ/cm^2 and 100mJ/cm^2 did not create strong isolation peaks within the wavelength range investigated. On increasing the fluence to 150mJ/cm^2 and 200mJ/cm^2 isolations peaks with a strength up to –13dB were produced. However, at 200mJ/cm^2, the transmission spectrum became irregular. At 250 mJ/cm^2, the strength of the isolation peaks decreased when a total exposure dose of 2500 J/cm^2 was used. Irregularity on the transmission spectrum was again present and increased as the exposure dose increased. The relationship between the increased dose and the strength of the isolation peak before decrease of the grating strength occurred following a linear correlation. The total dose needed to reach this maximum isolation strength turning point at an incident fluence of 250mJ/cm^2 was 1500J/cm^2 while at 500mJ/cm^2 this was 750 J/cm^2. Based on these results, further experiments made use of mask pattern five; line spacing period 0.32mm and exposure at a fluence of 250 mJ/cm^2.

The normalized transmission spectra taken from exposures made at 300mJ/cm^2, should have been identical to those taken during the mask pattern experiment because identical process parameters were used. However, the strength of the isolation peaks and the center wavelength position were found to be different. Isolation peaks of higher strength with regular shaped transmission spectra were characteristic of the mask pattern experiment whereas irregular spectra were seen in the fluence dependence experiment, with reduced isolation peak strength. As the filtering effect of the long period grating is not only related to the grating period but also the type of fibre, it is possible that the fibre had different degrees of photosensitivity.

8.3 Long period gratings via dose control exposure

In the previous experiments, LPGs were written only once and the repeatability of the process was not investigated. In the following experiment, eight LPGs were inscribed in photosensitive fibres using a fixed exposure dose. The dose cannot be controlled by firing a fixed number of laser pulses as the pulse-to-pulse energy stability of the KrF excimer laser is too large. It is necessary to measure the energy of each laser pulse and stop the exposure once the accumulated energy delivered reaches a pre set value. For this purpose the experimental setup previously used was upgraded with an automated dose control consisting of (i) an energy monitor, (ii) dose control software and (iii) an external excimer laser trigger. A plane parallel fused silica plate was positioned before the first homogenizer array and placed at an angle of 45° to the incident laser beam. The reflection from the surface of this is plate was detected by an energy monitor (Molectron, LP-8, R=845V/J), which was cross calibrated with the pulse energy measured at the image plane. The detector output was monitored by the dose control software which stopped the exposure when the accumulated energy reached the pre set exposure dose.

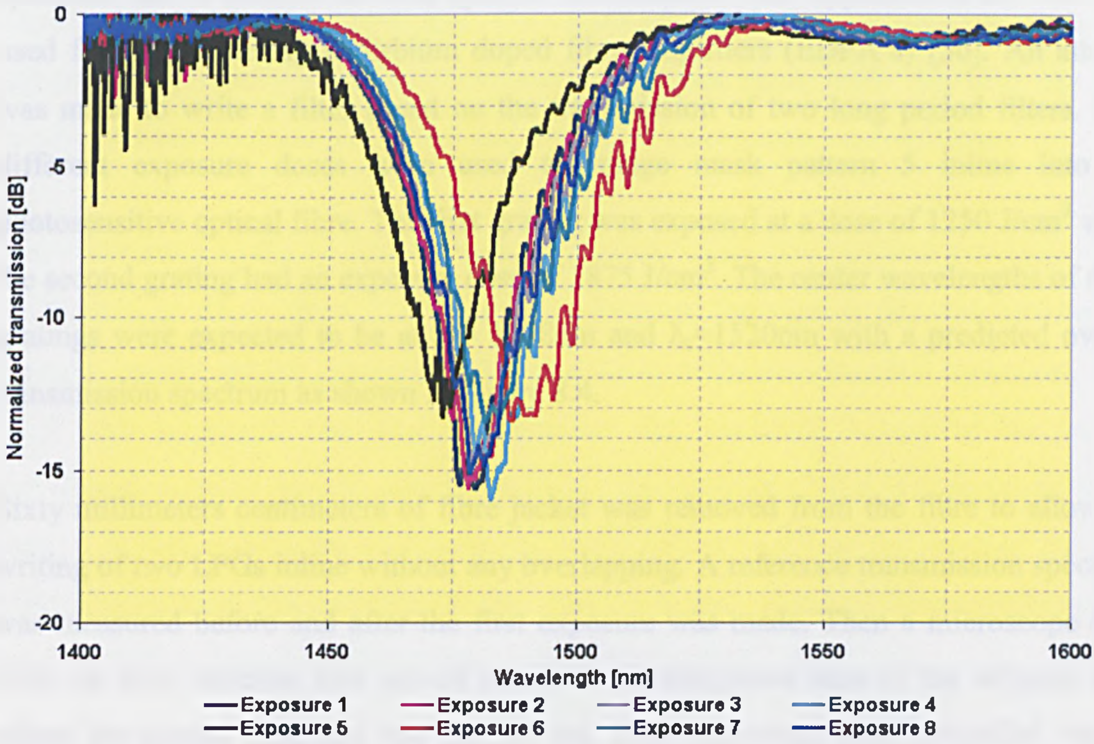

Figure 8.3: Transmission spectra of eight exposed LPGs with dose control operating on the exposure.

For this experiment, mask pattern 5 was used and the fluence at the optical fibre position was set to 250mJ/cm^2. The exposure dose for each fibre was set at 1000 J/cm^2. In total, eight Fibercore PS 1250 photosensitive fibres were exposed and their transmission spectra were measured before and after the exposure. After normalization, these were plotted against the scanning wavelength (Figure 8.3).

Variations in isolation strength as well as center wavelength position were seen when the transmission spectra of all eight exposures are compared. The maximum deviation of the center wavelength position was $\Delta\lambda \sim$ 16nm while a difference of 2dB was measured in the various isolation strengths. Comparing this result with incident fluence experiments with 250mJ/cm^2, it was found that the center wavelength position is comparable but the strength of the isolation achieved with the dose control experiment was stronger.

8.4 Combined long period grating transmission filter

As seen previously, the long period grating can be used as a spectrally selective loss element in transmission mode. By combining different LPGs in one optical fibre, the spectrum can be tailored towards specific transmission filter applications and has been used for gain flattering in Erbium doped fibre amplifiers (EDFA's) [36]. An attempt was made to write a filter based on the transmission of two long period filters. Two different exposure doses were used to image mask pattern 5 inline into the photosensitive optical fibre. The first grating was exposed at a dose of 1250 J/cm^2 while the second grating had an exposure dose of 1875 J/cm^2.. The center wavelengths of these gratings were expected to be at λ_c= 1488nm and λ_c=1520nm with a predicted overall transmission spectrum as shown in Figure 8.4.

Sixty millimeters centimeters of fibre jacket was removed from the fibre to allow the writing of two LPGs inline without any overlapping. A reference transmission spectrum was measured before and after the first exposure was made. Then a microscope slide with the fibre attached was moved across to an unexposed area of the stripped fibre where the second exposure was carried out. Both exposures were controlled via the integrated dose controller. After the second exposure, the transmission spectrum was measured and after normalization, plotted against the scanned wavelength Figure 8.4.

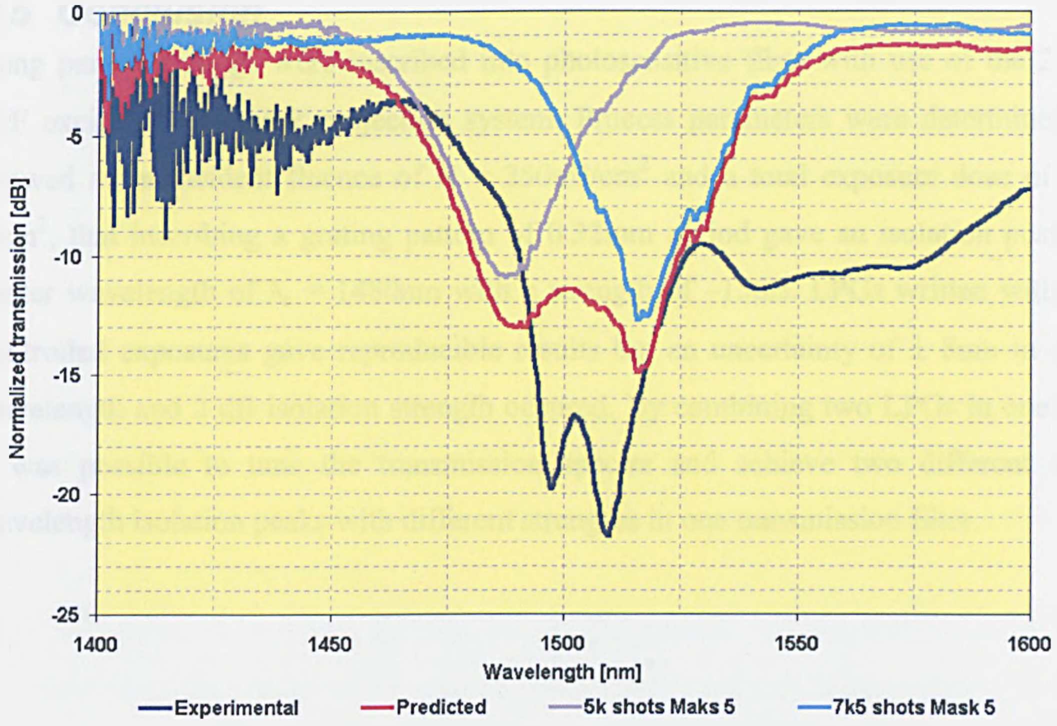

Figure 8.4: Normalized transmission of exposed combined long period gratings within one optical fibres compared to the predicted transmission spectra.

The transmission spectrum of the combined LPG showed two different isolation center wavelengths and isolation strengths. The values predicted by combining the two earlier independently recorded transmission spectra did not agree with the dual exposure spectrum; both the grating isolation and the center wavelength were different.

The uncertainty of the central wavelength position in the dose control experiment was determined as $\Delta\lambda \sim$ 16nm. The difference of central wavelength position between the predicted value and the measured value was for both the concatenated exposures, $\Delta\lambda \sim$ 8nm, and suggested that the experimental and predicted values of the central wavelength position were in agreement within the uncertainty of this experiment. In the case of isolation strength, an agreement could not be found as the error of the dose control experiment was estimated to be ~ 2dB while the isolation difference between the experimental and predicted value was, in both exposures, 5 dB.

8.5 Conclusion

Long period gratings were inscribed into photosensitive fibre with use of the 248nm KrF excimer laser mask projection system. Process parameters were determined and showed at an incident fluence of H = 250mJ/cm^2 and a total exposure dose of 1000 J/cm^2, that inscribing a grating pattern of 0.32mm period gave an isolation peak at a center wavelength of λ_c = 1480nm with a strength of –15dB. LPGs written with dose controlled exposures gave reproducible results but an uncertainty of ± 8nm in center wavelength and 2 dB isolation strength occured. By combining two LPGs in one fibre, it was possible to tune the transmission spectra and achieve two different center wavelength isolation peaks with different strengths in one transmission filter.

8.6 References

1. Erdogan, T., Fiber grating Spectra, *J. Lightwave Technol.* 15, 1277-1291 (1997)
2. Vensarkar, A. M., Lemaire, P. J., Judkins, J. B., Bhatia, V., Erdogan, T., Sipe, T. E., Long-period gratings as band-rejection filters, *J. Lightwave Technol.* 14, 58-65 (1996)
3. Vensarkar, A. M., Pedrazzani, J. R., Judkins, P. J., Lemaire, A. M., Long-period fiber-grating-based gain equalizers, *Opt. Lett.* 21, 336-338 (1996)
4. James, S. W., Tatam, R. P., Optical fibre long-period grating sensors: characteristics and applications, *Meas. Sci. Technol.* 14, R49-61, (2003)
5. Bhatia, V., Vengsarkar, A. M., Optical fiber long-period grating sensors, *Opt. Lett.* 21, 692-694 (1996)
6. Mizunami, T., Fukuda, T., Hayashi, A., Fabrication and characterization of long-period-grating temperature sensors using Ge-B-co-doped photosensitive fibre and single mode fibre, *Meas. Sci. Technol.* 15, 1467-1473 (2004)
7. Bhatia, V., Campbell, D., Claus, R. O., Vengsarkar, A. M., Simultaneous strain and temperature measurement with long-period gratings, *Opt. Lett.* 22, 648-650 (1997)
8. Liu, Y., Zhang, L., Bennion, I., Fibre optical load sensors with high transverse strain sensitivity based on long-period gratings in B/Ge co-doped fibre, *Electron. Lett.* 35, 661-663 (1999)
9. James, S. W., Tatam, R. P., Simultaneous temperature and bend sensing with long-period fiber gratings, *Opt. Lett.* 25, 1007-1009 (2000)
10. Rego, G., Marques, P.V.S., Salgado, H.M., Santos, J. L., Simulataneous measurement of temperature and strain based on arc-induced long-period fibre gratings, *Electron. Lett.*41, 60-62 (2005)
11. Thomas Lee, S., Dinesh Kumar, R., Suresh Kumar, P., Radhakrishman, P., Vallabhan, C. P. G., Nampoori, V. P. N., Long period gratings in multimode optical fibres: application in chemical sensing, *Opt. Commun.* 224, 237-241 (2003)
12. Chen, X., Zhou, K., Zhang, L., Bennion, I., Optical chemsensors utilizing long-period fibers gratings UV inscribed in D-fiber with enhanced sensitivity through cladding ethcing, *IEEE Photon. Tech. Lett.* 16, 1352-1354 (2004)

13. Savin, S., Digonnet, M. J. F., Kino, G. S., Shaw. H. J., Tunable mechanically induced long-period fiber gratings, *Opt. Lett.* 25, 710-712 (2000)
14. Sohn, I-B., Beak, J-G., Lee, N-W., Kwon, H-W., Song, J-W., Gain flattened and improved EDFA using microbending long-period fibre gratings, *Electron. Lett.* 38, 1324-1325 (2002)
15. Sohn, I-B., Song, J-W., Gain flattened and improved double-pass two stage EDFA using microbending long-period fiber gratings, *Opt. Commun.*236, 141-144 (2004)
16. Hwang, I. K., Yun, S. Y., Kim, B. Y., Long-period fiber gratings based on periodic microbends, *Opt. Lett.* 24, 1263-1265 (1999)
17. Palai, P., Styanarayan, M. N., Das, M., Thyagarajan, K., Pal, B. P., Characterization and simulation of long period gratings fabricated using electric discharge, *Opt. Comm.*193, 181-185 (2001)
18. Fujimaki, M., Ohki, Y., Brebner, J. L., Roorda, S., Fabrication of long-period optical fiber gratings by use of ion implantation, *Opt. Lett.* 25, 88-91 (2000)
19. Von Bibra, , M. L., Roberts, A., Fabrication of long-period fiber gratings by use of focused ion-beam irradiation, *Opt. Lett.* 26, 765-767 (2001)
20. Davis, D. D., Gaylord, T. K., Glytsis, E. N., Kosinski, S. G., Mettler, S. C., Vengsarker, A. M., Long-period fibre grating fabrication with focused CO_2 laser pulses, *Electron. Lett.* 34, 302-303 (1998)
21. Davis, D. D., Gaylord, T. K., Glytsis, E. N., Mettler, S. C., Very-high-temperature stable CO_2-laser induced long-period fibre gratings, *Electron. Lett.* 35, 40-41 (1999)
22. Rao, Y. J., Zhu, T., Ran, Wang, Y. P., Hu, A. Z., Novel long-period fiber gratings written by high-frequency CO_2 laser pulses and applications in optical fiber communication, *Opt. Commun.* 229, 209-221 (2004)
23. Blows, J., Tang, D. Y., Gratings written with tripled output of Q-switched Nd-YAG laser, *Electron. Lett.* 36, 1837-1838 (2000)
24. Kondo, Y., Nouchi, K., Mitsuyu, T., Watanabe, M., Kazansky, P. G., Hirao, K., Fabrication of long-period fiber gratings by focused irradation of infrared femtosecond laser pulses, *Opt. Lett.* 24, 646-648 (1999)

25. Chen, K. P., Herman, P. R., Zhang, J., Fabrication of strong long-period gratings in hydrogen-free fibers with 157nm F_2 laser radiation, *Opt. Lett.* 26, 771-773 (2001)
26. Hill, K. O., Fujii, Y., Johnson, D. C., Kawasaki, B. S., Photosensitivity in optical fibre waveguides: Application to reflection filter fabrication, *Appl. Phys Lett.* 32, 647-649 (1978)
27. Kawasaki, B. S., Hill, K. O., Johnson, D. C., Fujii, Y., Narrow-band Bragg reflectors in optical fibers, *Opt. Lett.* 3, 66-68 (1978)
28. Meltz, G., Morey, W. W., Glenn, W. H., Formation of Bragg gratings in optical fibers by a transverse holographic method, *Opt. Lett.* 14, 823-825 (1989)
29. Othonos, A., Kalli, K., *"Fiber Bragg Gratings"* (Artech House, 1999)
30. Kashyap, R., *"Fiber Bragg Gratings"* (Academic Press, 1998)
31. Lemaire, P. J., Atkins, R. M., Mizrahi, V., Reed, W. A., High pressure H2 loading as a technique for achieving ultrahigh UV photosensitivity and thermal sensitivity in GeO2 doped optical fibres, *Electron. Lett.* 29, 1191-1193 (1993)
32. Bilodeau, F., Malo, B., Albert, J., Johnson, D., Hill, K., Hibino, Y., Abe, M., Kawachi, M., Photosensitization of optical fiber and silica-on-silicon/silica waveguides, *Opt. Lett.* 18, 953-955 (1993)
33. Williams, D. L., Ainslie, B. J., Armitage, J. R., Kashyap, R., Campbell, R., Enhanced UV photosensitivity in boron codoped germanosilicate fibres, *Electron. Lett.* 29, 45-47 (1993)
34. Mihailow, S. J., Gower, M. C., Recording of efficient high-order BRAGG reflectors in optical fibres by mask image projection and single pulse exposure with an excimer laser, *Electron. Lett.* 30, 707-708 (1994)
35. Barber, D. A., Rizvi, N. H., Characterization of the effects of different lasers on the tensile strenght of fibers during laser writing of fiber Bragg gratings, *Proc. SPIE* 4876, 321-329 (2002)
36. Vengsarkar, A. M., Pedrazzani, J. R., Judkins, J. B., Lemaire, P. J., Long-period fiber grating based gain equalizers, *Opt. Lett.* 21, 336-338 (1996)

9 General conclusion

UV laser micromachining processes have been developed for four materials typically used for optical telecommunication devices: InP, $LiNbO_3$, Si and SiO_2. The aim of this research was to provide alternatives to the currently established methods of photonics device processing: dicing with fast rotating diamond blades and micro structuring with chemical etching. The development of alternatives has the potential to simplify device manufacturing processes and reduce design limitations to extend functional application potential.

For the development of alternative micromachining processes, UV solid state, excimer and fluorine lasers were used and integrated into their own laser micromachining systems. The UV solid-state laser was a 3rd harmonic Nd-YAG system with a wavelength of 355nm and was operated in a 'direct writing' mode. The excimer and fluorine laser were integrated into mask projection micromachining systems.

The 248nm KrF excimer laser micromachining system was installed with a fly's eye beam homogenizer and a high-resolution projection lens. A 193nm ArF excimer laser was also used, and to increase its beam uniformity a reduction telescope in combination with a blocking mask aperture was incorporated. For VUV processing a 157nm fluorine laser was integrated into a compact mask projection micromachining system in which bi-prisms increased the beam uniformity at the mask plane and a Schwarzschild projection lens was used to image the mask onto the material surface.

The average etch rate at different fluences was determined for all four materials. InP and the x- and z-cut $LiNbO_3$ crystal were exposed at each wavelength while the etch rate of Si was determined at wavelengths of 355nm, 193nm and 157nm. For fused silica, measurements were made at only one wavelengths, 157nm. In all experiments, the threshold fluence value, the point after which significant material removal occurred, was determined. The etch rate – fluence behaviour for x and z-cut $LiNbO_3$ showed similar characteristics.

The experimental threshold fluences were compared to calculated values, assuming the melting temperature of the material defines the threshold point after which significant material removal appears. For the experiments carried out at DUV wavelengths, there was an agreement between the calculated and experimental values, but with the VUV fluorine laser, a significant difference between the experimental and calculated value was seen.

Each etch rate experiment included an attempt to establish if the material removal was based on a thermal vaporization mechanism; one described possibly by an Arrhenius type thermal model. To determine this, the experimental data was re-plotted and the linear behaviour between ln (average etch per pulse) vs. inverse fluence was examined. The etch rate experiments carried out with VUV fluorine laser followed a linear trend but, with one exception, in the data collected with the DUV excimer and solid-state lasers, this linear relation could only be fitted at the low fluence settings while the material removal rate exceeded the predicted Arrhenius thermal model when the fluence was increased. It is possible that this change between the etch rate vs. fluence could be due to a change in the material removal process; a change from surface evaporation to volume evaporation. Further work is needed to explore this material removal process change in more detail.

Using a combination of two newly developed laser based micromachining processes it is possible to produce a passive fibre alignment platform out of x-cut and z-cut $LiNbO_3$. For this final product, a UV-solid state laser micromachining system was used to cut high quality 2-D structures out of 0.5mm thick $LiNbO_3$ wafers. A static mask – workpiece dragging process was developed with the KrF excimer laser micromachining system which was able to machine v-grooves for the alignment of optical fibres. Before introducing this laser based cutting process to a manufacturing environment, further process characterization would be required as this process is sensitive to thermal damage and hence cracking of the $LiNbO_3$ wafer. V-groove micromachining could be immediately introduced, but further characterization to optimise the surface roughness of the waveguide facet area, against which the optical fibre tip is positioned, would benefit light throughput and thus the quality of the manufactured device.

Optical microbenches with passive fibre alignment V-grooves were made in silicon by combining a newly developed cutting and a V-groove machining process. The cutting process allows the extraction of 2-D structures with debris free surfaces and high quality edges. As shown with the cutting of a microbench used in a prototype SOA, it is possible to cut complex designs microbenches and integrate them into hybrid based photonics devices. This could be immediately used in manufacturing. Again, improvements to the silicon V-groove machining process would be required before commercial application to improve surface quality on the v-shape surface and simplify the complex machining process which would contribute to the reproducibility of the groove shape, but these experiments suggest that both would be worth investigation.

The ability to machine fused silica with the fluorine laser micromachining system was explored on planar-based fused silica and optical fibres. By using static mask – work piece dragging techniques, processes for ridge optical waveguides and integrated micro mirrors were developed. Before being able to introduce fluorine laser to machine PLC based devices, the re-depositing of the process debris would need to be reduced, as no cladding layer would want be added with current amount of debris surrounding the machined ridge waveguide structures. Also, further process optimisation would need to be carried out to be able to produce similar surface quality as that already achieved with the reactive ion process.

Optical fibres, tip shaping and side polishing was attempted. Due to the core having a higher etch rate than the cladding, no effective fibre tip shaping was possible as the core was machined deeper when exposed at 157nm. Effective side polishing of the optical fibre was limited by the high numerical aperture of the mask projection system. This prevented the machining of deep vertical wall channels to access the fibre core and as a result, it was only possible to machine deep v-shaped grooves. The use of a low NA fluorine laser mask projection system would overcome the limitations of the current 157nm system to allow further process development of side polished optical fibres, which shows potential as a useful alternative to mechanical polishing.

A KrF excimer laser micromachining system was used to inscribe long period gratings into photosensitive fibres by mask projection technology. After a development process where the mask pattern, incident fluence and the number of laser pulses were trialled for optimum inscribing performance, a combined long period grating was written into a photosensitive fibre. The LPG center wavelength and its isolation strength were reproducible but the deviation within these two parameters could be reduced by using a spectrum analyser to control the exposure dose needed to write a LPG with the required specifications.

Acknowledgements

I would first and foremost like to thank my two supervisors: Dr. Nadeem Rizvi for his excellent supervision, advice and support throughout the experimental work reported here and Prof. Pete Dyer for his guidance, advice given and invaluable feedback particular during the writing process.

Also, I would like to thank Dr. Malcolm Gower and Dr. Phil Rumsby for giving me the opportunity to carry out this work at Exitech ltd. and my other colleagues, particularly Dr. Ric Allot, for their help during the duration of this work.

I would also like to thank Ailsa for all her support given!

Partial funding for this research was provided by the European Union in the form of a 'Marie Curie' grant, for which I am grateful.

Conference presentations

"UV laser micromachining of silicon, indium phosphide and lithium niobate for telecommunications applications"
Greuters, J., Rizvi, N. H.,
Proc. SPIE 4876, 479-489 (2002)

"Laser micromachining of optical materials with a 157-nm fluorine laser"
Greuters, J., Rizvi, N. H.,
Proc. SPIE 4941, 77-82 (2002)